

CONTROL OF LATERAL ELECTRON TRANSFER BETWEEN COMPOUNDS
ANCHORED TO SEMICONDUCTOR INTERFACES

Tyler Chase Motley

A dissertation submitted to the faculty of the University of North Carolina at Chapel Hill in
partial fulfillment of the requirements for the degree of Doctor of Philosophy in the
Department of Chemistry (Inorganic).

Chapel Hill
2018

Approved by:

Gerald J. Meyer

Joanna M. Atkin

Jillian L. Dempsey

Simon J. Meek

Thomas J. Meyer

© 2018
Tyler Chase Motley
ALL RIGHTS RESERVED

ABSTRACT

Tyler Chase Motley: Control of Lateral Electron Transfer between Compounds Anchored to Semiconductor Interfaces
(Under the direction of Gerald J. Meyer)

The need for a clean and renewable energy source is paramount to long term global economic and energy security and is the motivation for this work. The sun is one of the largest sources of renewable energy available. Dye-sensitized solar and photoelectrochemical cells that capture solar energy and convert it to either electricity or solar fuels provide an opportunity to investigate the relevant, molecular, reaction chemistry in such devices. One electron transfer pathway in both devices is lateral electron transfer between compounds anchored to the interface of the metal oxide films. The focus of this dissertation is to understand how structural changes to these compounds influence lateral electron transfer rates. The basic operating principles of dye-sensitized technologies and the relevant background to lateral electron transfer kinetics are given in Chapter 1.

Chapters 2-4 explore the effect of molecular structure on lateral electron transfer kinetics. In Chapters 2 and 3, the effect of 4 and 4' substituents are examined using a series of compounds of the type $[\text{Ru}(\text{R}_2\text{bpy})_2(\text{bpy}')]^{2+}$, where R_2bpy was a 4,4'-substituted-2,2'-bipyridine and bpy' was a 2,2'-bipyridine with either carboxylic or phosphonic acid binding groups at the 4 and 4' positions. These studies reveal that the steric bulk is the dominant factor controlling the measured self-exchange rate constants. In Chapter 4, four compounds with two redox active groups, a bis(tridentate) cyclometalated Ru^{II} metal center and a substituted-

triphenylamine donor connected by a thiophene bridge, are anchored to the TiO₂ interface and lateral intermolecular electron transfer is studied. This study shows that the intramolecular electronic coupling influences lateral charge transport rates.

Other processes relevant to dye-sensitized technologies are also explored. Thermal, bimolecular electron transfer between Co^{II} and Ru^{III} polypyridyl compounds that follows Marcus-inverted behavior is observed in acetonitrile and is the focus of Chapter 5. In Chapter 6, the photophysical properties and excited-state decay pathways are explored for a series of tris(bidentate) cyclometalated Ru^{II} chromophores which have emerged as a promising new paradigm for chromophore design in dye-sensitized solar cells. Temperature-dependent photoluminescence studies indicate that the dissociative ligand field states are not accessible at temperature, and that these compounds are photostable.

To my parents, my grandparents, my brother, and my nieces, thank you for all your love and support. I couldn't do it without you.

ACKNOWLEDGEMENTS

There are many people in my life to whom I am eternally grateful for facilitating my personal growth and for fanning the flames of curiosity.

First and foremost, I am indebted to my parents, Douglas and Terri, for being steadfast anchors throughout the roller-coaster that has been graduate school (and life). They have been constant sources of encouragement and strength, and they continue to remind me to “remember your roots.” I am grateful to my brother, Stuart, and my two wonderful nieces, Miley Rae and Allyson Grace, who remind me not to take myself too seriously and to continue to find joy in the small things. My grandparents, Edna Johnson and Ethel and Lewis Motley, always encouraged me to be the best that I could be and to always keep learning, lessons that I am thankful for. I am also grateful for the rest of my family who are too numerous to list here and who each hold a special place in my heart.

Second, I want to thank Dr. Jerry Meyer for being a great boss and a wonderful mentor over the past five years and encouraging me to be the scientist I have become. I would also like to say a special thank you to Dr. Alexander Miller who allowed me to work in his laboratory for several months while Jerry’s lab transitioned from Johns Hopkins to UNC.

During my time at UNC, I have had the privilege to work with a number of amazing scientists with whom I have had many insightful scientific discussions and who have been great sounding boards for many scientific ideas. So, I say thank you to Dr. Laura Casarin, Dr. Guocan Li, Dr. Renato N. Sampaio, Dr. Jenny Schneider, Dr. Ludovic Troian-Gautier, Dr. Cassandra L. Ward, Dr. Ke Hu, Dr. Ryan M. O’Donnell, Dr. Erinn C. Brigham, Dr. Timothy

J. Barr, Dr. Evan E. Beauvilliers, Dr. Brian N. DiMarco, Catherine G. Burton, Andrew B. Maurer, Eric J. Piechota, Matthew D. Brady, Victoria K. Davis, Erica M. James, Sara A. M. Wehlin, Rachel Bangle, Yuting F. Lin, and Michael D. Turlington, for your help and friendship over the past five years.

I would be remiss if I did not thank all of my friends here at UNC Chapel Hill for making this an enjoyable experience. I am especially grateful for my fellow cohort and dear friend, Dr. Wesley B. Swords, with whom I have been on this journey and who has been a constant source of encouragement and friendship. I also owe a special thank you to Erika Van Goethem who was always willing to listen to me vent about research and life. To the both of you, I say thanks, and I look forward to see where life leads you both. Thanks to my fellow teammates on the Dallas Cp Stars, Spring 2014 and 2018 co-rec intramural champions, for teaching me about hockey and being great people to be with both on the court and off. So, to Jake Green, Cortney Cavanaugh, Tony Carestia, and many others, thank you for being wonderful people.

Finally, I want to thank the numerous educators along the way both inside and outside of the classroom who encouraged me to always continue learning and ask questions of the world around me.

TABLE OF CONTENTS

LIST OF FIGURES	xiv
LIST OF TABLES	xxii
LIST OF SCHEMES.....	xxiii
CHAPTER 1: Strategies for Solar Energy Conversion and Storage and the Role of Lateral Charge Transport	1
1.1 Energy Supply and Demand: A Precarious Balancing Act	1
1.1.1 Current Energy Trends: The Case against Fossil Fuels	1
1.1.2 A Brighter Tomorrow: The Case for Solar Energy	4
1.2 The Photophysics of Ru ^{II} Polypyridyl Compounds	8
1.3 Dye-Sensitized Technologies	14
1.3.1 Dye-Sensitized Solar Cells.....	14
1.3.2 Dye-Sensitized Photoelectrochemical Cells	18
1.4 Lateral Electron Transfer at Semiconductor Interfaces	20
1.4.1 Introduction to Marcus Theory	21
1.4.2 Mechanism and Experimental Approaches for Lateral Electron Transfer	25
1.4.2.1 Quantifying Lateral Electron Transfer through Electrochemistry	28
1.4.2.2 Transient Absorption Spectroscopy to Quantify Lateral Electron Transfer Kinetics.....	31
1.4.3 Structural and Solvent Effects on Lateral Electron Transfer	33
1.4.4 Effects of Lateral Electron Transfer in DSSCs and DSPECs	38
1.5 Conclusion	41
REFERENCES	43

CHAPTER 2: A Distance Dependence to Lateral Self-Exchange across Nanocrystalline TiO ₂ . A Comparative Study of Three Homologous Ru ^{III/II} Polypyridyl Compounds	56
2.1 Introduction.....	56
2.2 Experimental Methods	61
2.2.1 Materials	61
2.2.2 Synthesis of [Ru(dmb) ₂ (deeb)](PF ₆) ₂ (1)	61
2.2.3 Synthesis of [Ru(dmb) ₂ (dcbH ₂)](PF ₆) ₂ (dmb)	62
2.2.4 Thin Film Preparation	63
2.2.5 UV-Visible Spectroscopy	63
2.2.6 Electrochemistry	64
2.2.7 Data Analysis	65
2.2.8 Calculation of c ₀ and R	66
2.3 Results.....	68
2.4 Discussion.....	76
2.4.1 Quantification of Reduction Potentials and Apparent Diffusion Coefficients	77
2.4.2 Self-Exchange Kinetics and Theory	80
2.5 Conclusions.....	82
2.6 Acknowledgements.....	83
2.7 Additional Content.....	84
2.6.1 Single Crystal X-ray Crystallography.....	85
REFERENCES	88
CHAPTER 3: Influence of 4 and 4' Substituents on Ru ^{III/II} Polypyridyl Self-Exchange Electron Transfer across Nanocrystalline TiO ₂ Surfaces.....	91
3.1 Introduction.....	91
3.2 Experimental Methods	96

3.2.1 Materials	96
3.2.2 Preparation of Thin Films	96
3.2.3 Spectroscopy	97
3.2.4 Chronoabsorptometry.....	97
3.2.5 Data Analysis	98
3.3 Results.....	98
3.4 Discussion.....	105
3.4.1 Quantification of Reduction Potentials and Apparent Diffusion Coefficients	106
3.4.2 Substituent Effects on Self-Exchange Electron Transfer at the Interface	109
3.5 Conclusions.....	113
3.6 Acknowledgements.....	114
3.7 Additional Content.....	114
REFERENCES	117
CHAPTER 4: Intramolecular Electronic Coupling Enhances Lateral Electron Transfer across Semiconductor Interfaces	122
4.1 Introduction.....	122
4.2 Experimental Methods	124
4.2.1 General Information.....	124
4.2.2 Preparation of TiO ₂ Thin Films	124
4.2.3 Electrochemistry	125
4.2.4 Data Analysis	125
4.3 Results and Discussion	126
4.4 Conclusion	131
4.5 Acknowledgements.....	132

4.6 Additional Content.....	132
REFERENCES	134
CHAPTER 5: Thermal Bimolecular Electron Transfer in the Marcus	
Inverted Region: Exploiting Nonadiabatic Electron Transfer	137
5.1 Introduction.....	137
5.2 Experimental Methods.....	139
5.2.1 Materials	139
5.2.2 General Procedure for the Synthesis of [Ru(R ₂ bpy) ₂ Cl ₂]	140
5.2.3 General Procedure for the Synthesis of the Cobalt Compounds.....	140
5.2.4 Synthesis of [Ru(dtb) ₂ (dab)](PF ₆) ₂	141
5.2.5 Synthesis of [Ru(dtb) ₂ (mab)](PF ₆) ₂	141
5.2.6 Synthesis of [Ru(MeObpy) ₂ (dmeb)](PF ₆) ₂	142
5.2.7 Synthesis of [Ru(dmb) ₂ (dmeb)](PF ₆) ₂	143
5.2.8 Synthesis of [Ru(Fbpy) ₂ (dcb)](PF ₆) ₂	143
5.2.9 Synthesis of [Ru(Fbpy) ₂ (dmeb)](PF ₆) ₂	144
5.2.10 Synthesis of [Ru(Brbpy) ₂ (dmeb)](PF ₆) ₂	144
5.2.11 Synthesis of [Ru(btmb) ₂ (dmeb)](PF ₆) ₂	145
5.2.12 Nuclear Magnetic Resonance Spectroscopy (NMR)	146
5.2.13 Electrospray Ionization Mass Spectrometry (ESI-MS)	146
5.2.14 Spectroscopy	147
5.2.15 Spectroelectrochemistry.....	148
5.2.16 Electrochemistry	148
5.2.17 Data Analysis	149
5.3 Results and Discussion	149
5.4 Conclusions.....	160
REFERENCES	161

CHAPTER 6: Excited-State Decay Pathways of Tris(bidentate) Cyclometalated Ruthenium(II) Compounds	167
6.1 Introduction.....	167
6.2 Experimental Methods	170
6.2.1 Materials	170
6.2.2 General Procedure for the Synthesis of $[\text{Ru}(\text{C}^{\wedge}\text{N})(\text{CH}_3\text{CN})_4](\text{PF}_6)$	171
6.2.3 Synthesis of $[\text{Ru}(\text{ppy})(\text{CH}_3\text{CN})_4](\text{PF}_6)$	171
6.2.4 Synthesis of $[\text{Ru}(\text{ppyF}_2)(\text{CH}_3\text{CN})_4](\text{PF}_6)$	171
6.2.5 Synthesis of $[\text{Ru}(\text{ppyCF}_3)(\text{CH}_3\text{CN})_4](\text{PF}_6)$	172
6.2.6 Synthesis of $[\text{Ru}(\text{deeb})_2(\text{ppy})](\text{PF}_6)$	172
6.2.7 Synthesis of $[\text{Ru}(\text{bpy})_2(\text{ppy})](\text{PF}_6)$	173
6.2.8 Synthesis of $[\text{Ru}(\text{dtb})_2(\text{ppy})](\text{PF}_6)$	173
6.2.9 Synthesis of $[\text{Ru}(\text{MeObpy})_2(\text{ppy})](\text{PF}_6)$	174
6.2.10 Synthesis of $[\text{Ru}(\text{deeb})_2(\text{ppyF}_2)](\text{PF}_6)$	174
6.2.11 Synthesis of $[\text{Ru}(\text{bpy})_2(\text{ppyF}_2)](\text{PF}_6)$	175
6.2.12 Synthesis of $[\text{Ru}(\text{MeObpy})_2(\text{ppyF}_2)](\text{PF}_6)$	176
6.2.13 Synthesis of $[\text{Ru}(\text{bpz})_2(\text{ppyCF}_3)](\text{PF}_6)$	176
6.2.14 Synthesis of $[\text{Ru}(\text{deeb})_2(\text{ppyCF}_3)](\text{PF}_6)$	177
6.2.15 Synthesis of $[\text{Ru}(\text{bpy})_2(\text{ppyCF}_3)](\text{PF}_6)$	178
6.2.16 Synthesis of $[\text{Ru}(\text{MeObpy})_2(\text{ppyCF}_3)](\text{PF}_6)$	178
6.2.17 Nuclear Magnetic Resonance Spectroscopy (NMR)	179
6.2.18 Electrospray Ionization-Mass Spectrometry (ESI-MS)	179
6.2.19 Elemental Analysis (EA)	180
6.2.20 Square Wave Voltammetry	180
6.2.21 UV-Visible Absorption	180

6.2.22 Steady-State Photoluminescence and Quantum Yield Determination	181
6.2.23 Temperature-Dependent, Time-Resolved Photoluminescence.....	181
6.2.24 Single-Mode, Franck-Condon Lineshape Analysis	182
6.2.25 Time-Correlated Single Photon Counting	182
6.2.26 Arrhenius Analysis.....	183
6.3 Results.....	183
6.4 Discussion.....	194
6.4.1 Effects of Ligand Substitution	195
6.4.2 Excited-State Characterization and the Energy Gap Law.....	196
6.4.3 Arrhenius Analysis.....	201
6.5 Conclusions.....	203
6.6 Acknowledgements.....	204
6.7 Additional Content.....	204
REFERENCES	211

LIST OF FIGURES

- Figure 1.1.** Historical average atmospheric CO₂ concentrations as measured from the Vostok ice core samples in Antarctica (black ■, taken from ref. ²³) or from atmospheric samples taken at the South Pole (red ●, taken from ref. ²⁴). 3
- Figure 1.2.** Net load reported by the California Independent System Operator (CA ISO) on the California electrical grid for March 31st of the specified years. The increasing contribution of photovoltaic solar energy production is decreasing the afternoon demand as indicated by the black arrow.⁴⁴ 6
- Figure 1.3.** (A) A simple molecular orbital diagram for [Ru(bpy)₃](PF₆)₂ in a pseudo-octahedral (*O_h*) geometry. In this diagram, the gray orbital sets indicate orbitals that are predominantly located on the 2,2'-bipyridine ligands and the black orbital sets indicate those that are primarily Ru-based. Some of the resulting molecular orbitals are omitted for clarity. Also depicted, are the common electronic transitions that are observed in the UV-visible electronic spectrum. (B) UV-visible electronic and the normalized photoluminescence spectra of [Ru(bpy)₃](PF₆)₂ acquired at room temperature in neat acetonitrile. 9
- Figure 1.4.** A Jablonski-type diagram for the [Ru(bpy)₃](PF₆)₂ in acetonitrile. The ¹GS is referenced to the *E*^o(Ru^{III/II}) of the compound. The energy of the ¹MLCT and ³MLCT states were determined from the energy of the peak in the UV-visible and photoluminescence spectra, respectively. The illustrated LF and fourth ³MLCT energies are the activation energies for crossing from the ³MLCT state. Intersystem crossing is abbreviated as ISC. 11
- Figure 1.5.** The standard solar irradiance (AM 1.5 Standard⁸⁸) measured on the surface of the Earth. The total area under the curve represents the amount of power per unit area that strikes the surface. The gray shaded box and the diagonal-filled box represents the photons with the appropriate energy for bandgap excitation of silicon and anatase TiO₂, respectively. 14
- Figure 1.6.** A schematic representation of an n-type DSSC using a generic Ru^{II} polypyridyl chromophore (Ru) and redox mediator (R). The favorable processes in the DSSC, in order, are (1) photoexcitation, (2) electron injection into the conduction band of TiO₂, (3) movement through the external circuit to perform work, (4) reduction of the redox mediator, (5) regeneration of the oxidized Ru sensitizer. Nonproductive pathways include (A) excited-state relaxation, (B) back-electron transfer, and (C) charge recombination all of which result in a loss of device efficiency. 16
- Figure 1.7.** A schematic of an n-type DSPEC with a generic Ru^{II} polypyridyl chromophore (Ru) and water-oxidation catalyst (WOC). Like a DSSC, the first three productive steps are (1) photoexcitation, (2) electron injection into the conduction band of TiO₂, and (3) movement of the electron to the counter-electrode. Next, the oxidized dye undergoes lateral electron transfer until an

oxidized dye reaches the WOC and is regenerated (4). Once the WOC has been oxidized four times, it oxidizes water (5). H₂ generation, a two-electron process, occurs at the Pt electrode (6). Nonproductive pathways include (A) excited-state relaxation, (B) back-electron transfer, and (C) charge recombination all of which result in a loss of device efficiency. 19

Figure 1.8. One-dimensional potential energy surfaces for the nonadiabatic, self-exchange electron transfer between an electron donor, D, and an electron acceptor, A. The reactant (black) and product (red) potential surfaces are represented as harmonic oscillators. Depicted is the structure of the encounter complex and inner-solvation sphere before, during, and after electron transfer. Indicated on the graph is the reorganization energy, λ , and the Gibbs free energy of activation, ΔG^\ddagger 22

Figure 1.9 One-dimensional potential energy surfaces depicting regimes of electron transfer predicted by nonadiabatic Marcus theory: (A) self-exchange electron transfer (Marcus normal) (B) Marcus normal region, (C) activationless region, and (D) Marcus inverted region. The reactant (black) and product (red) potential energy surfaces are depicted as harmonic oscillators. The crossing point for each regime is highlighted to emphasize the change between the three regimes. The reorganization energy (blue) and the Gibbs free energy of the reaction (green) are also depicted. 23

Figure 1.10. A typical Anson plot of the normalized change in absorbance as a function of the square root of time following a potential step sufficiently positive of the formal reduction potential of the surface-anchored compound. The red line is a fit to the Anson equation, eq 1.13, for the initial absorbance change. 29

Figure 1.11. (A) An idealized TiO₂ nanoparticle sensitized with and Ru^{II} polypyridyl compounds with the lowest-energy transition dipole moment depicted by the black arrow. Given the electric field vector of the linearly-polarized laser pulse, the probability that an incident photon would excite the chromophore is given. (B) The time evolution an idealized TiO₂ nanoparticle after photoexcitation with linearly-polarized laser pulse. 32

Figure 1.12. A depiction of the “dry cell” dye-sensitized solar cell which used lateral self-exchange electron transfer between the oxidized chromophore to complete the circuit rather than a redox mediator in solution. Photoexcitation leads to electron injection on the sensitized TiO₂ interface, and the electrons are collected at the FTO. Lateral self-exchange electron transfer shuttle the oxidizing equivalent to the Pt counter electrode. 39

Figure 2.1. Reaction coordinate for nonadiabatic (dashed lines) or adiabatic (solid lines) self-exchange electron transfer reaction. The orange and green spheres represent Ru molecules in the encounter complex before, during, and

after electron transfer. The blue spheres depict counterions and exaggerates their location and movement during the electron transfer process. 59

Figure 2.2. (a) Crystal structure of $[\text{Ru}(\text{dmb})_2(\text{deeb})](\text{PF}_6)_2$. b) Crystal structure of $[\text{Ru}(\text{dtb})_2(\text{dcbH}_2)](\text{ClO}_4)_2$. All hydrogen atoms and anions are omitted for clarity purposes. Color code: Pink, Ru; blue, N; red, O; gray, C. 69

Figure 2.3. Normalized absorption spectra of compounds **bpy**, **dmb**, and **dtb** anchored to TiO_2 in neat CH_3CN (solid line) or in a 0.1 M LiClO_4 solution in CH_3CN (dashed line). The TiO_2 absorption spectrum was subtracted out from the spectra of the surface-functionalized films. 70

Figure 2.4. Spectroelectrochemical oxidation of $\text{TiO}_2|\text{dmb}$ immersed in 0.1 M $\text{LiClO}_4/\text{CH}_3\text{CN}$ electrolyte. The inset plots the fraction of oxidized or reduced compound as a function of applied potential. Overlaid is a fit to a modified Nernst equation, eq 2.5. 71

Figure 2.5. Normalized absorption change measured after application of a potential sufficient to oxidize the indicated compounds plotted against the square root of time. Overlaid in gold is the fit based on eq 2.6. 73

Figure 2.6. Representative cyclic voltammograms for **dmb** anchored to TiO_2 immersed in 0.1 M LiClO_4 in CH_3CN at the indicated temperatures. 74

Figure 2.7. (A) Arrhenius plot for **bpy**, **dmb**, and **dtb** anchored to TiO_2 describing the variation of D_{CV} with inverse temperature as obtained by cyclic voltammetry. Overlaid are the best fits to the Arrhenius equation. (B) The temperature dependence of k_{SE} as described by nonadiabatic Marcus theory (overlaid curves). 76

Figure 2.8. The temperature dependence of k_{SE} with fits to non-adiabatic Marcus theory (overlaid curves) calculated with three different values of R for $\text{TiO}_2|\text{dmb}$ 84

Figure 2.9. UV-visible spectra generated during the oxidation of **bpy**. Conversion from Ru^{II} to Ru^{III} proceeds from purple to red. 84

Figure 2.10. UV-visible spectra generated during the oxidation of **dtb**. Conversion from Ru^{II} to Ru^{III} proceeds from purple to red. 85

Figure 3.1. The normalized UV-visible absorbance spectra for each $[\text{Ru}(\text{R}_2\text{bpy})_2(\text{P})]/\text{TiO}_2$ film submerged in CH_3CN solutions containing 0.1 M LiClO_4 with an unsensitized thin film as a reference. 99

Figure 3.2. The UV-visible absorption spectra measured after the application a potential sufficient to oxidize $[\text{Ru}(\text{dtb})_2(\text{P})]/\text{TiO}_2$. A bleach of the characteristic MLCT transition was observed at 470 nm as the film was oxidized from Ru^{II} to Ru^{III} . A new absorption feature associated with the Ru^{III} species was observed

to grow in centered at 675 nm. The inset shows the normalized absorbance change plotted against the square root of time. The data were fit to the Anson equation through the first 60% of the total absorbance change (red line). 101

Figure 3.3. The normalized change in absorbance after the application of sufficiently positive potential to oxidize the $[\text{Ru}(\text{R}_2\text{bpy})_2(\text{P})]/\text{TiO}_2$ plotted as a function of the square root of time for all compounds used in this study..... 102

Figure 3.4. The variation of the measured apparent diffusion coefficients (D_{CA}) for $[\text{Ru}(\text{bpy})_2(\text{P})]/\text{TiO}_2$ with the fractional surface coverage (Γ/Γ_0), where Γ_0 was the maximum surface coverage attained in the most concentrated dyeing solution (5 mM). The D_{CA} were measured in CH_3CN solutions with 0.1 M LiClO_4 electrolyte. Error bars for D_{CA} included for all data..... 103

Figure 3.5. The dependence of the measured $E_{1/2}(\text{Ru}^{\text{III/II}})$ (black, ■) and of $\log(k_{\text{H}}/k_{\text{R}})$ (red, ●) on the summative Hammett parameter, σ_{T} , for all $[\text{Ru}(\text{R}_2\text{bpy})_2(\text{P})]/\text{TiO}_2$. The measured $E_{1/2}(\text{Ru}^{\text{III/II}})$ displayed a strong correlation with σ_{T} with a slope of 0.09 V vs NHE. No such correlation was observed with $\log(k_{\text{H}}/k_{\text{R}})$. Error bars are given for the $\log(k_{\text{H}}/k_{\text{R}})$ data. 106

Figure 3.6. The dependence of the saturation surface coverage, Γ , with the steric size of the substituent in the 4 and 4' positions of $[\text{Ru}(\text{R}_2\text{bpy})_2(\text{P})]/\text{TiO}_2$ as given by the Charton value. Error bars are included for the measured Γ_0 111

Figure 3.7. The $\text{Ru}^{\text{III/II}}$ lateral self-exchange electron transfer rate constant versus the difference intermolecular distance, $\Delta\delta$. The distance was varied by either (A, black ■) changing the steric size of the -R group at the 4 and 4' positions ($\beta = 1.2 \pm 0.2 \text{ \AA}^{-1}$) or (B, red ●) functionalizing the TiO_2 with $[\text{Ru}(\text{bpy})_2(\text{P})]^{2+}$ from dilute dyeing solutions ($\beta = 1.18 \pm 0.09 \text{ \AA}^{-1}$). Error bars are given for the $\ln(k_{\text{R}})$ 112

Figure 3.8. The UV-visible spectral changes after the application a potential sufficient to oxidize $[\text{Ru}(\text{MeObpy})_2(\text{P})]/\text{TiO}_2$. A bleach of the characteristic MLCT transition was observed at 480 nm as the film was oxidized from Ru^{II} to Ru^{III} . A new peak associated with the Ru^{III} species was observed to grow in centered at 550 nm. The inset shows the normalized absorbance change plotted against the square root of time. The data were fit to the Anson equation through the first 60% of the total absorbance change (red line). 114

Figure 3.9. The UV-visible spectral changes after the application a potential sufficient to oxidize $[\text{Ru}(\text{dmb})_2(\text{P})]/\text{TiO}_2$. A bleach of the characteristic MLCT transition was observed at 465 nm as the film was oxidized from Ru^{II} to Ru^{III} . A new peak associated with the Ru^{III} species was observed to grow in centered at 675 nm. The inset shows the normalized absorbance change plotted against the square root of time. The data were fit to the Anson equation through the first 60% of the total absorbance change (red line). 115

Figure 3.10. The UV-visible spectral changes after the application a potential sufficient to oxidize [Ru(bpy)₂(P)]TiO₂. A bleach of the characteristic MLCT transition was observed at 455 nm as the film was oxidized from Ru^{II} to Ru^{III}. A new peak associated with the Ru^{III} species was observed to grow in centered at 700 nm. The inset shows the normalized absorbance change plotted against the square root of time. The data were fit to the Anson equation through the first 60% of the total absorbance change (red line). 115

Figure 3.11. The UV-visible spectral changes after the application a potential sufficient to oxidize [Ru(Brbpy)₂(P)]TiO₂. A bleach of the characteristic MLCT transition was observed at 465 nm as the film was oxidized from Ru^{II} to Ru^{III}. A new peak associated with the Ru^{III} species was observed to grow in centered at 700 nm. The inset shows the normalized absorbance change plotted against the square root of time. The data were fit to the Anson equation through the first 60% of the total absorbance change (red line). 116

Figure 3.12. The UV-visible spectral changes after the application a potential sufficient to oxidize [Ru(btmb)₂(P)]TiO₂. A bleach of the characteristic MLCT transition was observed at 440 nm as the film was oxidized from Ru^{II} to Ru^{III}. A new peak associated with the Ru^{III} species was observed to grow in centered at 740 nm. The inset shows the normalized absorbance change plotted against the square root of time. The data were fit to the Anson equation through the first 60% of the total absorbance change (red line). 116

Figure 4.1. The UV-visible absorption spectra for (A) **1x**, (B) **1p**, (C) **2x**, and (D) **2p** obtained after a potential step at time zero initiated the oxidation of the indicated compounds anchored to TiO₂ thin films immersed in a 0.1 M LiClO₄ solution in CH₃CN. The absorption decrease in the 400-600 nm region reported primarily on the Ru^{II} oxidation while the growth in the 650-800 nm region reported primarily on the TPA⁰ oxidation. 126

Figure 4.2. The normalized change in absorbance as a function of the square root of time measured after the application of a potential sufficient to oxidize both the TPA⁰ to TPA⁺ (A) and Ru^{II} to Ru^{III} (B). 128

Figure 4.3. The normalized change in absorbance plotted against the square root of time for **1x** (A) and **1p** (B) monitored at 525 nm (Ru^{III/II}) and 750 nm (TPA^{+/0}). Overlaid are the lines of best fit to the Anson equation for each set of kinetic data through the initial 60% of the total change. 132

Figure 4.4. The normalized change in absorbance plotted against the square root of time for **2x** (A) and **2p** (B) monitored at 525 nm (Ru^{III/II}) and 750 nm (TPA^{+/0}). Overlaid are the lines of best fit to the Anson equation for each set of kinetic data through the initial 60% of the total change. For **2p**, the Ru^{III/II} oxidation kinetics were also fit after the “induction” period ($t^{1/2} > 1.25 \text{ s}^{1/2}$) and is overlaid (gold line) on the data. 133

Figure 5.1. Spectroelectrochemical oxidation of $[\text{Ru}(\text{dtb})_2(\text{dmeb})](\text{PF}_6)_2$ in a CH_3CN solution containing 0.1 M LiClO_4 . The inset shows the mole fraction of the Ru^{2+} and Ru^{3+} compounds as a function of the applied potential. Overlaid is a fit to the modified Nernst equation, eq 5.2. 151

Figure 5.2. Spectroelectrochemical oxidation of $[\text{Co}(\text{bpy})_3](\text{PF}_6)_2$ in a CH_3CN solution containing 0.1 M LiClO_4 . The inset is a cyclic voltammogram obtained for $[\text{Co}(\text{bpy})_3](\text{PF}_6)_2$ in 0.1 M $\text{LiClO}_4/\text{CH}_3\text{CN}$ solutions at a scan rate of 0.1 V/s. 152

Figure 5.3. (A) Nanosecond transient kinetic data acquired for a CH_3CN solution containing only $[\text{Ru}(\text{dtb})_2(\text{dmeb})](\text{PF}_6)_2$ (black, λ_{exc} , 488 nm; probe, 520 nm) or only $[\text{Co}(\text{bpy})_3](\text{PF}_6)_2$ (red, λ_{exc} , 488 nm; probe, 470 nm). Overlaid in blue is a single-exponential fit for the excited-state decay of $[\text{Ru}(\text{dtb})_2(\text{dmeb})](\text{PF}_6)_2$. (B) Nanosecond transient kinetic data acquired for an acetonitrile solution containing 2.5×10^{-5} , 1×10^{-4} , and 2.5×10^{-3} M of $[\text{Ru}(\text{dtb})_2(\text{dmeb})](\text{PF}_6)_2$, $[\text{Co}(\text{bpy})_3](\text{PF}_6)_2$, and $[\text{Co}(\text{bpy})_3](\text{PF}_6)_3$, respectively (λ_{exc} , 488 nm; probe, 495 nm; laser fluence, 4.8 mJ/pulse). Overlaid in red is a fit to pseudo-first order kinetics. 154

Figure 5.4. The dependence of the back-electron transfer rate constant, k_{et} , on the driving force, ΔG° . Overlaid are the fits to the nonadiabatic Marcus equation, eq 5.1. The electronic coupling matrix element, H_{DA} , was a shared parameter during the fitting process and was found to be 0.02 ± 0.001 meV. The reorganization energies, λ , were found to be 1.1 ± 0.1 eV and 1.4 ± 0.1 eV for the back-electron transfer reactions with $[\text{Co}(\text{bpy})_3]^{2+}$ and $[\text{Co}(\text{dmb})_3]^{2+}$, respectively. 158

Figure 6.1. Square wave voltammogram for $[\text{Ru}(\text{bpy})_2(\text{ppy})]^+$ in an CH_3CN solution containing 0.1 M LiClO_4 at room temperature. 186

Figure 6.2. The UV-visible absorption (solid) and photoluminescence (dashed) spectra of (A) $[\text{Ru}(\text{deeb})_2(\text{C}^{\wedge}\text{N})]^+$, (B) $[\text{Ru}(\text{bpy})_2(\text{C}^{\wedge}\text{N})]^+$, (C) $[\text{Ru}(\text{MeObpy})_2(\text{C}^{\wedge}\text{N})]^+$, and (D) $[\text{Ru}(\text{N}^{\wedge}\text{N})_2(\text{C}^{\wedge}\text{N})]^+$ in Ar-sparged CH_3CN 187

Figure 6.3. The steady-state photoluminescence spectra (dotted) and the fits (solid) obtained from the single-mode, Franck-Condon lineshape analysis of (A) $[\text{Ru}(\text{deeb})_2(\text{C}^{\wedge}\text{N})]^+$, (B) $[\text{Ru}(\text{bpy})_2(\text{C}^{\wedge}\text{N})]^+$, (C) $[\text{Ru}(\text{MeObpy})_2(\text{C}^{\wedge}\text{N})]^+$, and (D) $[\text{Ru}(\text{N}^{\wedge}\text{N})_2(\text{C}^{\wedge}\text{N})]^+$ in 4:1 EtOH:MeOH at 77 K 189

Figure 6.4. (A) Time-resolved PL data of $[\text{Ru}(\text{bpy})_2(\text{ppy})]^+$ following 444 nm pulsed diode laser excitation in neat CH_3CN at different temperatures. (B) An example of the reconvolution fitting used to fit the time-resolved PL data where the black is the measured PL data, red is the measured instrument response function (IRF) and the yellow trace is the reconvoluted fit provided by the DecayFit software. The bottom plot shows the residual of this fit. 192

Figure 6.5. Photoluminescence lifetimes measured in CH ₃ CN plotted against the change in temperature in an Arrhenius plot for [Ru(deeb) ₂ (C [^] N)] ⁺ (A), [Ru(bpy) ₂ (C [^] N)] ⁺ (B), [Ru(MeObpy) ₂ (C [^] N)] ⁺ (C), and [Ru(N [^] N) ₂ (C [^] N)] ⁺ (D). Overlaid are the solid lines representing the best fits to the Arrhenius equation.....	194
Figure 6.6. A comparison of the S _M vs E ₀ for the indicated compounds, Table 6.3. The error in E ₀ and S _M is ±30 and ±0.01, respectively. Overlaid is the line of best fit with a slope of 1.23 ± 0.15 × 10 ⁻⁴ cm.....	197
Figure 6.7. An energy gap law plot of ln(k _{nr}) vs E ₀ measured at 293 K in CH ₃ CN. The overlaid fits to eq 6.6 represent the line of best fit for the [Ru(deeb) ₂ (C [^] N)] ⁺ , [Ru(bpy) ₂ (C [^] N)] ⁺ , and [Ru(MeObpy) ₂ (C [^] N)] ⁺ with slopes of (500 cm ⁻¹) ⁻¹ , (900 cm ⁻¹) ⁻¹ , and (1100 cm ⁻¹) ⁻¹ , respectively. Labels are given in Table 6.3.	199
Figure 6.8. An energy gap law plot with the vibronic wavefunction overlap, ln(F), computed from the FC fitting parameters obtained at 293 K in CH ₃ CN for [Ru(N [^] N) ₂ (C [^] N)] ⁺ (black ■) with a fit (black line) to eq 6.3 with a fixed slope of unity which yielded an intercept of -34.9. Previously reported data for for [Os(bpy) ₂ (LL)] ²⁺ (open red ●), [Os(phen) ₂ (LL)] ²⁺ (open blue ▲), and [Ru(bpy) ₂ (LL)] ²⁺ (open green ▼) are also shown. The red line is a fit of eq 6.3 to all the data with the slope fixed to unity.....	200
Figure 6.9. A Jablonski-type Diagram for [Ru(N [^] N) ₃] ²⁺ and [Ru(N [^] N) ₂ (C [^] N)] ⁺ . The ¹ GS is referenced to the E°(Ru ^{2+/+}). The dashed lines represent E _a from the ³ MLCT state. Note that ISC is short for intersystem crossing.	203
Figure 6.10. ¹ H NMR spectrum of [Ru(MeObpy) ₂ (ppy)] ⁺ in d ₆ -DMSO at 400 MHz and 298 K.....	204
Figure 6.11. ¹ H NMR spectrum of the aromatic region for [Ru(MeObpy) ₂ (ppy)] ⁺ in d ₆ -DMSO at 400 MHz and 298 K.....	205
Figure 6.12. ¹ H NMR spectrum of [Ru(MeObpy) ₂ (ppyF ₂)] ⁺ in d ₆ -DMSO at 400 MHz and 298 K.....	205
Figure 6.13. ¹ H NMR spectrum of the aromatic region for [Ru(MeObpy) ₂ (ppyF ₂)] ⁺ in d ₆ -DMSO at 400 MHz and 298 K.	206
Figure 6.14. ¹ H NMR spectrum of [Ru(bpz) ₂ (ppyCF ₃)] ⁺ in CD ₃ CN at 400 MHz and 298 K.....	206
Figure 6.15. ¹ H NMR spectrum of the aromatic region for [Ru(bpz) ₂ (ppyCF ₃)] ⁺ in CD ₃ CN at 400 MHz and 298 K.....	207

Figure 6.16. ^1H NMR spectrum of $[\text{Ru}(\text{deeb})_2(\text{ppyCF}_3)]^+$ in CD_3CN at 400 MHz and 298 K.....	207
Figure 6.17. ^1H NMR spectrum of the aromatic region for $[\text{Ru}(\text{deeb})_2(\text{ppyCF}_3)]^+$ in CD_3CN at 400 MHz and 298 K.	208
Figure 6.18. ^1H NMR spectrum of $[\text{Ru}(\text{bpy})_2(\text{ppyCF}_3)]^+$ in CD_3CN at 400 MHz and 298 K.....	208
Figure 6.19. ^1H NMR spectrum of the aromatic region for $[\text{Ru}(\text{bpy})_2(\text{ppyCF}_3)]^+$ in CD_3CN at 400 MHz and 298 K.....	209
Figure 6.20. ^1H NMR spectrum of $[\text{Ru}(\text{MeObpy})_2(\text{ppyCF}_3)]^+$ in CD_3CN at 400 MHz and 298 K.....	209
Figure 6.21. ^1H NMR spectrum of the aromatic region for $[\text{Ru}(\text{MeObpy})_2(\text{ppyCF}_3)]^+$ in CD_3CN at 400 MHz and 298 K.	210

LIST OF TABLES

Table 1.1. Selected Apparent Diffusion Coefficients, D , for Lateral Self-Exchange Electron Transfer.....	34
Table 2.1. Selected Crystal Structure Parameters	69
Table 2.2. Selected Spectral, Electrochemical, and Film Parameters for the Compounds Studied.....	71
Table 2.3. Apparent Diffusion Coefficients and Marcus Self-Exchange Parameters for Surface Anchored Ruthenium Compounds	73
Table 2.4. Variation of R and H_{AB} Using Different Methods of Determining R	85
Table 3.1. Relevant Electrochemical and Photophysical Properties of the $[Ru(R_2bpy)_2(P)](Br)_2$ Compounds.....	100
Table 3.2. Selected Hammett and Charton Parameters.....	107
Table 4.1. Relevant Thermodynamic and Electron-Transfer Dynamics.....	124
Table 5.1. Spectroscopic, Thermodynamic, and Kinetic Data for the Ru^{II} and Co^{II} Polypyridyl Compounds.....	153
Table 6.1. Electrochemical Data for the Studied Compounds.....	185
Table 6.2. Summary of the Spectroscopic and Photophysical Data.....	188
Table 6.3. Fitting Parameters Obtained from the Franck-Condon Lineshape Analysis.....	190
Table 6.4. Parameters Obtained from the Arrhenius Analysis.....	192

LIST OF SCHEMES

Scheme 1.1. Lateral Intermolecular Self-Exchange Electron Transfer across Anatase TiO ₂ Nanocrystallites	20
Scheme 1.2. A Depiction of the Time Evolution of the Complete Film Oxidation during a Chronoabsorptometry Experiment.....	27
Scheme 1.3. Schematic Representation of a Transient Absorption Experiment Utilizing a Co-Adsorbed Electron Donor to Measure Lateral Electron Transfer of a Free-Base Porphyrin	31
Scheme 1.4. Relevant Compounds used for Lateral Self-Exchange Electron Transfer.	33
Scheme 2.1. Illustration of Lateral Intermolecular Self-Exchange Electron Transfer across Anatase TiO ₂ Nanocrystallites Initiated at the Fluorine-Doped Tin Oxide (FTO) Substrate	57
Scheme 2.2. Chemical Structure of the Molecules Studied	60
Scheme 2.3. An Idealized Representation of Three Surface Functionalized Anatase Layers on an FTO Substrate during a Chronoabsorptometry (CA) Experiment.....	78
Scheme 3.1. A Depiction of the Time Evolution of the Complete Film Oxidation during a Chronoabsorptometry Experiment.....	92
Scheme 3.2. Ru ^{II} Polypyridyl Compounds Used in this Study	95
Scheme 4.1. Structure of the Compounds used in this Study.....	123
Scheme 4.2. An Idealized Representation of the Evolution of the Sensitized TiO ₂ Films during a Chronoabsorptometry Experiment.....	127
Scheme 5.1. Polypyridyl Ligands Utilized in this Study.....	149
Scheme 6.1. Tris(bidentate) Cyclometalated Ru(II) Compounds Used in this Study	169

CHAPTER 1: Strategies for Solar Energy Conversion and Storage and the Role of Lateral Charge Transport

1.1 Energy Supply and Demand: A Precarious Balancing Act

1.1.1 Current Energy Trends: The Case against Fossil Fuels

The total energy consumption in 2015 was ~160 petawatt hours (1 petawatt hour, PWh = 10^{12} kilowatt hours) with ~85% coming from nonrenewable energy sources (coal, oil, and natural gas).^{1,2} At the *present* rate of energy consumption, the proven global fossil fuel reserves are expected to fulfill the global energy needs for only another 40 years, and continued extraction using new techniques, such as hydraulic fracturing and horizontal drilling, could continue to satisfy demand well into the current millennium.² However, this estimate does not account for the projected rise in energy consumption with conservative estimates predicting that consumption will reach 216 PWh by 2040.¹ One of the primary driving forces for this increase in energy demand is the growing global population that is expected to reach 9.8 billion by 2050, a significant increase over the 7.6 billion reported in mid-2017.^{1,3} Further adding to the rising demand is the continued growth of emerging economies and the rise of the global standards of living.^{4,5} The limited fossil fuel resources and their geographical location has the potential to lead to political and economic instability in the coming decades as evidenced by the US oil crises in the 1970s and 2000s.⁶⁻⁸ Therefore, alternatives to the current energy mix will be necessary as fossil fuel resources become scarce, and economic and political security become increasingly more tenuous.

An inescapable consequence of fossil fuel extraction and use is the deleterious effects

on the environment and climate. The extraction of fossil fuels through surface and traditional mining, hydraulic fracturing, and drilling has been linked to local instances of higher stream- and groundwater contaminants and higher air particulate concentrations in the surrounding areas.^{9,10} These higher pollutant concentrations have been linked to increased risk of disease and illness among the local communities and damage to the local ecosystems.¹⁰⁻¹² The burning of fossil fuels, such as coal, releases particulates into the air that affect local air quality.¹³ In Beijing and many parts of China, the industrial use of coal has caused such poor air quality that the World Health Organization (WHO) has attributed air pollution as one of the leading causes of premature death in the region.¹⁴ In recent decades, several high-profile fossil fuel releases have highlighted the potential short-term and long-term adverse ecological and health effects: the *Exxon Valdez* oil spill in 1989 off the Alaskan coast,¹⁵ the *Deep Horizon* oil spill in 2010 off the Gulf Coast,¹⁶ and the Aliso Canyon gas leak in 2015-2016 in the greater Los Angeles metropolitan area to name a few.¹⁷

A more insidious problem with the extraction and use of fossil fuels is the release of greenhouse gasses with the most prominent being carbon dioxide (CO₂). In fact, the possible consequences of high CO₂ concentrations have been recognized since the late 1890s.¹⁸ Greenhouse gasses absorb the low, infrared energy photons emitted by the earth and radiates this energy back towards the surface which results in higher temperatures.^{19,20} Low concentrations of greenhouse gasses are necessary to sustain life on earth.²⁰ Since the beginning of the Industrial Revolution, starting around 1800, the use of fossil fuels has increased dramatically resulting in a large release of many greenhouse gasses.²¹ Pre-anthropogenic atmospheric CO₂ concentrations remained nearly constant between 150 and 300 ppm for over 400,000 years according to the Vostok and Law Dome ice core data extracted

from Antarctica.^{22,23} However, atmospheric CO₂ concentrations from the burning of fossil fuels and changing land-use practices has caused a surge from pre-anthropogenic levels to over 400 ppm in 2016 due to prolific fossil fuel use, Figure 1.1.^{19,21,22,24} During the same timeframe, global temperatures have risen by about 2 °C and climate patterns have begun to shift drastically.¹⁹ The coincidence of rising greenhouse gas concentrations and atmospheric temperatures has caused many within the scientific community to implicate anthropogenic greenhouse gas release as the cause of these climate changes.

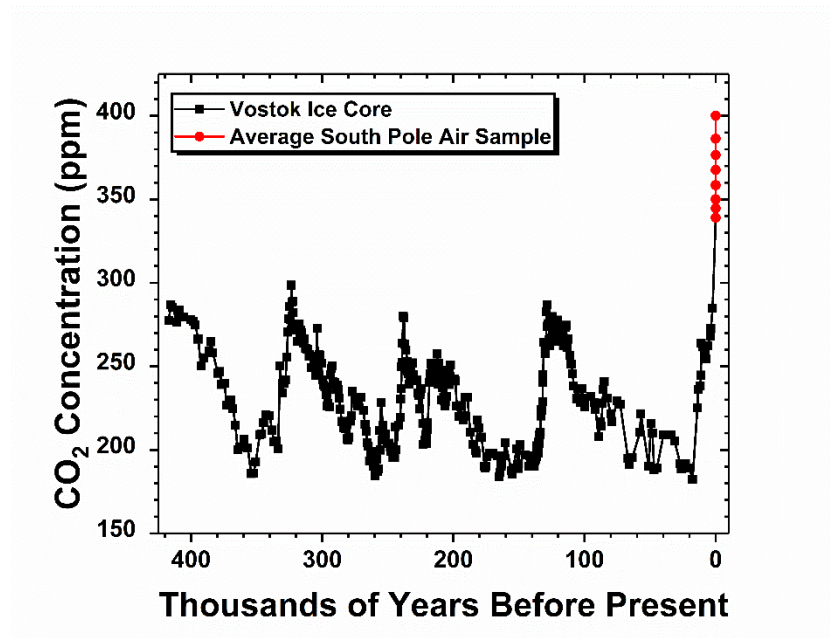


Figure 1.1. Historical average atmospheric CO₂ concentrations as measured from the Vostok ice core samples in Antarctica (black ■, taken from ref. ²³) or from atmospheric samples taken at the South Pole (red ●, taken from ref. ²⁴).

While the extent to which human activity has affected and will continue to affect naturally occurring climate fluctuations is contentious in the public sphere, there are numerous observations that are agreed upon by the scientific community that should raise concern over the next several decades. First, weather patterns are becoming more extreme with the frequency and intensity of localized areas of draught and heavy precipitation events rising.^{19,21} The

changing weather pattern coupled with warmer global temperatures has the potential to negatively impact agricultural food production and alter local ecosystems, potentially irreversibly.^{19,25,26} Second, rising CO₂ concentrations in the oceans have resulted in a decrease in ocean pH which threatens many marine ecosystems some of which are the sole food source for nearby coastal communities.^{19,21} Third, the melting of the polar ice caps and glaciers has led to a rise in sea levels which is resulting in more frequent coastal flooding and the loss of habitable lands.^{19,21} These three observations point to an increased risk of food shortages and the displacement of many communities in the coming years. Therefore, the need for an alternative, cleaner energy source is apparent and desired.

1.1.2 A Brighter Tomorrow: The Case for Solar Energy

The radiant energy from the sun represents one of the largest sources of green, renewable energy available on Earth. The amount of energy striking the surface of the earth ($5.10 \times 10^{14} \text{ m}^2$) in 1 h at a typical solar irradiance ($\sim 300 \text{ W/m}^2$) is 154 PWh.^{27,28} Therefore, in a little over an *hour*, the global energy demand for the *entire* year of 2015 could be satisfied.^{29,30} Even capturing roughly 10% of the energy that irradiates the earth in a given day, assuming 12 h of sunlight, would meet the entire global demand for a year. Even though the sun's ability to power the globe has been recognized as early as 1912, the amount of energy extracted artificially by photovoltaics is small.³¹ As of 2015, roughly 1.25% of the total electricity produced was from solar energy with this number projected to increase to 2.5% by 2040.¹ There are three main strategies that are available to capture solar energy and convert it to electricity: solar-to-thermal, solar-to-electricity, or solar-to-fuel conversions.³²

Solar-to-thermal energy conversion, first commercialized in the 1980s, is accomplished using large solar concentrators (mirrors) to focus direct sunlight onto a receiver.³³ Sunlight is absorbed by the receiver and is converted to thermal energy which is used to drive heat engines.

Through the Carnot cycle, thermal energy is converted to mechanical energy which in turn drives a turbine to produce electrical power. The maximum theoretical solar-to-thermal energy conversion efficiency is ~85%, though limits to maximum operating temperatures and materials performance have resulted in typical peak efficiency for these systems of only 15-20%.³³ Another downside to this conversion method is that solar-to-thermal energy conversion plants require large areas of land in locations that experience high average solar irradiation to collect the diffuse solar light and to be cost effective.³³

Direct conversion of solar energy to electricity has been the dominant conversion strategy used to capture solar energy through the use of photovoltaic, semiconductor materials, such as silicon.^{32,34} While photovoltaic materials have been known since the 1800s, commercial use of solar cells was not realized until the late 1950s, with the semiconductor of choice being crystalline silicon.³⁵ These materials have electronic bandgaps that are well-tuned to harvest solar photons to generate electricity. While the efficiency of single-junction silicon solar cells is approaching 23% (theoretical maximum under solar irradiation = 33%), the price to manufacture these materials at the high purity required has historically been a barrier to their widespread implementation.³⁵⁻³⁷ The high cost has driven many to research other next generation technologies such as dye-sensitized solar cells, organic solar cells, perovskite photovoltaics, and quantum dot solar cells.^{29,32,38,39} However, recent improvements to the manufacturing techniques has dramatically reduced the costs of silicon-based solar cells leading to devices that are more affordable and competitive with established energy sources.⁴⁰ Thus, silicon solar cells are finding more widespread implementation in both the residential and commercial markets.⁴⁰ Like many solar-to-thermal conversion methods, solar-to-electricity technologies require direct sunlight to efficiently produce electricity. Therefore, the

implementation of photovoltaic technologies is limited to regions with abundant sunshine. Even in such locations, energy conversion will be limited by weather conditions and the diurnal cycle of the sun.

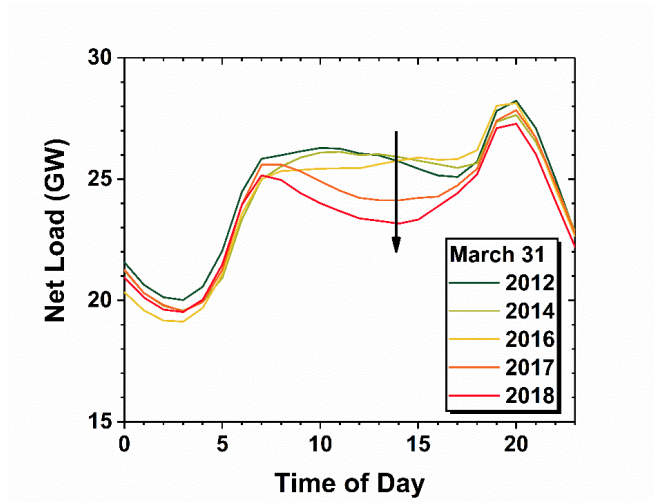


Figure 1.2. Net load reported by the California Independent System Operator (CA ISO) on the California electrical grid for March 31st of the specified years. The increasing contribution of photovoltaic solar energy production is decreasing the afternoon demand as indicated by the black arrow.⁴⁴

An unintended consequence of the increasing adoption of solar cell technologies in the short term is the risk placed on the existing national electrical grid.⁴¹⁻⁴³ Power plants adjust power production to match demand. There are two peak usage periods, a small one in the morning and a large one in the early evening. During the middle of the day and late at night, power plants ramp down the power production as less is needed. However, the peak solar irradiance occurs during the afternoon when demand is low. Therefore, the influx of electricity produced by solar devices during this period further reduces midday demand as seen in Figure 1.2. Thus, rapid ramp-downs and ramp-ups of energy production are necessary for power companies to maintain profits. Current fossil fuel power plants and the national electrical grid were not designed for rapid changes in production and are at risk of being damaged in the

short-term and failing in the long-term.⁴¹⁻⁴³ Therefore, efficient methods to store solar energy for later use are critical for the widespread implementation of solar energy technologies.

The final method for solar energy collection is solar-to-fuel production where solar energy is stored in chemical bonds, sometimes referred to as artificial photosynthesis. Chemical bonds represent one of the most energy-dense ways to store solar energy.⁴ Plants and some bacteria have evolved over millions of years to capture solar energy and use it to form carbohydrates, eq 1.1.⁴⁵ Known as photosynthesis, this process is only 1-4% efficient and the cascade of energy and electron transfer reactions required are complex with the formation of carbohydrates requiring a significant free energy input.^{45,46} Indeed, many of the target solar-fuel generating reactions for artificial photosynthesis (i.e. CO₂ reduction, N₂ reduction, H₂ generation) are multielectron process which are difficult chemical transformations.⁴⁵ The first artificial generation of solar fuel was by Honda and Fujishima in 1972 where direct bandgap excitation of titanium dioxide films (TiO₂) oxidized H₂O to O₂ with proton reduction occurring at a platinum counter electrode, a process that requires 1.23 V vs the normal hydrogen electrode (NHE) of energy at pH 0. An external bias or pH gradient was needed to carry out the complimentary proton reduction at the platinum counter electrode meaning this was not a 100% photodriven process.^{45,47} Since the Fujishima and Honda discovery, artificial photosynthesis has been explored with a wide range of materials and catalysts to drive artificial photosynthesis with some strategies reaching efficiencies of 10%.⁴⁵ However, artificial photosynthesis remains a significant challenge in the solar energy conversion field with catalyst degradation and long-term device stability being the primary issues.⁴⁵ More research is necessary to optimize light absorption, charge transport, and catalysis to design cost-effective, long-lasting, competitive systems.



Molecular approaches to capturing, converting, and storing solar energy have been an active area of research for the last 50 years.⁴⁸⁻⁵⁰ Two solar cell devices that have been at the heart of this research in recent years are the dye-sensitized solar cell, which converts photons to electricity, and the dye-sensitized photoelectrochemical cell, which converts solar energy into fuels.^{45,51,52} The discussion that follows will focus on these two approaches and the relevant fundamental processes involved.

1.2 The Photophysics of Ru^{II} Polypyridyl Compounds

Dye-sensitized solar and photoelectrochemical cells often utilize molecular chromophores to capture the sun's energy. Therefore, an understanding of the photophysical and electrochemical properties of the chosen chromophore is critical when discussing such technologies. The most widely used chromophore in dye-sensitized solar cells are those based on the Ru^{II} polypyridyl compounds.^{30,51} This class of compounds is arguably one of the most well studied due to their stability, the tunability of the photophysical and electrochemical properties, and their synthetic ease. Owing to these properties, Ru^{II} polypyridyl compounds have found use in a wide range of applications from energy harvesting,^{30,53} photocatalysis,^{45,54,55} chemical sensing,⁵⁶ and photodynamic therapy^{57,58} to name a few. The prototypical compound for this class of chromophore is [Ru(bpy)₃](PF₆)₂, where bpy is 2,2'-bipyridine and PF₆⁻ is the hexafluorophosphate anion, and the following discussion will be based upon it; however, the principles discussed below can easily be extended to other chromophores.

A simple molecular orbital diagram for [Ru(bpy)₃]²⁺ in a pseudo-octahedral (*O_h*) geometry is shown in Figure 1.3A. Ru^{II} is a second-row transition metal ion with a *d*⁶ electronic

configuration. The five degenerate d orbitals of the free metal ion interact with the bipyridine ligands in two ways. First, σ -bonding interactions with the nitrogen lone pairs result in the destabilization of the Ru^{II} $d_{x^2-y^2}$ and d_{z^2} orbitals ($d\sigma^*$ collectively) to energies higher than the π^* orbitals in the final molecule. Second, Ru^{II} undergoes π -backbonding interactions with the π^* orbitals of the bipyridine rings resulting in the stabilization of the d_{xy} , d_{yz} , and d_{xz} orbitals ($d\pi$ collectively). The ligand field splitting between the two sets of d orbitals is further enhanced by the diffuse nature of the $4d$ orbitals resulting in better overlap with those on the bipyridine. This large ligand field splitting and its d^6 electronic configuration are responsible for the stability of these compounds.

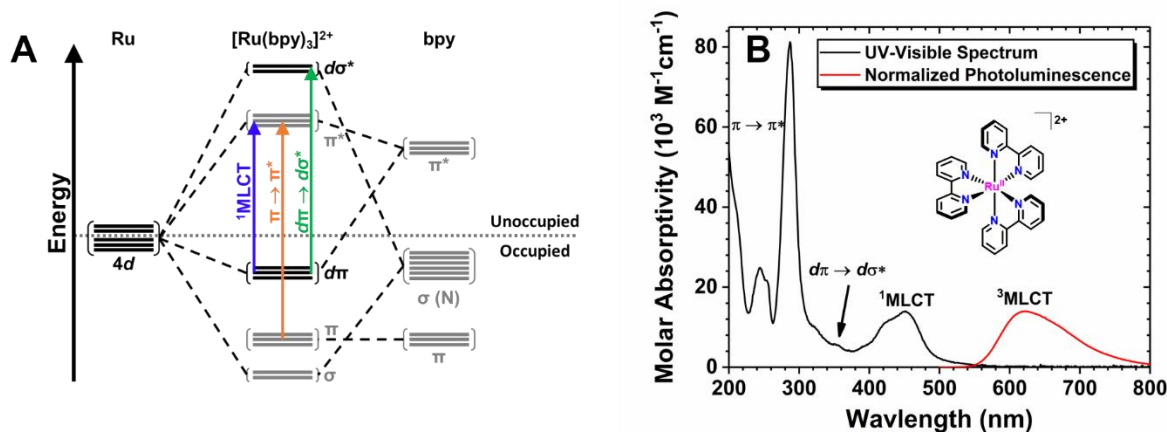


Figure 1.3. (A) A simple molecular orbital diagram for $[\text{Ru}(\text{bpy})_3](\text{PF}_6)_2$ in a pseudo-octahedral (O_h) geometry. In this diagram, the gray orbital sets indicate orbitals that are predominantly located on the 2,2'-bipyridine ligands and the black orbital sets indicate those that are primarily Ru-based. Some of the resulting molecular orbitals are omitted for clarity. Also depicted, are the common electronic transitions that are observed in the UV-visible electronic spectrum. (B) UV-visible electronic and the normalized photoluminescence spectra of $[\text{Ru}(\text{bpy})_3](\text{PF}_6)_2$ acquired at room temperature in neat acetonitrile.

The molecular orbital diagram in Figure 1.3A also reveals the parentage and localization of the frontier orbitals which govern the photophysical and electrochemical properties. The highest-occupied molecular orbital (HOMO) is localized primarily on the Ru^{II} metal center and the lowest-unoccupied molecular orbital (LUMO) is a bipyridine ligand-based

π^* orbital. Electrochemical techniques, the most common of which is cyclic voltammetry, have been used to measure the energy of these orbitals. In the case of $[\text{Ru}(\text{bpy})_3](\text{PF}_6)_2$ in 0.1 M LiClO_4 solutions in acetonitrile, the first metal-based oxidation and ligand-centered reduction, $E^\circ(\text{Ru}^{3+/2+})$ and $E^\circ(\text{Ru}^{2+/+})$, have been reported to be 1.51 and -1.07 V vs NHE.⁵⁹ The energy of these orbitals can readily be tuned by substituting a bipyridine ligand with non-chromophoric ligand, such as CN^- or SCN^- , or by placing substituents onto the bipyridine rings themselves.

The HOMO-LUMO energy gap represents the lowest energy electronic transition that for $[\text{Ru}(\text{bpy})_3]^{2+}$ is a metal-to-ligand charge transfer (MLCT).^{55,60} As implied by the Figure 1.3A, excitation of this transition promotes an electron from the Ru^{II} metal center to one of the bipyridine ligands. Figure 1.3B shows the UV-visible electronic spectra for $[\text{Ru}(\text{bpy})_3](\text{PF}_6)_2$ in acetonitrile with a MLCT absorption band centered at 450 nm.⁶⁰⁻⁶⁵ MLCT transitions are spin and symmetry allowed with molar absorptivity coefficients on the order of 10,000 to 20,000 $\text{M}^{-1}\text{cm}^{-1}$.⁶⁰⁻⁶⁵

Also evident in the electronic spectra is the existence of higher energy transitions. The small absorption feature near 350 nm has been assigned to the $d\pi$ to $d\sigma^*$ (ligand field or metal-centered) transition and is both Laporte and spin forbidden consistent with the small molar extinction coefficients on the order of 10 to 100 $\text{M}^{-1}\text{cm}^{-1}$; however, this assignment has been the subject of much debate.⁶⁰ Population of these $d\sigma^*$ orbitals results in photo-induced ligand loss due to the fact that these orbitals are anti-bonding in nature with respect to the Ru-N bond.^{60,63,65,66} The intense transitions above 300 nm arises from the allowed intraligand π to π^* transitions that occur with large extinction coefficients.⁶⁰ For $[\text{Ru}(\text{bpy})_3](\text{PF}_6)_2$, excitation into the MLCT band at room temperature results in a broad, featureless photoluminescence spectra

with maximum that occur between 600 and 700 nm, a substantial Stokes-like shift from the initial excitation.^{60,63,65,66} In acetonitrile, the photoluminescence maximum occurs at 620 nm (red spectrum, Figure 1.3B).^{67,68}

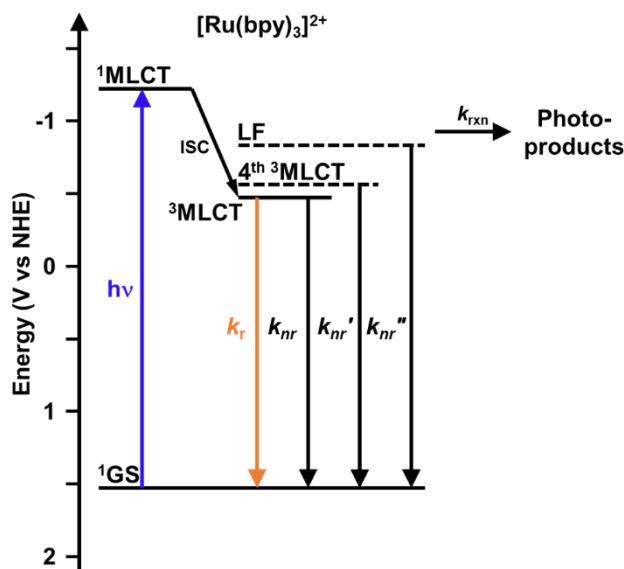


Figure 1.4. A Jablonski-type diagram for the $[\text{Ru}(\text{bpy})_3](\text{PF}_6)_2$ in acetonitrile. The ^1GS is referenced to the $E^\circ(\text{Ru}^{\text{III/II}})$ of the compound. The energy of the $^1\text{MLCT}$ and $^3\text{MLCT}$ states were determined from the energy of the peak in the UV-visible and photoluminescence spectra, respectively. The illustrated LF and fourth $^3\text{MLCT}$ energies are the activation energies for crossing from the $^3\text{MLCT}$ state. Intersystem crossing is abbreviated as ISC.

The Jablonski-type diagram in Figure 1.4 depicts the time evolution of the excited state after photoexcitation until its return to the ground state. Initial photoexcitation of the $[\text{Ru}(\text{bpy})_3](\text{PF}_6)_2$ yields a $^1\text{MLCT}$ excited state.^{55,65} This state is incredibly short-lived and quickly undergoes intersystem crossing (≤ 300 fs) and vibrational relaxation (ps) to form the $^3\text{MLCT}$ excited state.^{55,65,69-71} It is important to note that the spin-orbit coupling in these compounds means that the spin quantum number is a poor descriptor of the excited states; however, the formalism is well established in the field and is still useful when discussing the nature of photophysical properties.^{55,71-73} In accordance with Kasha's rule, the relaxation to the ground state occurs from the $^3\text{MLCT}$ excited state by radiative, k_r , and nonradiative, k_{nr} ,

pathways. The $^3\text{MLCT}$ excited-state lifetime for $[\text{Ru}(\text{bpy})_3](\text{PF}_6)_2$ in acetonitrile has been reported to be 855 ns and is consistent with the 100 ns to 10 μs lifetimes typically reported for Ru^{II} polypyridyl compounds.⁷⁴⁻⁷⁶ These two decay pathways occur in kinetic competition with one another, and the quantum yield for photoluminescence, Φ , is described by equations 1.2 and 1.3 and reports on the number of photons emitted by the chromophore relative to those absorbed.^{55,77} The reported Φ for $[\text{Ru}(\text{bpy})_3](\text{PF}_6)_2$ in acetonitrile is 0.095.⁷⁸ From these equations, k_r and k_{nr} have been found to be on the order 10^4 s^{-1} and 10^6 s^{-1} .⁶⁸

$$\Phi = \frac{k_r}{k_0} \quad (1.2)$$

$$k_0 = k_r + k_{nr} \quad (1.3)$$

At room temperature, excited-state decay from the $^3\text{MLCT}$ appears to occur from one state. However, Crosby and co-workers have shown through temperature-dependent, time-resolved photoluminescence studies that the $^3\text{MLCT}$ state observed at 298 K actually consists of at least three closely-spaced $^3\text{MLCT}$ states with varying degrees of singlet character.^{61,62,73,79,80} Above 120 K, these three states are at thermal equilibrium and the ensemble is referred to as the thermally-equilibrated excited state, or “thexi” state.^{61,62,73,79,80} Furthermore, the excited-state lifetime of $[\text{Ru}(\text{bpy})_3](\text{PF}_6)_2$ displays an additional, strong temperature dependence that has been attributed to activated crossing from the $^3\text{MLCT}$ state to the ligand field (LF) excited state with activation barriers approaching 500 mV (4000 cm^{-1}).^{58,63,81} Population of the LF states have been shown to lead to photo-induced ligand loss and provide additional nonradiative pathways for excited-state relaxation (k_{rxn} and k_{nr}'' , Figure 1.4).

In the case of other Ru^{II} polypyridyl compounds, a weak temperature dependence of the excited-state lifetime is observed that is not sufficiently described by models that only

include the thermally-equilibrated $^3\text{MLCT}$ and LF excited states leading many to invoke the existence of another $^3\text{MLCT}$ -like state often referred to as a fourth $^3\text{MLCT}$.^{60,67,74,82-84} Barriers for activated crossing into this state have been found to lie between 75 and 125 mV (400 to 1000 cm^{-1}), and population of this state also enhances excited-state relaxation (k_{nr} ’, Figure 1.4).^{60,67,84} These observations have been successfully extended to cyclometalated tris(bidentate) Ru(II) polypyridyl compounds and Os(II) polypyridyl compounds.^{68,84}

When using molecular chromophores to drive photochemical reactions, it is critical to consider the excited-state oxidation, $E^\circ(\text{Ru}^{3+/2+*})$, and reduction, $E^\circ(\text{Ru}^{2+*/+})$, potentials. The choice of chromophore is important as it should be a potent enough photoreductant or photooxidant to transfer an electron to, or receive an electron from, the desired substrate. With the experimentally measured $E^\circ(\text{Ru}^{3+/2+})$, $E^\circ(\text{Ru}^{2+/+})$, and the Gibbs free energy stored in the excited state, ΔG_{ES} , the excited-state reduction potentials can be calculated using equations 1.4 and 1.5.^{30,85,86} The magnitude of ΔG_{ES} is typically determined by performing a Franck-Condon lineshape analysis of the steady-state photoluminescence spectrum of the chromophore or through a linear extrapolation of the high-energy side of the photoluminescence band to the baseline.^{55,87}

$$E^\circ(\text{Ru}^{3+/2+*}) = E^\circ(\text{Ru}^{3+/2+}) - \Delta G_{\text{ES}} \quad (1.4)$$

$$E^\circ(\text{Ru}^{2+*/+}) = E^\circ(\text{Ru}^{2+/+}) + \Delta G_{\text{ES}} \quad (1.5)$$

Chapter 6 will explore the excited-state properties and photophysics of cyclometalated bis(tridentate) Ru^{II} compounds which have emerged as a promising new chromophore for application within dye-sensitized solar cells.

1.3 Dye-Sensitized Technologies

1.3.1 Dye-Sensitized Solar Cells

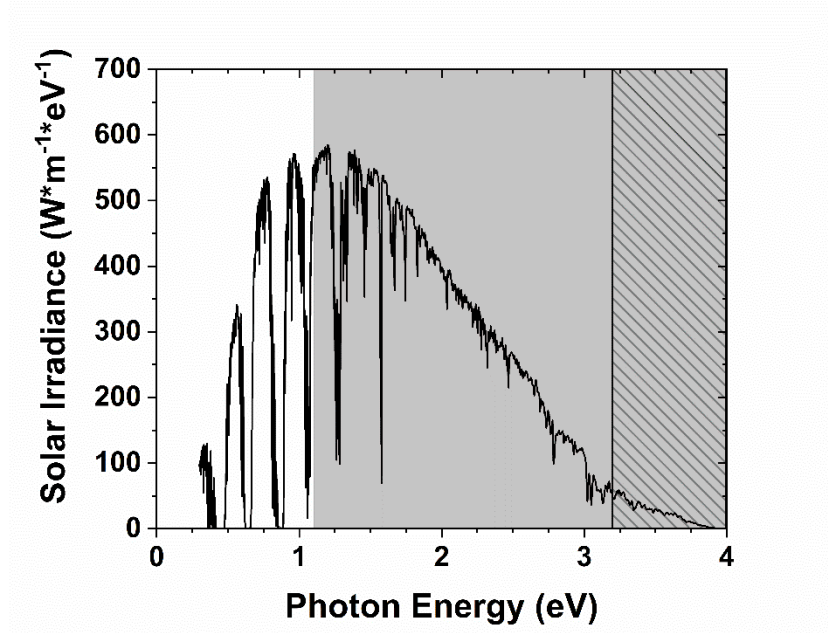


Figure 1.5. The standard solar irradiance (AM 1.5 Standard⁸⁸) measured on the surface of the Earth. The total area under the curve represents the amount of power per unit area that strikes the surface. The gray shaded box and the diagonal-filled box represents the photons with the appropriate energy for bandgap excitation of silicon and anatase TiO_2 , respectively.

The most ubiquitous semiconductor used for solar cells is silicon. In fact, silicon is the semiconductor of choice for single-junction solar cells and has dominated the photovoltaic industry for decades.^{32,34,51} Silicon possess a bandgap of ~ 1.1 eV allowing it to absorb a wide portion of the AM1.5 solar spectrum, shown in Figure 1.5.⁸⁸ The advantage of a small bandgap is that it allows for a large fraction of the solar photons to be absorbed which enhances the photocurrents. However, the photons with energy greater than 1.1 eV will lose the excess energy as heat when the excited state thermalizes to the band edge energy.³⁷ One strategy to overcome these thermalization losses and increase photovoltages, and thus power output, is to use a semiconductor material with a wide bandgap, like anatase TiO_2 which has a bandgap of 3.2 eV, at the expense of capturing lower energy photons.⁸⁹ Thus, TiO_2 is only capable of

absorbing the UV region of the solar spectrum which only represents a small fraction of the light emitted from the sun resulting in small photocurrents, Figure 1.5.^{30,38}

An ingenious solution which allowed for the use of the inexpensive TiO_2 semiconductor was to sensitize it to visible light using surface-bound chromophores. This allowed TiO_2 to absorb a larger portion of the solar spectrum, which increased the photocurrents, while still allowing for the possibility of having large photovoltages.⁸⁹⁻⁹² If the device was designed to convert solar energy directly to electricity, these devices are known as dye-sensitized solar cells (DSSCs).⁵¹ On the other hand, if the captured energy is used to form solar fuels, these devices are known as dye-sensitized photoelectrochemical cells (DSPECs).⁴⁵ This approach to capturing solar energy benefits from the fact that the roles of light absorption and charge carrier transport, traditionally fulfilled by only the semiconductor, has been separated allowing for each to be optimized independently.^{51,52,91,93}

Dye-sensitized solar cells emerged in the early 1990s as a promising next-generation solar cell that had the potential to undercut the high price of traditional silicon solar cells.⁹¹ The key breakthrough that propelled DSSCs to prominence was the incorporation of high-surface area semiconducting substrates that allowed for higher chromophore concentrations and led to a 1000-fold enhancement of their light absorbing capabilities and enhancing short-circuit currents. Since this breakthrough, advancements in materials, chromophores, and device design have led to verified power conversion efficiencies that have reached 12% with some published reaching as high as 14%.^{30,51,94-97}

As stated to in Section 1.1.2, the cost of silicon-based solar cells has fallen due to advances in manufacturing leading some to question the benefit of continued research into DSSCs.⁴⁰ However, DSSCs possess the ability to operate efficiently under diffuse light

conditions something that traditional solar cells cannot do efficiently. Indeed, many researchers have pursued niche applications for DSSCs such as indoor light-reclamation that was recently reported to have a 32% efficiency.^{98,99} Note that this efficiency was calculated based on the power density of the chosen light source and not under solar irradiation.

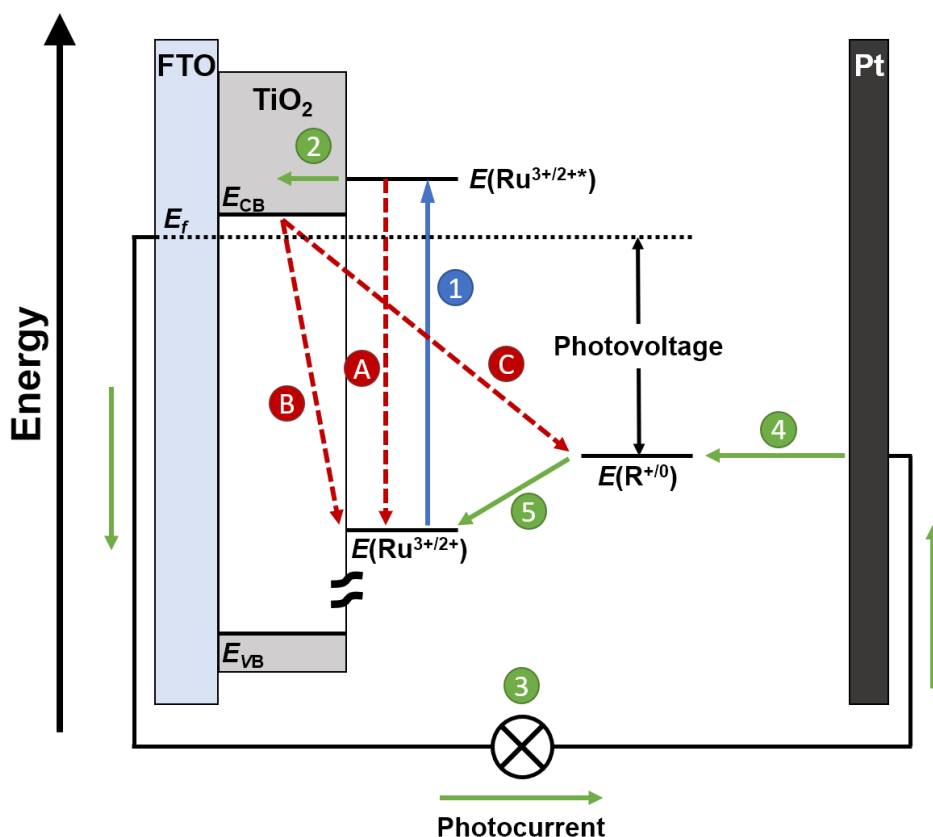


Figure 1.6. A schematic representation of an n-type DSSC using a generic Ru^{II} polypyridyl chromophore (Ru) and redox mediator (R). The favorable processes in the DSSC, in order, are (1) photoexcitation, (2) electron injection into the conduction band of TiO₂, (3) movement through the external circuit to perform work, (4) reduction of the redox mediator, (5) regeneration of the oxidized Ru sensitizer. Nonproductive pathways include (A) excited-state relaxation, (B) back-electron transfer, and (C) charge recombination all of which result in a loss of device efficiency.

A schematic and energetic diagram of a generic n-type DSSC is given in Figure 1.6. In a typical DSSC, a chromophore is anchored to the surface of a mesoporous, nanocrystalline TiO₂ thin film which is deposited onto a transparent conductive oxide current collector,

typically fluorine-doped tin oxide (FTO).^{30,51,92} The energy conversion process is initiated when the surface-bound chromophore absorbs an incident solar photon to form an excited state (step 1).^{30,51,92} Assuming that the $E^\circ(\text{Ru}^{3+/2+*})$ is of the appropriate energy, the excited chromophore injects an electron into the acceptor states of TiO_2 yielding an oxidized chromophore in a process known as electron injection (step 2).^{30,51,92} After injection, the electron in TiO_2 diffuses through the film until it reaches the FTO, where it enters an external circuit to perform work (step 3) after which, it is transported to the platinum counter electrode where it reduces the redox mediator (step 4).^{30,51,92} The reduced redox mediator, R^0 , diffuses through the liquid electrolyte to the oxidized chromophore where it undergoes a final electron transfer to yield R^+ and reset the entire cycle in a process known as regeneration (step 5).^{30,51,92} Additionally, the oxidizing equivalent, or hole, that remains on the chromophore after electron injection can transfer to neighboring chromophores on the surface in a process known as lateral electron transfer (not shown).^{100,101} Since the starting and end points are the same, no net chemistry occurs.

There are a few unwanted electron transfer processes that occur in competition with those described above.^{30,51,92,102} First, the excited state can undergo relaxation through radiative and nonradiative pathways before electron injection can occur resulting in the ground-state chromophore (step A). Additionally, the injected electron can undergo interfacial electron transfer with the oxidized chromophore on the surface or the oxidized redox mediator in solution before moving through the external circuit in processes called back-electron transfer (step B) and charge recombination (step C), respectively. All these processes reduce the overall short-circuit current of the device, and thus the power conversion efficiency.^{30,51,102} In the case of some chromophores, the energy of the absorbed photon is sufficient induce unwanted

photochemistry leading to degradation of the adsorbed chromophore and a decrease in the cell performance.^{30,67}

Therefore, the optimization of the DSSC performance relies on a kinetic balancing act between the wanted and unwanted electron transfer pathways. Most of the research over the last 30 years have sought to optimize device performance through the choice of semiconductor, chromophore, redox mediator, and electrolyte composition. The research towards this end has been reviewed extensively.^{30,51,95-97}

1.3.2 Dye-Sensitized Photoelectrochemical Cells

The dye-sensitized photoelectrochemical cell (DSPEC) seeks to address the challenge of solar energy storage by converting solar energy directly to fuels and/or value-added chemicals.^{45,103} It was recognized in the 1990s that the oxidizing equivalent generated after excited-state electron injection could be used for to drive chemical reactions.¹⁰⁴ In a DSSC, the typical redox mediator of choice is I^-/I_3^- .^{30,51,102} However, if a catalyst is co-adsorbed with the chromophore and the redox mediator is replaced with a suitable substrate, the turnover of the catalyst could be used to regenerate the oxidized chromophore for further light absorption.

The first reported DSPEC was by Meyer and co-workers in 1999 where a Ru water oxidation catalyst was covalently linked to a Ru^{II} polypyridyl chromophore.¹⁰⁴ In this study, they demonstrated that these chromophore-catalyst assemblies on the surface of nanocrystalline, mesoporous TiO_2 thin films could dehydrogenate 2-propanol to form acetone and hydrogen, which is a nonspontaneous by 0.88 V vs NHE. The absorption of photons provided the energy necessary to carry out this reaction and was a proof-of-concept model for DSPECs. Since this report, numerous device designs, using n-type and p-type semiconductors for oxidation and reduction reactions, respectively, and chromophore-catalyst assemblies probing the best methods to link the chromophore and the catalyst have been explored.

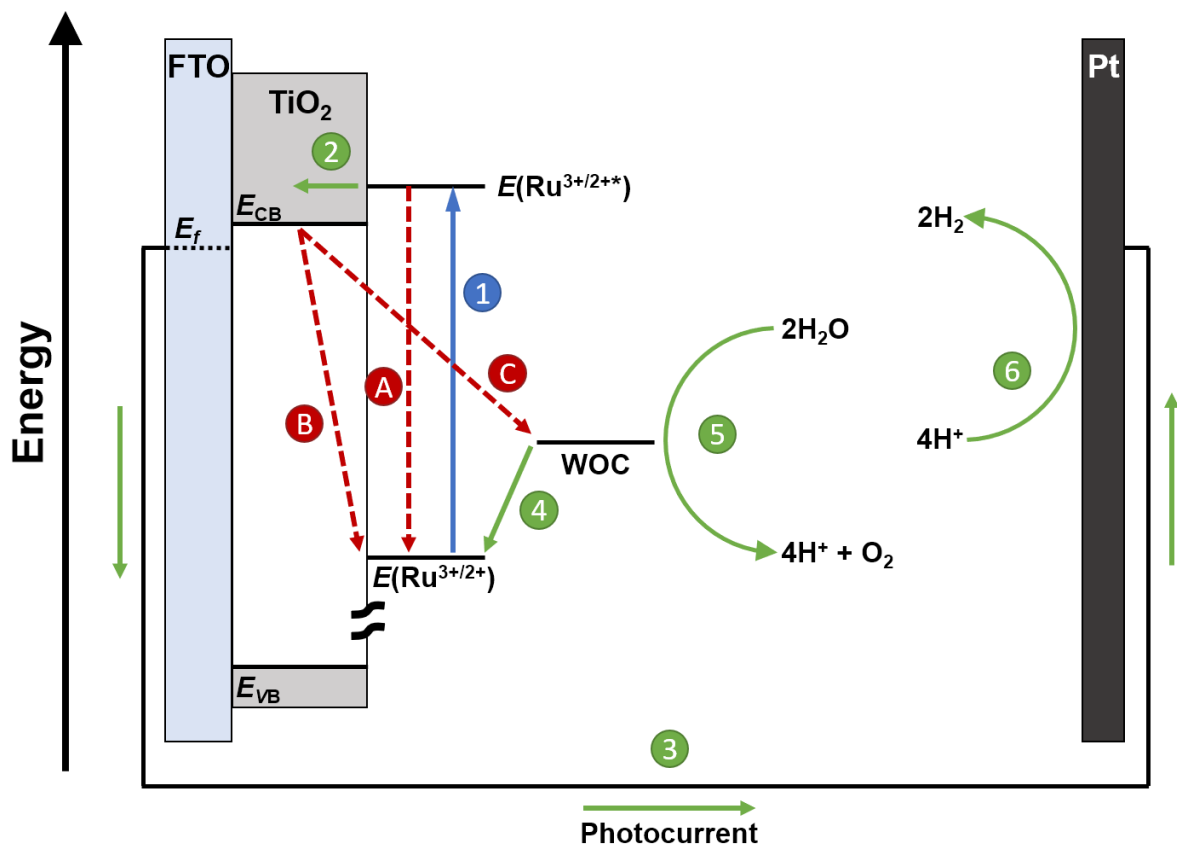


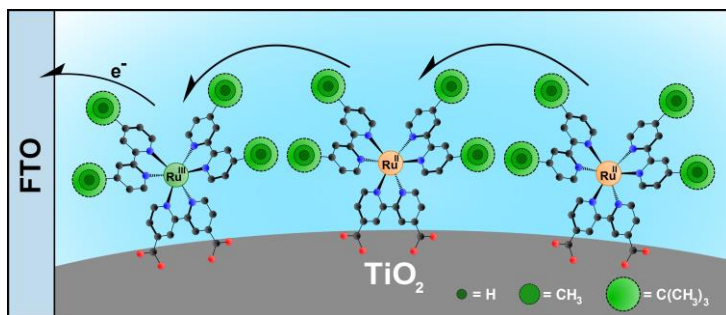
Figure 1.7. A schematic of an n-type DSPEC with a generic Ru^{II} polypyridyl chromophore (Ru) and water-oxidation catalyst (WOC). Like a DSSC, the first three productive steps are (1) photoexcitation, (2) electron injection into the conduction band of TiO_2 , and (3) movement of the electron to the counter-electrode. Next, the oxidized dye undergoes lateral electron transfer until an oxidized dye reaches the WOC and is regenerated (4). Once the WOC has been oxidized four times, it oxidizes water (5). H_2 generation, a two-electron process, occurs at the Pt electrode (6). Nonproductive pathways include (A) excited-state relaxation, (B) back-electron transfer, and (C) charge recombination all of which result in a loss of device efficiency.

A schematic of an n-type DSPEC is shown in Figure 1.7. Like the DSSC, photoexcitation of a surface-bound chromophore results in an excited state that injects an electron into TiO_2 where it diffuses through the TiO_2 to the current collector and through the external circuit.^{4,45,103} However, in DSPECs the oxidized chromophore mediates water oxidation with a covalently-linked or co-adsorbed catalyst through a series of lateral self-exchange electron transfer.⁴⁵ Four oxidation reactions must occur before the catalyst can carry

out the desired catalytic transformation and generate O_2 from H_2O .⁴⁵ The electrons from water oxidation have been coupled to a counter electrode where they drive other reactions such as H_2 production or CO_2 reduction.^{4,45} In DSPECs, it is necessary to design chromophores and catalysts with the appropriate formal reduction potentials for all the necessary electron transfer steps to occur.^{45,105}

1.4 Lateral Electron Transfer at Semiconductor Interfaces

Scheme 1.1. Lateral Intermolecular Self-Exchange Electron Transfer across Anatase TiO_2 Nanocrystallites



Lateral electron transfer between molecules at semiconductor interfaces, depicted in Scheme 1.1, has received increased attention over the past decade as it is a way to transport charge without the loss of Gibbs free energy.¹⁰¹ This lateral electron transfer, sometimes referred to “hole-hopping,” has been shown to be a suitable replacement for traditional redox mediators in DSSCs resulting in solar cells with large photovoltages.^{106,107} Additionally, lateral electron transfer is crucial in order to shuttle multiple redox equivalents onto a catalyst, such as in a DSPEC, to carry out useful chemical transformations.^{45,108,109} Furthermore, an experimentally established link between unwanted back-electron transfer and lateral electron transfer kinetics indicates that rapid lateral charge transport increases back-electron transfer rates.¹¹⁰⁻¹¹² Therefore, a detailed understanding of the principles and tunability of lateral

electron transfer reactions at the interface is critical to the optimization of dye-sensitized technologies.

1.4.1 Introduction to Marcus Theory

Electron transfer reactions represents one of the primary classes of reactions taught in a general chemistry course and have been extensively studied since the end of World War II.¹¹⁴⁻¹¹⁶ First proposed in the 1950s, Marcus theory of electron transfer was originally derived to describe outer-sphere, nonadiabatic (weakly-coupled) electron transfer between molecules in solution by a simple harmonic-oscillator model.^{114,117} However, further developments by Marcus and others have extended Marcus theory to encompass a broad range of conditions and environments.^{114,115} Many examples of electron transfer between transition metal compounds have been shown to occur via an outer-sphere, nonadiabatic type mechanism, and immobilization of these compounds at the semiconductor interface has been shown to push electron transfer even farther into the weak-coupling limit.^{101,114,118-122} Therefore, the discussion that follows will focus on thermal, outer-sphere, nonadiabatic electron transfer.

Figure 1.8 shows an example of one-dimensional potential energy surfaces for an electron transfer between an electron donor, D, and an electron acceptor, A, under the harmonic oscillator approximation. One of the key realizations that Marcus had over his contemporaries was that prior to electron transfer (i.e. electron jump from the reactant potential energy surface to the product), the solvated D and A must reach an intermediate nuclear geometry that is isoenergetic between the two surfaces at the crossing in the activated.^{116,117,123,124} In this model, energy is conserved during the electron process as opposed to the models proposed by others. The Gibbs free energy of activation for this process, ΔG^\ddagger , arises from vibrations within activated complex (inner-sphere) and motions of the solvent molecules in the solvation sphere around the activated complex (outer-sphere).^{114,116,122,124} The inner-sphere, λ_i and outer-sphere,

λ_0 , reorganization energies comprise the total reorganization energy, λ , which is defined as the energy required to move an electron from the reactant potential energy surface the product potential energy surface while maintaining the equilibrium geometry of the former. The reorganization energy is directly proportional to the ΔG^\ddagger . The classical treatment of the potential energy surfaces allowed for the geometrical formulation of the classical Marcus equation as given in equations 1.6 and 1.7, where k_{et} is the rate of electron transfer, κ is the transmission coefficient (probability of crossing between potential energy surfaces), ν is the frequency of approaching this barrier, k_B is the Boltzmann constant, T is the absolute temperature, and ΔG° is the driving force for electron transfer.^{114,123,124}

$$k_{et} = \kappa \nu e^{\left(\frac{-\Delta G^\ddagger}{k_B T}\right)} \quad (1.6)$$

$$\Delta G^\ddagger = \frac{\lambda}{4} \left(\frac{\Delta G^\circ}{\lambda} + 1 \right)^2 \quad (1.7)$$

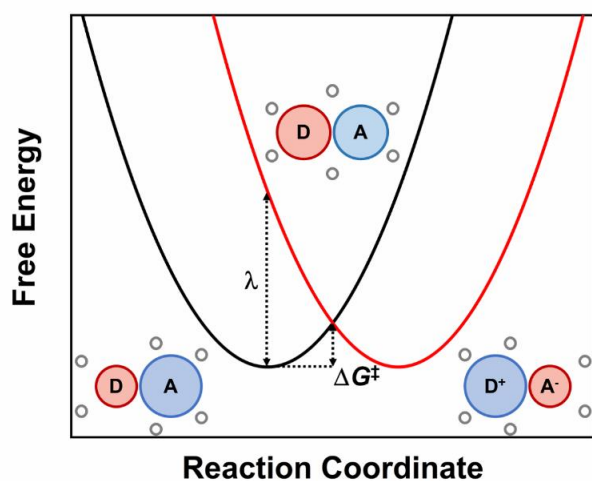


Figure 1.8. One-dimensional potential energy surfaces for the nonadiabatic, self-exchange electron transfer between an electron donor, D, and an electron acceptor, A. The reactant (black) and product (red) potential surfaces are represented as harmonic oscillators. Depicted is the structure of the encounter complex and inner-solvation sphere before, during, and after electron transfer. Indicated on the graph is the reorganization energy, λ , and the Gibbs free energy of activation, ΔG^\ddagger .

For electron transfer in the nonadiabatic regime, the probability of crossing potential energy surfaces in the activated complex becomes low and potentially rate limiting.^{123,125} This led Levich to apply Fermi's golden rule to modify the classical Marcus equation and to treat the probability of crossing the potential energy surfaces quantum mechanically resulting in the semi-classical Marcus equation, eq 1.8, where H_{DA} is the electronic coupling matrix element between electron donor and electron acceptor and \hbar is the reduced Planck constant.^{123,125} Lateral electron transfer across oxide semiconductor surfaces has been modelled with this semi-classical equation.^{101,126}

$$k = \left(\frac{2\pi}{\hbar}\right) \left(\frac{|H_{DA}|^2}{\sqrt{4\pi\lambda k_B T}}\right) e^{\left(\frac{-(\Delta G^\circ + \lambda)^2}{4\lambda k_B T}\right)} \quad (1.8)$$

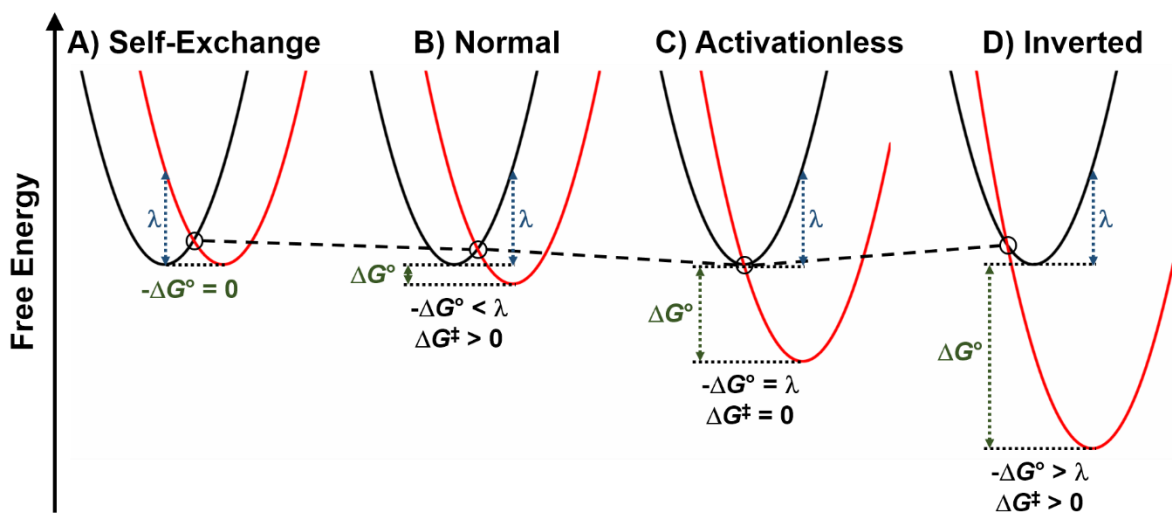


Figure 1.9 One-dimensional potential energy surfaces depicting regimes of electron transfer predicted by nonadiabatic Marcus theory: (A) self-exchange electron transfer (Marcus normal) (B) Marcus normal region, (C) activationless region, and (D) Marcus inverted region. The reactant (black) and product (red) potential energy surfaces are depicted as harmonic oscillators. The crossing point for each regime is highlighted to emphasize the change between the three regimes. The reorganization energy (blue) and the Gibbs free energy of the reaction (green) are also depicted.

Marcus theory predicts that electron transfer will occur in three different kinetic regimes depicted in Figure 1.9.^{114,115,123} In the Marcus normal region, an increase in the

exergonicity of the electron transfer reaction between D and A results in an increase in the rate constant as long as $-\Delta G^\circ < \lambda$, Figure 1.9A and 1.9B. If the driving force continues to increase until $-\Delta G^\circ = \lambda$, electron transfer becomes activationless resulting in the maximum electron transfer rate constant for the reaction, Figure 1.9C. Counterintuitively, further increases in the electron transfer driving force is predicted to decrease electron transfer rate constants, Figure 1.9D. This occurs when $-\Delta G^\circ > \lambda$ due to the nested potential energy surfaces and an increase in ΔG^\ddagger , and this regime is called the Marcus inverted region.

The prediction of the Marcus inverted region was quite counterintuitive.¹²³ Prior to this, electron transfer rates were known to increase with increasing driving force but inverted kinetic behavior was less apparent.¹²⁷ Validation of Marcus theory ultimately required covalently linking the donor and acceptor to overcome diffusion-limited rate constants.^{123,124} Indeed, in the early 1980s, inverted electron transfer behavior was reported.^{125,128} The seminal paper published by Closs and Miller used organic D and A molecules that were tethered at a fixed distance from one another using a steroid spacer.¹²⁵ This steroid tether removed the need for diffusion to bring the D and A molecules together which overcame the diffusion-limited kinetics previously observed. Through pulse radiolysis, they were able to generate the $D^{\bullet-}$ and then spectroscopically quantified kinetics for the electron transfer from $D^{\bullet-}$ to A. The observed rate constants spanned 4 orders of magnitude and decreased unambiguously with increasing exergonicity.

Since the Closs-Miller experiments, numerous examples of inverted-region electron transfer have been shown for tethered or pre-associated D and A systems.¹²⁹⁻¹³⁴ However, more elusive are examples of thermal, bimolecular electron transfer in the Marcus inverted region. The few examples that do exist use photoexcitation of a D molecule and subsequent excited-

state quenching to generate a D^+ and A^- after which, the highly exergonic, thermal, back-electron transfer reaction is monitored.^{129,130,132,133} Furthermore, many of these studies have taken advantage of D and A molecules that are significantly different in size.^{130,133} In accordance with the Einstein-Smoluchowski relation, the size mismatch results in raising the diffusion limited reaction rate in a given solvent, eq 1.9, where k_d is the rate of diffusion, R is the gas constant, η is the solvent viscosity, and r_D and r_A is the molecular radius of the D and A, respectively. **Chapter 5** will detail thermal, bimolecular electron transfer reactions between Ru^{III} and Co^{II} polypyridyl compounds that display Marcus inverted behavior.¹³⁰

$$k_d = \frac{2RT}{3\eta 10^3} \left[\frac{(r_D + r_A)}{r_D} + \frac{(r_D + r_A)}{r_A} \right] \quad (1.9)$$

Another prediction of Marcus theory is that electron transfer is distance dependent. At constant ΔG° , λ , and T , the Marcus equation predicts that the electron transfer rate should depend only on H_{DA} . It has been both theoretically predicted and experimentally demonstrated that H_{DA} decreases exponentially with the D-A distance, δ , as described by eq. 1.10, where β is the attenuation factor, and H_{DA}^O is the electronic coupling at van der Waals separation, δ_O .^{125,135-137}

$$H_{DA} = H_{DA}^O e^{-\frac{\beta}{2}(\delta - \delta_O)} \quad (1.10)$$

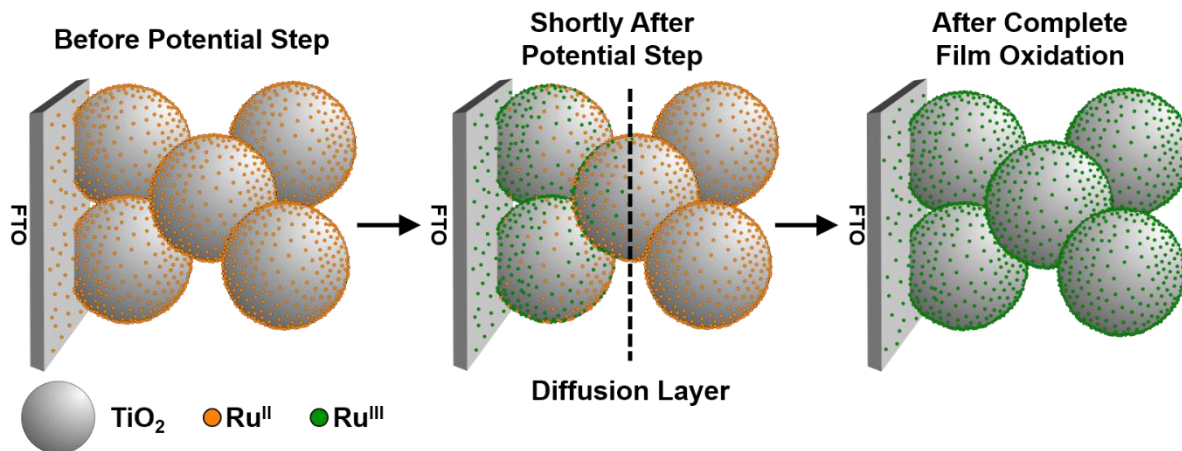
1.4.2 Mechanism and Experimental Approaches for Lateral Electron Transfer

It was first noticed in the 1990s that monolayers of redox active molecules, such as Ru^{II} polypyridyl and substituted-triphenylamine (TPA) compounds, anchored to the surface of wide bandgap semiconductors, such as anatase TiO_2 , could undergo completely reversible electrochemical oxidation despite possessing formal reduction potentials that lie within the forbidden bandgap.^{100,138} Recall that anatase TiO_2 has a bandgap of approximately 3.2 eV with the conduction band, E_{CB} , and valence band edge energies, E_{VB} , at -0.8 and 2.4 V vs NHE,

respectively, as measured in acetonitrile solutions containing 0.1 M LiClO₄.³⁰ Therefore, there should be no electronic states present in the TiO₂ that could mediate the oxidation and reduction of these films.

Bonhôte and co-workers were the first to explore the reversible electrochemistry in detail.¹⁰⁰ They found that nanocrystalline, mesoporous thin films of TiO₂, zirconium(IV) dioxide (ZrO₂), and aluminum(III) oxide (Al₂O₃) functionalized with a substituted-TPA compound were rapidly oxidized upon the application of potential step more positive than the TPA⁺⁰ formal reduction potential. The only requirement for the complete oxidation of all the TPA compounds was that the surface coverage must be above some minimum value, termed the percolation threshold.¹⁰⁰ The observation of a percolation threshold indicated that film oxidation was occurring by discrete electron transfer reactions between neighboring TPA and TPA⁺ molecules rather than by physical diffusion of the molecules across the surface or in the electrolyte solution.^{139,140} This led Bonhôte and co-workers to propose the mechanism, depicted for Ru^{III/II} self-exchange in Scheme 1.2, where an initial electron transfer to the FTO from nearby molecules initiates the film oxidation followed by self-exchange electron transfer to shuttle more electrons toward the FTO.^{100,101,113,138,141-144} As time progresses, the diffusion layer moves through the film until it is completely oxidized. This behavior has been demonstrated for many organic and transition metal compounds.^{100,113,141,142,145}

Scheme 1.2. A Depiction of the Time Evolution of the Complete Film Oxidation during a Chronoabsorptometry Experiment



Concurrently with film oxidation, anions from the electrolyte solution diffuse to the oxidized molecules to maintain charge balance. Bonhôte and co-workers concluded that ion motion was necessary for self-exchange through the dependence on the solvent dielectric constant.¹⁰⁰ As the dielectric constant increased, the measured lateral electron transfer rates also increased. This increase in rate was counter to the prediction of the Marcus two-sphere continuum model which predicted that λ_O should increase with more polar solvents, eq 1.11, where e is the elementary charge transferred, ϵ_0 is the permittivity of free space, and ϵ_∞ and ϵ_s are the optical and static dielectric constants of the electrolyte, respectively.^{114,115,122,123} The authors reasoned that high dielectric solvents aid in the separation of the ion pairs of the electrolyte salt in solution. This leads to more free anions that can diffuse to the interface to balance the increasing charge during oxidation. The necessity of ion mobility was consistent with a report by Ardo *et al.* who found that lateral self-exchange electron transfer between Ru^{II} polypyridyl compounds did not occur in the absence of a supporting electrolyte.⁹³ However, upon the addition of 0.01 M LiClO₄ to the solvent, electron transfer across the surface was observed.⁹³

$$\lambda_O = \frac{e^2}{4\pi\epsilon_0} \left(\frac{1}{r_D} + \frac{1}{r_A} - \frac{1}{\delta} \right) \left(\frac{1}{\epsilon_\infty} - \frac{1}{\epsilon_s} \right) \quad (1.11)$$

1.4.2.1 Quantifying Lateral Electron Transfer through Electrochemistry

Both electrochemical and spectroscopic techniques exist to quantify lateral electron transfer reactions across the semiconductor interface. By far the dominant experimental approaches have been through electrochemical techniques utilizing either a potential step (chronocoulometry, CC, or chronoabsorptometry, CA) or a potential sweep (cyclic voltammetry, CV).^{100,101,141-143,145} In the potential step methods, a potential is applied that is sufficiently positive of the formal reduction potential to oxidize the compound of interest and either the amount of charge passed, Q , or the change in absorbance, ΔA , is monitored as a function of the square root of time, t .^{100,101} A sample Anson plot for a CA experiment is given in Figure 1.10. To extract the apparent diffusion coefficient, the initial linear portion of the data is fit to a modified-Anson equation, eq 1.12 for chronocoulometry and eq. 1.13 for chronoabsorptometry, where Q_f is the total amount of charge passed in the experiment, ΔA_f is the total change in absorbance of the film, D_{CC} and D_{CA} is the apparent diffusion coefficient from chronocoulometry and chronoabsorptometry, respectively, and d is the film thickness. From the slope of this fit, the apparent diffusion coefficient is extracted.

$$Q = \frac{2Q_f D_{CC}^{1/2} t^{1/2}}{d\pi^{1/2}} \quad (1.12)$$

$$\Delta A = \frac{2\Delta A_f D_{CA}^{1/2} t^{1/2}}{d\pi^{1/2}} \quad (1.13)$$

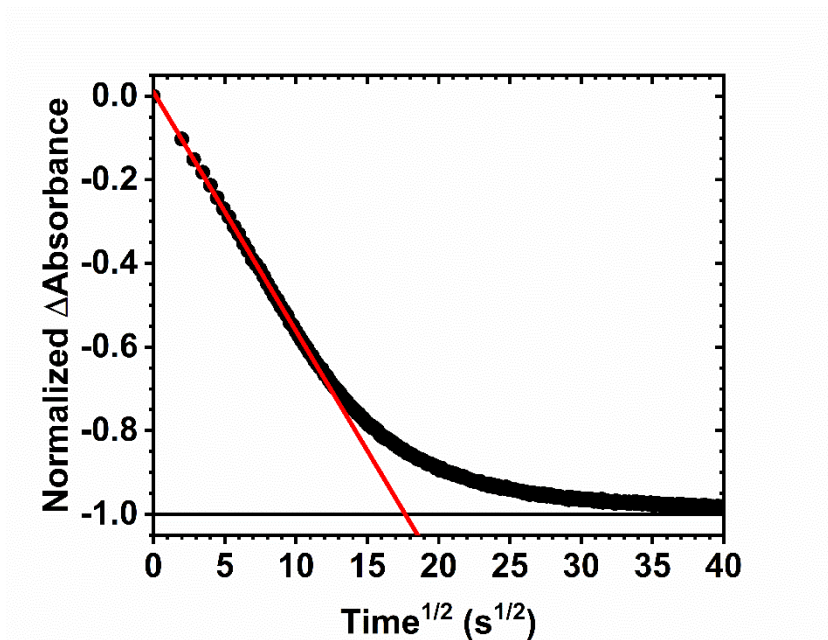


Figure 1.10. A typical Anson plot of the normalized change in absorbance as a function of the square root of time following a potential step sufficiently positive of the formal reduction potential of the surface-anchored compound. The red line is a fit to the Anson equation, eq 1.13, for the initial absorbance change.

Equations 1.12 and 1.13 were derived using the semi-infinite diffusion boundary conditions; however, the semiconductor thin films have a finite thickness.¹⁰⁰ Therefore, this method of analysis is only valid until the oxidation front reaches the remote edge of the dye-sensitized metal oxide thin film. It has been shown that these boundary condition holds for the oxidation of the first 60% of the film.^{100,101,113,145} As the diffusion layer, depicted in Scheme 1.2, reaches the outer edges of the film, the boundary conditions begin to fail as the number of electron transfer pathways begins to diminish. Thus, the kinetic data in Figure 1.10 deviates from linearity. Once all of the molecules on the surface are oxidized, the measured Q or ΔA becomes time invariant.

Cyclic voltammetry is also used to measure the lateral electron transfer kinetics across the interface. In a typical cyclic voltammetry experiment, the peak current density, j_p , is measured for the desired process and the apparent diffusion coefficient, D_{CV} , is found using

the Randles-Sevcik equation, eq. 1.14, where q is the elementary charge, c_0 is the volume concentration, and v is the scan rate.¹⁴³

$$D_{CV} = \frac{5.02k_bTj_p^2}{q^3c_0^2v} \quad (1.14)$$

Experimental results have shown that $D_{CC} \approx D_{CA} > D_{CV}$ for a given compound with the D_{CV} values consistently reported to be about an order of magnitude smaller than the D_{CC} and D_{CA} values.^{113,142} This deviation is not well understood since the D values are expected to be independent of the technique used to quantify them. A possible explanation is that while the potential step methods oxidize the entire film, CV only probes lateral electron transfer kinetics through some fraction of the film depending on the scan rate.¹¹³ It may be for this reason that apparent diffusion coefficients measured by potential step and potential sweep methods often differ. Nevertheless, when comparing diffusion coefficients, it is important to note which experimental technique was used.

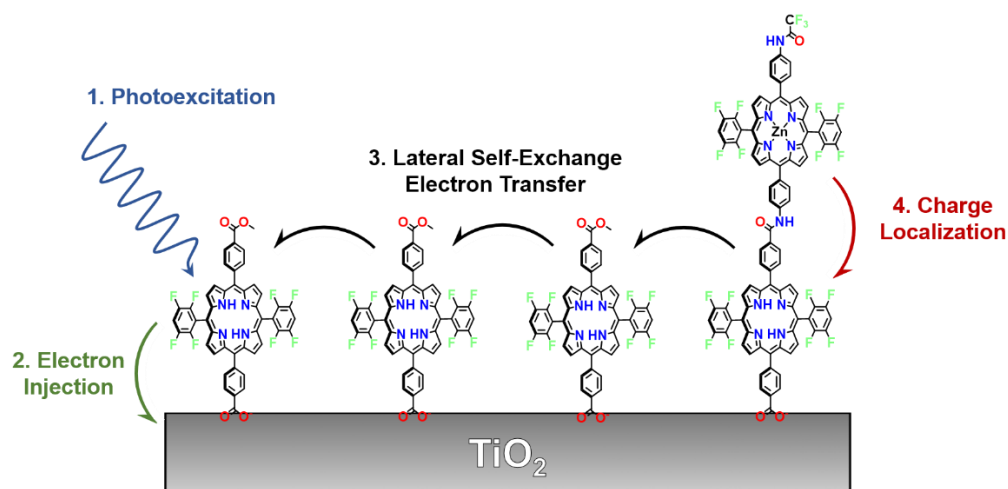
When comparing measured diffusion coefficients to other reaction processes, it is often convenient to convert D to a first- or second-order electron transfer rate constant.^{101,113,143} The measured diffusion coefficient is directly proportion to the first-order “hopping” rate constant, k_{et} , and the second-order electron transfer rate constant, k'_{et} , by the Dahms-Ruff equation, eq 1.15, where C is the concentration of the electroactive species on the surface and n is the number of nearest neighbors.^{101,139,140} Unfortunately, concentration is a nebulous parameter at the interface of these films due to the mesoporous nature of the underlying substrate.¹⁰¹ Oftentimes, estimates of C and δ are made through spectroscopic means with numerous assumptions about the molecular arrangement at the interface which allows for the conversion of D to k_{et} .^{101,113,143}

$$D = \frac{k_{et}\delta^2}{n} = \frac{k'_{et}C\delta^2}{n} \quad (1.15)$$

1.4.2.2 Transient Absorption Spectroscopy to Quantify Lateral Electron Transfer Kinetics

Lateral electron self-exchange kinetics spectroscopically have been determined through transient absorption spectroscopy. While less often used, transient absorption techniques have an advantage over the bulk electrochemical techniques in that lateral electron transfer kinetics can be quantified under conditions that resemble those of operational DSSCs or DSPECs and in the absence of electrolyte.^{93,108,109,146-149} However, determination of first-order hopping rate constants for lateral electron transfer requires modelling, often Monte-Carlo simulations with a random-walk model.

Scheme 1.3. Schematic Representation of a Transient Absorption Experiment Utilizing a Co-Adsorbed Electron Donor to Measure Lateral Electron Transfer of a Free-Base Porphyrin



One transient absorption method used to measure lateral self-exchange electron transfer kinetics, depicted in Scheme 1.3, uses the color change associated with favorable electron transfer, *i.e.* $\Delta G^\circ \neq 0$, from the exchanging compound of interest to a co-adsorbed electron donor.^{108,109,146} After selective photoexcitation and electron injection of the chromophore, steps 1 and 2 in Scheme 1.3, the resultant oxidizing equivalent can move across the surface in a series of lateral self-exchange electron transfer reactions, step 3. When the oxidizing equivalent approaches the electron donor, electron transfer localizes the charge on the donor, step 4, and

this thermodynamically favored electron transfer is monitored spectroscopically. All of the above reactions occur in kinetic competition with back-electron transfer. Monte Carlo simulations employing a random walk model have been used in conjunction with kinetic rate laws describing the system to model the transient data and extract k_{et} .^{108,109,146}

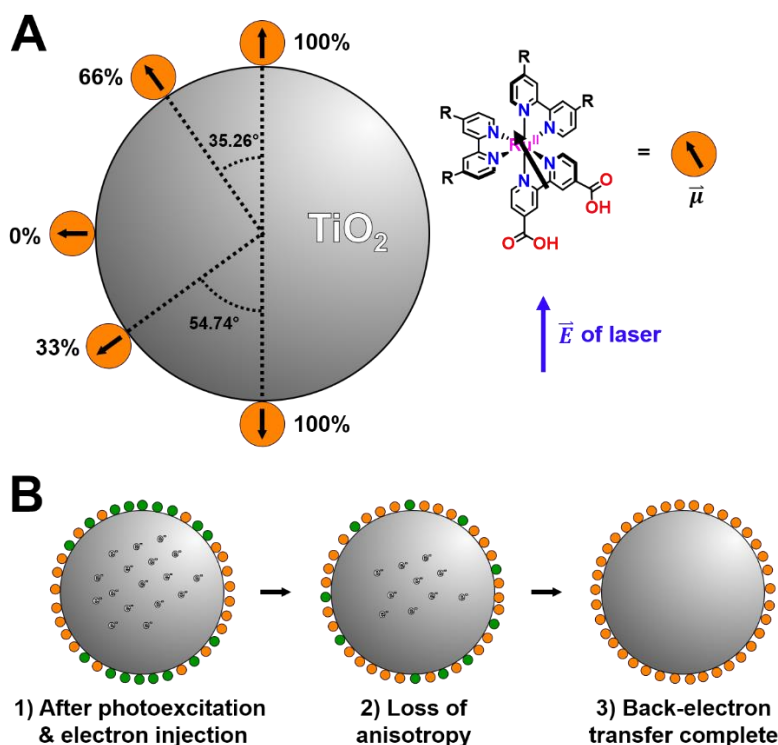


Figure 1.11. (A) An idealized TiO_2 nanoparticle sensitized with an Ru^{II} polypyridyl compound with the lowest-energy transition dipole moment depicted by the black arrow. Given the electric field vector of the linearly-polarized laser pulse, the probability that an incident photon would excite the chromophore is given. (B) The time evolution of an idealized TiO_2 nanoparticle after photoexcitation with a linearly-polarized laser pulse.

In a second approach, a linearly-polarized laser pulse is used for photoexcitation, Figure 1.11A. The probability of photoexcitation is proportional to $\cos^2\theta$, where θ is the angle between the electric field vector, \vec{E} , of the polarized light and the transition dipole moment, $\vec{\mu}$, of the chromophore.^{93,149} With the \vec{E} oriented as depicted in Figure 1.11A, the chromophores at the “north” and “south” poles of the idealized TiO_2 nanoparticle will be preferentially excited

creating an anisotropic distribution of oxidized chromophores on the surface as depicted in step 1 of Figure 1.11B. In the absence of molecular or nanoparticle rotation, the transient anisotropy decay has been attributed to lateral self-exchange electron transfer, step 2.^{93,149} Again, all of the above reactions occur in kinetic competition with back-electron transfer. The transient anisotropy decay of the sample is simulated with Monte-Carlo simulations and k_{et} has been extracted.^{93,150}

1.4.3 Structural and Solvent Effects on Lateral Electron Transfer

To date, few studies have systematically examined lateral electron transfer across the semiconductor interface. However, from the scattered reports of lateral electron transfer in the literature, the influence of the electrolyte, semiconductor substrate, and molecular structure can be inferred.^{101,150} Two recent reviews have tabulated the apparent diffusion coefficients for a large number of compounds as well as the experimental method used to measure them.^{101,150} For the ease of discussion, selected diffusion coefficients are given in Table 1.1 for the compounds depicted in Scheme 1.4.

Scheme 1.4. Relevant Compounds used for Lateral Self-Exchange Electron Transfer

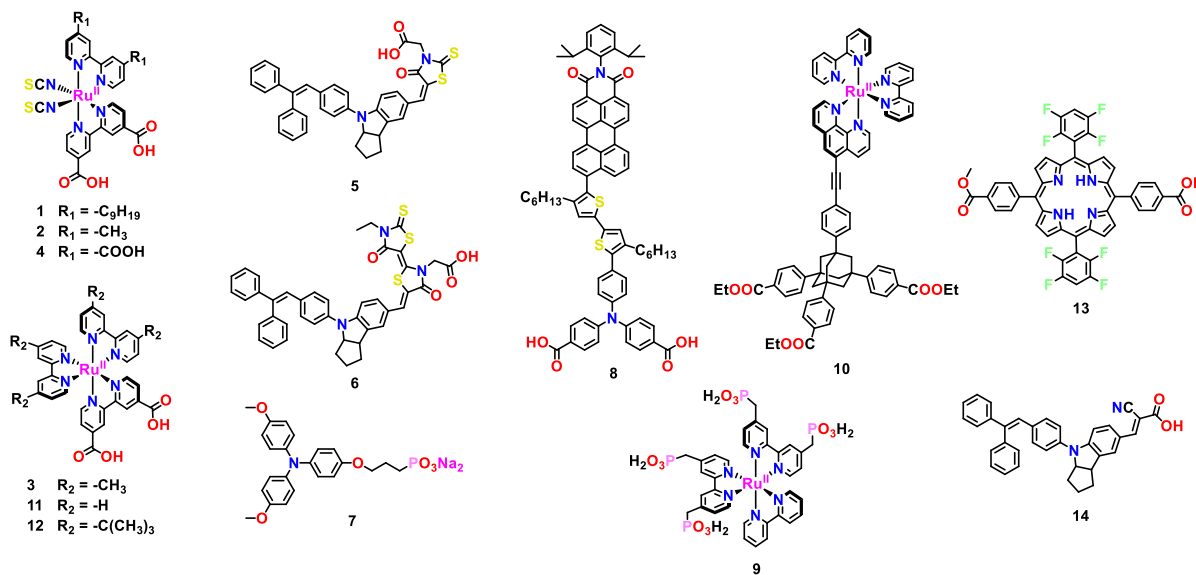


Table 1.1. Selected Apparent Diffusion Coefficients, D , for Lateral Self-Exchange Electron Transfer

#	Metal Oxide	Electrolyte ^a	D (cm ² /s)	k_{et} (s ⁻¹)	Experimental Technique	Ref.
1	TiO ₂	0.1 M EMITFSI/CH ₃ CN	4.1×10^{-9}	-	CV	142
2	TiO ₂	0.1 M EMITFSI/CH ₃ CN	1.1×10^{-8}	-	CV	142
3	TiO ₂	0.1 M EMITFSI/CH ₃ CN	3×10^{-10}	-	CV	142
4	TiO ₂	0.1 M EMITFSI/CH ₃ CN	0	-	CV	142
5	TiO ₂	0.1 M TBAClO ₄ /CH ₃ CN	6.4×10^{-8}	-	CV	151
6	TiO ₂	0.1 M TBAClO ₄ /CH ₃ CN	1.7×10^{-7}	-	CV	151
7	TiO ₂	1:1 EMITFSI:CH ₃ CN	1.1×10^{-8}	-	CA	100
	ZrO ₂	1:1 EMITFSI:CH ₃ CN	4.6×10^{-9}	-	CA	100
	TiO ₂	EMITFSI	2.8×10^{-9}	-	CA	100
	Al ₂ O ₃	EMITFSI	3.5×10^{-11}	-	CA	100
8	TiO ₂	EMITFSI	2.3×10^{-8}	-	CC	141
	Al ₂ O ₃	EMITFSI	3.5×10^{-9}	-	CC	141
9	TiO ₂	0.1 M LiClO ₄ /CH ₃ CN	1.6×10^{-10}	-	CA	152
	NiO	0.1 M LiClO ₄ /CH ₃ CN	7.1×10^{-11}	-	CA	152
10	TiO ₂	0.1 M TBAClO ₄ /CH ₃ CN	10^{-11}	-	CA	153
11	TiO ₂	0.1 M TBAClO ₄ /CH ₃ CN	10^{-11}	-	CA	153
12	TiO ₂	0.1 M LiClO ₄ /CH ₃ CN	2.4×10^{-10}	-	CA	113
13	SnO ₂	H ₂ O	-	3.6×10^8	TAS	146
	SnO ₂	3:1 H ₂ O:CH ₃ CN	-	8.9×10^7	TAS	146
	SnO ₂	1:1 H ₂ O:CH ₃ CN	-	5.0×10^7	TAS	146
	SnO ₂	1:3 H ₂ O:CH ₃ CN	-	2.5×10^7	TAS	146
	SnO ₂	CH ₃ CN	-	5.6×10^5	TAS	146
	SnO ₂	PC	-	3.6×10^5	TAS	146
14	TiO ₂	0.1 M TBAClO ₄ /CH ₃ CN	2.8×10^{-8}	-	CV	143

^aEMITFSI = 1-ethyl-2-methylimidazolium bis(trifluoromethylsulfonyl)imide, CH₃CN = acetonitrile, TBAP = tetrabutylammonium perchlorate, PC = propylene carbonate. ^bCV = cyclic voltammetry, CA = chronoabsorptometry, CC = chronocoulometry, TAS = transient absorption spectroscopy.

Lateral self-exchange electron transfer has been reported for many redox-active compounds on metal oxide surfaces.^{101,143,150} It is clear from these published results that the molecular structure and the location of the frontier orbitals affect the measured rates. This is readily reflected in results published by Wang *et al.* using Ru^{II} chromophores (**1-4**, Scheme 1.4).¹⁴² The location of the frontier orbitals in compounds **1** and **2** were delocalized across the Ru-NCS moiety and displayed D_{CV} values at least an order of magnitude larger than the Ru^{II} polypyridyl compound, **3**, where the frontier orbitals were almost entirely metal centered. The larger values for **1** and **2** were attributed to better intermolecular orbital overlap between neighboring chromophores when compared with **3** resulting in larger H_{DA} . Furthermore, the spatial orientation of the frontier orbitals with respect to its neighboring molecules was also shown to affect to the lateral electron transfer rates. Unlike **1** and **2**, compound **4**, which also bares NCS⁻ groups displayed no measurable D_{CV} . Wang *et al.* attributed this behavior to the orientation of the isothiocyanate groups.¹⁴² In **4**, they reasoned that the compound was likely bound to the surface through two carboxylate groups, one from each bipyridyl ligand, which oriented the isothiocyanate groups away from the surface and from its neighbors resulting in little intermolecular orbital overlap and small H_{DA} . In support of this observation, Vaissier and co-workers concluded that variations in molecular orientation and packing on the surface contributed to the difference in D_{CV} values measured for two indoline chromophores (**5** and **6**, Scheme 1.4).¹⁵¹ Using computational methods, these authors also demonstrated that structural fluctuations in **5** and **6** occurring on the timescale of electron transfer allowed for conformations between neighboring compounds that possessed large H_{DA} and that these fluctuations contributed to the experimentally rapid lateral electron transfer kinetics observed. The influence of molecular structure is the focus of **Chapters 2** and **3** where subtle structural

modifications to a series of Ru^{II} polypyridyl compounds were used to tune lateral self-exchange electron transfer kinetics on the surface.

Another factor which may influence lateral electron transfer kinetics is the nature of the underlying metal oxide. Lateral electron transfer reactions have been reported on TiO₂, ZrO₂, Al₂O₃, tin(IV) oxide (SnO₂), and nickel(II) oxide (NiO).^{100,101,109,113,141-143,145,146,152} Several reports demonstrate that the apparent diffusion coefficients for a given compound are faster on TiO₂ than on Al₂O₃ when measured by the same experimental technique under the same conditions. Bonhôte and co-workers measured D_{CA} values for a substituted-TPA compound, **7** in Scheme 1.4, and found that diffusion coefficients measured on TiO₂ were two orders of magnitude faster than when measured on Al₂O₃ despite possessing similar surface coverages.¹⁰⁰ More recently, Wang *et al.* corroborated this result using compound **8** where D_{CC} values were found to be an order of magnitude faster on TiO₂ than on Al₂O₃.¹⁴¹ A similar result was obtained by Bonhôte using compound **7** when comparing lateral electron transfer rates on TiO₂ and ZrO₂.¹⁰⁰ The measured D_{CA} values were found to be twice as large on TiO₂ than on ZrO₂. Finally, Shan *et al.* showed that D_{CA} values for a Ru^{II} polypyridyl compound, **9**, displayed D_{CA} values on TiO₂ that were double those found on NiO.¹⁵² While speculative, the origins of these varied D_{CA} may come from a difference in the dielectric constant or surface charge of the semiconductor substrate which may influence the total reorganization energy of the electron transfer process, as has been supported by theoretical calculations.¹⁵⁵ However, one cannot rule out the possible differences in molecular packing on the surface or metal oxide morphologies influencing the observed kinetics.

A separate report by Gallopini *et al.* has suggested that the proximity of the redox-active site to the semiconductor interface has little influence on the lateral self-exchange

electron transfer kinetics.¹⁵³ Apparent diffusion coefficients were measured for a tripodal Ru^{II} polypyridyl compound and for [Ru(bpy)₂(deeb)]²⁺, compounds **7** and **8** in Scheme 1.4. For **7**, the redox site was held 17 Å from the surface as opposed to only 6-7 Å as it was for **8**. The authors found the measured D_{CA} values to be within error the same and reasoned that the intermolecular distance between neighboring metal centers for the two compounds were approximately the same therefore resulting in the similarity of the measured D_{CA} .¹⁵³ From these observations, the authors concluded that the TiO₂ surface did not contribute to the reorganization energy of the electron transfer process. This result conflicts with those above and underscores the need for more research to understand the influence of the metal oxide on lateral electron transfer kinetics.

The nature of the electrolyte solution has also been shown to influence lateral electron transfer rates. Base pre-treated TiO₂ films functionalized with **4** displayed an unexpected cation dependence of the anodic current in cyclic voltammetry.¹⁵⁵ In electrolyte solutions containing 0.1 M TBAClO₄ in acetonitrile, there was no evidence of redox chemistry associated with self-exchange. However, completely reversible electrochemistry was reported when the electrolyte cation was exchanged with Li⁺. Further work by Ardo and co-workers, demonstrated that [Ru(dtb)₂(dcb)]²⁺ (**6** in Scheme 1.4) did not undergo photoinduced lateral self-exchange electron transfer in neat acetonitrile; however, self-exchange was observed with the addition of 0.01 M LiClO₄ salt.⁹³ These authors concluded that the Lewis acidic Li⁺ cation lowered the work term for electron transfer and thus enabled lateral charge transport for these polypyridyl compounds.⁹³

Another report has detailed the solvent dependence of lateral electron transfer between a surface-anchored, free base porphyrin compound (**7**, Scheme 1.4) on SnO₂ surfaces.¹⁴⁶

Through transient absorption spectroscopy, a deceleration of lateral electron transfer rates were reported when the solvent was changed from acetonitrile to propylene carbonate containing 0.1 M LiClO₄ as expected from Marcus two-sphere continuum model, which predicts an inverse relationship with the solvent dielectric constant, eq 1.11.^{114,122,123,146} However, upon the addition of water, aggregation of the porphyrin molecule was observed resulting in faster electron transfer rates. This demonstrated that the solvent identity could be an effective tool to tune lateral electron transfer rates.

1.4.4 Effects of Lateral Electron Transfer in DSSCs and DSPECs

The importance of lateral electron transfer between surface-immobilized molecules at the semiconductor interface is becoming increasingly more apparent in dye-sensitized technologies. In DSSCs, recent studies published by the Barnes and Nelson groups have shown that lateral self-exchange electron transfer between surface anchored indoline chromophores (**14**, Scheme 1.4) is instrumental for regeneration when solid hole-transport materials are used, *i.e.* solid-state DSSCs.¹⁰⁶ In these devices, a solid hole-transport material is used to replace the liquid electrolyte containing the redox mediator to shuttle electrons from the counter-electrode to the oxidized chromophores. Traditional hole-transport material deposition methods are often limited by partial pore-filling of the mesoporous thin film. Using transient absorption spectroscopy and transient anisotropy measurements, Moia and co-workers showed that lateral self-exchange electron transfer contributed significantly to the regeneration efficiency of a solar cell when the fraction of chromophores in contact with the hole-transport medium was small.¹⁰⁶

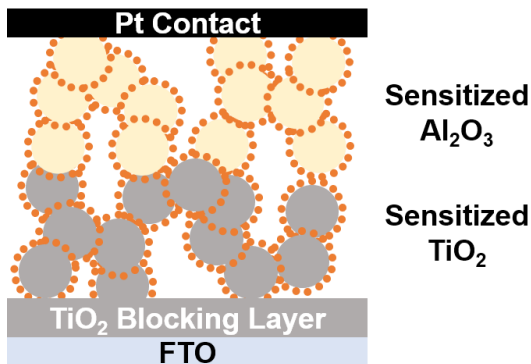


Figure 1.12. A depiction of the “dry cell” dye-sensitized solar cell which used lateral self-exchange electron transfer between the oxidized chromophore to complete the circuit rather than a redox mediator in solution. Photoexcitation leads to electron injection on the sensitized TiO₂ interface, and the electrons are collected at the FTO. Lateral self-exchange electron transfer shuttle the oxidizing equivalent to the Pt counter electrode.

In a proof-of-concept example, lateral self-exchange electron transfer was used to shuttle oxidizing equivalents to the counter-electrode instead of a redox mediator.¹⁰⁷ This process is highly desirable because it allows for charge transport without a loss of free energy and hence could lead to more efficient devices. Indeed, Moia *et al.* demonstrated that lateral self-exchange electron transfer was sufficient to shuttle a small fraction of the oxidizing equivalents to the counter electrode to complete the circuit.¹⁰⁷ The structure of such a solar cell, which they referred to as a “dry cell,” is shown in Figure 1.12. In this device, photoexcitation of **14** anchored to the TiO₂ interface resulted in electron injection. The electrons in TiO₂ move through the TiO₂ substrate and are collected at the FTO. The oxidized chromophore undergoes sequential self-exchange electron transfer reactions to shuttle the oxidizing equivalent to the Pt counter electrode. To prevent a short-circuit in the cell, Al₂O₃ is used as the conduction band potential is too negative to allow for electron injection from **14** and electron transfer from the TiO₂ to the Al₂O₃. This resulted in solar cells with photovoltages of ~1 V; however, only a small fraction of the photogenerated charge-separated states were

collected due to high rates of charge recombination resulting in small photovoltages. The incident photon-to-current efficiency in these solar cells was ~13%.¹⁰⁷

Back-electron transfer between an electron in TiO₂ and the oxidized chromophore occurs with kinetics that generally do not follow first- or second-order kinetic models.^{30,102} These kinetics are typically fit to the Koulrausch-Williams-Watts function, which accounts for back-electron transfer occurring with a distribution of rates.^{30,102} Such dispersive kinetics are often attributed to electron mobility in TiO₂, which is rate-limited by a trapping-detrapping model, allowing back-electron transfer to occur from many different sites on the surface.¹⁵⁶ However, it has been demonstrated that the self-exchange rate constant is proportional to the back-electron transfer rates.¹¹⁰⁻¹¹² Moia and co-workers showed that that when the surface coverage of the chromophore was below the percolation threshold, back-electron transfer rates were slower than at high surface coverages.¹¹² These results were corroborated by two reports from Sampaio *et al.* where both the surface coverage and the inherent self-exchange rate constant were used to control back-electron transfer kinetics.^{110,111} Again, when sensitizer self-exchange rate was sluggish, back-electron transfer was also found to be slow. Through temperature dependent studies, Sampaio and DiMarco concluded that rapid lateral electron transfer rates lowered the barrier for the back-electron transfer.¹¹⁰ These results indicated that self-exchange on the surface contributes to the dispersive kinetics measured.

In DSPECs, lateral electron transfer provides a mechanism for shuttling redox equivalents to a co-adsorbed model catalyst, Scheme 1.3.^{45,108,109} Several recent studies have demonstrated that the lateral electron transfer process could compete with back-electron transfer reactions and shuttle an oxidizing equivalent to a co-adsorbed electron donor to localize the charge on a single molecule.¹⁰⁹ However, these authors report surface coverage

dependent back-electron transfer rates from the oxidized donor. At a 25:1 chromophore to electron donor ratio, back-electron transfer rates from the donor were small. Higher electron donor coverages provide lateral self-exchange electron transfer pathways between the donors that increase back-electron transfer rates which were in agreement with the results of Moia and Sampaio.^{110-112,115}

Multi-electron accumulation onto a model catalyst was recently reported by Chen and Ardo.¹⁰⁸ Kinetic control of lateral self-exchange electron enabled accumulation of two oxidizing equivalents onto a single model catalyst. Furthermore, they found the largest yield of the doubly-oxidized model catalyst occurred at low catalyst surface coverages. Presumably at higher proxy catalyst coverages, comproportionation reactions resulted in the formation of two singly-oxidized proxy catalysts. These results present proof-of-concept that lateral electron transfer can accumulate multiple oxidizing equivalents onto a catalyst. Therefore, lateral electron transfer kinetics is paramount for the optimization of solar cells and is the focus of this thesis.

1.5 Conclusion

The need to efficiently capture and store solar energy would help enable a sustainable global energy supply for mankind. Dye-sensitized solar and photoelectrochemical cells that convert solar energy to electricity or chemical fuels provide an opportunity to investigate the reaction chemistry at the molecular level. One important process in both solar cells is lateral electron transfer across the semiconductor surface. However, few systematic studies exist to understand the how lateral electron transfer affects other processes that occur in these dye-sensitized technologies, or the available tools to tune it.

In **Chapters 2-4**, the molecular structure was found to influence lateral self-exchange electron transfer. In **Chapters 2 and 3**, substituents at the 4 and 4' positions of a homologous series of Ru^{II} 2,2'-polypyridyl compounds influenced the kinetics of self-exchange electron transfer. It was found that the steric bulk was the dominant factor controlling the measured rate constants. In **Chapter 4**, four compounds with two redox active groups, a bis(tridentate) cyclometalated Ru^{II} metal center and a substituted-triphenylamine donor connected by a thiophene bridge, were anchored to TiO₂ surfaces to study of lateral intermolecular electron transfer. It was found that the intramolecular electronic coupling influenced the rate and mechanism of lateral charge transport.

Thermal, bimolecular electron transfer between Co^{II} and Ru^{III} polypyridyl compounds that followed Marcus-inverted behavior were observed in acetonitrile and is the focus of **Chapter 5**. In **Chapter 6**, the photophysical properties and excited-state decay pathways were explored for a series of tris(bidentate) cyclometalated Ru^{II} chromophores which have emerged as a promising new paradigm for chromophore design in DSSCs. Temperature-dependent photoluminescence studies indicated that the dissociative ligand field states were not accessible near room temperature, and that these compounds were photostable.

REFERENCES

- (1) *International Energy Outlook 2017*; DOE/EIA-0484(2017); U.S. Energy Information Administration, Department of Energy: Washington, D.C., 2017; 1-152.
- (2) *BP Statistical Review of World Energy*; Technical Report for BP p.l.c.; Pureprint Group Limited: London, United Kingdom, June 2017; 1-50.
- (3) *World Population Prospects: The 2017 Revision, Key Findings and Advance Tables. Working Paper*; ESA/P/WP/248; United Nations, Department of Economic and Social Affairs, Population Division: New York, 2017; 1-46.
- (4) House, R. L.; Iha, N. Y. M.; Coppo, R. L.; Alibabaei, L.; Sherman, B. D.; Kang, P.; Brennaman, M. K.; Hoertz, P. G.; Meyer, T. J. Artificial photosynthesis: Where are we now? Where can we go? *J. Photochem. Photobio. C* **2015**, 25, 32-45.
- (5) *World Energy Outlook 2017: Executive Summary*; International Energy Association, Organisation for Economic Co-operation and Development; IEA Publications: November 2017, 1-13.
- (6) Ekener-Petersen, E.; Höglund, J.; Finnveden, G. Screening potential social impacts of fossil fuels and biofuels for vehicles. *Energy Policy* **2014**, 73, 416-426.
- (7) Myre, G. The 1973 Arab Oil Embargo: The Old Rules No Longer Apply. <https://www.npr.org/sections/parallels/2013/10/15/234771573/the-1973-arab-oil-embargo-the-old-rules-no-longer-apply> (accessed May 31, 2018)
- (8) Mouawad, J. Rising Demand for Oil Porvokes New Energy Crisis. <https://www.nytimes.com/2007/11/09/business/worldbusiness/09oil.html> (accessed May 31, 2018),
- (9) Palmer, M. A.; Bernhardt, E. S.; Schlesinger, W. H.; Eshleman, K. N.; Foufoula-Georgiou, E.; Hendryx, M. S.; Lemly, A. D.; Likens, G. E.; Loucks, O. L.; Power, M. E.; White, P. S.; Wilcock, P. R. Mountaintop Mining Consequences. *Science* **2010**, 327, 148-149.
- (10) Hendryx, M.; O'Donnell, K.; Horn, K. Lung cancer mortality is elevated in coal-mining areas of Appalachia. *Lung Cancer* **2008**, 62, 1-7.
- (11) Epstein, P. R.; Buonocore, J. J.; Eckerle, K.; Hendryx, M.; Stout, B. M., III; Heinberg, R.; Clapp, R. W.; May, B.; Reinhart, N. L.; Ahern, M. M.; Doshi, S. K.; Glustrom, L. Full cost accounting for the life cycle of coal. *Ann. N.Y. Acad. Sci.* **2011**, 1219, 73-98.
- (12) Adgate, J. L.; Goldstein, B. D.; McKenzie, L. M. Potential Public Health Hazards, Exposures and Health Effects from Unconventional Natural Gas Development. *Environ. Sci. Technol.* **2014**, 48, 8307-8320.

- (13) Li, J.; Qi, Z.; Li, M.; Wu, D.; Zhou, C.; Lu, S.; Yan, J.; Li, X. Physical and Chemical Characteristics of Condensable Particulate Matter from an Ultralow-Emission Coal-Fired Power Plant. *Energy Fuels* **2017**, *31*, 1778-1785.
- (14) Wong, E. Air Pollution Linked to 1.2 Million Premature Deaths in China. <https://www.nytimes.com/2013/04/02/world/asia/air-pollution-linked-to-1-2-million-deaths-in-china.html> (accessed May 27, 2018)
- (15) Peterson, C. H.; Rice, S. D.; Short, J. W.; Esler, D.; Bodkin, J. L.; Ballachey, B. E.; Irons, D. B. Long-Term Ecosystem Response to the Exxon Valdez Oil Spill. *Science* **2003**, *302*, 2082-2086.
- (16) Mendelsohn, I. A.; Andersen, G. L.; Baltz, D. M.; Caffey, R. H.; Carman, K. R.; Fleeger, J. W.; Joye, S. B.; Lin, Q.; Maltby, E.; Overton, E. B.; Rozas, L. P. Oil Impacts on Coastal Wetlands: Implications for the Mississippi River Delta Ecosystem after the Deepwater Horizon Oil Spill. *BioScience* **2012**, *62*, 562-574.
- (17) Conley, S.; Franco, G.; Faloon, I.; Blake, D. R.; Peischl, J.; Ryerson, T. B. Methane emissions from the 2015 Aliso Canyon blowout in Los Angeles, CA. *Science* **2016**, *351*, 1317-1320.
- (18) Arrhenius, S. XXXI. On the influence of carbonic acid in the air upon the temperature of the ground. *The London, Edinburgh, and Dublin Philosophical Magazine and Journal of Science* **1896**, *41*, 237-276.
- (19) Hartmann, D.L., A.M.G. Klein Tank, M. Rusticucci, L.V. Alexander, S. Brönnimann, Y. Charabi, F.J. Dentener, E.J. Dlugokencky, D.R. Easterling, A. Kaplan, B.J. Soden, P.W. Thorne, M. Wild and P.M. Zhai, 2013: Observations: Atmosphere and Surface. In: *Climate Change 2013: The Physical Science Basis. Contribution of Working Group I to the Fifth Assessment Report of the Intergovernmental Panel on Climate Change* [Stocker, T.F., D. Qin, G.-K. Plattner, M. Tignor, S.K. Allen, J. Boschung, A. Nauels, Y. Xia, V. Bex and P.M. Midgley (eds.)]. Cambridge University Press, Cambridge, United Kingdom and New York, NY, USA.
- (20) Jain, P. C. Greenhouse effect and climate change: scientific basis and overview. *Renew. Energ.* **1993**, *3*, 403-420.
- (21) Ciais, P., C. Sabine, G. Bala, L. Bopp, V. Brovkin, J. Canadell, A. Chhabra, R. DeFries, J. Galloway, M. Heimann, C. Jones, C. Le Quéré, R.B. Myneni, S. Piao and P. Thornton, 2013: Carbon and Other Biogeochemical Cycles. In: *Climate Change 2013: The Physical Science Basis. Contribution of Working Group I to the Fifth Assessment Report of the Intergovernmental Panel on Climate Change* [Stocker, T.F., D. Qin, G.-K. Plattner, M. Tignor, S.K. Allen, J. Boschung, A. Nauels, Y. Xia, V. Bex and P.M. Midgley (eds.)]. Cambridge University Press, Cambridge, United Kingdom and New York, NY, USA.
- (22) Modern Records of Atmospheric Carbon Dioxide (CO₂) and a 2000-year Ice-core Record from Law Dome, Antarctica, Carbon Dioxide Information Analysis Center, Oak Ridge

- National Laboratory, U.S. Department of Energy. http://cdiac.ess-dive.lbl.gov/trends/co2/modern_co2.html. (accessed May 27, 2018)
- (23) Barnola, J.-M., D. Raynaud, C. Lorius, and N.I. Barkov. 2003. Historical CO₂ record from the Vostok ice core. In *Trends: A Compendium of Data on Global Change*. Carbon Dioxide Information Analysis Center, Oak Ridge National Laboratory, U.S. Department of Energy, Oak Ridge, Tenn., U.S.A. <http://cdiac.ess-dive.lbl.gov/trends/co2/vostok.html>. (accessed May 27, 2018)
- (24) Dlugokencky, E.J., P.M. Lang, J.W. Mund, A.M. Crotwell, M.J. Crotwell, and K.W. Thoning (2017), Atmospheric Carbon Dioxide Dry Air Mole Fractions from the NOAA ESRL Carbon Cycle Cooperative Global Air Sampling Network, 1968-2016, Version: 2017-07-28. ftp://aftp.cmdl.noaa.gov/data/trace_gases/co2/flask/surface/. (accessed May 27, 2018)
- (25) Piao, S.; Ciais, P.; Huang, Y.; Shen, Z.; Peng, S.; Li, J.; Zhou, L.; Liu, H.; Ma, Y.; Ding, Y.; Friedlingstein, P.; Liu, C.; Tan, K.; Yu, Y.; Zhang, T.; Fang, J. The impacts of climate change on water resources and agriculture in China. *Nature* **2010**, *467*, 43-51.
- (26) Hatfield, J.; Takle, G.; Grotjahn, R.; Holden, P.; Izaurralde, R. C.; Mader, T.; Marshall, E.; Liverman, D. Chapter 6: Agriculture. In *Climate Change Impacts in the United States: The Third National Climate Assessment*; Melillo, J. M., Richmond, T. C., Yohe, G. W., Ed.; U.S. Global Change Research Program: 2014; pp 150-174.
- (27) *World Energy Assessment: Energy and the Challenge of Sustainability*; United Nations Development Program; Bureau for Development Policy: New York, New York, 2000; 1-508.
- (28) NASA Science Solar System Exploration: Earth, By the Numbers. <https://solarsystem.nasa.gov/planets/earth/by-the-numbers/>. (assessed May 22, 2018)
- (29) Lewis, N. S.; Nocera, D. G. Powering the planet: Chemical challenges in solar energy utilization. *Proc. Natl. Acad. Sci. U.S.A.* **2006**, *103*, 15729-15735.
- (30) Ardo, S.; Meyer, G. J. Photodriven heterogeneous charge transfer with transition-metal compounds anchored to TiO semiconductor surfaces. *Chem. Soc. Rev.* **2009**, *38*, 115-164.
- (31) Ciamician, G. The Photochemistry of the Future. *Science* **1912**, *36*, 385-394.
- (32) Lewis, N. S. Introduction: Solar Energy Conversion. *Chem. Rev.* **2015**, *115*, 12631-12632.
- (33) Weinstein, L. A.; Loomis, J.; Bhatia, B.; Bierman, D. M.; Wang, E. N.; Chen, G. Concentrating Solar Power. *Chem. Rev.* **2015**, *115*, 12797-12838.
- (34) Lee, T. D.; Ebong, A. U. A review of thin film solar cell technologies and challenges. *Renew. Sust. Energ. Rev.* **2017**, *70*, 1286-1297.

- (35) Chopra, K. L.; Paulson, P. D.; Dutta, V. Thin-film solar cells: an overview. *Prog. Photovolt: Res. and Appl.* **2004**, *12*, 69-92.
- (36) Taguchi, M.; Yano, A.; Tohoda, S.; Matsuyama, K.; Nakamura, Y.; Nishiwaki, T.; Fujita, K.; Maruyama, E. 24.7% Record Efficiency HIT Solar Cell on Thin Silicon Wafer. *IEEE J. of Photovolt.* **2014**, *4*, 96-99.
- (37) Shockley, W.; Queisser, H. J. Detailed Balance Limit of Efficiency of p-n Junction Solar Cells. *J. Appl. Phys.* **1961**, *32*, 510-519.
- (38) Meyer, G. J. The 2010 Millennium Technology Grand Prize: Dye-Sensitized Solar Cells. *ACS Nano* **2010**, *4*, 4337-4343.
- (39) Jacoby, M. The future of low-cost solar cells. *Chem. Eng. News* **2016**, *94*, 30-35.
- (40) Fu, R.; Feldman, D.; Margolis, R.; Woodhouse, M.; Ardani, K., *U.S. Solar Photovoltaic System Cost Benchmark: Q1 2017*; NREL/TP-6A20-68925; National Renewable Energy Laboratory, Department of Energy: Golden, Colorado, United States, August 2017. 1-73
- (41) Waters, C. This “duck curve” is solar energy’s greatest challenge. <https://www.vox.com/2018/5/9/17336330/duck-curve-solar-energy-supply-demand-problem-caiso-nrel>. (accessed May 27, 2018)
- (42) Denholm, P.; O'Connell, M.; Brinkman, G.; Jorgenson, J. *Overgeneration from Solar Energy in California: A Field Guide to the Duck Chart*; NREL/TP-6A20-65023; National Renewable Energy Laboratory, Department of Energy: Golden, Colorado, United States, September 2017. 1-46.
- (43) California Independent System Operator. *What the duck curve tells us about managing a green grid*. https://www.caiso.com/Documents/FlexibleResourcesHelpRenewables_FastFacts.pdf (accessed May 27, 2018).
- (44) California Independent System Operator. *California ISO Open Access Same-time Information System (OASIS)*. <http://oasis.caiso.com>, (accessed May 27, 2018)
- (45) Ashford, D. L.; Gish, M. K.; Vannucci, A. K.; Brennaman, M. K.; Templeton, J. L.; Papanikolas, J. M.; Meyer, T. J. Molecular Chromophore–Catalyst Assemblies for Solar Fuel Applications. *Chem. Rev.* **2015**, *115*, 13006-13049.
- (46) Blankenship, R. E.; Tiede, D. M.; Barber, J.; Brudvig, G. W.; Fleming, G.; Ghirardi, M.; Gunner, M. R.; Junge, W.; Kramer, D. M.; Melis, A.; Moore, T. A.; Moser, C. C.; Nocera, D. G.; Nozik, A. J.; Ort, D. R.; Parson, W. W.; Prince, R. C.; Sayre, R. T. Comparing Photosynthetic and Photovoltaic Efficiencies and Recognizing the Potential for Improvement. *Science* **2011**, *332*, 805-809.

- (47) Fujishima, A.; Honda, K. Electrochemical Photolysis of Water at a Semiconductor Electrode. *Nature* **1972**, *238*, 37-38.
- (48) Hedstrand, D. M.; Kruizinga, W. H.; Kellogg, R. M. Light induced and dye accelerated reductions of phenacyl onium salts by 1,4-dihydropyridines. *Tetrahedron Lett.* **1978**, *19*, 1255-1258.
- (49) Spitler, M. T.; Calvin, M. Electron transfer at sensitized TiO₂ electrodes. *J. Chem. Phys.* **1977**, *66*, 4294-4305.
- (50) Dressick, W. J.; Meyer, T. J.; Durham, B.; Rillema, D. P. Excited-state photoelectrochemical cells for the generation of hydrogen and oxygen based on Ru(bpy)₃²⁺. *Inorg. Chem.* **1982**, *21*, 3451-3458.
- (51) Hagfeldt, A.; Boschloo, G.; Sun, L.; Kloo, L.; Pettersson, H. Dye-Sensitized Solar Cells. *Chem. Rev.* **2010**, *110*, 6595-6663.
- (52) Hardin, B. E.; Snaith, H. J.; McGehee, M. D. The renaissance of dye-sensitized solar cells. *Nat. Photonics* **2012**, *6*, 162-169.
- (53) Meyer, T. J. Chemical Approaches to Artificial Photosynthesis. *Acc. Chem. Res.* **1989**, *22*, 163-170.
- (54) Teegardin, K.; Day, J. I.; Chan, J.; Weaver, J. Advances in Photocatalysis: A Microreview of Visible Light Mediated Ruthenium and Iridium Catalyzed Organic Transformations. *Org. Process Res. Dev.* **2016**, *20*, 1156-1163.
- (55) Arias-Rotondo, D. M.; McCusker, J. K. The photophysics of photoredox catalysis: a roadmap for catalyst design. *Chem. Soc. Rev.* **2016**, *45*, 5803-5820.
- (56) Beer, P. D.; Cadman, J. Electrochemical and optical sensing of anions by transition metal based receptors. *Coord. Chem. Rev.* **2000**, *205*, 131-155.
- (57) Higgins, S. L. H.; Brewer, K. J. Designing Red-Light-Activated Multifunctional Agents for the Photodynamic Therapy. *Angew. Chem. Int. Ed.* **2012**, *51*, 11420-11422.
- (58) White, J. K.; Schmehl, R. H.; Turro, C. An overview of photosubstitution reactions of Ru(II) imine complexes and their application in photobiology and photodynamic therapy. *Inorg. Chim. Acta* **2017**, *454*, 7-20.
- (59) Juris, A.; Barigelletti, F.; Balzani, V.; Belser, P.; Von Zelewsky, A. Luminescence of Ruthenium(II) Tris Chelate Complexes Containing the Ligands 2,2'-Bipyridine and 2,2'-Biisoquinoline. Behavior of the Ru(bpy)₃²⁺ and Ru(bpy)₂²⁺ emitting units. *Inorg. Chem.* **1985**, *24*, 202-206.
- (60) Meyer, T. J. Photochemistry of metal coordination complexes: metal to ligand charge transfer excited states. *Pure Appl. Chem.* **1986**, *58*, 1193-1206.

- (61) Hager, G. D.; Crosby, G. A. Charge-Transfer Excited States of Ruthenium(II) Complexes. I. Quantum Yield and Decay Measurements. *J. Am. Chem. Soc.* **1975**, *97*, 7031-7037.
- (62) Hipps, K. W.; Crosby, G. A. Charge-Transfer Excited States of Ruthenium(II) Complexes. III. Electron-Ion Coupling Model for $d\pi^*$ Configurations. *J. Am. Chem. Soc.* **1975**, *97*, 7042-7048.
- (63) Durham, B.; Caspar, J. V.; Nagle, J. K.; Meyer, T. J. Photochemistry of $\text{Ru}(\text{bpy})_3^{2+}$. *J. Am. Chem. Soc.* **1982**, *104*, 4803-4810.
- (64) Creutz, C.; Chou, M.; Netzel, T. L.; Okumura, M.; Sutin, N. Lifetimes, Spectra, and Quenching of the Excited States of Polypyridine Complexes of Iron(II), Ruthenium(II), and Osmium(II). *J. Am. Chem. Soc.* **1980**, *102*, 1309-1319.
- (65) Thompson, D. W.; Ito, A.; Meyer, T. J., $[\text{Ru}(\text{bpy})_3]^{2+*}$ and other remarkable metal-to-ligand charge transfer (MLCT) excited states. *Pure Appl. Chem.*, **2013**, *85*, 1257-1305.
- (66) Juris, A.; Balzani, V.; Barigelletti, F.; Campagna, S.; Belser, P.; von Zelewsky, A. Ru(II) polypyridine complexes: photophysics, photochemistry, eletrochemistry, and chemiluminescence. *Coord. Chem. Rev.* **1988**, *84*, 85-277.
- (67) O'Donnell, R. M.; Johansson, P. G.; Abrahamsson, M.; Meyer, G. J. Excited-State Relaxation of Ruthenium Polypyridyl Compounds Relevant to Dye-Sensitized Solar Cells. *Inorg. Chem.* **2013**, *52*, 6839-6848.
- (68) Motley, T. C.; Troian-Gautier, L.; Brennaman, M. K.; Meyer, G. J. Excited-State Decay Pathways of Tris(bidentate) Cyclometalated Ruthenium(II) Compounds. *Inorg. Chem.* **2017**, *56*, 13579-13592.
- (69) Yeh, A. T.; Shank, C. V.; McCusker, J. K. Ultrafast Electron Localization Dynamics Following Photo-Induced Charge Transfer. *Science* **2000**, *289*, 935-938.
- (70) Damrauer, N. H.; Cerullo, G.; Yeh, A.; Boussie, T. R.; Shank, C. V.; McCusker, J. K. Femtosecond Dynamics of Excited-State Evolution in $[\text{Ru}(\text{bpy})_3]^{2+}$. *Science* **1997**, *275*, 54-57.
- (71) McCusker, J. K. Femtosecond Absorption Spectroscopy of Transition Metal Charge-Transfer Complexes. *Acc. Chem. Res.* **2003**, *36*, 876-887.
- (72) Crosby, G. A.; Demas, J. N. Quantum Efficiencies on Transition Metal Complexes. II. Charge-Transfer Luminescence. *J. Am. Chem. Soc.* **1971**, *93*, 2841-2847.
- (73) Harrigan, R. W.; Hager, G. D.; Crosby, G. A. Evidence for Multiple-State Emission from Ruthenium(II) Complexes. *Chem. Phys. Lett.* **1973**, *21*, 487-490.
- (74) Rillema, D. P.; Allen, G.; Meyer, T. J.; Conrad, D. Redox Properties of Ruthenium(II) Tris Chelate Complexes Containing the Ligands 2,2'-Bipyrazine, 2,2'-Bipyridine, and 2,2'-Bipyrimidine. *Inorg. Chem.* **1983**, *22*, 1617-1622.

- (75) Ito, A.; Meyer, T. J. The Golden Rule. Application for fun and profit in electron transfer, energy transfer, and excited-state decay. *Phys. Chem. Chem. Phys.* **2012**, *14*, 13731-13745.
- (76) Kasha, M. Characterization of electronic transitions in complex molecules. *Discuss. Faraday Soc.* **1950**, *9*, 14-19.
- (77) Crosby, G. A.; Demas, J. N. The Measurement of Photoluminescence Quantum Yields. A Review. *J. Phys. Chem.* **1971**, *75*, 991-1024.
- (78) Ishida, H.; Tobita, S.; Hasegawa, Y.; Katoh, R.; Nozaki, K. Recent advances in instrumentation for absolute emission quantum yield measurements. *Coord. Chem. Rev.* **2010**, *254*, 2449-2458.
- (79) Hager, G. D.; Watts, R. J.; Crosby, G. A. Charge-Transfer Excited States of Ruthenium(II) Complexes. II. Relation of Level Parameters to Molecular Structure. *J. Am. Chem. Soc.* **1975**, *97*, 7037-7042.
- (80) Kober, E. M.; Meyer, T. J. An electronic structural model for the emitting MLCT excited states of $\text{Ru}(\text{bpy})_3^{2+}$ and $\text{Os}(\text{bpy})_3^{2+}$. *Inorg. Chem.* **1984**, *23*, 3877-3886.
- (81) Van Houten, J.; Watts, R. J. Photochemistry of Tris(2,2'-bipyridyl)ruthenium(II) in Aqueous Solutions. *Inorg. Chem.* **1978**, *17*, 3381-3385.
- (82) Barigelletti, F.; Juris, A.; Balzani, V.; Belser, P.; Von Zelewsky, A. Excited-State Properties of Complexes of the $\text{Ru}(\text{diimine})_3^{2+}$ Family. *Inorg. Chem.* **1983**, *22*, 3335-3339.
- (83) Wacholtz, W. F.; Auerbach, R. A.; Schmehl, R. H. Independent Control of Charge-Transfer and Metal-Centered Excited States in Mixed-Ligand Polypyridine Ruthenium(II) Complexes via Specific Ligand Design. *Inorg. Chem.* **1986**, *25*, 227-234.
- (84) Lumpkin, R. S.; Kober, E. M.; Worl, L. A.; Murtaza, Z.; Meyer, T. J. Metal-to-Ligand Charge-Transfer (MLCT) Photochemistry: Experimental Evidence for the Participation of a Higher Lying MLCT State in Polypyridyl Complexes of Ruthenium(II) and Osmium(II). *J. Phys. Chem.* **1990**, *94*, 239-243.
- (85) Farnum, B. H.; Jou, J. J.; Meyer, G. J. Visible light generation of I-I bonds by $\text{Ru-tris}(\text{diimine})$ excited states. *Proc. Natl. Acad. Sci. U.S.A.* **2012**, *109*, 15628-15633.
- (86) Ashford, D. L.; Brennaman, M. K.; Brown, R. J.; Keinan, S.; Concepcion, J. J.; Papanikolas, J. M.; Templeton, J. L.; Meyer, T. J. Varying the Electronic Structure of Surface-Bound Ruthenium(II) Polypyridyl Complexes. *Inorg. Chem.* **2015**, *54*, 460-469.
- (87) Kober, E. M.; Caspar, J. V.; Lumpkin, R. S.; Meyer, T. J. Application of the Energy Gap Law to Excited-State Decay of Osmium(II)-Polypyridine Complexes: Calculation of

- Relative Nonradiative Decay Rates from Emission Spectral Profiles. *J. Phys. Chem.* **1986**, *90*, 3722-3734.
- (88) ASTM G173-03, Reference Solar Spectral Irradiance: Air Mass 1.5. <http://rredc.nrel.gov/solar/spectra/am1.5/>. (accessed June 4, 2018)
- (89) Grätzel, M. Photoelectrochemical cells. *Nature* **2001**, *414*, 338-344.
- (90) Gerischer, H.; Michel-Beyerle, M. E.; Rebentrost, F.; Tributsch, H. Sensitization of charge injection into semiconductors with large band gap. *Electrochim. Acta* **1968**, *13*, 1509-1515.
- (91) O'Regan, B.; Grätzel, M. A low-cost, high-efficiency solar cell based on dye-sensitized colloidal TiO₂ films. *Nature* **1991**, *353*, 737-740.
- (92) Hagfeldt, A.; Grätzel, M. Molecular Photovoltaics. *Acc. Chem. Res.* **2000**, *33*, 269-277.
- (93) Ardo, S.; Meyer, G. J. Characterization of Photoinduced Self-Exchange Reactions at Molecule-Semiconductor Interfaces by Transient Polarization Spectroscopy: Lateral Intermolecular Energy and Hole Transfer across Sensitized TiO₂ Thin Films. *J. Am. Chem. Soc.* **2011**, *133*, 15384-15396.
- (94) Mathew, S.; Yella, A.; Gao, P.; Humphry-Baker, R.; Curchod, B. F.; Ashari-Astani, N.; Tavernelli, I.; Rothlisberger, U.; Nazeeruddin, M. K.; Grätzel, M. Dye-sensitized solar cells with 13% efficiency achieved through the molecular engineering of porphyrin sensitizers. *Nat. Chem.* **2014**, *6*, 242-247.
- (95) Green, M. A.; Emery, K.; Hishikawa, Y.; Warta, W.; Dunlop, E. D.; Levi, D. H. Ho-Baillie, A. W. Y. Solar cell efficiency tables (version 49). *Prog. Photovolt: Res. Appl.* **2017**, *25*, 3-13.
- (96) Sundin, E.; Abrahamsson, M. Long-lived charge separation in dye-semiconductor assemblies: a pathway to multi-electron transfer reactions. *Chem. Commun.* **2018**, *54*, 5289-5298.
- (97) Pashaei, B.; Shahroosvand, H.; Grätzel, M.; Nazeeruddin, M. K. Influence of Ancillary Ligands in Dye-Sensitized Solar Cells. *Chem. Rev.* **2016**, *116*, 9485-9564.
- (98) Cao, Y.; Liu, Y.; Zakeeruddin, S. M.; Hagfeldt, A.; Grätzel, M. Direct Contact of Selective Charge Extraction Layers Enables High-Efficiency Molecular Photovoltaics. *Joule* **2018**, *2*, 1-10.
- (99) Zhang, X.; Xu, Y.; Giordano, F.; Schreier, M.; Pellet, N.; Hu, Y.; Yi, C.; Robertson, N.; Hua, J.; Zakeeruddin, S. M.; Tian, H.; Grätzel, M. Molecular Engineering of Potent Sensitizers for Very Efficient Light Harvesting in Thin-Film Solid-State Dye-Sensitized Solar Cells. *J. Am. Chem. Soc.* **2016**, *138*, 10742-10745.

- (100) Bonhôte, P.; Gogniat, E.; Tingry, S.; Barbé, C.; Vlachopoulos, N.; Lenzmann, F.; Comte, P.; Grätzel, M. Efficient Lateral Electron Transport inside a Monolayer of Aromatic Amines Anchored on Nanocrystalline Metal Oxide Films. *J. Phys. Chem. B* **1998**, *102*, 1498-1507.
- (101) Hu, K.; Meyer, G. J. Lateral Intermolecular Self-Exchange Reactions for Hole and Energy Transport on Mesoporous Metal Oxide Thin Films. *Langmuir* **2015**, *31*, 11164-11178.
- (102) Listorti, A.; O'Regan, B.; Durrant, J. R. Electron Transfer Dynamics in Dye-Sensitized Solar Cells. *Chem. Mater.* **2011**, *23*, 3381-3399.
- (103) Coggins, M. K.; Meyer, T. J. Dye Sensitized Photoelectrosynthesis Cells for Making Solar Fuels: From Basic Science to Prototype Devices. In *Photoelectrochemical Solar Fuel Production: From Basic Principles to Advanced Devices*; Giménez, S., Bisquert, J., Ed.; Springer International Publishing: Cham, 2016; pp 513-548.
- (104) Treadway, J. A.; Moss, J. A.; Meyer, T. J. Visible Region Photooxidation on TiO₂ with a Chromophore–Catalyst Molecular Assembly. *Inorg. Chem.* **1999**, *38*, 4386-4387.
- (105) Meyer, T. J.; Sheridan, M. V.; Sherman, B. D. Mechanisms of molecular water oxidation in solution and on oxide surfaces. *Chem. Soc. Rev.* **2017**, *46*, 6148-6169.
- (106) Moia, D.; Cappel, U. B.; Leijtens, T.; Li, X.; Telford, A. M.; Snaith, H. J.; O'Regan, B. C.; Nelson, J.; Barnes, P. R. F. The Role of Hole Transport between Dyes in Solid-State Dye-Sensitized Solar Cells. *J. Phys. Chem. C* **2015**, *119*, 18975-18985.
- (107) Moia, D.; Leijtens, T.; Noel, N.; Snaith, H. J.; Nelson, J.; Barnes, P. R. F. Dye Monolayers Used as the Hole Transporting Medium in Dye-Sensitized Solar Cells. *Adv. Mater.* **2015**, *27*, 5889-5894.
- (108) Chen, H.-Y.; Ardo, S. Direct observation of sequential oxidations of a titania-bound molecular proxy catalyst generated through illumination of molecular sensitizers. *Nat. Chem.* **2017**, *10*, 17-23.
- (109) Brennan, B. J.; Durrell, A. C.; Koepf, M.; Crabtree, R. H.; Brudvig, G. W. Towards multielectron photocatalysis: a porphyrin array for lateral hole transfer and capture on a metal oxide surface. *Phys. Chem. Chem. Phys.* **2015**, *17*, 12728-12734.
- (110) Sampaio, R. N.; DiMarco, B. N.; Meyer, G. J. Activation Energies for Electron Transfer from TiO₂ to Oxidized Dyes: A Surface Coverage Dependence Correlated with Lateral Hole Hopping. *ACS Energy Lett.* **2017**, *2*, 2402-2407.
- (111) Sampaio, R. N.; Müller, A. V.; Polo, A. S.; Meyer, G. J. Correlation Between Charge Recombination and Lateral Hole-Hopping Kinetics in a Series of cis-Ru(phen')(dcb)(NCS)₂ Dye-Sensitized Solar Cells. *ACS Appl. Mater. Interfaces* **2017**, *9*, 33446-33454.

- (112) Moia, D.; Szumska, A.; Vaissier, V.; Planells, M.; Robertson, N.; O'Regan, B. C.; Nelson, J.; Barnes, P. R. F. Interdyde Hole Transport Accelerates Recombination in Dye Sensitized Mesoporous Films. *J. Am. Chem. Soc.* **2016**, *138*, 13197-13206.
- (113) DiMarco, B. N.; Motley, T. C.; Balok, R. S.; Li, G.; Siegler, M. A.; O'Donnell, R. M.; Hu, K.; Meyer, G. J. A Distance Dependence to Lateral Self-Exchange across Nanocrystalline TiO₂. A Comparative Study of Three Homologous Ru^{III/II} Polypyridyl Compounds. *J. Phys. Chem. C* **2016**, *120*, 14226-14235.
- (114) Sutin, N. Theory of Electron Transfer Reactions: Insights and Hindsights. In *Prog. Inorg. Chem.*; John Wiley & Sons, Inc.: 1983; pp 441-498.
- (115) Barbara, P. F.; Meyer, T. J.; Ratner, M. A. Contemporary Issues in Electron Transfer Research. *J. Phys. Chem.* **1996**, *100*, 13148-13168.
- (116) Likhtenshtein, G. Electron Transfer Theories. In *Solar Energy Conversion*; Wiley-VCH Verlag GmbH & Co.: Weinheim, Germany, 2012; Chapter 1, pp 1-44.
- (117) Marcus, R. A. On the Theory of Oxidation-Reduction Reactions Involving Electron Transfer. I. *J. Chem. Phys.* **1956**, *24*, 966-978.
- (118) Young, R. C.; Keene, F. R.; Meyer, T. J. Measurement of rates of electron transfer between Ru(bpy)₃³⁺ and Fe(phen)₃²⁺ ions and between Ru(phen)₃³⁺ and Ru(bpy)₃²⁺ ions by differential excitation flash photolysis. *J. Am. Chem. Soc.* **1977**, *99*, 2468-2473.
- (119) Chan, M.-S.; Wahl, A. C. Rate of electron exchange between iron, ruthenium, and osmium complexes containing 1,10-phenanthroline, 2,2'-bipyridyl, or their derivatives from nuclear magnetic resonance studies. *J. Phys. Chem.* **1978**, *82*, 2542-2549.
- (120) Brown, G. M.; Sutin, N. A comparison of the rates of electron exchange reactions of ammine complexes of ruthenium(II) and -(III) with the predictions of adiabatic, outer-sphere electron transfer models. *J. Am. Chem. Soc.* **1979**, *101*, 883-892.
- (121) Sutin, N.; Weaver, M. J.; Yee, E. L. Correlations between outer-sphere self-exchange rates and reaction entropies for some simple redox couples. *Inorg. Chem.* **1980**, *19*, 1096-1098.
- (122) Sutin, N. Nuclear, electronic, and frequency factors in electron transfer reactions. *Acc. Chem. Res.* **1982**, *15*, 275-282.
- (123) Turro, N. J.; Ramamurthy, V.; Scaiano, J. C. *Principles of Molecular Spectroscopy*. University Science Books: Sausalito, California, United States, 2009; p 1-495.
- (124) Marcus, R. A. Electron Transfer Reactions in Chemistry: Theory and Experiment (Nobel Lecture). *Angew. Chem. Int. Ed.* **1993**, *32*, 1111-1121.
- (125) Closs, G. L.; Miller, J. R. Intramolecular Long-Distance Electron Transfer in Organic Molecules. *Science* **1988**, *240*, 440-447.

- (126) Vaissier, V.; Barnes, P.; Kirkpatrick, J.; Nelson, J. Influence of polar medium on the reorganization energy of charge transfer between dyes in a dye sensitized film. *Phys. Chem. Chem. Phys.* **2013**, *15*, 4804-4814.
- (127) Rehm, D.; Weller, A. Kinetics of Fluorescence Quenching by Electron and H-Atom Transfer. *Isr. J. Chem.* **1970**, *8*, 259-271.
- (128) Miller, J. R.; Calcaterra, L. T.; Closs, G. L. Intramolecular long-distance electron transfer in radical anions. The effects of free energy and solvent on the reaction rates. *J. Am. Chem. Soc.* **1984**, *106*, 3047-3049.
- (129) Fox, L. S.; Kozik, M.; Winkler, J. R.; Gray, H. B. Gaussian Free-Energy Dependence of Electron-Transfer Rates in Iridium Complexes. *Science* **1990**, *247*, 1069-1071.
- (130) Guldi, D. M.; Asmus, K.-D. Electron Transfer from C₇₆ (C_{2v}') and C₇₈ (D₂) to Radical Cations of Various Arenes: Evidence for the Marcus Inverted Region. *J. Am. Chem. Soc.* **1997**, *119*, 5744-5745.
- (131) Kumbhakar, M.; Manna, A.; Sayed, M.; Kumar, A.; Pal, H. Observation of the Marcus Inverted Region for Bimolecular Photoinduced Electron-Transfer Reactions in Viscous Media. *J. Phys. Chem. B* **2014**, *118*, 10704-10715.
- (132) Gould, I. R.; Ege, D.; Moser, J. E.; Farid, S. Efficiencies of photoinduced electron-transfer reactions: role of the Marcus inverted region in return electron transfer within geminate radical-ion pairs. *J. Am. Chem. Soc.* **1990**, *112*, 4290-4301.
- (133) Turró, C.; Zaleski, J. M.; Karabatsos, Y. M.; Nocera, D. G. Bimolecular Electron Transfer in the Marcus Inverted Region. *J. Am. Chem. Soc.* **1996**, *118*, 6060-6067.
- (134) Venkatesh, Y.; Munisamy, V.; Ramakrishna, B.; Kumar, P. H.; Mandal, H.; Bangal, P. R. Photoinduced bimolecular electron transfer from aromatic amines to pentafluorophenyl porphyrin combined with ultrafast charge recombination persistence with Marcus inverted region. *Phys. Chem. Chem. Phys.* **2017**, *19*, 5658-5673.
- (135) Winkler, J. R.; Gray, H. B. Long-Range Electron Tunneling. *J. Am. Chem. Soc.* **2014**, *136*, 2930-2939.
- (136) Wenger, O. S.; Leigh, B. S.; Villahermosa, R. M.; Gray, H. B.; Winkler, J. R. Electron Tunneling Through Organic Molecules in Frozen Glasses. *Science* **2005**, *307*, 99-102.
- (137) Edwards, P. P.; Gray, H. B.; Lodge, M. T. J.; Williams, R. J. P. Electron Transfer and Electronic Conduction through an Intervening Medium. *Angew. Chem. Int. Ed.* **2008**, *47*, 6758-6765.
- (138) Heimer, T. A.; D'Arcangelis, S. T.; Farzad, F.; Stipkala, J. M.; Meyer, G. J. An Acetylacetonate-Based Semiconductor-Sensitizer Linkage. *Inorg. Chem.* **1996**, *35*, 5319-5324.

- (139) Blauch, D. N.; Saveant, J. M. Dynamics of electron hopping in assemblies of redox centers. Percolation and diffusion. *J. Am. Chem. Soc.* **1992**, *114*, 3323-3332.
- (140) Blauch, D. N.; Saveant, J. M. Effects of long-range electron transfer on charge transport in static assemblies of redox centers. *J. Phys. Chem.* **1993**, *97*, 6444-6448.
- (141) Wang, Q.; Zakeeruddin, S. M.; Cremer, J.; Bäuerle, P.; Humphry-Baker, R.; Grätzel, M. Cross Surface Ambipolar Charge Percolation in Molecular Triads on Mesoscopic Oxide Films. *J. Am. Chem. Soc.* **2005**, *127*, 5706-5713.
- (142) Wang, Q.; Zakeeruddin, S. M.; Nazeeruddin, M. K.; Humphry-Baker, R.; Grätzel, M. Molecular Wiring of Nanocrystals: NCS-Enhanced Cross-Surface Charge Transfer in Self-Assembled Ru-Complex Monolayer on Mesoscopic Oxide Films. *J. Am. Chem. Soc.* **2006**, *128*, 4446-4452.
- (143) Moia, D.; Vaissier, V.; Lopez-Duarte, I.; Torres, T. S.; Nazeeruddin, M. K.; O'Regan, B. C.; Nelson, J.; Barnes, P. R. F. The reorganization energy of intermolecular hole hopping between dyes anchored to surfaces. *Chem. Sci.* **2014**, *5*, 281-290.
- (144) Hanson, K.; Brennaman, M. K.; Ito, A.; Luo, H.; Song, W.; Parker, K. A.; Ghosh, R.; Norris, M. R.; Glasson, C. R. K.; Concepcion, J. J.; Lopez, R.; Meyer, T. J. Structure–Property Relationships in Phosphonate-Derivatized, RuII Polypyridyl Dyes on Metal Oxide Surfaces in an Aqueous Environment. *J. Phys. Chem. C* **2012**, *116*, 14837-14847.
- (145) Trammell, S. A.; Meyer, T. J. Diffusional Mediation of Surface Electron Transfer on TiO₂. *J. Phys. Chem. B* **1999**, *103*, 104-107.
- (146) Brennan, B. J.; Regan, K. P.; Durrell, A. C.; Schmittenmaer, C. A.; Brudvig, G. W. Solvent Dependence of Lateral Charge Transfer in a Porphyrin Monolayer. *ACS Energy Lett.* **2017**, *2*, 168-173.
- (147) Gardner, J. M.; Beyler, M.; Karnahl, M.; Tschierlei, S.; Ott, S.; Hammarström, L. Light-Driven Electron Transfer between a Photosensitizer and a Proton-Reducing Catalyst Co-adsorbed to NiO. *J. Am. Chem. Soc.* **2012**, *134*, 19322-19325.
- (148) Hu, K.; Robson, K. C.; Beauvilliers, E. E.; Schott, E.; Zarate, X.; Arratia-Perez, R.; Berlinguette, C. P.; Meyer, G. J. Intramolecular and lateral intermolecular hole transfer at the sensitized TiO₂ interface. *J. Am. Chem. Soc.* **2014**, *136*, 1034-1046.
- (149) Ardo, S.; Meyer, G. J. Direct Observation of Photodriven Intermolecular Hole Transfer across TiO₂ Nanocrystallites: Lateral Self-Exchange Reactions and Catalyst Oxidation. *J. Am. Chem. Soc.* **2010**, *132*, 9283-9285.
- (150) Wang, J. C.; Hill, S. P.; Dilbeck, T.; Ogunsolu, O. O.; Banerjee, T.; Hanson, K. Multimolecular assemblies on high surface area metal oxides and their role in interfacial energy and electron transfer. *Chem. Soc. Rev.* **2017**, *47*, 104-148.

- (151) Vaissier, V.; Mosconi, E.; Moia, D.; Pastore, M.; Frost, J. M.; De Angelis, F.; Barnes, P. R. F.; Nelson, J. Effect of Molecular Fluctuations on Hole Diffusion within Dye Monolayers. *Chem. Mater.* **2014**, *26*, 4731-4740.
- (152) Shan, B.; Nayak, A.; Brennaman, M. K.; Liu, M.; Marquard, S. L.; Eberhart, M. S.; Meyer, T. J. Controlling Vertical and Lateral Electron Migration Using a Bifunctional Chromophore Assembly in Dye-Sensitized Photoelectrosynthesis Cells. *J. Am. Chem. Soc.* **2018**, *140*, 6493-6500.
- (153) Galoppini, E.; Guo, W.; Zhang, W.; Hoertz, P. G.; Qu, P.; Meyer, G. J. Long-Range Electron Transfer across Molecule–Nanocrystalline Semiconductor Interfaces Using Tripodal Sensitizers. *J. Am. Chem. Soc.* **2002**, *124*, 7801-7811.
- (154) Manke, F.; Frost, J. M.; Vaissier, V. r.; Nelson, J.; Barnes, P. R. F. Influence of a nearby substrate on the reorganization energy of hole exchange between dye molecules. *Phys. Chem. Chem. Phys.* **2015**, *17*, 7345-7354.
- (155) Qu, P.; Meyer, G. J. Proton-Controlled Electron Injection from Molecular Excited States to the Empty States in Nanocrystalline TiO₂. *Langmuir* **2001**, *17*, 6720-6728.
- (156) Nelson, J.; Chandler, R. E. Random walk models of charge transfer and transport in dye sensitized systems. *Coord. Chem. Rev.* **2004**, *248*, 1181-1194.

CHAPTER 2: A Distance Dependence to Lateral Self-Exchange across Nanocrystalline TiO₂. A Comparative Study of Three Homologous Ru^{III/II} Polypyridyl Compounds¹

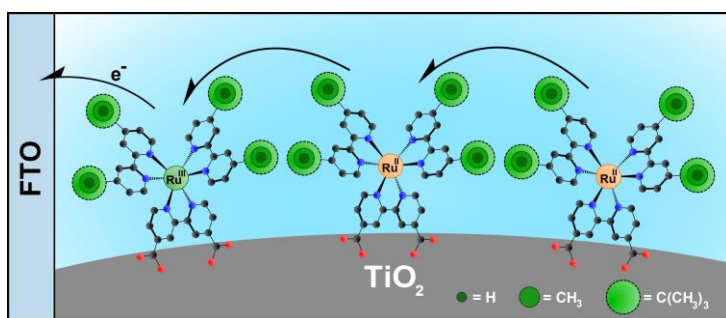
2.1 Introduction

Studies as far back as 1998 have demonstrated that molecules anchored to the mesoporous nanocrystalline (anatase) TiO₂ thin films commonly used in dye-sensitized solar cells can be reversibly oxidized and reduced in standard electrochemical cells.^{1,2} Molecules with formal reduction potentials that lie within the forbidden 3.2 eV band gap of TiO₂ are rapidly and quantitatively oxidized indicating that the redox chemistry does not involve the conduction or valence bands. Instead, a model was proposed wherein electron transfer was initiated at the transparent conductive oxide substrate that supports the thin film and continues across the TiO₂ nanocrystallites by lateral intermolecular self-exchange electron transfer, now commonly referred to as “hole hopping”.^{1,3} A simplified description of Ru^{III/II} self-exchange for three Ru compounds linked to a single TiO₂ nanocrystallite on a fluorine-doped tin oxide (FTO) substrate is given in Scheme 2.1. A more realistic description would display about 500 Ru compounds anchored to each ~20 nm anatase crystallite interconnected in an ~5 μm thin film. The importance of self-exchange electron *transfer* between surface immobilized

¹This chapter was previously published in the *Journal of Physical Chemistry C*. Reprinted with permission from DiMarco, B. N.; Motley, T. C.; Balok, R. S.; Li, G.; Siegler, M. A.; O'Donnell, R. M.; Hu, K.; Meyer, G. J. A Distance Dependence to Lateral Self-Exchange across Nanocrystalline TiO₂. A Comparative Study of Three Homologous Ru^{III/II} Polypyridyl Compounds. *J. Phys. Chem. C* **2016**, *120*, 14226-14235. Copyright 2016 American Chemical Society.

molecules is that it provides a means to *transport* charge across nanocrystalline surfaces without a loss of free energy. Here it is shown for the first time that such transport can be controlled at the molecular level with insulating organic functional groups.

Scheme 2.1. Illustration of Lateral Intermolecular Self-Exchange Electron Transfer across Anatase TiO₂ Nanocrystallites Initiated at the Fluorine-Doped Tin Oxide (FTO) Substrate



It was previously found that a minimal surface coverage of the redox active molecules was required for complete oxidation and reduction.¹ At least 50% of the saturation (often assumed to be a monolayer) surface coverage was necessary to ensure that all of the surface anchored molecules could be electrochemically accessed.^{1,4} This minimum surface coverage, termed a percolation threshold, helped demonstrate that oxidation occurs through electron self-exchange, rather than physical diffusion of the anchored molecules. More recent chronoamperometric studies have provided apparent electron diffusion coefficients (D) for lateral self-exchange for a growing number of redox active molecules.^{3,5-10} From this prior work, it is clear that self-exchange dynamics on TiO₂ nanocrystallites can, in some particular cases, be controlled at the molecular level. For example, the inclusion of two isothiocyanate groups in a *cis*-geometry about the ruthenium center has been demonstrated to significantly increase D .⁶ However, the extent to which self-exchange rate constants, and hence charge transport, across nanocrystalline surfaces can be controlled by molecular structures remains uncertain. This is unfortunate as recent studies have shown that dye-sensitized solar cells do

not require mediators such as iodide and can instead use self-exchange electron transfer to the complete the circuit and generate electrical power.¹¹ Lateral self-exchange also has relevance for the photo-oxidation of water to oxygen by molecular catalysts.^{3,12} This manuscript seeks to identify structure-property relationships for self-exchange “hole hopping” in a family of three Ru polypyridyl compounds.

Nonadiabatic Marcus theory has been extensively used to quantify or predict electron-transfer rate constants^{13,14} such as self-exchange electron-transfer reactions in homogenous fluid solutions. A generic potential energy diagram for self-exchange electron-transfer is shown in Figure 2.1. A key feature of self-exchange electron-transfer reactions is that $\Delta G^\circ = 0$, due to the equivalence of the products and reactants. The reactant and product surfaces are split at their intersection by $2 H_{AB}$, the electronic coupling matrix element. For outer-sphere bimolecular self-exchange in fluid solution, electronic coupling in the encounter complex is weak, $H_{AB} \ll kT$. Constraining molecules undergoing exchange electron transfer to a surface is expected to further decrease H_{AB} , justifying the use of non-adiabatic Marcus theory.

The self-exchange electron transfer rate constant, k_{SE} , is described by eq 2.1. This equation relates k_{SE} to temperature (T), H_{AB} , and the total reorganization energy (λ) for the reaction. The total reorganization energy is related to the free energy of activation (ΔG^\ddagger) = $\lambda/4$ and is typically partitioned into inner sphere, λ_I , and outer sphere, λ_O components, $\lambda = \lambda_I + \lambda_O$. Inner-sphere reorganization reflects changes in bond lengths and angles that accompany electron transfer, while λ_O reflects reorientation of the solvent molecules and ions present in the electrolyte.

$$k_{SE} = \left(\frac{2\pi}{\hbar} \right) \left(\frac{|H_{AB}|^2}{\sqrt{4\pi\lambda k_b T}} \right) \exp \left(-\frac{\lambda}{4k_b T} \right) \quad (2.1)$$

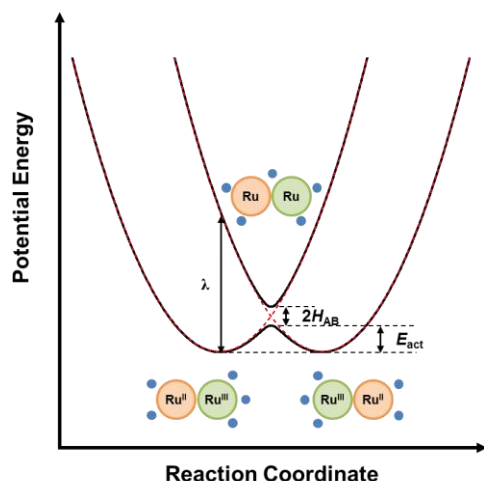


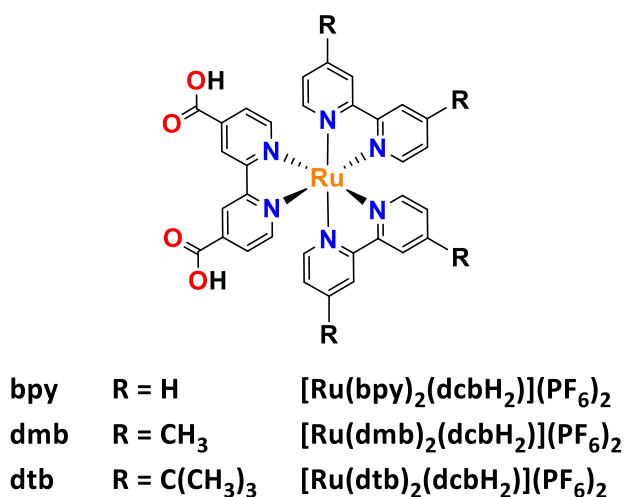
Figure 2.1. Reaction coordinate for nonadiabatic (dashed lines) or adiabatic (solid lines) self-exchange electron transfer reaction. The orange and green spheres represent Ru molecules in the encounter complex before, during, and after electron transfer. The blue spheres depict counterions and exaggerates their location and movement during the electron transfer process.

The state-of-the-art in characterization of lateral self-exchange in mesoporous TiO₂ thin films was recently reported by Moia and coworkers.⁵ These authors quantified self-exchange among 10 different dye molecules as a function of temperature for the first time. Self-exchange was found to be an activated process with E_{act} that ranged from 170-370 meV, values that were dependent on the nature of the redox active molecule. A Marcus analysis yielded λ and H_{AB} for self-exchange in macrocyclic, ruthenium polypyridyl, and organic push-pull (i.e., D- Δ -A) molecules. The λ 's abstracted from the transient kinetic data were found to be in good agreement with expectations based on density functional theory. Reorganization energies associated with highly delocalized frontier orbitals and rigid molecular structures with extended conjugation were concluded to be small. There was also some evidence that non-conjugated functional groups on the molecules could potentially influence lateral self-exchange. This report compliments this previous study through characterization of a homologous series of compounds where λ is expected to be held near parity, yet the steric bulk

of the bipyridine ligand was intentionally varied. The data provide compelling evidence that these side groups can be used to tune the self-exchange between immobilized redox sites.

Herein a comparative study of three analogous Ru diimine compounds of the general form $[\text{Ru}(\text{LL})_2(\text{dcbH}_2)](\text{PF}_6)_2$, where dcbH₂ is 2,2'-bipyridyl-4,4'-dicarboxylic acid and LL is 2,2'-bipyridine (**bpy**), 4,4'-dimethyl-2,2'-bipyridine (**dmb**), or 4,4'-di-*tert*-butyl-2,2'-bipyridine (**dtb**), is reported, Scheme 2.2. These compounds share a tris-chelated, pseudo-octahedral geometry, and hence the reorganization energy for the Ru^{III/II} redox chemistry is expected to be approximately the same across the series. Each compound possesses a single dcb ligand for surface binding to TiO₂ with two other substituted bipyridine ligands possessing substitutions at the 4,4'-position that were expected to influence lateral self-exchange reactivity. In fact, small changes to the molecular structure, such as replacement of a H atom with a methyl group, was found to have a surprisingly large influence on the *D*, as observed through both chronoabsorptometry and temperature-dependent cyclic voltammetry studies.

Scheme 2.2. Chemical Structure of the Molecules Studied



2.2 Experimental Methods

2.2.1 Materials

The following solvents and reagents were purchased from the indicated supplier, and were used without further purification: titanium(IV) isopropoxide ($\text{Ti}(i\text{-OPr})_4$; Aldrich, $\geq 97.0\%$); deionized water; acetonitrile (CH_3CN , Burdick and Jackson, spectrophotometric grade); diethyl ether (Et_2O ; Fisher Scientific, 99.9%); anhydrous ethanol (EtOH , Fisher Scientific, 99%); silver nitrate (AgNO_3 ; Stream, 99.9%); sodium hydroxide (NaOH ; Sigma-Aldrich, $>97\%$); hexafluorophosphonic acid (HPF_6 ; 65% solution in H_2O , Sigma-Aldrich); lithium perchlorate (LiClO_4 ; Sigma-Aldrich 99.99%); ammonium hexafluorophosphate (NH_4PF_6 ; Sigma-Aldrich, 99.8%); 4,4'-dimethyl-2,2'-bipyridine (**dmb**; Combi-Blocks), argon (Airgas, $\geq 99.998\%$); oxygen (O_2 , Airgas, $\geq 99.998\%$); fluorine-doped tin(IV) oxide (FTO; Hartford Glass Co., Inc., 2.3 mm thick, $15\ \Omega/\square$), $[\text{Ru}(\text{bpy})_2(\text{dcbH}_2)](\text{PF}_6)_2$ (**bpy**; Solaronix). The complexes $[(p\text{-cymene})\text{Ru}(\text{deeb})\text{Cl}]\text{Cl}$, where **deeb** is the 2,2'-bipyridyl-4,4'-diethyl ester, and $[\text{Ru}(\text{dtb})_2(\text{dcbH}_2)](\text{PF}_6)_2$ (**dtb**) were available from previous studies.^{15,16} Anion metathesis of **dtb** was used to generate a ClO_4^- salt. Single crystals of the perchlorate salt of **dtb** suitable for X-ray structure determination were obtained by slow diffusion of hexanes into concentrated acetonitrile solutions.

2.2.2 Synthesis of $[\text{Ru}(\text{dmb})_2(\text{deeb})](\text{PF}_6)_2$ (**1**)

The $[(p\text{-cymene})\text{Ru}(\text{deeb})\text{Cl}]\text{Cl}$ (80.1 mg, 0.13 mmol) precursor was combined with **dmb** (49.0 mg, 0.27 mmol) and AgNO_3 (61.6 mg, 0.36 mmol) in 10 mL of EtOH . The solution was purged with N_2 for >15 min and then heated to a reflux under an N_2 atmosphere for 14 h. After this time had elapsed, the solution was cooled to room temperature and the solvent was removed. The colored product was redissolved in a minimal amount of water. The aqueous

solution was filtered to remove any remaining Ag^+ salts. To the filtrate was added an excess of NH_4PF_6 , which yielded a brown solid. The solid was filtered and dissolved in dichloromethane to prevent any remaining Ag^+ salts from being carried forward. The solvent was removed, and the product was dissolved in CH_3CN . Slow diffusion of Et_2O into a concentrated CH_3CN solution afforded 128.3 mg of product as large brown crystals, which were suitable for X-ray structure determination (yield = 92%). ^1H NMR (400 MHz, CD_3CN) δ 9.00 (s, 2H), 8.334(d, J = 6.2Hz, 4H), 7.94(d, J = 5.8Hz, 2H), 7.80(d, J = 5.9 Hz), 7.50-7.43 (M, 4H), 7.26-7.18(M, 4H), 4.24(q, J =6.9, 14.1, 4H) 2.52(d, J =9.92Hz, 12H), 1.41(t, J =7.1Hz, 12H) ^{13}C NMR (150 MHz, CD_3CN) δ 164.8, 159.2, 157.5, 154.0, 152.3, 152.1, 152.1, 151.8, 139.6, 129.7, 129.6, 127.6, 126.3, 124.8, 63.9, 21.6, 14.6. HS-ESI-MS: m/z = 915.1826 (calcd. for $\text{RuC}_{40}\text{H}_{40}\text{N}_6\text{O}_4\text{PF}_6$ $[\text{Ru}(\text{dmb})_2(\text{deeb})](\text{PF}_6)^+$: 915.1796); m/z = 385.1077 (calcd. for $\text{RuC}_{40}\text{H}_{40}\text{N}_6\text{O}_4$ $[\text{Ru}(\text{dmb})_2(\text{deeb})]^{2+}$: 385.1077).

2.2.3 Synthesis of $[\text{Ru}(\text{dmb})_2(\text{dcbH}_2)](\text{PF}_6)_2$ (**dmb**)

$[\text{Ru}(\text{dmb})_2(\text{deeb})](\text{PF}_6)_2$ (60.9 mg, 57 μmol) and NaOH (9 mg, 230 μmol) were added to 30 mL of a 1:5 EtOH/ H_2O solution. The solution was purged with N_2 for >20 mins and then heated to reflux. The reflux was maintained for 15 h under a N_2 atmosphere, after which the solution was allowed to cool to room temperature. The solution volume was reduced, and the remaining the water was acidified with HPF_6 . The resulting solid was filtered, washed with Et_2O and H_2O , and left under vacuum overnight to dry. This afforded 51.1 mg of a reddish brown solid (yield = 88.6%). ^1H NMR (500 MHz, CD_3CN) δ 9.52 (s, 2H), 8.33(d, J = 8.1Hz, 4H), 7.82(dd, J = 5.8, 21.5Hz, 4H), 7.48(dd, J = 5.8, 21.1Hz, 4H), 7.24(d, J = 5.2Hz, 2H), 7.17(d, J = 5.7Hz, 2H), 2.51(d, J = 14.2Hz, 12H) ^{13}C NMR (150 MHz, CD_3CN) 167.3, 159.4, 157.7, 157.6, 153.3, 152.2, 151.8, 129.62, 129.60, 128.0, 126.25, 126.22, 21.6. HS-ESI-MS: m/z =

859.1162 (calcd. for $\text{RuC}_{36}\text{H}_{32}\text{N}_6\text{O}_4\text{PF}_6 [\text{Ru}(\text{dmb})_2(\text{dcbH}_2)](\text{PF}_6)^+$: 859.1142); $m/z = 357.0758$
(calcd. For $\text{RuC}_{36}\text{H}_{32}\text{N}_6\text{O}_4 [\text{Ru}(\text{dmb})_2(\text{dcbH}_2)]^{2+}$: 357.0764)

2.2.4 Thin Film Preparation

Titania nanocrystallites were made by hydrolysis of $\text{Ti}(i\text{-OPr})_4$ via a previously published sol-gel technique.² Thin, mesoporous films were cast through doctor blading onto an ethanol cleaned FTO substrate using Scotch tape ($\sim 50\ \mu\text{m}$ thick) as a spacer for consistent thickness. The films were first dried while covered for 30 min and then sintered at $450\ ^\circ\text{C}$ for 30 min under O_2 flow at $\sim 1\ \text{atm}$. Films were either used immediately or stored in an oven ($\sim 70^\circ\text{C}$) until use. Film thicknesses ($\sim 4\text{-}6\ \mu\text{m}$) were determined using a Bruker Dektak XT profilometer using the Vision 64 software.

Titania films were submerged into concentrated CH_3CN solutions of **bpy**, **dmb**, or **dtb** to allow the molecules to anchor to the nanocrystallite surface. Films were submerged for a minimum of 48 h to ensure saturated surface coverages. Prior to use, the films were soaked for $\sim 1\ \text{h}$ in neat CH_3CN to remove any weakly adsorbed molecules from the film in order to minimize dye desorption during the course of the experiments.

2.2.5 UV-Visible Spectroscopy

Steady-state UV-visible spectra were obtained on either Hewlett Packard 8453 photodiode array or a Varian Cary 60 spectrophotometer at room temperature. All measurements were made in custom-made 1 cm path length quartz cuvettes with a 24/40 ground glass joint affixed to the top. Surface-functionalized films were placed along the diagonal of the cuvette at a 45° angle to the incident probe beam.

2.2.6 Electrochemistry

Electrochemical measurements were performed with a potentiostat (Bioanalytical Scientific Instruments model CV-50W or Epsilon electrochemical analyzer) using a standard three-electrode arrangement. A surface-functionalized TiO₂ film was employed as the working electrode, while a platinum mesh was used as the auxiliary electrode. Potentials were applied against a non-aqueous silver wire pseudoreference electrode (Pine Research Instruments), which was filled with 0.1 M LiClO₄ containing CH₃CN. Unless otherwise noted, the pseudoreference electrode was externally calibrated against the ferrocenium/ferrocene (Fc⁺⁰) reduction potential in 0.2 M LiClO₄ containing CH₃CN, where the Fc⁺⁰ potential is 0.31 V vs the saturated calomel electrode (SCE), and SCE is 0.241 V vs the normal hydrogen electrode (NHE).¹⁷ The three electrodes were placed within a custom quartz cuvette, consisting of a 1 cm pathlength square quartz cuvette attached by ~8 cm of round glass tubing to a 24/40 ground glass joint, which allowed the TiO₂ film to be monitored spectroscopically. The electrode connections were fed through a rubber septum, which was used to seal the cuvette. For measurement taken at room temperature, the Fc⁺⁰ potential was measured before and after the experiment to ensure reference electrode stability.

Spectroelectrochemical measurements were used to quantify E° for TiO₂ anchored complexes. The experiment monitored the absorbance of the surface-functionalized TiO₂ film while applying increasingly positive electrochemical biases. The films were held at each potential for a minimum of 1 min, or until no additional spectral changes were observed, in order to ensure the film was equilibrated. Chronoabsorptometry (CA) was used to investigate the apparent diffusion coefficient, D , for the molecules studied. In contrast to the spectroelectrochemical experiment, a single oxidizing potential was applied to the film, and

the oxidation rate was monitored spectroscopically as a function of time. Full oxidation of the film was achieved after stepping the potential to $E^\circ + 0.5$ V for several minutes. A new surface-functionalized film was used for each experiment to minimize the impact of dye desorption. All spectroelectrochemical experiments were performed in argon purged CH₃CN containing 0.1 M LiClO₄ as the supporting electrolyte.

Cyclic voltammetry (CV) was also used to investigate D for the surface bound compounds. Variable temperature CV experiments were performed within a custom cell comprised of a ~ 1 cm² square tubing attached to a 19/22 ground glass joint. The electrodes were arranged in a manner analogous to the CA experiments. The argon purged electrochemical cell was placed within a UniSoku CoolSpek USP-203-B liquid nitrogen cryostat, which allowed the temperature to be adjusted to ± 1 °C of the desired temperature. The apparatus was allowed to thermally equilibrate at each temperature for >10 min prior to performing the measurement. Again, a new film was used for each experiment. Note that D_{CV} and D_{CA} denote diffusion coefficients that were measured by CV or CA respectively.

2.2.7 Data Analysis

Kinetic modeling was performed in Origin 9.0, and least-squares error minimization accomplished by the Levenberg-Marquardt iteration method. Resulting values from the best fit are reported with the standard error from the fitting procedure. In the case of the CA measurements, the error reported is the standard deviation of multiple trials. Spectral modeling of the spectroelectrochemical data was performed a least-squares fitting function written into a custom script in Mathematica 9

2.2.8 Calculation of c_0 and R

The “concentration” of redox active molecules within the mesoporous TiO₂ thin films is an ill-defined parameter. To determine the volume concentration (cm⁻³), c_0 , and consequently, the intermolecular spacing between ruthenium compounds (cm), R , assumptions about the porosity of the film and close packed nature of the molecules were required. Below are presented methods to determine the upper and lower limits as well as one intermediate value of R .

Upper Limit of R . This approach represents an upper limit to R as the molecules are assumed to be distributed throughout both the TiO₂ nanoparticle and pore volume as opposed to the more reasonable situation where they are localized on the TiO₂ surface. Further calculations of R in this regime lead to upper limits for both self-exchange rate constant and electronic coupling matrix element, Table 2.4 in the 2.7 Additional Content section. To estimate c_0 and R , the surface coverage (mol/cm²), Γ , was first determined with eq 2.2, where A and ε are the absorbance and molar extinction coefficient (M⁻¹ cm⁻¹) of the film at a given wavelength and 1000 is a factor to convert from L to cm³. Note that the wavelength used for each compound is the wavelength where the absorbance of the surface-functionalized TiO₂ film is the same in neat and 0.1 M LiClO₄ solutions in acetonitrile (*vide infra*). The extinction coefficient at the absorbance peak observed in fluid solution is assumed to be retained upon anchoring.

$$A = 1000 \times \varepsilon \times \Gamma \quad (2.2)$$

Next, Γ was converted to c_0 using eq 2.3, where N is Avogadro’s number and d is the film thickness (cm). The inclusion of $\cos(45^\circ)$ adjusts for the path length of the probe being

incident to the film at a 45°. The Ru compounds were assumed to be distributed evenly throughout the total film volume.

$$c_0 = \frac{\Gamma \times N \times d}{\cos(45^\circ)} \quad (2.3)$$

Finally, to convert to R , the cubic lattice arrangement was assumed on the surface as was done previously by Daum, *et al.* for redox sites immobilized in polymer films¹⁸ and by Moia, *et al.* for molecules anchored to TiO₂ films.⁵ This relation is given simply by eq 2.4.

$$R = c_0^{-1/3} \quad (2.4)$$

Intermediate Value of R. For a more accurate value of R , the pore volume of the mesoporous TiO₂ film must be accounted for. In the present study, the films were assumed to have a ~50% porosity. In this method, the c_0 was calculated as it was in the upper limiting case. To adjust for the pore volume, the c_0 was multiplied by a factor of two. This approximation still assumes that the Ru compounds are evenly distributed throughout the volume occupied by the TiO₂ nanoparticles, but now the volume has decreased by half which results in a doubling of the calculated concentration. R was calculated as before.

Lower Limit of R. The lower limit of R was estimated from crystal structures of the Ru molecules, where R represents the distance between the substituents in the 4 positions of the bipyridine group trans to one another, Figure 2.2. In order to carry out further calculations needed to determine the apparent diffusion coefficients from the CV experiments, eq 2.4 was used to calculate c_0 . This value gives an estimate for the spacing between molecules close to the van der Waals radii limit allowed by the compounds, and calculations based on these values lead to a lower limit for the self-exchange rate constant and electronic coupling matrix element.

2.3 Results

Preparation of the $[\text{Ru}(\text{dmb})_2(\text{deeb})](\text{PF}_6)_2$ (**1**) precursor was achieved in high yield using a modified, previously reported procedure for the synthesis of similar ruthenium polypyridyl compounds.¹⁵ Base catalyzed hydrolysis of the ethyl ester groups in **1** generated the desired carboxylic acid form of the compound, **dmb**. Structural identity was confirmed through ^1H and ^{13}C NMR and high-resolution mass spectroscopy.

Slow diffusion of Et_2O into concentrated CH_3CN solutions of **1** gave crystals suitable for X-ray diffraction, Figure 2.2. The average Ru-N distance is 2.054 Å. The Ru-N distance for the deeb ligand is slightly shorter than those for the dmb ligands, indicative of stronger back-bonding from the Ru non-bonding d-orbitals to deeb π^* orbitals. The average N-Ru-N bite angle is 78.73° , while the bite angle for the deeb ligand is 0.5° smaller than the dmb ligand, consistent with the shorter Ru-N bond lengths for deeb ligand. The Ru compounds appear in pairs in the crystal structure through π - π interaction between the deeb ligands with an interlayer distance of 4.331 Å. A weaker π - π intermolecular interaction with neighboring dmb ligands was also evident in the solid state. Saponification of the ester is not expected to significantly impact the Ru-N bond distances, or the N-Ru-N bite angles. No significant structure differences were observed for $[\text{Ru}(\text{dtb})_2(\text{dcbH}_2)](\text{ClO}_4)_2$ when compared to **1**. An average Ru-N bond length of 2.056 Å and an average N-Ru-N bite angle of 78.62° was observed.

A pertinent value for this study is the “molecular diameter”, or the distance between the farthest points on the molecule. This value was taken to be the distance between substituents in the 4 positions of bipyridine that were trans to one another on adjacent coordinated ligands. More specifically, this is the H to H distance for **bpy**, the C to C of the methyl groups for **dmb**, or CH_3 group to CH_3 group of the *tert*-butyl groups for **dtb**. A

summary of these values and other relevant parameters for all three compounds are given in Table 2.1. Additional crystallographic data for **dtb** and **1** are found in the 2.7 Additional Content section.

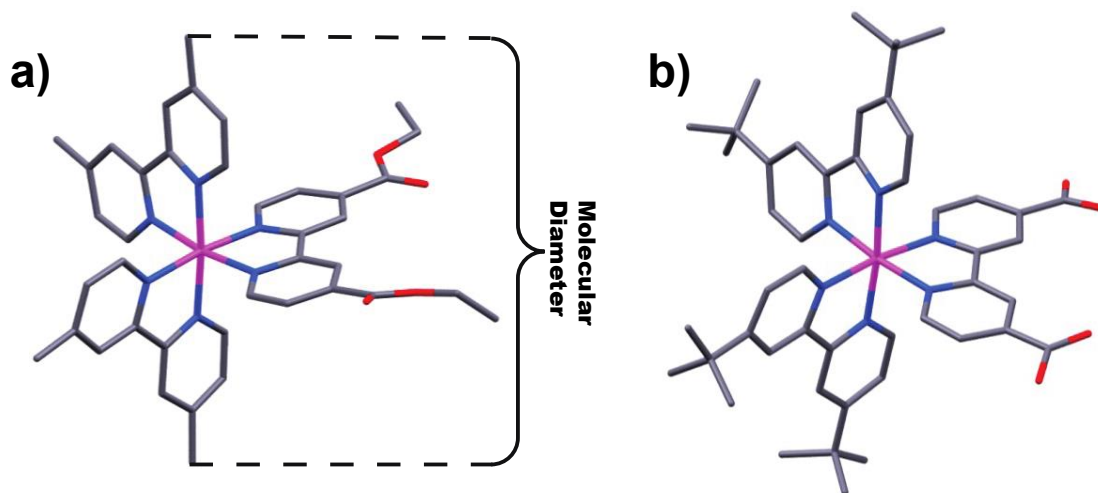


Figure 2.2. (a) Crystal structure of $[\text{Ru}(\text{dmb})_2(\text{deeb})](\text{PF}_6)_2$. b) Crystal structure of $[\text{Ru}(\text{dtb})_2(\text{dcbH}_2)](\text{ClO}_4)_2$. All hydrogen atoms and anions are omitted for clarity purposes. Color code: Pink, Ru; blue, N; red, O; gray, C.

Table 2.1. Selected Crystal Structure Parameters

	Average Ru-N Distance (Å)	Average N-Ru-N Bite Angle (°)	Molecular Diameter (nm)
bpy ^{a,b}	2.056	79.01	1.15
dmb ^b	2.054	78.83	1.27
dtb	2.056	78.62	1.37

^aTaken from ref 19. ^bValues shown are for the ethyl ester complex.

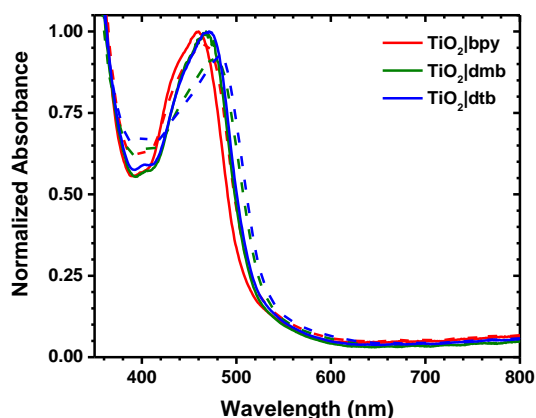


Figure 2.3. Normalized absorption spectra of compounds **bpy**, **dmb**, and **dtb** anchored to TiO_2 in neat CH_3CN (solid line) or in a 0.1 M LiClO_4 solution in CH_3CN (dashed line). The TiO_2 absorption spectrum was subtracted out from the spectra of the surface-functionalized films.

The TiO_2 thin films were reacted with the desired Ru compounds by submersion into concentrated CH_3CN solutions. Extended reaction times (>48 h) were used to ensure that maximum surface coverages were achieved. Representative spectra of the TiO_2 films placed in neat CH_3CN after surface-functionalization, abbreviated $\text{TiO}_2|\text{X}$, are seen in Figure 2.3 (solid lines). The main absorption feature centered at ~450 nm observed in neat CH_3CN is reasonably assigned to metal-to-ligand charge transfer (MLCT) transitions. It is assumed that the peak extinction coefficients, ϵ , are retained upon surface anchoring, Table 2.2.

The addition of 0.1 M LiClO_4 to the neat CH_3CN induced a bathochromic shift of the MLCT absorption (Figure 2.3, dashed lines). This has previously been reported for ruthenium polypyridyl complexes and is attributed to a change in the electric field at the surface of the TiO_2 upon cation adsorption.²⁰⁻²² The peak absorption for each compound in the presence of Li^+ is shown in Table 2.2. The surface coverage Γ , was calculated using a modified Beer's law expression, Table 2.2.⁴ Note that Γ was calculated with the assumption that the ϵ value measured in fluid solution was the same as that for the surface anchored molecules. Though several assumptions are made during this calculation, a comparison of values between the three

compounds provides insight into the molecular environment present at the surface. A decrease in Γ was seen with increasing steric bulk, suggesting that the side groups influence the intermolecular distance.

Table 2.2. Selected Spectral, Electrochemical, and Film Parameters for the Compounds Studied

	$\lambda_{\max}^{\text{soln}}$ (nm) (ϵ , $\text{M}^{-1}\text{cm}^{-1}$) ^a	$\lambda_{\max}^{\text{neat}}$ (nm) ^b	$\lambda_{\max}^{\text{Li}^+}$ (nm) ^c	E° (V vs NHE) (α)	Γ (10^{-7} mol/cm ²)	c_0 (10^{19} cm ⁻³)
bpy	471 (12000) ^d	460	467	1.48 (1.4) ^d	1.9 ± 0.14	38 ± 2
dmb	475 (14200)	468	475	1.39 (1.6)	0.95 ± 0.20	19 ± 1
dtb	465 (16400) ^e	471	482	1.36 (1.2) ^e	0.77 ± 0.13	12 ± 1

^aPeak absorption of the compound in neat CH₃CN. ^bPeak absorption of the TiO₂ anchored compound in neat CH₃CN. ^cPeak absorption of the TiO₂ anchored compound in 0.1 M LiClO₄ containing CH₃CN. ^dTaken from Ref 23. ^eTaken from Ref 14.

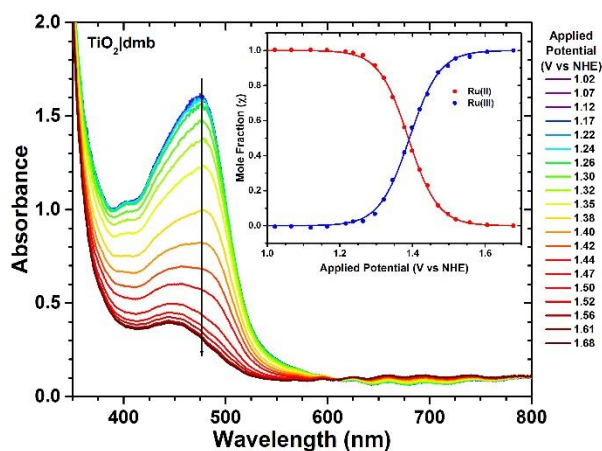


Figure 2.4. Spectroelectrochemical oxidation of TiO₂|**dmb** immersed in 0.1 M LiClO₄/CH₃CN electrolyte. The inset plots the fraction of oxidized or reduced compound as a function of applied potential. Overlaid is a fit to a modified Nernst equation, eq 2.5.

Spectroelectrochemical measurements were performed on TiO₂|**dmb** to quantify the $E^\circ(\text{Ru}^{\text{III/II}})$ potential. Application of a positive applied potential resulted in spectral changes consistent with oxidation of Ru^{II} to Ru^{III}, Figure 2.4. Complete oxidation to yield Ru^{III} was determined when an increased applied potential no longer induced a spectral change. The mole

fraction, χ , of oxidized and reduced species present at a given applied potential was determined through spectral modeling using a linear combination of the Ru^{II} and Ru^{III} species.

The formal reduction potential, E° , was determined using eq 2.5. In this equation, E_{app} is an applied potential and α is an ideality factor that accounts for deviations from Nernstian behavior. Values for E° and α are given in Table 2.2. The equivalent data for **bpy** and **dtb** can be found in the 2.7 Additional Content section (Figure 2.9 and 2.10).

$$\chi = \left(1 - 10^{\frac{E_{app} - E^\circ}{\alpha \times 59}} \right)^{-1} \quad (2.5)$$

Insight into intermolecular electron self-exchange was gained by spectroscopically monitoring the oxidation process as function of time after a potential step to potentials ~0.5 V positive of $E^\circ(\text{Ru}^{\text{III/II}})$. A comparison of this rate for the three Ru compound of interest is seen in Figure 2.5. The rate of this conversion was recast as the apparent diffusion coefficient, D_{CA} , using eq 2.6.¹ In this equation, ΔA_f is the final change in absorbance and d is TiO₂ film thickness. A linear fit to the initial CA data allowed for the determination of D_{CA} using eq 2.6. The wavelengths monitored during the oxidation were 468, 480 and 482 nm for **bpy**, **dmb**, and **dtb**, respectively. During the analysis, care was taken to only fit the linear portion of the data. Deviations from linearity indicates movement away from diffusion-limited conditions, which is typical as the oxidation front approaches the edge of the film. Bonhôte and coworkers reported that linearity was maintained for the oxidation of ~60% of the molecules within the mesoporous thin film.¹ Thus, only the first 60% of the total observed absorption change was fit, gold overlay, Figure 2.5. The observed rate of oxidation, as well as the calculated D_{CA} value, was seen to increase following **dtb** < **bpy** < **dmb**.

$$\Delta A = \frac{2\Delta A_f \sqrt{D_{CA}}}{d\sqrt{\pi}} \sqrt{t} \quad (2.6)$$

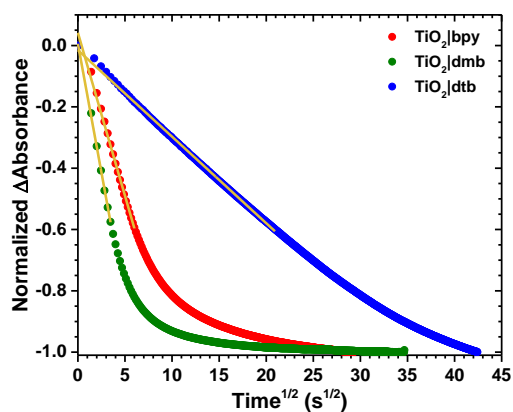


Figure 2.5. Normalized absorption change measured after application of a potential sufficient to oxidize the indicated compounds plotted against the square root of time. Overlaid in gold is the fit based on eq 2.6.

Table 2.3. Apparent Diffusion Coefficients and Marcus Self-Exchange Parameters for Surface Anchored Ruthenium Compounds

	D_{CA} ($10^{-9} \text{ cm}^2/\text{s}$)	D_{CV}^a ($10^{-10} \text{ cm}^2/\text{s}$)	E_{act} (meV)	A ($10^{-7} \text{ cm}^2/\text{s}$)	H_{AB}^b (meV)	R (nm)
TiO₂ bpy	2.2 ± 1.1	1.1 ± 0.1	240 ± 30	5 ± 6	0.07 ± 0.04	1.4 ± 0.03
TiO₂ dmb	5.3 ± 0.6	3.1 ± 0.2	240 ± 20	30 ± 30	0.10 ± 0.06	1.8 ± 0.03
TiO₂ dtb	0.24 ± 0.01	0.14 ± 0.01	270 ± 30	4 ± 5	0.02 ± 0.02	2.0 ± 0.06

^aValue taken at 30 °C. ^b $\lambda = 900 \pm 100 \text{ meV}$ shared between data sets.

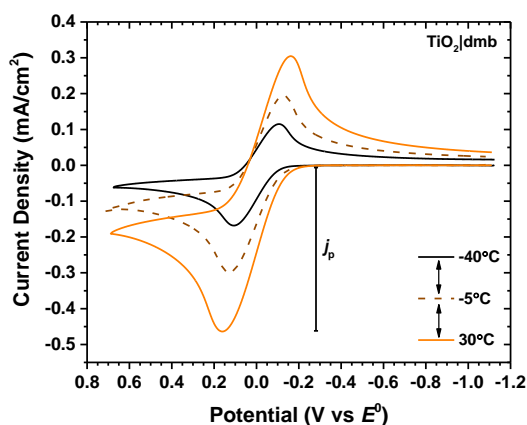


Figure 2.6. Representative cyclic voltammograms for **dmb** anchored to TiO₂ immersed in 0.1 M LiClO₄ in CH₃CN at the indicated temperatures.

The apparent diffusion coefficients were determined over a range of temperatures for each compound by cyclic voltammetry (CV), Figure 2.6. The peak current density, j_p , observed during the CV, was related to D_{CV} using eq 2.7.⁵ In this equation, k_b , q , T , c_0 , and ν are the Boltzmann constant, the elementary charge, temperature, the volume concentration, and scan rate, respectively. Determination of c_0 was nontrivial, as concentrations at nanocrystalline TiO₂ interfaces are an ill-defined parameter. For the purposes of this study, the total volume available to the molecule was assumed to be the volume of the TiO₂ film, excluding pores, with the Ru molecules uniformly dispersed throughout the remaining volume. The Γ value was initially quantified using a modified Beer's law. Γ was then converted to c_0 by eq 2.3, where $\cos(45^\circ)$ accounts for the increase in path length due to the film being at a 45° angle to the probe. To account for a ~50% porosity, the calculated c_0 was multiplied by a factor of 2. Table 2.2 shows the c_0 obtained for the compounds studied. Other methods used to calculate c_0 are discussed in the experimental section and provided quantitatively different values of D_{CV} , yet the same trend was observed. Throughout all experiments, ν was kept to be 0.1 V/s, applied against a self-contained Ag wire. The expected temperature dependence of the reference

electrode was not important to the experiment. A linear correction was made to all the data in order to compensate for nonfaradaic processes, as was described previous by Moia *et al.*⁵ j_p was determined by dividing the observed peak current from the initial scan by the geometric area of the TiO₂ film ($\sim 1.5 \text{ cm}^2$).

$$D_{CV} = \frac{5.02k_bTj_p^2}{q^3c_0^2v} \quad (2.7)$$

$$D_{CV} = Ae^{\frac{-E_{act}}{k_bT}} \quad (2.8)$$

Activation energies, E_{act} , for self-exchange on the surface were extracted from the variable temperature data with the Arrhenius equation, eq 2.8. Figure 2.7A shows the D_{CV} obtained over a range of temperatures fit to eq 2.8. E_{act} along with the associated pre-exponential factors, A , are included in Table 2.3. The abstracted E_{act} values were between 240 and 270 meV.

In order to perform a Marcus analysis on these data, D_{CV} was converted into an effective electron transfer rate constant, k_{SE} , using eq 2.9.⁵ This required knowledge of the intermolecular distance, R , between redox active sites. It was assumed that the molecules were evenly distributed in a cubic lattice throughout the porosity corrected volume of the film, eq 2.4. Values of R for each compound are shown in Table 2.3. These values represent an “intermediate” estimate of the true and unknown intermolecular distance on the TiO₂ surface. Upper and lower limits of R were also established and are given in Table 2.4 in the 2.7 Additional Content section.

$$k_{SE} = \frac{4D_{CV}}{R^2} \quad (2.9)$$

The magnitude of H_{AB} was determined by fitting the data shown in Figure 2.7B to non-adiabatic Marcus theory for electron self-exchange, eq 2.1. To aid in the fitting process, a

global fitting analysis was used and λ was shared between the three data sets. Table 2.3 shows the resulting H_{AB} values. As previously mentioned, the value of R utilized directly influenced the value of H_{AB} determined. Figure 2.8 shows the variation of H_{AB} and k_{SE} based on each method used to determine R . A summary of these parameters is found in Table 2.4 of the 2.7 Additional Content section.

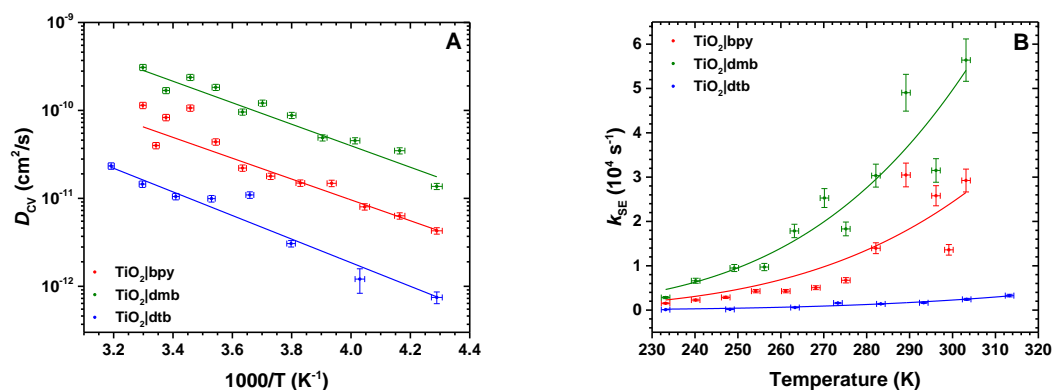


Figure 2.7. (A) Arrhenius plot for **bpy**, **dmb**, and **dtb** anchored to TiO_2 describing the variation of D_{CV} with inverse temperature as obtained by cyclic voltammetry. Overlaid are the best fits to the Arrhenius equation. (B) The temperature dependence of k_{SE} as described by nonadiabatic Marcus theory (overlaid curves).

2.4 Discussion

As was described in the introduction section, self-exchange between surface immobilized molecules results in the transport of charge and is hence of interest for energy applications.¹¹ A key finding disseminated here is that insulating organic side-groups on the redox active molecules can be used to tune self-exchange “hole hopping” and hence charge transport across nanocrystalline TiO_2 surfaces. This was most readily quantified by abstraction of an apparent diffusion constant, D , from the temporal data. Indeed, an experimental challenge was to identify methods by which the intrinsic self-exchange rate constants and activation parameters could be reliably abstracted from bulk kinetic electrochemical data. The two techniques utilized herein relied upon a ramped (cyclic voltammetry) or stepped

(chronoabsorptometry) potential to quantify $\text{Ru}^{\text{III/II}}$ self-exchange and while both techniques revealed the same trend in D , **dmb** > **bpy** > **dtb**, the quantitative values differed significantly. Below we discuss the electrochemical methods used to quantify self-exchange followed by an analysis of the kinetic data within the framework of Marcus theory for nonadiabatic electron transfer.

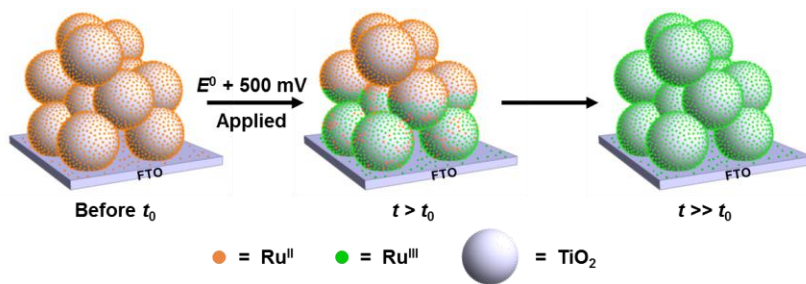
2.4.1 Quantification of Reduction Potentials and Apparent Diffusion Coefficients

The formal $E^\circ(\text{Ru}^{\text{III/II}})$ reduction potentials were taken as the equilibrium potential where equal numbers of compounds measured spectroscopically were present in the formal oxidation states of III and II. The electron donating methyl- and *tert*-butyl groups in the **dmb** and **dtb** ligands induced a measurable negative shift in the formal reduction potentials relative to that measured for $\text{TiO}_2|\text{bpy}$. A complication in data analysis was the non-Nernstian behavior of the interfacial redox chemistry. An ~80 mV potential step was required to induce a factor of 10 change in the $\text{Ru}^{\text{III}}/\text{Ru}^{\text{II}}$ ratio for **bpy**, and ~70 mV was required for **dtb** rather than the Nernstian value of 59 mV. The spectroelectrochemical data were adequately modeled by including α to account for deviation from Nernstian behavior, as has been done in the past, however such modeling does not address the origin(s) of the nonideality. Prior studies with metalloporphyrins and molecules with two redox active groups have indicated that the nonideality arises from local electric fields present at the oxide-electrolyte interface.²³ The α increased in the order **dmb** > **bpy** > **dtb** suggesting that intermolecular interactions like those in the Frumkin isotherm model may also underlie this behavior.⁹ If instead the nonideality arises from a distribution of formal reduction potentials, then the data may reflect a greater degree of heterogeneity for **bpy** than for **dtb**. Regardless of the nonideality origin(s), the steady

state spectroelectrochemical data suggests that the true self-exchange electron transfer hole-hopping may not occur with $\Delta G^\circ = 0$ throughout the mesoporous film.

Chronoabsorptometry (CA) and cyclic voltammetry (CV) experiments were performed to estimate the diffusion coefficient D for self-exchange. The data analysis is based upon a semi-infinite diffusion boundary approximation that has been previously described.⁵ Since the mesoporous TiO₂ thin film has a finite thickness, this analysis is only valid if the ‘front’ of oxidized molecules does not reach the outer edge of the mesoporous thin film. This boundary condition is maintained through the CV experiments, where only about 5% of the redox active molecules within the thin film were oxidized. This value was determined by using $L = (D_{CV} \times t)^{1/2}$, where L is the linear diffusion length and t is the elapsed time from the onset of oxidation to the peak oxidation current. In contrast, all of the electrochemically accessible compounds were oxidized over the course of the CA experiments, Scheme 2.3.

Scheme 2.3. An Idealized Representation of Three Surface Functionalized Anatase Layers on an FTO Substrate during a Chronoabsorptometry (CA) Experiment^a



^aAt time t_0 all of the ruthenium compounds are in the formal oxidation state of II. After a potential step 500 mV more positive than the formal $E^\circ(\text{Ru}^{\text{III/II}})$ reduction potential, the FTO substrate oxidizes the Ru^{II} compounds present on the FTO surface followed by self-exchange “hopping” across the nanocrystalline TiO₂ surface. A moving front of oxidized dyes nearly equidistant from the FTO substrate is observed at $t > t_0$. At longer times $t \gg t_0$ all the molecules within the mesoporous thin film are oxidized. The semi-infinite diffusion boundary approximation restricts data analysis to about 60% oxidation of the thin film. In contrast, only about 5% of the film is oxidized during a cyclic voltammetry experiment.

Deviation from linearity was observed when ~60% of the compounds were oxidized, which has been previously attributed to the breakdown of the boundary conditions.²⁴ Both experiments revealed that D decreased in the order **dmb** > **bpy** > **dtb**; however, the values abstracted from cyclic voltammetry data were consistently about an order of magnitude larger, $D_{CV} > D_{CA}$. This behavior has previously been reported and is not fully understood.²⁵ Since a larger fraction of the self-exchange occurs near the fluorine-doped tin oxide (FTO) substrate in the voltammetry measurements, the larger diffusion coefficient may reflect more rapid self-exchange near the FTO interface.

Values of D have previously been determined for other metal polypyridyl complexes anchored to TiO₂ surfaces and provide context for the values reported here. Trammel and Meyer previously determined $D_{CA} = 1.4 \times 10^{-9}$ cm²/s for the Os^{III/II} self-exchange in the compound [Os(bpy)₂(dcb)]²⁺.⁴ This value is within experimental error the same as that measured for the analogous Ru compound, yet is in contrast to solution phase self-exchange studies, where [Os(bpy)₃]^{3+/2+} self-exchange rate constants were more than double that of [Ru(bpy)₃]^{3+/2+}.²⁶ Comparisons such as these draw attention to the differences that may exist between electron-transfer reactions between molecules in fluid solution, and those anchored at a semiconductor interface. In another literature report, D_{CA} was quantified for [Ru(bpy)₂(4,4'-(PO₃H₂)₂-bpy)]^{3+/2+} in an 0.1 M HClO₄ aqueous medium.¹⁰ Remarkably similar values for D were quantified for this compound (1.33×10^{-9} cm²/s) as for those reported herein. Similar values were also reported by Mallouk *et al.*²⁷ Hence the nature of the anchoring groups, carboxylic acids versus phosphonic acids, has a less significant impact than does the inclusion of insulating organic functional groups on the ancillary ligands. However, it should be emphasized that the details of the mesoporous TiO₂ film structure may have a significant yet

undocumented influence on D . Factors such as film porosity, nanocrystallite size, and surface chemistry have an unknown impact on the electron transfer kinetics. Until such parameters are better understood, systematic studies similar to the one reported here are needed.

2.4.2 Self-Exchange Kinetics and Theory

Estimation of rate constant for self-exchange, k_{SE} , from D_{CV} requires knowledge of the distance between the surface anchored molecules. While it is sometimes stated that dcb-containing molecules bind to the TiO_2 surface in monolayer surface coverage, the ill-defined surface area make such statements difficult to validate experimentally. There is little data to suggest that these dicationic complexes form multi-layers on TiO_2 , but whether any or all are within van der Waals radii of each other is unclear. However, in the raw measured visible absorption spectra of the thin films it was clear that the saturation surface coverage increased in the order **dtb** < **dmb** < **bpy**. This correlates well with a steric increase in R when *tert*-butyl groups replace methyl groups or H atoms and suggests that on average the Ru centers are further apart in **dtb**.

The number of molecules present within the mesoporous film is reasonably estimated through absorption measurements using Beer's Law, though the distance between the molecules and their homogeneity is much more difficult to assess. An analysis described in the experimental section takes the total number of redox active molecules and disperses them within the mesoporous thin film as if there were no TiO_2 present, to give the largest value of R , as well as the case where the molecules pack as tightly as they do in the solid-state crystal structure. These analyses provide upper and lower limits to R , that are within a factor of ten of what would be expected when molecules as 10 Å spheres are close-packed on a planar idealized surface. Furthermore, the mean separation distance in the encounter complex formed

between $\text{Ru}(\text{bpy})_3^{3+/2+}$ for solution-phase self-exchange reaction has been calculated to be 13.6 Å which is comparable to the intermolecular distances determined from the crystal structures of the compounds.²⁸ The k_{SE} values abstracted in such a manner were in good agreement with previous literature reports that are discussed in more detail below.

An Arrhenius analysis of k_{SE} revealed activation energies for each studied complex were within experimental error the same, $E_{\text{act}} = 250 \pm 50$ mV. Within the framework of Marcus theory for nonadiabatic electron transfer, the activation energy for electron transfer is approximately equal to the sum of the work require to bring the two species together and one fourth the total reorganization energy, $\lambda/4$. Assuming the work term is zero for the reaction between anchored molecules, this activation data implies a reorganization energy of ~ 1 eV, a value that is consistent with literature values for similar electron transfer reactions between Ru based chromophores anchored to TiO_2 nanocrystallites.⁵ As the inner-sphere contributions to the total reorganization energy are mainly associated with the Ru-N bond lengths and angles, there was no *a priori* reason to suspect that the methyl or *tert*-butyl substituents would contribute to λ and no evidence of significant bond length alterations were evident in the crystal structures. Moreover, the structural changes observed upon oxidation of similar Ru polypyridyl complexes are minimal and therefore λ_{I} contribute negligibly to the total reorganization.²⁹ As a result, the primary contribution to the total reorganization energy arises from outer sphere contributions that are difficult to determine experimentally. Based on the negligible contribution of λ_{I} to the total reorganization energy, we conclude that the changes in steric bulk have a minimal influence on λ_{O} .

Application of Marcus theory using a shared λ in the fitting procedure revealed that the electronic coupling matrix element, H_{AB} , increased from 0.02 to 0.10 meV in going from **dtb**

to **dmb**. A λ value of 900 ± 100 meV was found to provide the most satisfactory fit to all three data sets under the assumption that the reorganization energies do not change appreciable between the compounds investigated. In contrast to those observed here, values of H_{AB} observed for the electron self-exchange reaction for the parent complex $\text{Ru}(\text{bpy})_3^{3+/2+}$ in fluid solution are reported to be between 2.5 meV and 12.4 meV.¹³ The significant decrease in H_{AB} is likely a result of the increased molecular distance, and the heterogeneous nature of the interface.

Self-exchange and activation parameters garnered from studies of $\text{TiO}_2|\text{dtb}$ were dramatically different than those obtained with **dmb** or **bpy** providing compelling evidence that bulky side groups do indeed influence H_{AB} . This finding supports the previous suggestion that long-chain side groups can be used to tune self-exchange at these same interfaces. In side-by-side comparative studies both H_{AB} and D were consistently the largest for **dmb** which was intriguing as this is counter-intuitive to what was expected based on the steric bulk of the compounds. While it is not clear why this is the case, it suggests that the electron donating behavior of the alkyl substituents is also playing a role. The self-exchange rate constants for $\text{Ru}(\text{bpy})_3^{3+/2+}$ are orders of magnitude larger than those of the corresponding ammine or aqua compounds, behavior that Sutin rationalized by concluding that the π -acidic nature of the bipyridine provides sufficient electron density on the ligands for self-exchange.¹³ It is hence likely that substituents modify the ligand electron density in a manner sufficient to alter self-exchange between immobilized redox centers.

2.5 Conclusions

Self-exchange intermolecular $\text{Ru}^{\text{III/II}}$ electron transfer across the surface of mesoporous nanocrystalline (anatase) TiO_2 thin film was characterized by cyclic voltammetry and

chronoabsorptometry techniques for a series of three Ru polypyridyl compounds $[\text{Ru}(\text{LL})_2(\text{dcbH}_2)](\text{PF}_6)_2$, where LL is 2,2'-bipyridine (**bpy**), 4,4'-dimethyl-2,2'-bipyridine (**dmb**) or 4,4'-di-*tert*-butyl-2,2'-bipyridine (**dtb**) and dcb is 2,2'-bipyridyl-4,4'-dicarboxylic acid. Apparent diffusion coefficients, D , abstracted from the electrochemical data revealed that the self-exchange was much slower for the *tert*-butyl containing compounds. Temperature dependent measurements revealed that this was due to lower intermolecular electronic coupling that result from the sterically bulky *tert*-butyl groups. The results indicate that insulating side groups can indeed be placed on redox active molecules to tune the electronic coupling, and hence self-exchange rate constants, without significantly altering the reorganization energy for electron transfer. Such behavior can be exploited in artificial photosynthetic assemblies both to enhance and inhibit lateral charge transport across oxide surfaces.

2.6 Acknowledgements

The research is supported by the National Science Foundation (NSF) under Award CHE-1213357 and the NSF Graduate Research Fellowship Program under Grant No. DGE-1144081 (T.C.M.). The authors would like to thank Evan E. Beauvilliers for assistance in preparing the TOC and Scheme 3.

2.7 Additional Content

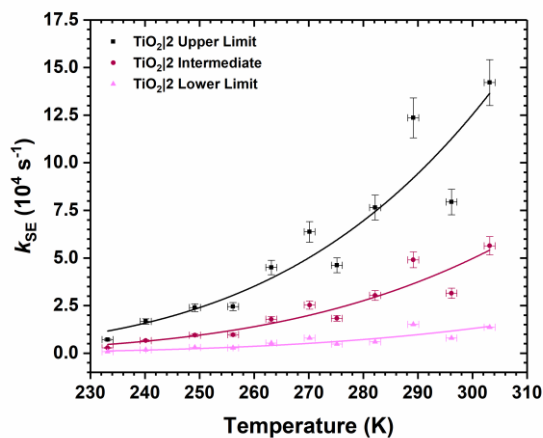


Figure 2.8. The temperature dependence of k_{SE} with fits to non-adiabatic Marcus theory (overlaid curves) calculated with three different values of R for $\text{TiO}_2|\text{dmb}$.

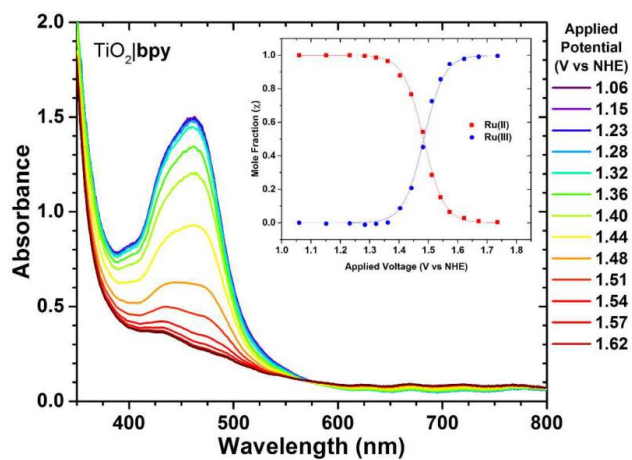


Figure 2.9. UV-visible spectra generated during the oxidation of **bpy**. Conversion from Ru^{II} to Ru^{III} proceeds from purple to red.

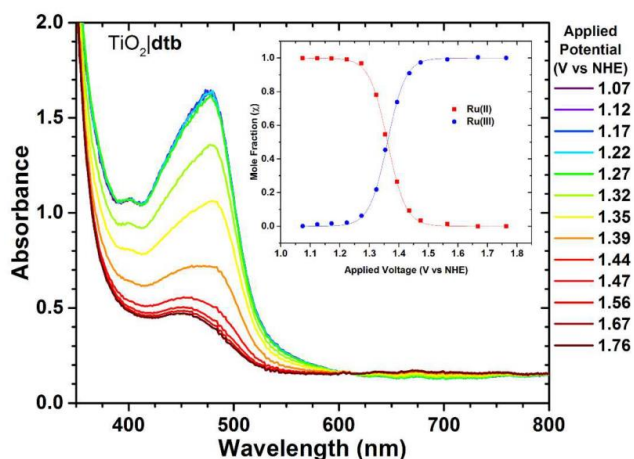


Figure 2.10. UV-visible spectra generated during the oxidation of **dtb**. Conversion from Ru^{II} to Ru^{III} proceeds from purple to red.

Table 2.4. Variation of R and H_{AB} Using Different Methods of Determining R

	R_{UL} (nm)	R_{I} (nm)	R_{LL} (nm)	$H_{\text{AB}}^{\text{UL}a}$ (meV)	$H_{\text{AB}}^{\text{I}a}$ (meV)	$H_{\text{AB}}^{\text{LL}a}$ (meV)
TiO₂ bpy	1.8 ± 0.03	1.4 ± 0.03	1.15	0.11 ± 0.04	0.07 ± 0.04	0.03 ± 0.02
TiO₂ dmb	2.2 ± 0.04	1.8 ± 0.03	1.27	0.17 ± 0.09	0.11 ± 0.05	0.04 ± 0.02
TiO₂ dtb	2.5 ± 0.07	2.0 ± 0.06	1.37	0.04 ± 0.03	0.02 ± 0.02	0.01 ± 0.01

^a $\lambda = 900 \pm 100$ meV shared between data sets. ^b $\lambda = 900 \pm 100$ meV shared between data sets.

^c $\lambda = 820 \pm 130$ meV shared between data sets.

2.6.1 Single Crystal X-ray Crystallography

All reflection intensities were measured at 110(2) K using a KM4/Xcalibur (detector: Sapphire3) with enhance graphite-monochromated Mo $K\alpha$ radiation ($\lambda = 0.71073$ Å) for **3** or a SuperNova diffractometer (equipped with Atlas detector) with Mo $K\alpha$ radiation ($\lambda = 0.71073$ Å) for **4** under the program CrysAlisPro (Versions 1.171.36.24 or 1.171.36.32 Agilent Technologies, 2012-2013). The same program was used to refine the cell dimensions and for data reduction. The structure was solved with the program SHELXS-2013 or SHELXS-2014/7 and was refined on F^2 with SHELXL-2013 or SHELXL-2014/7.³⁰ Analytical (**3**) or numerical

(4) absorption corrections based on a multifaceted crystal model were applied using CrysAlisPro. The temperature of the data collection was controlled using the system Cryojet (manufactured by Oxford Instruments). The H atoms were placed at calculated positions (unless otherwise specified) using the instructions AFIX 23, AFIX 43, AFIX 137 or AFIX 147 (only for **3**) with isotropic displacement parameters having values 1.2 or 1.5 times U_{eq} of the attached C or O atoms. For **3**, the H atoms attached to the major component of the disordered lattice water molecule (*i.e.*, O1W) were found from difference Fourier maps. Their coordinates were refined freely but the O–H bond lengths and the H...H distance were restrained to be 0.84(3) and 1.33(3) Å using the DFIX instructions, respectively. The H atoms attached to the minor component (O1') of the disordered lattice water molecule could not be retrieved.

3, Fw = 2365.03, elongated red plate, $0.40 \times 0.24 \times 0.05$ mm³, triclinic, $P-1$ (no. 2), $a = 11.4357(2)$, $b = 15.3159(3)$, $c = 17.6072(3)$ Å, $\alpha = 110.3534(19)$, $\beta = 92.4345(17)$, $\gamma = 102.7437(19)^\circ$, $V = 2796.04(10)$ Å³, $Z = 1$, $D_x = 1.405$ g cm⁻³, $\mu = 0.444$ mm⁻¹, abs. corr. range: 0.873–0.979. 34323 Reflections were measured up to a resolution of $(\sin \theta/\lambda)_{\max} = 0.62$ Å⁻¹. 11276 Reflections were unique ($R_{\text{int}} = 0.0750$), of which 9507 were observed [$I > 2\sigma(I)$]. 803 Parameters were refined using 275 restraints. $R1/wR2$ [$I > 2\sigma(I)$]: 0.0436/0.1111. $R1/wR2$ [all refl.]: 0.0546/0.1172. $S = 1.041$. Residual electron density found between -0.67 and 0.97 e Å⁻³. The asymmetric unit contains one Ru complex, two ClO₄⁻ counterions, as well as some lattice solvent molecules (hexane, water and acetonitrile). The structure is mostly ordered. The two perchlorate counterions are both disordered over two orientations, and the occupancy factors of the major components refine to 0.587(17) and 0.581(5). The hexane solvent molecule is found at sites of inversion symmetry (and therefore, only half of the molecule is crystallographically independent). The water molecule is found to be disordered over two

positions. The occupancy factor of the major component refines to 0.704(6). The checkCIF report generates 3 Alert level B that are concerned with the minor component of the disordered lattice water molecule. Because its occupancy factor is too low, the H atoms cannot be retrieved experimentally.

4, Fw = 1096.94, dark thick red lath, $0.31 \times 0.15 \times 0.08 \text{ mm}^3$, triclinic, *P*-1 (no. 2), $a = 13.6824(3)$, $b = 13.6984(3)$, $c = 14.2579(3) \text{ \AA}$, $\alpha = 98.249(2)$, $\beta = 101.025(2)$, $\gamma = 115.285(2)^\circ$, $V = 2294.10(9) \text{ \AA}^3$, $Z = 2$, $D_x = 1.588 \text{ g cm}^{-3}$, $\mu = 0.510 \text{ mm}^{-1}$, abs. corr. range: 0.786–1.000. 35221 Reflections were measured up to a resolution of $(\sin\theta/\lambda)_{\text{max}} = 0.65 \text{ \AA}^{-1}$. 10524 Reflections were unique ($R_{\text{int}} = 0.0299$), of which 9340 were observed [$I > 2\sigma(I)$]. 743 Parameters were refined using 498 restraints. $R1/wR2$ [$I > 2\sigma(I)$]: 0.0369/0.0900. $R1/wR2$ [all refl.]: 0.0432/0.0945. $S = 1.059$. Residual electron density found between -0.64 and 0.90 e \AA^{-3} . The two PF_6^- counterions are found to be disordered over two orientations. The occupancy factors of the major components of the disorder refine to 0.917(3) and 0.821(8). The occupancy factor of the lattice solvent CH_3CN molecule was refined freely, and its occupancy factor refines to 0.907(7).

REFERENCES

- (1) Bonhôte, P.; Gogniat, E.; Tingry, S.; Barbé, C.; Vlachopoulos, N.; Lenzmann, F.; Comte, P.; Grätzel, M. Efficient Lateral Electron Transport inside a Monolayer of Aromatic Amines Anchored on Nanocrystalline Metal Oxide Films. *J. Phys. Chem. B* **1998**, *102*, 1498-1507.
- (2) Heimer, T. A.; D'Arcangelis, S. T.; Farzad, F.; Stipkala, J. M.; Meyer, G. J. An Acetylacetonate-Based Semiconductor–Sensitizer Linkage. *Inorg. Chem.* **1996**, *35*, 5319-5324.
- (3) Hu, K.; Meyer, G. J. Lateral Intermolecular Self-Exchange Reactions for Hole and Energy Transport on Mesoporous Metal Oxide Thin Films. *Langmuir* **2015**, *31*, 11164-11178.
- (4) Trammell, S. A.; Meyer, T. J. Diffusional Mediation of Surface Electron Transfer on TiO₂. *J. Phys. Chem. B* **1999**, *103*, 104-107.
- (5) Moia, D.; Vaissier, V.; Lopez-Duarte, I.; Torres, T. S.; Nazeeruddin, M. K.; O'Regan, B. C.; Nelson, J.; Barnes, P. R. F. The reorganization energy of intermolecular hole hopping between dyes anchored to surfaces. *Chem. Sci.* **2014**, *5*, 281-290.
- (6) Wang, Q.; Zakeeruddin, S. M.; Cremer, J.; Bäuerle, P.; Humphry-Baker, R.; Grätzel, M. Cross Surface Ambipolar Charge Percolation in Molecular Triads on Mesoscopic Oxide Films. *J. Am. Chem. Soc.* **2005**, *127*, 5706-5713.
- (7) Moia, D.; Cappel, U. B.; Leijtens, T.; Li, X.; Telford, A. M.; Snaith, H. J.; O'Regan, B. C.; Nelson, J.; Barnes, P. R. F. The Role of Hole Transport between Dyes in Solid-State Dye-Sensitized Solar Cells. *J. Phys. Chem. C* **2015**, *119*, 18975-18985.
- (8) Hu, K.; Robson, K. C. D.; Johansson, P. G.; Berlinguette, C. P.; Meyer, G. J. Intramolecular Hole Transfer at Sensitized TiO₂ Interfaces. *J. Am. Chem. Soc.* **2012**, *134*, 8352-8355.
- (9) Hu, K.; Robson, K. C.; Beauvilliers, E. E.; Schott, E.; Zarate, X.; Arratia-Perez, R.; Berlinguette, C. P.; Meyer, G. J. Intramolecular and Lateral Intermolecular Hole Transfer at the Sensitized TiO₂ Interface. *J. Am. Chem. Soc.* **2014**, *136*, 1034-1046.
- (10) Hanson, K.; Brennaman, M. K.; Ito, A.; Luo, H.; Song, W.; Parker, K. A.; Ghosh, R.; Norris, M. R.; Glasson, C. R. K.; Concepcion, J. J.; Lopez, R.; Meyer, T. J. Structure–Property Relationships in Phosphonate-Derivatized, Ru^{II} Polypyridyl Dyes on Metal Oxide Surfaces in an Aqueous Environment. *J. Phys. Chem. C* **2012**, *116*, 14837-14847.
- (11) Moia, D.; Leijtens, T.; Noel, N.; Snaith, H. J.; Nelson, J.; Barnes, P. R. F. Dye Monolayers Used as the Hole Transporting Medium in Dye-Sensitized Solar Cells. *Adv. Mater.* **2015**, *27*, 5889-5894.
- (12) Penner, R. M.; Gogotsi, Y. The Rising and Receding Fortunes of Electrochemists. *ACS Nano* **2016**, *10*, 3875-3876.

- (13) Sutin, N. Nuclear, electronic, and frequency factors in electron transfer reactions. *Acc. Chem. Res.* **1982**, *15*, 275-282.
- (14) Barbara, P. F.; Meyer, T. J.; Ratner, M. A. Contemporary Issues in Electron Transfer Research. *J. Phys. Chem.* **1996**, *100*, 13148-13168.
- (15) Swords, W. B.; Li, G.; Meyer, G. J. Iodide Ion Pairing with Highly Charged Ruthenium Polypyridyl Cations in CH₃CN. *Inorg. Chem.* **2015**, *54*, 4512-4519.
- (16) O'Donnell, R. M.; Sampaio, R. N.; Li, G.; Johansson, P. G.; Ward, C. L.; Meyer, G. J. Photoacidic and Photobasic Behavior of Transition Metal Compounds with Carboxylic Acid Group(s). *J. Am. Chem. Soc.* **2016**, *138*, 3891-3903.
- (17) Bard, A. J.; Faulkner, L. R. *Electrochemical Methods : Fundamentals and Applications*. 2nd Edition ed.; Wiley: New York, 2001.
- (18) Daum, P.; Lenhard, J. R.; Rolison, D.; Murray, R. W. Diffusional charge transport through ultrathin films of radiofrequency plasma polymerized vinylferrocene at low temperature. *J. Am. Chem. Soc.* **1980**, *102*, 4649-4653.
- (19) Marton, A.; Clark, C. C.; Srinivasan, R.; Freundlich, R. E.; Narducci Sarjeant, A. A.; Meyer, G. J. Static and Dynamic Quenching of Ru(II) Polypyridyl Excited States by Iodide. *Inorg. Chem.* **2006**, *45*, 362-369.
- (20) DiMarco, B. N.; O'Donnell, R. M.; Meyer, G. J. Cation-Dependent Charge Recombination to Organic Mediators in Dye-Sensitized Solar Cells. *J. Phys. Chem. C* **2015**, *119*, 21599-21604.
- (21) Ward, C. L.; O'Donnell, R. M.; DiMarco, B. N.; Meyer, G. J. Kinetic Resolution of Charge Recombination and Electric Fields at the Sensitized TiO₂ Interface. *J. Phys. Chem. C* **2015**, *119*, 25273-25281.
- (22) O'Donnell, R. M.; Sampaio, R. N.; Barr, T. J.; Meyer, G. J. Electric Fields and Charge Screening in Dye Sensitized Mesoporous Nanocrystalline TiO₂ Thin Films. *J. Phys. Chem. C* **2014**, *118*, 16976-16986.
- (23) Ardo, S.; Achey, D.; Morris, A. J.; Abrahamsson, M.; Meyer, G. J. Non-Nernstian Two-Electron Transfer Photocatalysis at Metalloporphyrin–TiO₂ Interfaces. *J. Am. Chem. Soc.* **2011**, *133*, 16572-16580.
- (24) Li, X.; Nazeeruddin, M. K.; Thelakkat, M.; Barnes, P. R. F.; Vilar, R. N.; Durrant, J. R. Spectroelectrochemical studies of hole percolation on functionalised nanocrystalline TiO₂ films: a comparison of two different ruthenium complexes. *Phys. Chem. Chem. Phys.* **2011**, *13*, 1575-1584.
- (25) Wang, Q.; Zakeeruddin, S. M.; Nazeeruddin, M. K.; Humphry-Baker, R.; Grätzel, M. Molecular Wiring of Nanocrystals: NCS-Enhanced Cross-Surface Charge Transfer in

- Self-Assembled Ru-Complex Monolayer on Mesoscopic Oxide Films. *J. Am. Chem. Soc.* **2006**, *128*, 4446-4452.
- (26) Chan, M.-S.; Wahl, A. C. Rate of electron exchange between iron, ruthenium, and osmium complexes containing 1,10-phenanthroline, 2,2'-bipyridyl, or their derivatives from nuclear magnetic resonance studies. *J. Phys. Chem.* **1978**, *82*, 2542-2549.
- (27) Swierk, J. R.; McCool, N. S.; Saunders, T. P.; Barber, G. D.; Mallouk, T. E. Effects of Electron Trapping and Protonation on the Efficiency of Water-Splitting Dye-Sensitized Solar Cells. *J. Am. Chem. Soc.* **2014**, *136*, 10974-10982.
- (28) Brown, G. M.; Sutin, N. A comparison of the rates of electron exchange reactions of ammine complexes of ruthenium(II) and -(III) with the predictions of adiabatic, outer-sphere electron transfer models. *J. Am. Chem. Soc.* **1979**, *101*, 883-892.
- (29) Biner, M.; Buergi, H. B.; Ludi, A.; Roehr, C. Crystal and molecular structures of [Ru(bpy)₃](PF₆)₃ and [Ru(bpy)₃](PF₆)₂ at 105 K. *J. Am. Chem. Soc.* **1992**, *114*, 5197-5203.
- (30) Sheldrick, G. M. Crystal structure refinement with *SHELXL*. *Acta Crystallogr. C* **2015**, *71*, 3-8.

CHAPTER 3: Influence of 4 and 4' Substituents on Ru^{III/II} Polypyridyl Self-Exchange Electron Transfer across Nanocrystalline TiO₂ Surfaces²

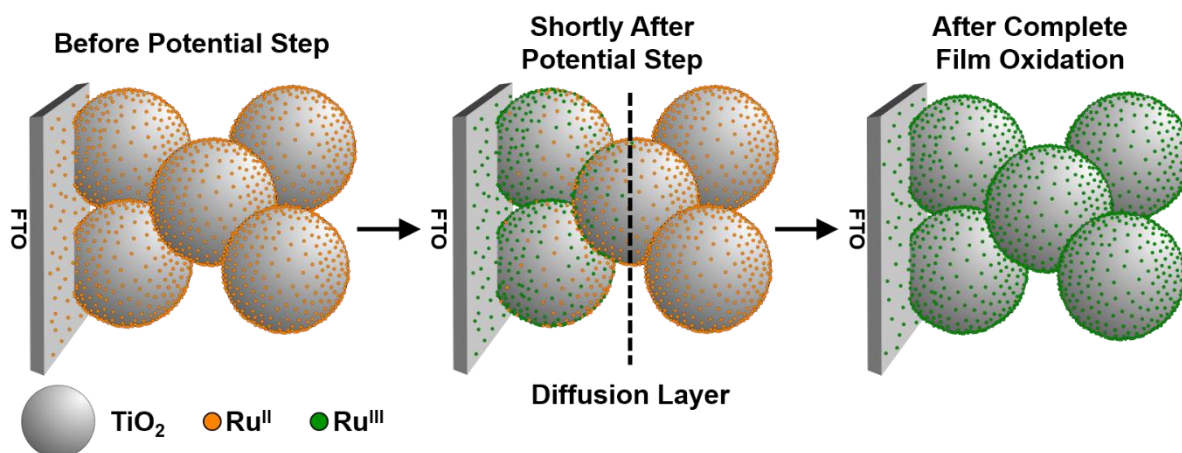
3.1 Introduction

Lateral electron transfer, commonly referred to as hole-hopping, between surface-immobilized, redox active compounds at semiconductor interfaces has emerged as an important, yet often overlooked, process in many solar energy capture and conversion schemes. Recent reports revealed that after photoinduced electron injection into TiO₂, rapid lateral self-exchange electron transfer rates between chromophores in dye-sensitized solar cells (DSSCs) enhanced charge recombination rates between the oxidized chromophore and the TiO₂ electron.¹⁻³ Moia and co-workers recently reported a DSSC where lateral self-exchange replaced traditional redox mediators as the shuttle of electron holes to the counter-electrode and resulted in devices with large open circuit voltages.^{4,5} Furthermore, limiting lateral electron transfer rates between chromophore-catalyst assemblies anchored to the surface of TiO₂ has been shown to be integral for the accumulation of multiple redox equivalents onto a catalyst and the inhibition of unwanted comproportionation chemistry.⁶⁻⁸ Therefore, controlling lateral electron transfer kinetics at the semiconductor interface is important for device optimization. Here, we expand upon a previous report⁹ using a homologous series of Ru^{II} polypyridyl

²This work has been submitted to the *Journal of Physical Chemistry C* for publication. Reprinted with permission from Motley, T. C.; Brady, M. D.; Meyer, G. J. Influence of 4 and 4' Substituents on Ru^{III/II} Polypyridyl Self-Exchange Electron Transfer across Nanocrystalline TiO₂ Surfaces. *J. Phys. Chem. C* **2018**, submitted for publication. Unpublished work copyright 2018 American Chemical Society.

compounds to determine whether the steric size or the electron withdrawing/donating ability of substituents on a 4,4'-substituted-2,2'-bipyridine ligand affect the lateral self-exchange electron transfer rates at the TiO_2 interface.

Scheme 3.1. A Simplistic Depiction of the Time Evolution of the Complete Film Oxidation during a Chronoabsorptometry Experiment



It is well-established that surface-anchored Ru^{II} polypyridyl compounds on TiO_2 thin films can undergo complete oxidation upon application of a sufficiently positive potential despite possessing formal reduction potentials within the forbidden bandgap.¹⁰⁻¹² The key requirement is that the surface coverage be above a minimum value, termed a percolation threshold, which is typically 50-60% of the maximum possible surface coverage.^{9,11-13} The accepted mechanism, depicted in Scheme 3.1, invokes an initial electron transfer to the transparent conductive oxide, typically fluorine-doped tin oxide (FTO), from nearby molecules followed by self-exchange electron transfer to shuttle more electrons toward the FTO.^{9-11,13-17} As time progresses, the diffusion layer, sometimes referred to in these films as the oxidation front, moves through the film until it reaches the outer edges and the film is completely oxidized. This behavior has been demonstrated for numerous classes of compounds.^{9,11,12,14,15}

Self-exchange electron transfer between Ru^{II} polypyridyl compounds in fluid solution and on the surface of metal oxides has been well-described by nonadiabatic Marcus theory for electron transfer.^{9,18} For self-exchange ($\Delta G^\circ = 0$), the nonadiabatic Marcus equation is given by eq. 3.1, where k_R is the rate constant for electron transfer, H_{DA} is the intermolecular electronic coupling matrix element between electron donor (Ru^{II}) and electron acceptor (Ru^{III}), k_B is the Boltzmann constant, \hbar is the reduced Planck constant, T is the absolute temperature, and λ is the total reorganization energy with inner- (λ_I) and outer-sphere (λ_O) components. At constant λ and T , the rate is expected to depend only on H_{DA} that varies exponentially with distance as described by eq. 3.2, where δ is the intermolecular distance between the donor and acceptor, β is the attenuation factor, and H_{DA}^O is the electronic coupling at van der Waals separation, δ_O .¹⁹⁻²²

$$k_R = \left(\frac{2\pi}{\hbar}\right) \left(\frac{|H_{DA}|^2}{\sqrt{4\pi\lambda k_B T}}\right) e^{\left(\frac{-\lambda}{4k_B T}\right)} \quad (3.1)$$

$$H_{DA} = H_{DA}^O e^{-\frac{\beta}{2}(\delta - \delta_O)} \quad (3.2)$$

Recently, a homologous series of [Ru(R₂bpy)₂(dcb)]²⁺ compounds, where R₂bpy was a 4,4'-substituted-2,2'-bipyridine and dcb was 2,2'-bipyridyl-4,4'-dicarboxylic acid, was reported where the steric bulk of the substituent in the 4 and 4' positions of R₂bpy was systematically increased from -H, -CH₃, and -C(CH₃)₃ to determine if the addition of insulating side groups would alter the Ru^{III/II} self-exchange rate constants by increasing the intermolecular distance.⁹ It was found that the self-exchange electron transfer rates increased from -C(CH₃)₃ to -H to -CH₃, a trend that was not adequately explained by the differences in steric size of the functional groups. This suggested that the electron withdrawing or donating nature of the substituents might also influence the measured rates. Additionally, it was found through

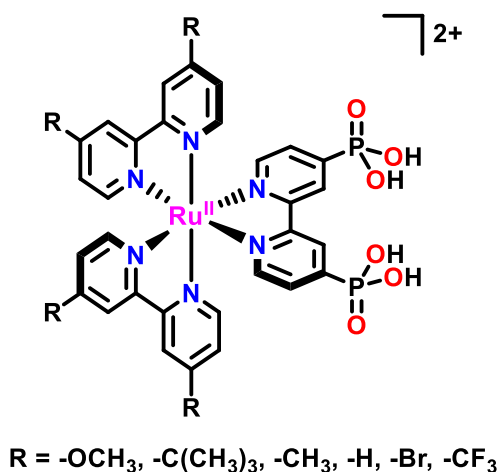
temperature-dependent electrochemical studies that the λ was within error the same for the functional group chosen.⁹

$\text{Ru}^{\text{III/II}}$ self-exchange has been reported to be significantly faster for Ru^{II} polypyridyl compounds than for related amine and aquo compounds in fluid solution.^{23,24} The π^* orbitals in the bipyridine rings are of the appropriate symmetry and energy to stabilize the $d\pi$ orbitals on the Ru^{II} metal center leading to the delocalization of the Ru-based $d\pi$ orbitals onto the bipyridine rings.^{23,25-28} This delocalization effectively reduces the intermolecular distance (*i.e.* increasing H_{DA}) between the donor and the acceptor for Ru^{II} polypyridyl compounds relative to their amine and aquo counterparts and was invoked to rationalize the faster self-exchange kinetics.²³ Various experimental and computational studies have suggested that 2-25% of electron density of highest-occupied molecular orbital (HOMO) in Ru^{II} polypyridyl compounds is located on the π -acidic diimine ligands.^{29,30} Therefore, one might expect the electron withdrawing or donating groups in the 4 and 4' positions of the bipyridine ring to tune self-exchange electron transfer rates by modulating the degree of orbital mixing. This was directly demonstrated by Kubiak and co-workers for bimolecular electron transfer in a series of oxo-centered ruthenium clusters.^{31,32} In these studies, it was shown that decreasing the pK_{a} of 4-substituted pyridine groups coordinated to these clusters increased the self-exchange rate constants over several orders of magnitude. Through NMR studies, they showed an increased delocalization of the HOMO onto the pyridine ring as the pK_{a} decreased. However, when molecular symmetry prevented significant orbital mixing between the Ru cluster and the π^* orbitals of the pyridine rings, no observable rate enhancement was observed.³¹

In the present study, a series of compounds of the type $[\text{Ru}(\text{R}_2\text{bpy})_2(\text{P})]^{2+}$, where P is 2,2'-bipyridyl-4,4'-diphosphonic acid and R_2bpy was a 4,4'-substituted-2,2'-bipyridine with 6

different R groups: -OCH₃, -C(CH₃)₃, -CH₃, -H, -Br, and -CF₃, Scheme 3.2. The functional groups were chosen to test the effects of both the electron withdrawing/donating ability and the steric size on lateral self-exchange electron transfer. Chronoabsorptometry was used to measure the apparent diffusion coefficients, which are proportional to the self-exchange rate constants. Nonadiabatic Marcus theory was used to investigate the interplay of the effects of steric size and the electron withdrawing or donating ability of the substituents on [Ru(R₂bpy)₂(P)]^{3+/2+} self-exchange kinetics for compounds anchored to the surface of TiO₂. Variable surface coverages were obtained using dilute dyeing solutions and the distance dependence was examined. An exponential dependence of the electron transfer rates with intermolecular distance was discovered. It was concluded that only steric size, and more specifically the intermolecular distance, predominantly determined the rates of self-exchange electron transfer at the TiO₂ interface.

Scheme 3.2. Ru^{II} Polypyridyl Compounds Used in this Study



3.2 Experimental Methods

3.2.1 Materials

The following solvents and reagents were obtained from the indicated commercial supplier and used without further purification: acetonitrile (CH_3CN , Burdick and Jackson, Spectrophotometric grade); lithium perchlorate (LiClO_4 , Sigma-Aldrich, 99.99%); perchloric acid (HClO_4 , Alfa Aesar, 70%), titanium(IV) isopropoxide (Aldrich, $\geq 97.0\%$); fluorine-doped tin(IV) oxide (FTO; Hartford Glass Co., Inc., 2.3 mm thick $15 \Omega/\square$); and oxygen (O_2 , Airgas, $\geq 99.998\%$). The following compounds were made as previously described or were available from previous studies: $[\text{Ru}(\text{MeObpy})_2(\text{P})]\text{Br}_2$, $[\text{Ru}(\text{dtb})_2(\text{P})]\text{Br}_2$, $[\text{Ru}(\text{dmb})_2(\text{P})]\text{Br}_2$, $[\text{Ru}(\text{bpy})_2(\text{P})]\text{Br}_2$, $[\text{Ru}(\text{Brbpy})_2(\text{P})]\text{Br}_2$, and $[\text{Ru}(\text{btfmb})_2(\text{P})]\text{Br}_2$.³³⁻³⁹

3.2.2 Preparation of Thin Films

Titania nanocrystallites were prepared via the hydrolysis of titanium(IV) isopropoxide using a previously reported sol-gel method.¹⁰ Mesoporous thin films were prepared by a doctor blade method on an ethanol-cleaned FTO substrate using Scotch tape ($\sim 50 \mu\text{m}$ thick) as a spacer to ensure a uniform thickness. The doctor-bladed films were covered and allowed to dry at room temperature for 30 min. Once dry, the films were sintered under an O_2 atmosphere ($\sim 1 \text{ atm}$) for 30 min at 450°C . These films were stored in a $\sim 70^\circ\text{C}$ oven until used. The resulting films were $3\text{--}5 \mu\text{m}$ as measured using a Bruker Dektak XT profilometer running the Vision 64 software.

The titania thin films were placed into concentrated aqueous dying solutions of the desired $[\text{Ru}(\text{R}_2\text{bpy})_2(\text{P})]\text{Br}_2$ compound in 0.1 M HClO_4 to allow for surface functionalization. For studies with variable surface coverages, 25 mL aqueous solutions of $[\text{Ru}(\text{bpy})_2(\text{P})]\text{Br}_2$ in 0.1 M HClO_4 were made with concentrations ranging from $2 \mu\text{M}$ to 5 mM for 14 total solutions.

Films were submerged for at least 48 h to ensure uniform, saturation surface coverages were achieved. Prior to use, the films were soaked in neat CH₃CN solutions for at least 1 h to remove any weakly adsorbed molecules from the surface in order to minimize dye desorption during the course of the experiments.

3.2.3 Spectroscopy

All steady-state UV-visible spectra were recorded on an AvaSpec UL2048 UV-Visible spectrometer and an AvaLight Deuterium/Halogen light source (Avantes) at room temperature. All measurements were obtained using a 1 cm² cuvette with the functionalized titania films placed along the diagonal at a 45° angle to the incident probe light.

3.2.4 Chronoabsorptometry

Chronoabsorptometry (CA) was performed using a WaveNow potentiostat (Pine Research Instrumentation, Inc.) coupled to an AvaSpec UL2048 UV-Visible spectrometer and an AvaLight Deuterium/Halogen light source (Avantes) all controlled by the AfterMath software (Pine Research Instrumentation, Inc.). A standard three-electrode arrangement was used with the functionalized titania films as the working electrode, a Pt mesh counter electrode, a Ag/AgCl pseudoreference electrode. The nonaqueous Ag/AgCl pseudoreference electrode (Pine Research Instrumentation, Inc.) was filled with a 0.1 M LiClO₄ solution in CH₃CN, and the applied potential was referenced to the $E_{1/2}(\text{Ru}^{\text{III/II}})$ of the [Ru(R₂bpy)₂(P)]²⁺ on the surface. To measure D_{CA} , a potential of $E_{1/2}(\text{Ru}^{\text{III/II}}) + 500$ mV was applied, and full UV-visible spectra were taken at fixed time intervals. All chronoabsorptometry studies were performed using CH₃CN solutions containing 0.1 M LiClO₄.

To measure the $E_{1/2}(\text{Ru}^{\text{III/II}})$, cyclic voltammetry was used with the same three electrode arrangement as described above. For these measurements, the pseudoreference electrode was

externally calibrated versus the ferrocenium/ferrocene ($\text{Fc}^{+/0}$) reduction potential in a CH_3CN solution containing 0.2 M LiClO_4 , which is 0.31 V vs the standard calomel electrode (SCE).⁴⁰ SCE is 0.241 V vs the normal hydrogen electrode (NHE).⁴⁰ All potentials reported are vs NHE unless otherwise stated.

3.2.5 Data Analysis

Data fitting was performed in OriginPro 2016, with least-squares error minimization achieved using the Levenberg-Marquardt method. The errors reported for fitting parameters are the standard errors. The errors reported for the for data obtained for using $[\text{Ru}(\text{R}_2\text{bpy})_2(\text{P})]/\text{TiO}_2$ was the standard deviation of 2 to 3 trials. The error reported for the variable surface coverage data was obtained through the propagation of error for all of the measurements utilized to compute the values.

3.3 Results

A series of 6 Ru^{II} polypyridyl compounds of the type $[\text{Ru}(\text{R}_2\text{bpy})_2(\text{P})]\text{Br}_2$, where R_2bpy is a 4,4'-substituted-2,2'-bipyridine and P is a 2,2'-bipyridyl-4,4'-diphosphonic acid, were synthesized using standard methods, Scheme 3.2.³⁷ The R groups used were $-\text{OCH}_3$, $-\text{C}(\text{CH}_3)_3$, $-\text{CH}_3$, $-\text{H}$, $-\text{Br}$, and $-\text{CF}_3$ (MeObpy, dtb, dmb, bpy, Brbpy, and btmb, respectively). These functional groups were chosen to allow for wide range of variability in electron withdrawing or donating strength as well as steric size.

The TiO_2 thin films were functionalized with the desired $[\text{Ru}(\text{R}_2\text{bpy})_2(\text{P})]\text{Br}_2$ from concentrated dyeing solution in aqueous 0.1 M HClO_4 solutions. Thin films were left submerged for a minimum of 48 h to ensure the saturation surface coverage, Γ_0 , was reached. Upon functionalization, the films displayed the characteristic metal-to-ligand charge transfer (MLCT) bands of $[\text{Ru}(\text{R}_2\text{bpy})_2(\text{P})]^{2+}$ compounds, Figure 3.1. Assuming that the absorbance

maximum, λ_{MLCT} , and the molar absorptivity coefficient, ϵ , remain unchanged on the surface relative to solution, Γ_0 was calculated using eq. 3.3, where A_{MLCT} is the absorbance at λ_{MLCT} . In order to account for the pathlength of the film, the incidence angle of the probe beam (45°) and the refractive index (1.59) measured for similar mesoporous, nanocrystalline TiO_2 thin films was used.⁴¹ Through the Snell-Descartes law, the angle of refraction through the film was determined to be 36.7° and $d/\cos(36.7^\circ)$ was added to equation 3.3 to adjust the measured surface coverage for the thickness of the film. Note that Γ_0 calculated in this way has units of $\text{mol} \times \text{cm}^{-2} \times \mu\text{m}^{-1}$ and corrects for any film-to-film thickness variations. The measured Γ_0 as well as the relevant spectroscopic properties for these compounds are listed in Table 3.1.

$$A = 1000 * \Gamma_0 * \epsilon * (d / \cos(36.7^\circ)) \quad (3.3)$$

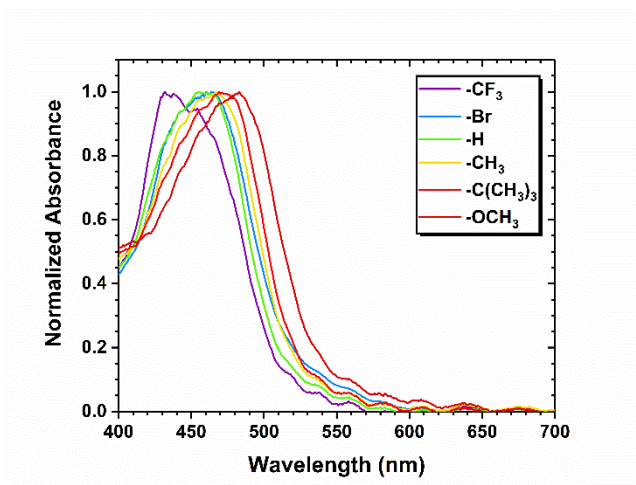


Figure 3.1. The normalized UV-visible absorbance spectra for each $[\text{Ru}(\text{R}_2\text{bpy})_2(\text{P})]/\text{TiO}_2$ film submerged in CH_3CN solutions containing 0.1 M LiClO_4 with an unsensitized thin film as a reference.

Table 3.1. Relevant Electrochemical and Photophysical Properties of the [Ru(R₂bpy)₂(P)](Br)₂ Compounds

	λ_{MLCT} (nm) ^a (ϵ , 10 ⁴ M ⁻¹ cm ⁻¹)	$E_{1/2}(\text{Ru}^{\text{III/II}})$ ^e (V vs NHE)	D (10 ⁻⁹ cm ² /s)	Γ_0 (10 ⁻⁸ mol×cm ⁻² ×μm ⁻¹)	δ (nm)	k_R (10 ⁵ s ⁻¹)
-OCH₃	477 (1.18) ^b	1.24	7.9 ± 0.3	2.24 ± 0.03	1.64 ± 0.01	17.6 ± 0.7
-C(CH₃)₃	460 (1.40) ^c	1.37 ^c	0.4 ± 0.2	1.6 ± 0.2	1.83 ± 0.06	0.7 ± 0.4
-CH₃	461 (1.28) ^b	1.38	4 ± 1	2.0 ± 0.4	1.7 ± 0.1	8 ± 2
-H	458 (1.20) ^b	1.44	5.1 ± 0.2	2.41 ± 0.05	1.60 ± 0.01	11.9 ± 0.5
-Br	465 (1.34) ^b	1.58	7 ± 1	3.1 ± 0.2	1.48 ± 0.04	19 ± 2
-CF₃	460 (1.66) ^d	1.74	0.028 ± 0.004	1.18 ± 0.02	2.04 ± 0.01	0.040 ± 0.06

^aReported in H₂O due to low solubility in CH₃CN. ^bValue taken from reference 37. ^cValue taken from reference 39. ^dValue taken from reference 38. ^eMeasured in 0.1 M LiClO₄ solutions in CH₃CN. Error in the reported values is ±10 mV.

Cyclic voltammetry was used to determine the half wave potentials, $E_{1/2}(\text{Ru}^{\text{III/II}})$, of the sensitized thin film in 0.1 M LiClO_4 CH_3CN solutions. The cyclic voltammograms displayed quasi-reversible waves with peak-to-peak splitting between 100-300 mV.¹⁰ The measured values ranged from 1.24 to 1.74 V vs NHE and were consistent with the one electron oxidation of the compounds, Table 3.1. The measured half wave potentials increased with the electron withdrawing ability of the functional groups.

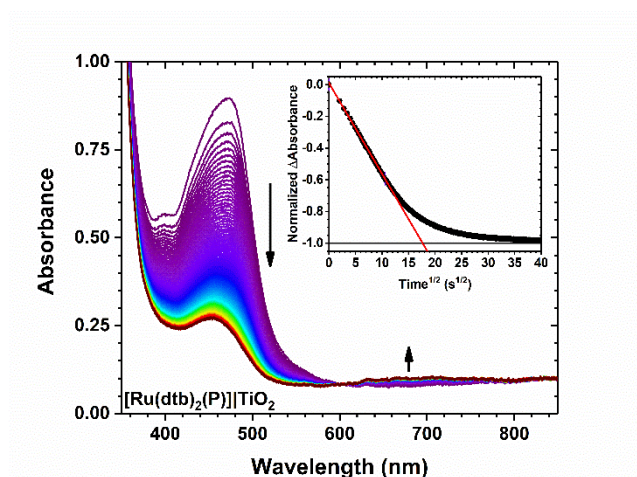


Figure 3.2. The UV-visible absorption spectra measured after the application a potential sufficient to oxidize $[\text{Ru}(\text{dtb})_2(\text{P})]/\text{TiO}_2$. A bleach of the characteristic MLCT transition was observed at 470 nm as the film was oxidized from Ru^{II} to Ru^{III} . A new absorption feature associated with the Ru^{III} species was observed to grow in centered at 675 nm. The inset shows the normalized absorbance change plotted against the square root of time. The data were fit to the Anson equation through the first 60% of the total absorbance change (red line).

To investigate the substituent effects on self-exchange electron transfer rates between surface-immobilized compounds, chronoabsorptometry (CA) was used. In these experiments, a potential step 500 mV more positive than the $E_{1/2}(\text{Ru}^{\text{III/II}})$ was applied to oxidize the $[\text{Ru}(\text{R}_2\text{bpy})_2(\text{P})]/\text{TiO}_2$, and the spectral changes were monitored as a function of time. Figure 3.2 shows representative data for $[\text{Ru}(\text{dtb})_2(\text{P})]/\text{TiO}_2$ and spectra for all other $[\text{Ru}(\text{R}_2\text{bpy})_2(\text{P})]/\text{TiO}_2$ can be found in the 3.7 Additional Content section (Figures 3.8-3.12). Upon oxidation, all of the compounds exhibited a loss of the characteristic Ru^{II} MLCT

transition and a growth of a weak, broad absorbance feature at wavelengths above 600 nm. Both spectral changes were indicative of the one electron oxidation of the compound from Ru^{II} to Ru^{III}.

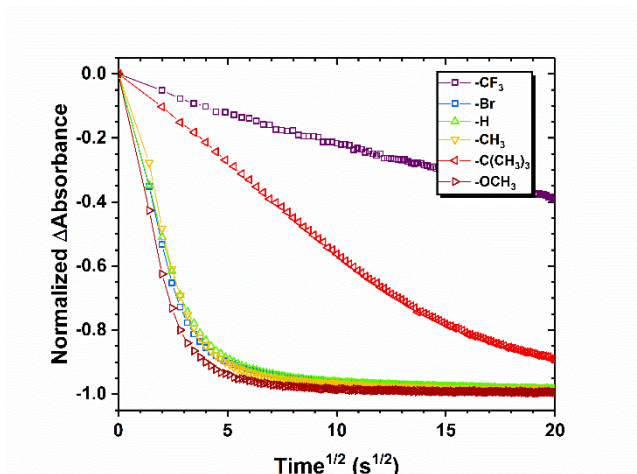


Figure 3.3. The normalized change in absorbance after the application of sufficiently positive potential to oxidize the [Ru(R₂bpy)₂(P)]TiO₂ plotted as a function of the square root of time for all compounds used in this study.

Single-wavelength kinetics were monitored at the λ_{MLCT} and were plotted as the normalized absorbance change, ΔA , versus the square-root of time, t , Figure 3.3, for all 6 compounds. These data were fit to the Anson equation, eq. 3.4, where D_{CA} is the apparent diffusion. The calculated D_{CA} values are given in Table 3.1. The Anson equation was previously derived using semi-infinite diffusion boundary conditions for molecules diffusing to the electrode surface.^{9,11,12} Here, Ru^{II} polypyridyl compounds were anchored to the TiO₂ film of a finite thickness. Therefore, the data deviates from the predicted linear relationship described by the Anson equation, inset Figure 3.2 and Figure 3.3. It has been shown by several groups that a linear relationship is maintained for the first 60% of the total absorbance change in CA experiments.^{9,11,12} Thus, only 60% of the total change was fit during the analysis, inset Figure 3.2 for [Ru(dtb)₂(P)]TiO₂ and Figures 3.8-3.10 in the 3.7 Additional Content section for the others. The smallest D_{CA} measured was $2.8 \times 10^{-11} \text{ cm}^2/\text{s}$ for [Ru(CF₃bpy)₂(P)]TiO₂.

followed by $[\text{Ru}(\text{dtb})_2(\text{P})]/\text{TiO}_2$ which was an order of magnitude larger with a value of $3.6 \times 10^{-10} \text{ cm}^2/\text{s}$. The other five compounds measured all had diffusion coefficients that were on the same order of magnitude with values between 3.8×10^{-9} to $7.9 \times 10^{-9} \text{ cm}^2/\text{s}$. These values agreed with those published for similar Ru^{II} polypyridyl compounds anchored to TiO_2 with phosphonic acid and carboxylic acid binding groups.^{6,9,13,17,42} Throughout the course of the experiments, no desorption of the surface bound compounds was observed.

$$\Delta A = \frac{2D^{1/2}t^{1/2}}{d\pi^{1/2}} \quad (3.4)$$

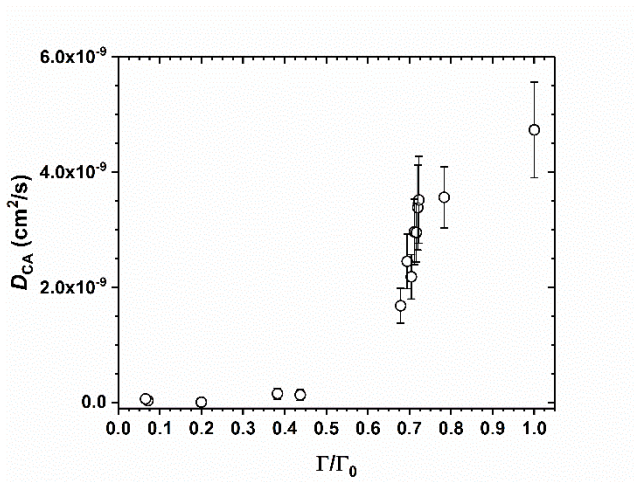


Figure 3.4. The variation of the measured apparent diffusion coefficients (D_{CA}) for $[\text{Ru}(\text{bpy})_2(\text{P})]/\text{TiO}_2$ with the fractional surface coverage (Γ/Γ_0), where Γ_0 was the maximum surface coverage attained in the most concentrated dyeing solution (5 mM). The D_{CA} were measured in CH_3CN solutions with 0.1 M LiClO_4 electrolyte. Error bars for D_{CA} included for all data.

As a control to test the effects of intermolecular distance, the apparent diffusion coefficients were measured for films at sub-saturation surface coverages. Sub-saturation surface coverages were achieved by functionalizing the films from aqueous 0.1 M HClO_4 solutions of different concentrations of $[\text{Ru}(\text{bpy})_2(\text{P})]\text{Br}_2$ that ranged from 2 μM to 5 mM and resulted in surface coverages between 4.4×10^{-9} and $6.2 \times 10^{-8} \text{ mol} \times \text{cm}^{-2} \times \mu\text{m}^{-1}$. The diffusion coefficient for electron transfer was measured for each of these films, Figure 3.4. The onset for

self-exchange electron transfer, *i.e.* the percolation threshold, was between 50% to 60% of the saturation surface coverage and was in agreement with what has been reported previously for Ru^{II} polypyridyl compounds.^{6,13} The observation of a percolation threshold also indicated that physical diffusion of the molecules was not contributing significantly to the measured diffusion coefficients.^{43,44}

Conversion of the measured diffusion coefficients to a first order self-exchange “hopping” rate constant, k_R , required knowledge of the intermolecular distance, δ , between the molecules on the interface. The determination of δ is experimentally quite challenging as the concentration in the monolayer on the interface as well as the packing arrangement of the molecules are difficult to measure for these irregular, mesoporous films. In order to get an estimate for δ , it was assumed the molecules were evenly distributed within the pore volume of the TiO₂ film as opposed to the more reasonable case of being located at the interface. To do this, a “concentration” for the molecules in the pore volume was determined from the measured Γ_0 using eq 3.5 where $\Gamma_0 \times 10^4$ is the surface coverage converted to concentration with units of mol/cm³, N is Avogadro’s number, and p is the porosity, which was assumed to be 60%.⁴⁵ This “concentration” was converted to an intermolecular distance with the assumption that the molecules were in a cubic lattice arrangement using $\delta = (c_0)^{-1/3}$ as has been done previously.^{9,16} Note that the δ calculated with these assumptions represents an upper limit as the compounds are assumed to be evenly distributed within the pore volume of the film as opposed to being localized at the interface. With the computed δ , the k_R was calculated for each compound using the Dahms-Ruff equation, eq. 3.6.^{9,13,43}

$$c_0 = \frac{(\Gamma_0 * 10^4) * N}{p} \quad (3.5)$$

$$D_{CA} = \frac{k_R \delta^2}{6} \quad (3.6)$$

3.4 Discussion

A detailed understanding of the synthetic handles available to tune lateral self-exchange electron transfer rates at semiconductor interfaces is important for the optimization of many solar energy conversion schemes.¹⁻⁸ Previous work to determine if small structural changes in a homologous series of Ru^{II} polypyridyl compounds of the type [Ru(R₂bpy)₂(dcb)]²⁺, where R₂bpy was a 4,4'-substituted-2,2'-bipyridine and dcb was 2,2'-bipyridyl-4,4'-dicarboxylic acid, revealed that substituents in the 4 and 4' positions of the bipyridine rings did influence the self-exchange rate though it was unclear if the variation in the measured apparent diffusion coefficients, D_{CA} , was due to the steric size, the relative electron withdrawing or donating ability, or both for the chosen functional groups.⁹ Here, an expanded series of Ru^{II} polypyridyl compounds of the type [Ru(R₂bpy)₂(P)]²⁺, where P is 2,2'-bipyridyl-4,4'-diphosphonic acid, was reported with a wide variety of functional groups of varying electron withdrawing or donating strength and steric size to elucidate the degree of influence each has on lateral self-exchange. Chronoabsorptometry was used to quantify the D_{CA} , and the measured values were analyzed within the framework of nonadiabatic Marcus theory. The data indicated that the steric size of the substituent was the sole factor that influenced lateral self-exchange electron transfer across semiconductor interfaces through variations in surface coverage, and thus intermolecular distance.

3.4.1 Quantification of Reduction Potentials and Apparent Diffusion Coefficients

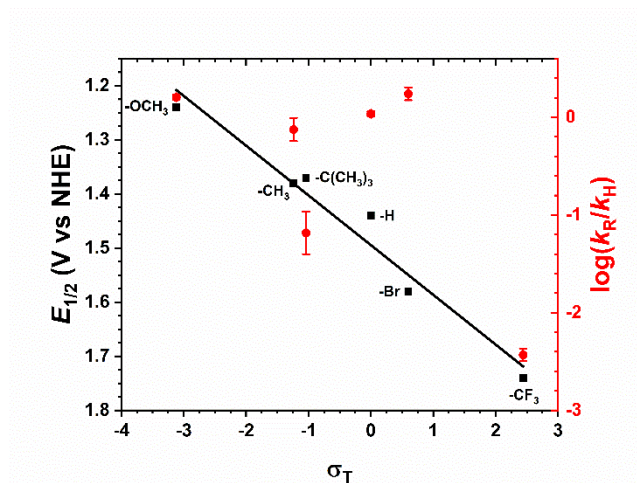


Figure 3.5. The dependence of the measured $E_{1/2}(\text{Ru}^{\text{III/II}})$ (black, ■) and of $\log(k_H/k_R)$ (red, ●) on the summative Hammett parameter, σ_T , for all $[\text{Ru}(\text{R}_2\text{bpy})_2(\text{P})]/\text{TiO}_2$. The measured $E_{1/2}(\text{Ru}^{\text{III/II}})$ displayed a strong correlation with σ_T with a slope of 0.09 V vs NHE. No such correlation was observed with $\log(k_H/k_R)$. Error bars are given for the $\log(k_H/k_R)$ data.

The $\text{Ru}^{\text{III/II}}$ formal reduction potentials, $E_{1/2}(\text{Ru}^{\text{III/II}})$, were measured for each compound anchored to the TiO_2 interface using cyclic voltammetry in 0.1 M LiClO_4 in CH_3CN . The peak-to-peak separation between the cathodic and anodic waves in the cyclic voltammogram fell between 100 and 300 mV which was consistent of a quasi-reversible electrochemical process.¹⁰ The measured $E_{1/2}(\text{Ru}^{\text{III/II}})$ reflect the energy of the $d\pi$ orbitals. As such, comparing the $E_{1/2}(\text{Ru}^{\text{III/II}})$ between the compounds anchored to the surface reports directly on the degree of stabilization imparted on the Ru $d\pi$ orbitals from π -backbonding with the bipyridine π^* orbitals. $[\text{Ru}(\text{MeObpy})_2(\text{P})]/\text{TiO}_2$ possessed the least positive $E_{1/2}(\text{Ru}^{\text{III/II}})$, 1.24 V vs NHE, while $[\text{Ru}(\text{btfmb})_2(\text{P})]/\text{TiO}_2$ was the most positive, 1.74 V vs NHE. These observations agreed with the notion the electron withdrawing groups stabilize the π^* orbitals of the bipyridine rings and increased the π -acidity of the orbitals.²⁵⁻²⁸ In fact, the summative Hammett parameter, σ_T , of each compound given by eq 3.7, was found to be strongly correlated with the measured $E_{1/2}(\text{Ru}^{\text{III/II}})$, Figure 3.5. In eq 3.7, the sum of the Hammett parameters for *para*-substitution,

σ_p^+ , are summed for all the substituents on the bipyridine rings. The σ_p^+ values were used to reflect the substituents ability to stabilize the increasing positive charge in the transition state during Ru^{II} oxidation through resonance. Note that the σ_p^+ values have been previously shown to correlate well with $E_{1/2}(\text{Ru}^{\text{III/II}})$ for substituted Ru^{II} polypyridyl compounds.^{27,28} The slope of the linear regression line in Figure 3.5 was 0.09 V vs NHE, and matched values observed for similar analysis with Ru^{II} tris(bipyridyl) type compounds.²⁷ Both the σ_p^+ for the substituents as well as the σ_T for each compound are listed in Table 3.2. Note that the -PO(OH)₂ substituents are not included in σ_T as no values of σ_p^+ were found in the literature; however, the slope of the trendline in Figure 3.5 would remain unchanged with or without their inclusion since the σ_T for each compound has the same contribution from -PO(OH)₂.

$$\sigma_T = \sum_i \sigma_p^+ \quad (3.7)$$

Table 3.2. Selected Hammett and Charton Parameters^{46,47}

	Hammett Parameter^a (σ_p^+)	Summative Hammett Parameter^b (σ_T)	Charton Parameter (ν)
-OCH₃	-0.78	-3.12	0.36
-C(CH₃)₃	-0.26	-1.04	1.24
-CH₃	-0.31	-1.24	0.52
-H	0	0	0
-Br	0.15	0.60	0.65
-CF₃	0.61	2.44	0.91

^aValue given for a single substituent. ^bValue given for [Ru(R₂bpy)₂(P)]²⁺ omitting the contribution from the -PO(OH)₂ function groups.

Chronoabsorptometry (CA) allowed for the measurement of the apparent diffusion coefficients, D_{CA} , for each compound at the TiO₂ interface. The D_{CA} values were used as an analogue to the second-order self-exchange electron transfer rate constants, k_R' , for compounds anchored to the interface as they are directly proportional to one another, eq 3.6.^{11-13,16} However, direct measurement of k_R' was difficult because of the nebulousness of concentration

at these interfaces. The measured D_{CA} values were between 10^{-11} and 10^{-9} cm²/s. These values were consistent with other reported values for Ru^{II} polypyridyl compounds measured by CA.^{6,9,17,48} Previous studies with [Ru(bpy)₂(P)]/TiO₂ reported D_{CA} values to be between 1.1×10^{-9} and 1.3×10^{-9} cm²/s.^{6,17} These values were about a factor 2 smaller than the value measured here. In those reports, the surface coverages were smaller than those reported here for the same compound which would result in a smaller D_{CA} value (*vide infra*). DiMarco and co-workers previously concluded that [Ru(CF₃bpy)₂(dcb)]/TiO₂ displayed no or extremely slow lateral self-exchange electron transfer under the conditions of their study.² This was consistent with the small D_{CA} value measured for [Ru(CF₃bpy)₂(P)]/TiO₂ reported here.

It is often more convenient to convert the measured D_{CA} values to a first order hopping rate constant, k_R , to compare the measured rates with other techniques; however, one must make numerous assumptions about the molecular arrangement at the interface. Here, it was assumed that the compounds were arranged in a cubic lattice pattern within the pore volume of the film. The intermolecular distances calculated in this way necessarily represented an upper limit to the intermolecular spacing as it is often asserted that the molecules form a monolayer and are not freely diffusing in the pores.¹³ The k_R values were calculated to be between 10^3 to 10^6 s⁻¹. In operational DSSCs, photoinitiated excited-state electron injection from the surface-bound molecule leaves behind an oxidized chromophore that can undergo self-exchange electron transfer.^{13,49} Lateral self-exchange hopping rate constants measured under these conditions were found to be on the order of 10^6 s⁻¹ for both [Ru(dmb)₂(dcb)]/TiO₂ and [Ru(dtb)₂(dcb)]/TiO₂ measured by nanosecond transient absorption spectroscopy.^{8,50} These values are 1 to 2 orders of magnitude larger than what was calculated from the D_{CA} . In our studies, interparticle electron transfer must occur multiple times in order to oxidize the

entire film; however, it is asserted that few if any interparticle electron transfer reactions occur before charge recombination can occur in the transient absorption experiments.^{8,50,51} Though speculative, it may be that electron transfer between molecules on different TiO₂ particles is slower than between those on the same nanoparticle which would be reflected in the measured rate constants.

3.4.2 Substituent Effects on Self-Exchange Electron Transfer at the Interface

Marcus theory has been successfully and extensively applied to describe and predict electron transfer between donor and acceptor compounds, including nonadiabatic self-exchange electron transfer between Ru^{II} polypyridyl compounds in fluid solution and anchored to semiconductor interfaces.^{9,18,24} For self-exchange electron transfer where $\Delta G^\circ = 0$, the nonadiabatic Marcus equation is given by eq 3.1. For lateral self-exchange between Ru^{II} polypyridyl compounds at the TiO₂ interface, λ has been shown to be independent of the substituents in the 4 and 4' position.⁹ Thus, the only way to alter k_R is to tune H_{DA} , as described by eq 3.2, through increasing the intermolecular distance (steric size) or decreasing the effective electron transfer distance through orbital delocalization (electron withdrawing or donating ability).

As shown above, the measured $E_{1/2}(\text{Ru}^{\text{III/II}})$ values displayed a strong linear correlation with σ_T values and was indicative of the better energetic overlap between the Ru-based $d\pi$ and bpy-based π^* orbitals with increasing electron withdrawing strength. This enhanced overlap would lead to more orbital mixing as demonstrated by Kubiak *et al.* for oxo-centered ruthenium clusters.^{31,32} If the enhanced delocalization affected self-exchange electron transfer at the interface, one would also expect a correlation of the first order hopping rate constants with σ_T as described by eq 3.8, where ρ is the sensitivity factor of lateral self-exchange electron transfer

to the electron withdrawing or donating ability of the functional groups, R is the gas constant, $\Delta\Delta G^\ddagger$ is the differences in the free energy of activation between $[\text{Ru}(\text{bpy})_2(\text{P})]/\text{TiO}_2$ ($\Delta G_{\text{H}}^\ddagger$) and $[\text{Ru}(\text{R}_2\text{bpy})_2(\text{P})]/\text{TiO}_2$ ($\Delta G_{\text{R}}^\ddagger$), and k_{H} and k_{R} is the first-order hopping rate constant for $[\text{Ru}(\text{bpy})_2(\text{P})]/\text{TiO}_2$ and $[\text{Ru}(\text{R}_2\text{bpy})_2(\text{P})]/\text{TiO}_2$, respectively.^{47,52} However, no correlation was observed between $\ln(k_{\text{R}}/k_{\text{H}})$ and σ_{T} , Figure 3.5. This implies that there is no significant change in the degree of delocalization as the energetic separation between the $d\pi$ orbitals and the π^* orbitals became smaller. In the nonadiabatic limit of Marcus theory, the $\Delta G_{\text{R}}^\ddagger$ is described by eq 3.9.²⁴ Since λ has been previously demonstrated to be invariant to the identity of the alkyl functional groups, it would be expected that $\Delta\Delta G^\ddagger$ is equal to 0 in the absence of significant orbital delocalization, and no correlation of $\ln(k_{\text{R}}/k_{\text{H}})$ and σ_{T} would be observed.

$$\ln \frac{k_{\text{R}}}{k_{\text{H}}} = \frac{\Delta\Delta G^\ddagger}{RT} = \rho\sigma_{\text{T}} \quad (3.8)$$

$$\Delta G_{\text{R}}^\ddagger = \frac{\lambda}{4} \quad (3.9)$$

The steric bulk of the 4 and 4' substituents have been shown to decrease the saturation surface coverages, Γ_0 , for Ru^{II} polypyridyl compounds.^{9,15} Therefore, it was expected that the substituents used here would also influence the surface coverage. One measure for the steric size of substituents is known as the Charton value, ν , and is derived from the difference in the van der Waals radii of a given substituent and a proton.^{53,54} Figure 3.6 shows the relationship between Γ_0 and ν . Several observations are clear from these data. First, as the steric size of the aliphatic groups increased, the measured Γ_0 decreased as was previously reported.⁹ Second, $[\text{Ru}(\text{btfmb})_2(\text{P})]/\text{TiO}_2$ yielded a smaller surfaces coverage than expected. Fluorinated alkyl groups have been reported to be larger than their non-fluorinated congener, behavior attributed to a large electronic repulsion of the electron clouds around the strongly electronegative F atoms.⁵⁵ It has also been noted that typical measures of steric size often underestimate the size

of these fluorinated groups.⁵⁵ Thus, the small Γ_0 value for $[\text{Ru}(\text{btfmb})_2(\text{P})]/\text{TiO}_2$ was not unexpected. Finally, the -Br substituents resulted in the largest surface coverages despite their atomic size relative to an H atom. Typically, Langmuir-type binding is used to describe surface functionalization of TiO_2 thin films which assumes that intermolecular interactions do not influence surface binding.¹³ In the case of the -Br, it may be that halogen bonding interactions between a halogen and a $-\text{PO}(\text{OH})_2$ on a neighboring compound may act as directing groups as the molecules approach the surface leading to more efficient packing and higher surface coverages.^{56,57}

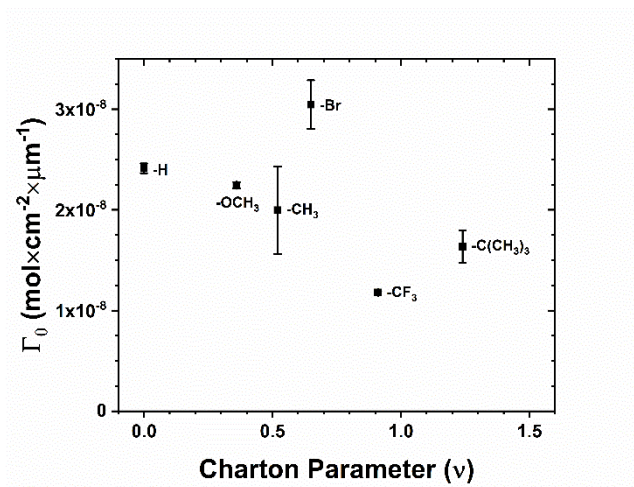


Figure 3.6. The dependence of the saturation surface coverage, Γ , with the steric size of the substituent in the 4 and 4' positions of $[\text{Ru}(\text{R}_2\text{bpy})_2(\text{P})]/\text{TiO}_2$ as given by the Charton value. Error bars are included for the measured Γ_0 .

As stated in the introduction, the intermolecular electronic coupling is expected to have an exponential dependence on intermolecular distance, eq 3.2. In the absence of measured H_{DA} values in these self-exchange reactions, the calculated first-order hopping rate constants were used to compare the differences in electronic coupling, eq 3.10, where $\Delta\delta$ is the difference between the calculated δ and the smallest δ for a given dataset, and these data are plotted in Figure 3.7. From Figure 3.7, it is immediately clear that the measured rates of lateral self-

exchange rate constants correlate well with the variation in intermolecular distance determined from the measured surface coverages. From the slope of the linear regression line, β was determined to be $1.2 \pm 0.2 \text{ \AA}^{-1}$ for self-exchange across the semiconductor surface. Note that this β value represents a lower limit based on the assumptions used to calculate δ .

$$k_R = e^{-\beta \Delta \delta_R} \quad (3.10)$$

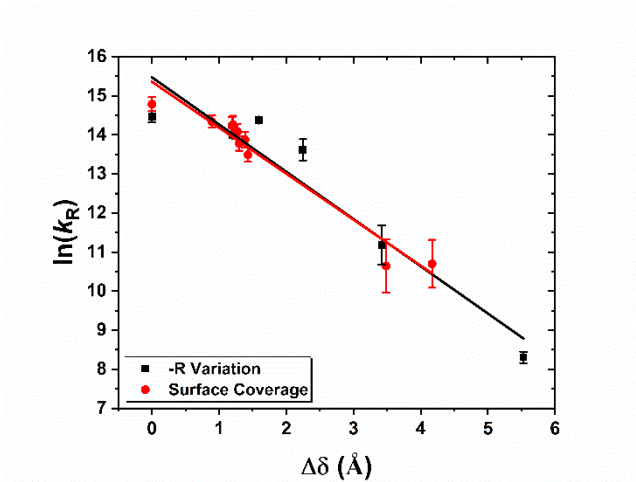


Figure 3.7. The $\text{Ru}^{\text{III/II}}$ lateral self-exchange electron transfer rate constant versus the difference intermolecular distance, $\Delta\delta$. The distance was varied by either (A, black ■) changing the steric size of the -R group at the 4 and 4' positions ($\beta = 1.2 \pm 0.2 \text{ \AA}^{-1}$) or (B, red ●) functionalizing the TiO_2 with $[\text{Ru}(\text{bpy})_2(\text{P})]^{2+}$ from dilute dye solutions ($\beta = 1.18 \pm 0.09 \text{ \AA}^{-1}$). Error bars are given for the $\ln(k_R)$.

The apparent diffusion coefficient was measured for $[\text{Ru}(\text{bpy})_2(\text{P})]/\text{TiO}_2$ at variable surface coverages, and the distance dependence examined as above. The β was found to be $1.18 \pm 0.09 \text{ \AA}^{-1}$ which was reasonably close to that obtained by changing the functional group. The similarity of the two measured β values coupled with the observed exponential dependence of the rate constant with δ strongly suggests that the variation in measured k_R between different functional groups represents a distance effect.

To our knowledge, these are the first reported β values for lateral self-exchange electron transfer between molecules anchored to the TiO_2 interface. Typical attenuation factors reported

for bimolecular electron transfer between compounds in frozen and fluid solvents range from 0.8 to 1.5 Å⁻¹.^{18,20,21,58-61} The only reported β value for electron transfer in acetonitrile was 0.95 Å⁻¹ for photoinduced, intermolecular electron transfer between Rhodamine 3B and *N,N*-dimethylaniline; however, the authors acknowledge a large error in this value.⁶⁰ Assuming that the above is correct, the β values reported here are somewhat higher. Additionally, it is unclear how the TiO₂ interface and the structure of the electrochemical double-layer would influence β . Nevertheless, the measured exponential dependence of electron transfer with the measured β value is consistent with electron superexchange tunneling in these systems.

3.5 Conclusions

A homologous series of 6 compounds of the type [Ru(R₂bpy)₂(P)]/TiO₂, where P is 2,2'-bipyridyl-4,4'-diphosphonic acid and R₂bpy is a 4,4'-substituted-2,2'-bipyridine, is reported and their lateral self-exchange electron transfer kinetics across the metal oxide surface were measured using chronoabsorptometry. The measured apparent diffusion coefficients ranged from 10⁻¹¹ to 10⁻⁹ cm²/s. The functional groups used were -OCH₃, -C(CH₃)₃, -CH₃, -H, -Br, and -CF₃ and were chosen to determine the influence of both the electron withdrawing/donating ability and steric size of each substituent on the measured rates. Through the use nonadiabatic Marcus theory, it was determined that the steric size of the functional group was the key factor that measurably influenced self-exchange rates with a measured attenuation factor, β , of 1.2 ± 0.2 Å⁻¹. Studies examining the distance dependence through varying surface coverages also yielded a β value of 1.18 ± 0.09 Å⁻¹. The results herein suggest steric size is a reliable synthetic tool to tune the self-exchange electron transfer rates across semiconductor interfaces.

3.6 Acknowledgements

This research is supported by the National Science Foundation (NSF) under Award CHE-1465060. T.C.M. would like to acknowledge the NSF Graduate Research Fellowship for support (Grant No. DGE-1144081).

3.7 Additional Content

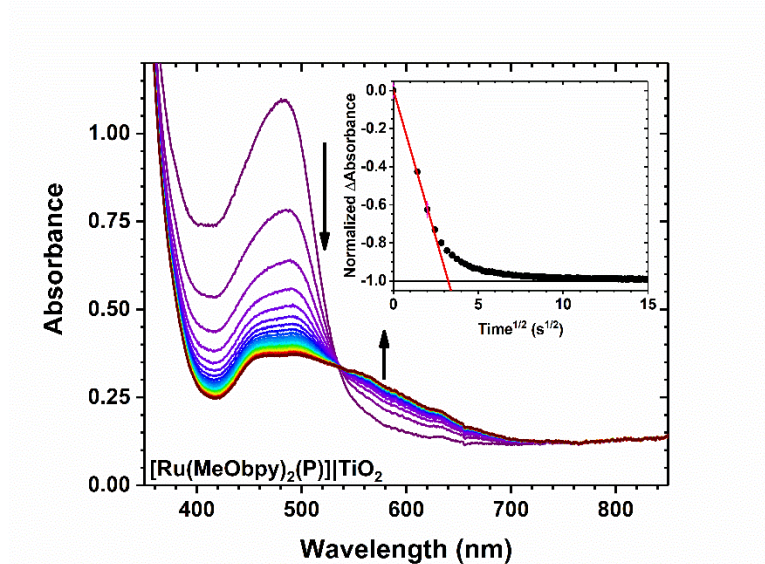


Figure 3.8. The UV-visible spectral changes after the application a potential sufficient to oxidize $[\text{Ru}(\text{MeObpy})_2(\text{P})]\text{TiO}_2$. A bleach of the characteristic MLCT transition was observed at 480 nm as the film was oxidized from Ru^{II} to Ru^{III} . A new peak associated with the Ru^{III} species was observed to grow in centered at 550 nm. The inset shows the normalized absorbance change plotted against the square root of time. The data were fit to the Anson equation through the first 60% of the total absorbance change (red line).

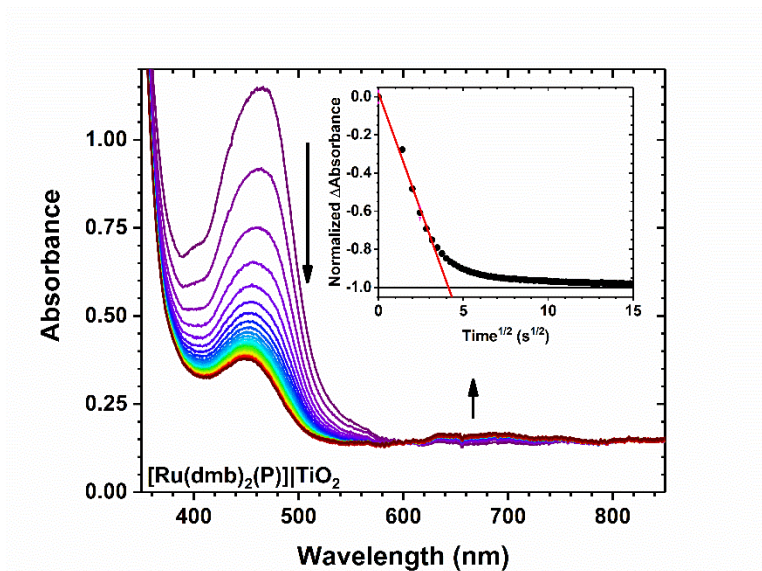


Figure 3.9. The UV-visible spectral changes after the application a potential sufficient to oxidize [Ru(dmb)₂(P)]/TiO₂. A bleach of the characteristic MLCT transition was observed at 465 nm as the film was oxidized from Ru^{II} to Ru^{III}. A new peak associated with the Ru^{III} species was observed to grow in centered at 675 nm. The inset shows the normalized absorbance change plotted against the square root of time. The data were fit to the Anson equation through the first 60% of the total absorbance change (red line).

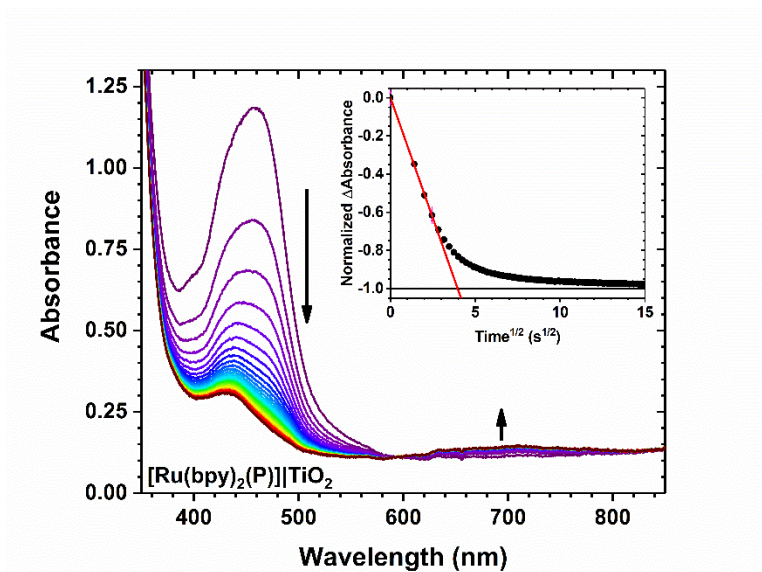


Figure 3.10. The UV-visible spectral changes after the application a potential sufficient to oxidize [Ru(bpy)₂(P)]/TiO₂. A bleach of the characteristic MLCT transition was observed at 455 nm as the film was oxidized from Ru^{II} to Ru^{III}. A new peak associated with the Ru^{III} species was observed to grow in centered at 700 nm. The inset shows the normalized absorbance change plotted against the square root of time. The data were fit to the Anson equation through the first 60% of the total absorbance change (red line).

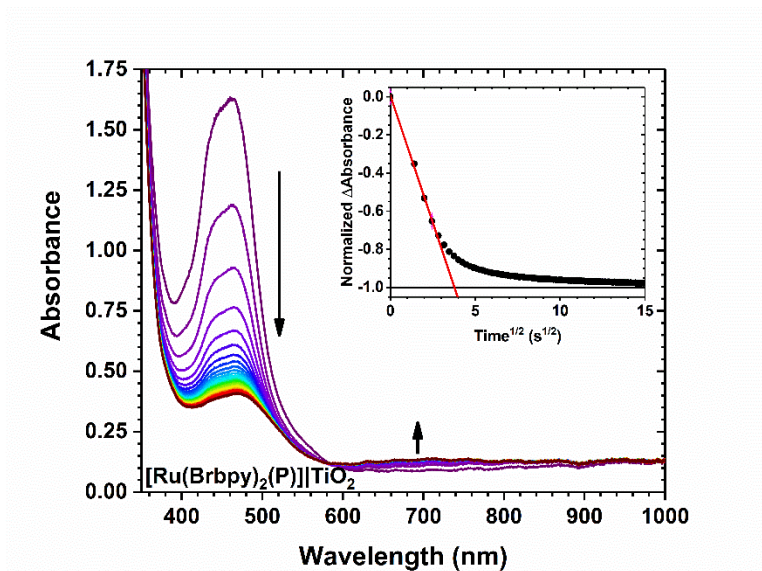


Figure 3.11. The UV-visible spectral changes after the application a potential sufficient to oxidize [Ru(Brbpy)₂(P)]/TiO₂. A bleach of the characteristic MLCT transition was observed at 465 nm as the film was oxidized from Ru^{II} to Ru^{III}. A new peak associated with the Ru^{III} species was observed to grow in centered at 700 nm. The inset shows the normalized absorbance change plotted against the square root of time. The data were fit to the Anson equation through the first 60% of the total absorbance change (red line).

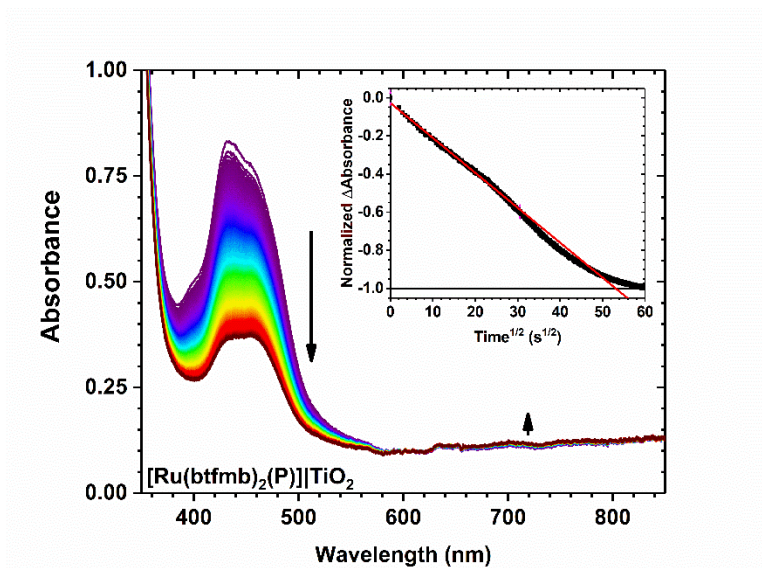


Figure 3.12. The UV-visible spectral changes after the application a potential sufficient to oxidize [Ru(btmb)₂(P)]/TiO₂. A bleach of the characteristic MLCT transition was observed at 440 nm as the film was oxidized from Ru^{II} to Ru^{III}. A new peak associated with the Ru^{III} species was observed to grow in centered at 740 nm. The inset shows the normalized absorbance change plotted against the square root of time. The data were fit to the Anson equation through the first 60% of the total absorbance change (red line).

REFERENCES

- (1) Moia, D.; Szumska, A.; Vaissier, V.; Planells, M.; Robertson, N.; O'Regan, B. C.; Nelson, J.; Barnes, P. R. F. Interdye Hole Transport Accelerates Recombination in Dye Sensitized Mesoporous Films. *J. Am. Chem. Soc.* **2016**, *138*, 13197-13206.
- (2) Sampaio, R. N.; DiMarco, B. N.; Meyer, G. J. Activation Energies for Electron Transfer from TiO₂ to Oxidized Dyes: A Surface Coverage Dependence Correlated with Lateral Hole Hopping. *ACS Energy Lett.* **2017**, *2*, 2402-2407.
- (3) Sampaio, R. N.; Müller, A. V.; Polo, A. S.; Meyer, G. J. Correlation between Charge Recombination and Lateral Hole-Hopping Kinetics in a Series of *cis*-Ru(phen')(dcb)(NCS)₂ Dye-Sensitized Solar Cells. *ACS Appl. Mater. Interfaces* **2017**, *9*, 33446-33454.
- (4) Moia, D.; Leijtens, T.; Noel, N.; Snaith, H. J.; Nelson, J.; Barnes, P. R. F. Dye Monolayers Used as the Hole Transporting Medium in Dye-Sensitized Solar Cells. *Adv. Mater.* **2015**, *27*, 5889-5894.
- (5) Moia, D.; Cappel, U. B.; Leijtens, T.; Li, X.; Telford, A. M.; Snaith, H. J.; O'Regan, B. C.; Nelson, J.; Barnes, P. R. F. The Role of Hole Transport between Dyes in Solid-State Dye-Sensitized Solar Cells. *J. Phys. Chem. C* **2015**, *119*, 18975-18985.
- (6) Swierk, J. R.; McCool, N. S.; Saunders, T. P.; Barber, G. D.; Mallouk, T. E. Effects of Electron Trapping and Protonation on the Efficiency of Water-Splitting Dye-Sensitized Solar Cells. *J. Am. Chem. Soc.* **2014**, *136*, 10974-10982.
- (7) Hu, K.; Sampaio, R. N.; Marquard, S. L.; Brennaman, M. K.; Tamaki, Y.; Meyer, T. J.; Meyer, G. J. A High-Valent Metal-Oxo Species Produced by Photoinduced One-Electron, Two-Proton Transfer Reactivity. *Inorg. Chem.* **2018**, *57*, 486-494.
- (8) Chen, H.-Y.; Ardo, S. Direct Observation of Sequential Oxidations of a Titania-Bound Molecular Proxy Catalyst Generated through Illumination of Molecular Sensitizers. *Nat. Chem.* **2017**, *10*, 17-23.
- (9) DiMarco, B. N.; Motley, T. C.; Balok, R. S.; Li, G.; Siegler, M. A.; O'Donnell, R. M.; Hu, K.; Meyer, G. J. A Distance Dependence to Lateral Self-Exchange across Nanocrystalline TiO₂. A Comparative Study of Three Homologous Ru^{III/II} Polypyridyl Compounds. *J. Phys. Chem. C* **2016**, *120*, 14226-14235.
- (10) Heimer, T. A.; D'Arcangelis, S. T.; Farzad, F.; Stipkala, J. M.; Meyer, G. J. An Acetylacetonate-Based Semiconductor-Sensitizer Linkage. *Inorg. Chem.* **1996**, *35*, 5319-5324.
- (11) Bonhôte, P.; Gogniat, E.; Tingry, S.; Barbé, C.; Vlachopoulos, N.; Lenzmann, F.; Comte, P.; Grätzel, M. Efficient Lateral Electron Transport inside a Monolayer of Aromatic Amines Anchored on Nanocrystalline Metal Oxide Films. *J. Phys. Chem. B* **1998**, *102*, 1498-1507.

- (12) Trammell, S. A.; Meyer, T. J. Diffusional Mediation of Surface Electron Transfer on TiO₂. *J. Phys. Chem. B* **1999**, *103*, 104-107.
- (13) Hu, K.; Meyer, G. J. Lateral Intermolecular Self-Exchange Reactions for Hole and Energy Transport on Mesoporous Metal Oxide Thin Films. *Langmuir* **2015**, *31*, 11164-11178.
- (14) Wang, Q.; Zakeeruddin, S. M.; Cremer, J.; Bäuerle, P.; Humphry-Baker, R.; Grätzel, M. Cross Surface Ambipolar Charge Percolation in Molecular Triads on Mesoscopic Oxide Films. *J. Am. Chem. Soc.* **2005**, *127*, 5706-5713.
- (15) Wang, Q.; Zakeeruddin, S. M.; Nazeeruddin, M. K.; Humphry-Baker, R.; Grätzel, M. Molecular Wiring of Nanocrystals: NCS-Enhanced Cross-Surface Charge Transfer in Self-Assembled Ru-Complex Monolayer on Mesoscopic Oxide Films. *J. Am. Chem. Soc.* **2006**, *128*, 4446-4452.
- (16) Moia, D.; Vaissier, V.; Lopez-Duarte, I.; Torres, T. S.; Nazeeruddin, M. K.; O'Regan, B. C.; Nelson, J.; Barnes, P. R. F. The Reorganization Energy of Intermolecular Hole Hopping between Dyes Anchored to Surfaces. *Chem. Sci.* **2014**, *5*, 281-290.
- (17) Hanson, K.; Brennaman, M. K.; Ito, A.; Luo, H.; Song, W.; Parker, K. A.; Ghosh, R.; Norris, M. R.; Glasson, C. R. K.; Concepcion, J. J.; Lopez, R.; Meyer, T. J. Structure–Property Relationships in Phosphonate-Derivatized, Ru^{II} Polypyridyl Dyes on Metal Oxide Surfaces in an Aqueous Environment. *J. Phys. Chem. C* **2012**, *116*, 14837-14847.
- (18) Marcus, R. A.; Sutin, N. Electron Transfers in Chemistry and Biology. *Biochim. Biophys. Acta, Bioenerg.* **1985**, *811*, 265-322.
- (19) Winkler, J. R.; Gray, H. B. Long-Range Electron Tunneling. *J. Am. Chem. Soc.* **2014**, *136*, 2930-2939.
- (20) Wenger, O. S.; Leigh, B. S.; Villahermosa, R. M.; Gray, H. B.; Winkler, J. R. Electron Tunneling through Organic Molecules in Frozen Glasses. *Science* **2005**, *307*, 99-102.
- (21) Edwards, P. P.; Gray, H. B.; Lodge, M. T. J.; Williams, R. J. P. Electron Transfer and Electronic Conduction through an Intervening Medium. *Angew. Chem. Int. Ed.* **2008**, *47*, 6758-6765.
- (22) Closs, G. L.; Miller, J. R. Intramolecular Long-Distance Electron Transfer in Organic Molecules. *Science* **1988**, *240*, 440-447.
- (23) Brown, G. M.; Sutin, N. A Comparison of the Rates of Electron Exchange Reactions of Ammine Complexes of Ruthenium(II) and -(III) with the Predictions of Adiabatic, Outer-Sphere Electron Transfer Models. *J. Am. Chem. Soc.* **1979**, *101*, 883-892.
- (24) Sutin, N. Theory of Electron Transfer Reactions: Insights and Hindsight. In *Prog. Inorg. Chem.*; John Wiley & Sons, Inc.: 2007; pp 441-498.

- (25) Skarda, V.; Cook, M. J.; Lewis, A. P.; McAuliffe, G. S. G.; Thomson, A. J.; Robbins, D. J. Luminescent Metal Complexes. Part 3. Electrochemical Potentials of Ground and Excited States of Ring-Substituted 2,2'-Bipyridyl and 1,10-Phenanthroline Tris-Complexes of Ruthenium. *J. Chem. Soc., Perk. Trans. 2* **1984**, 1309-1311.
- (26) Juris, A.; Balzani, V.; Barigelletti, F.; Campagna, S.; Belser, P.; von Zelewsky, A. Ru(II) Polypyridine Complexes: Photophysics, Photochemistry, Electrochemistry, and Chemiluminescence. *Coord. Chem. Rev.* **1988**, *84*, 85-277.
- (27) Al-Rawashdeh, N. A. F.; Chatterjee, S.; Krause, J. A.; Connick, W. B. Ruthenium Bis-Diimine Complexes with a Chelating Thioether Ligand: Delineating 1,10-Phenanthroline and 2,2'-Bipyridyl Ligand Substituent Effects. *Inorg. Chem.* **2014**, *53*, 294-307.
- (28) Nazeeruddin, M. K.; Zakeeruddin, S. M.; Kalyanasundaram, K. Enhanced Intensities of the Ligand-to-Metal Charge-Transfer Transitions in Ruthenium(III) and Osmium(III) Complexes of Substituted Bipyridines. *J. Phys. Chem.* **1993**, *97*, 9607-9612.
- (29) Ronca, E.; De Angelis, F.; Fantacci, S. Time-Dependent Density Functional Theory Modeling of Spin-Orbit Coupling in Ruthenium and Osmium Solar Cell Sensitizers. *J. Phys. Chem. C* **2014**, *118*, 17067-17078.
- (30) Mines, G. A.; Roberts, J. A.; Hupp, J. T. Electrochemical and Spectral Probes of Metal/Ligand Orbital Mixing in $\text{Ru}(\text{NH}_3)_4(\text{bpy})^{2+}$ and $\text{Ru}(\text{NH}_3)_4(\text{phen})^{2+}$. *Inorg. Chem.* **1992**, *31*, 125-128.
- (31) Goeltz, J. C.; Benson, E. E.; Kubiak, C. P. Electronic Structural Effects in Self-Exchange Reactions. *J. Phys. Chem. B* **2010**, *114*, 14729-14734.
- (32) Goeltz, J. C.; Hanson, C. J.; Kubiak, C. P. Rates of Electron Self-Exchange Reactions between Oxo-Centered Ruthenium Clusters Are Determined by Orbital Overlap. *Inorg. Chem.* **2009**, *48*, 4763-4767.
- (33) Maerker, G.; Case, F. H. The Synthesis of Some 4,4'-Disubstituted 2,2'-Bipyridines. *J. Am. Chem. Soc.* **1958**, *80*, 2745-2748.
- (34) Doi, T.; Nagamiya, H.; Kokubo, M.; Hirabayashi, K.; Takahashi, T. Synthesis of a Tetrabenzyl-Substituted 10-Membered Cyclic Diamide. *Tetrahedron* **2002**, *58*, 2957-2963.
- (35) Staats, H.; Eggers, F.; Haß, O.; Fahrenkrug, F.; Matthey, J.; Lüning, U.; Lützen, A. Towards Allosteric Receptors – Synthesis of Resorcinarene-Functionalized 2,2'-Bipyridines and Their Metal Complexes. *Eur. J. Org. Chem.* **2009**, *2009*, 4777-4792.
- (36) Norris, M. R.; Concepcion, J. J.; Glasson, C. R. K.; Fang, Z.; Lapidés, A. M.; Ashford, D. L.; Templeton, J. L.; Meyer, T. J. Synthesis of Phosphonic Acid Derivatized Bipyridine Ligands and Their Ruthenium Complexes. *Inorg. Chem.* **2013**, *52*, 12492-12501.

- (37) Ashford, D. L.; Brennaman, M. K.; Brown, R. J.; Keinan, S.; Concepcion, J. J.; Papanikolas, J. M.; Templeton, J. L.; Meyer, T. J. Varying the Electronic Structure of Surface-Bound Ruthenium(II) Polypyridyl Complexes. *Inorg. Chem.* **2015**, *54*, 460-469.
- (38) Brady, M. D.; Sampaio, R. N.; Wang, D.; Meyer, T. J.; Meyer, G. J. Dye-Sensitized Hydrobromic Acid Splitting for Hydrogen Solar Fuel Production. *J. Am. Chem. Soc.* **2017**, *139*, 15612-15615.
- (39) Troian-Gautier, L.; DiMarco, B. N.; Sampaio, R. N.; Marquard, S. L.; Meyer, G. J. Evidence That ΔS^\ddagger Controls Interfacial Electron Transfer Dynamics from Anatase TiO₂ to Molecular Acceptors. *J. Am. Chem. Soc.* **2018**, *140*, 3019-3029.
- (40) Bard, A. J.; Faulkner, L. R. *Electrochemical Methods : Fundamentals and Applications*. 2nd Edition ed.; Wiley: New York, 2001.
- (41) Boschloo, G.; Fitzmaurice, D. Spectroelectrochemical Investigation of Surface States in Nanostructured TiO₂ Electrodes. *J. Phys. Chem. B* **1999**, *103*, 2228-2231.
- (42) Hanson, K.; Losego, M. D.; Kalanyan, B.; Parsons, G. N.; Meyer, T. J. Stabilizing Small Molecules on Metal Oxide Surfaces Using Atomic Layer Deposition. *Nano Lett.* **2013**, *13*, 4802-4809.
- (43) Blauch, D. N.; Saveant, J. M. Dynamics of Electron Hopping in Assemblies of Redox Centers. Percolation and Diffusion. *J. Am. Chem. Soc.* **1992**, *114*, 3323-3332.
- (44) Blauch, D. N.; Saveant, J. M. Effects of Long-Range Electron Transfer on Charge Transport in Static Assemblies of Redox Centers. *J. Phys. Chem.* **1993**, *97*, 6444-6448.
- (45) Barbé, C. J.; Arendse, F.; Comte, P.; Jirousek, M.; Lenzmann, F.; Shklover, V.; Grätzel, M. Nanocrystalline Titanium Oxide Electrodes for Photovoltaic Applications. *J. Am. Ceram. Soc.* **1997**, *80*, 3157-3171.
- (46) Hansch, C.; Leo, A. *Substituent Constants for Correlation Analysis in Chemistry and Biology*. Wiley: New York, 1979.
- (47) Hansch, C.; Leo, A.; Taft, R. W. A Survey of Hammett Substituent Constants and Resonance and Field Parameters. *Chem. Rev.* **1991**, *91*, 165-195.
- (48) Farzad, F. Molecular Level Energy and Electron Transfer Processes at Nanocrystalline Titanium Dioxide Interfaces. Johns Hopkins University, 1999.
- (49) Ardo, S.; Meyer, G. J. Photodriven Heterogeneous Charge Transfer with Transition-Metal Compounds Anchored to TiO₂ Semiconductor Surfaces. *Chem. Soc. Rev.* **2009**, *38*, 115-164.
- (50) Ardo, S.; Meyer, G. J. Characterization of Photoinduced Self-Exchange Reactions at Molecule–Semiconductor Interfaces by Transient Polarization Spectroscopy: Lateral

- Intermolecular Energy and Hole Transfer across Sensitized TiO₂ Thin Films. *J. Am. Chem. Soc.* **2011**, *133*, 15384-15396.
- (51) Hu, K.; Robson, K. C.; Beauvilliers, E. E.; Schott, E.; Zarate, X.; Arratia-Perez, R.; Berlinguette, C. P.; Meyer, G. J. Intramolecular and Lateral Intermolecular Hole Transfer at the Sensitized TiO₂ Interface. *J. Am. Chem. Soc.* **2014**, *136*, 1034-46.
- (52) Anslyn, E. V.; Dougherty, D. A. *Modern Physical Organic Chemistry*. University Science: Sausalito, Calif., 2006.
- (53) Charton, M. Nature of the Ortho Effect. II. Composition of the Taft Steric Parameters. *J. Am. Chem. Soc.* **1969**, *91*, 615-618.
- (54) Charton, M. Steric Effects. I. Esterification and Acid-Catalyzed Hydrolysis of Esters. *J. Am. Chem. Soc.* **1975**, *97*, 1552-1556.
- (55) Timperley, C. M.; White, W. E. The Steric and Electronic Effects of Aliphatic Fluoroalkyl Groups. *J. Fluorine Chem.* **2003**, *123*, 65-70.
- (56) Gutzler, R.; Ivashenko, O.; Fu, C.; Brusso, J. L.; Rosei, F.; Perepichka, D. F. Halogen Bonds as Stabilizing Interactions in a Chiral Self-Assembled Molecular Monolayer. *Chem. Commun.* **2011**, *47*, 9453-9455.
- (57) Pierangelo, M.; Franck, M.; Tullio, P.; Giuseppe, R.; Giancarlo, T. Halogen Bonding in Supramolecular Chemistry. *Angew. Chem. Int. Ed.* **2008**, *47*, 6114-6127.
- (58) Kobori, Y.; Yago, T.; Akiyama, K.; Tero-Kubota, S.; Sato, H.; Hirata, F.; Norris, J. R. Superexchange Electron Tunneling Mediated by Solvent Molecules: Pulsed Electron Paramagnetic Resonance Study on Electronic Coupling in Solvent-Separated Radical Ion Pairs. *J. Phys. Chem. B* **2004**, *108*, 10226-10240.
- (59) Murata, S.; Matsuzaki, S. Y.; Tachiya, M. Transient Effect in Fluorescence Quenching by Electron Transfer. 2. Determination of the Rate Parameters Involved in the Marcus Equation. *J. Phys. Chem.* **1995**, *99*, 5354-5358.
- (60) Tavernier, H. L.; Kalashnikov, M. M.; Fayer, M. D. Photoinduced Intermolecular Electron Transfer in Complex Liquids: Experiment and Theory. *J. Chem. Phys.* **2000**, *113*, 10191-10201.
- (61) Miller, J. R.; Beitz, J. V.; Huddleston, R. K. Effect of Free Energy on Rates of Electron Transfer between Molecules. *J. Am. Chem. Soc.* **1984**, *106*, 5057-5068.

CHAPTER 4: Intramolecular Electronic Coupling Enhances Lateral Electron Transfer across Semiconductor Interfaces³

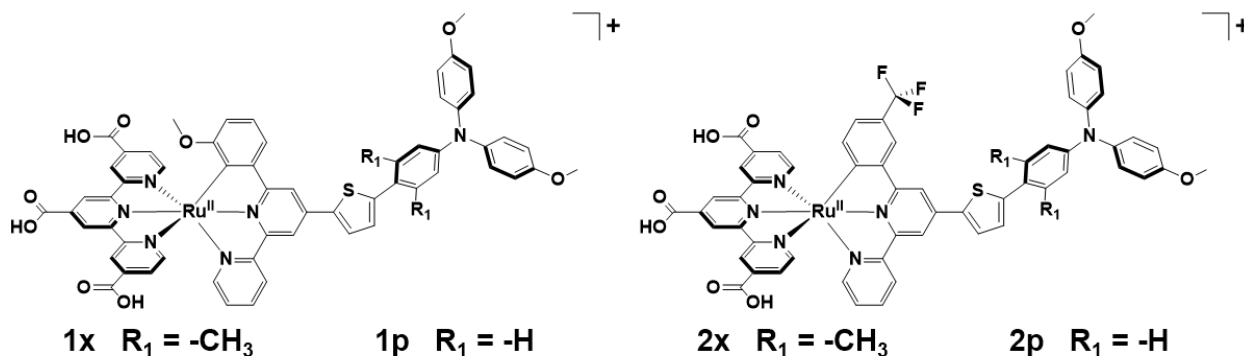
4.1 Introduction

Electron transfer and transport are important processes with applications in solar energy conversion and storage. Lateral *intermolecular* electron-transfer reactions, commonly referred to as hole-hopping, between redox active compounds anchored to TiO₂ surfaces has been utilized to activate water oxidation catalysts and has also been shown to enhance unwanted charge recombination reactions.¹⁻⁸ As such, it is desirable to control electron transfer so as to optimize solar cell performance. Previous research has shown that *intermolecular* electron transfer across metal oxide surfaces is sensitive to the steric bulk around the redox site and to the physical location of the highest-occupied molecular orbital.⁹⁻¹⁵ Most of these studies have focused on molecules with a single redox center. Here, *intermolecular* electron transfer was quantified with compounds that have two redox active groups. The primary questions of this study were as follows: *Does the presence of two redox active groups influence lateral electron transfer?* Might rapid electron-transfer dynamics of TPA⁺⁰ self-exchange electron transfer be leveraged to enhance those of Ru^{III/II}? The data reported herein provided compelling evidence that *intramolecular* electronic coupling between the two redox groups significantly influenced,

³This chapter was previously published in the *Journal of Physical Chemistry C*. Reprinted with permission from Motley, T. C.; Meyer, G. J. Intramolecular Electronic Coupling Enhances Lateral Electron Transfer across Semiconductor Interfaces. *J. Phys. Chem. C* **2018**, *122*, 14420-14424. Copyright 2018 American Chemical Society.

and in certain cases, enhanced, $\text{Ru}^{\text{III/II}}$ electron-transfer dynamics.

Scheme 4.1. Structure of the Compounds used in this Study



The compounds utilized possessed a bis(tridentate) cyclometalated Ru^{II} metal center linked to a substituted-triphenylamine donor (TPA) through an aromatic bridge, Scheme 4.1, and have been studied elsewhere for their *intramolecular* electron-transfer properties.¹⁶⁻¹⁸ These compounds allowed two interesting comparisons to be made. First, the electronic coupling between the $\text{Ru}^{\text{III/II}}$ and $\text{TPA}^{+/0}$ was tuned through the choice of the aromatic bridge. The methyl groups on the *xylyl* (**x**) bridge decreased the planarity with the thiophene and enforced weak electronic coupling ($H_{\text{DA}} < 100 \text{ cm}^{-1}$) while the *phenyl* (**p**) bridge enabled strong electronic coupling ($H_{\text{DA}} > 1000 \text{ cm}^{-1}$). Second, the order in which the redox active centers were oxidized was tuned with electron donating ($-\text{OCH}_3$) or withdrawing ($-\text{CF}_3$) substituents on the cyclometalating ring such that the Ru^{II} was oxidized before (**1**) or after (**2**) the TPA whose reduction potential was held at parity. The formal reduction potentials, E° , are given in Table 4.1. The combination of H_{DA} and ΔE° between the $\text{Ru}^{\text{III/II}}$ and $\text{TPA}^{0/+}$ tuned the equilibrium for the location of the electron in the single-oxidized molecule. The equilibrium constant, K_{eq} , favors the left for **1x** and **1p** and the right for **2x** and **2p** but is close to unity in all cases.



Table 4.1. Relevant Thermodynamic and Electron-Transfer Dynamics

Compound	$E^\circ(\text{Ru}^{\text{III/II}})^a$ (V vs NHE)	$E^\circ(\text{TPA}^{+/0})^a$ (V vs NHE)	t_{exp} (s)	D_{Ru}^b ($10^{-8} \text{ cm}^2/\text{s}$)	D_{TPA}^c ($10^{-8} \text{ cm}^2/\text{s}$)
1x	0.87	0.96	18.4	4.6 ± 0.7	3.1 ± 0.5
1p	0.87	0.96	8.3	4.5 ± 0.8	3.9 ± 0.7
2x	1.03	0.94	>100	0.49 ± 0.07	2.6 ± 0.4
2p	1.06	0.94	22.6	2.1 ± 0.4^d	4.6 ± 0.8

^aValues taken from Ref 17. ^bExtracted from the best fit to the Anson equation at 525 nm.

^cExtracted from the best fit to the Anson equation at 750 nm. ^dFits starting after the initial “induction” period ($t^{1/2} > 1.25 \text{ s}^{1/2}$) yielded a $D_{\text{Ru}} = 4.5 (\pm 0.7) \times 10^{-8} \text{ cm}^2/\text{s}$.

4.2 Experimental Methods

4.2.1 General Information

All compounds used were synthesized as preciously described.¹⁷ Lithium perchlorate (LiClO_4 , Sigma-Aldrich, 99.99%), oxygen (O_2 , Airgas, $\geq 99.998\%$), and acetonitrile (CH_3CN , Burdick & Jackson, spectrophotometric grade) were used without further purification from the indicated supplier.

4.2.2 Preparation of TiO_2 Thin Films

Titanium nanocrystallites were prepared via a sol-gel method.¹⁹ Mesoporous thin films were prepared via a doctor-blade method on ethanol-cleaned, fluorine-doped tin(IV) oxide (FTO, Hartford Glass Co, Inc., 2.3 mm thick, $15 \Omega/\square$) and allowed to dry in air for in air for 30 min. After drying, the films were sintered under an O_2 atmosphere ($\sim 1 \text{ atm}$) for 30 min and slowly cooled. The films were stored in a 70°C oven until used. Film thicknesses were measured to be $4.1 \pm 0.4 \mu\text{m}$ using a Bruker Dektak XT profilometer and the Vision 64 software.

The TiO_2 films were sensitized with the desired compound using concentrated CH_3CN dying solutions. Films were submerged for a minimum of 48 h to ensure that saturation surface

coverages were achieved. Surface coverages were determined at the lowest energy MLCT maximum using eq 4.2, where Γ is the surface coverage, ε is the molar extinction coefficient and 1000 is a conversion factor (L to cm³).¹¹ The measured Γ were between 7.0-9.5×10⁻⁸ mol/cm².

$$A = 1000 \times \Gamma \times \varepsilon \quad (4.2)$$

4.2.3 Electrochemistry

Chronoabsorptometry was performed using a WaveNow potentiostat (Pine Research Instrumentation, Inc.) coupled to an AvaSpec UL2048 UV-Visible spectrometer and an AvaLight Deuterium/Halogen light source (Avantes) all controlled by the AfterMath software. A three-electrode arrangement was used with a sensitized TiO₂ film on FTO as the working electrode and a Pt mesh counter electrode. A nonaqueous Ag/AgCl pseudoreference electrode (Pine Research Instrumentation, Inc.) filled with 0.1 M LiClO₄ in CH₃CN was used, and potentials applied relative to the E° of the compound. Full film oxidation was achieved by applying a potential of $E^\circ + 300$ mV, where E° was the most positive of the two E° for a given compound. Full spectra were acquired every 0.116 s during the oxidation process.

4.2.4 Data Analysis

Data fitting was performed in OriginPro 2016, with least-squares error minimization achieved using the Levenberg-Marquardt method.

4.3 Results and Discussion

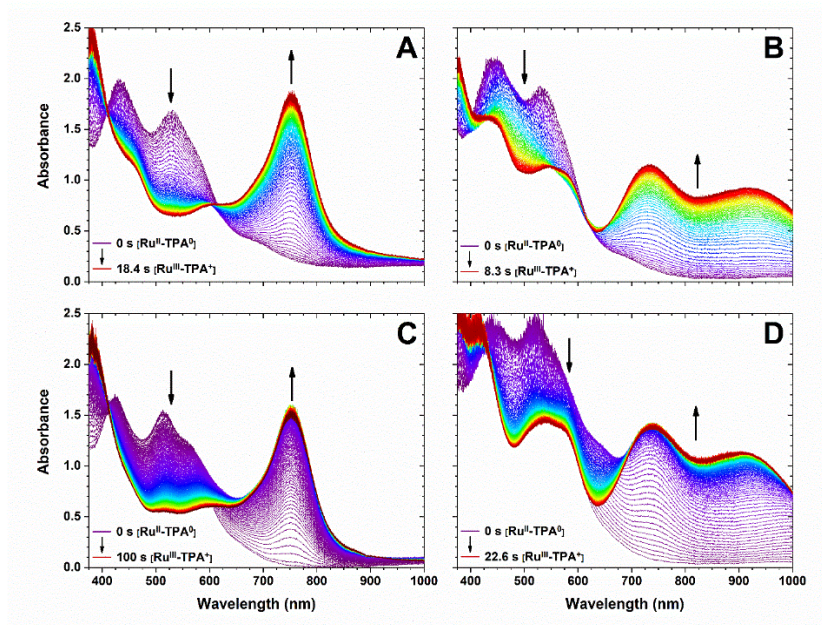
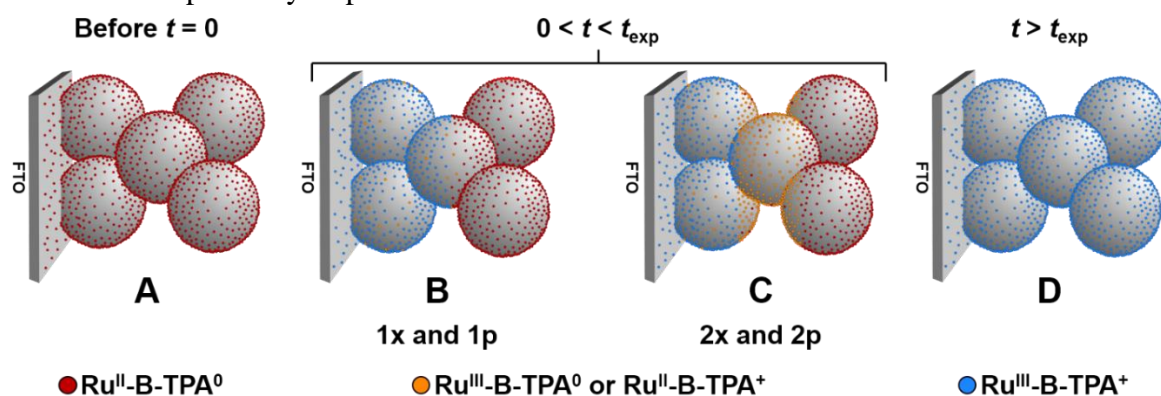


Figure 4.1. The UV-visible absorption spectra for (A) **1x**, (B) **1p**, (C) **2x**, and (D) **2p** obtained after a potential step at time zero initiated the oxidation of the indicated compounds anchored to TiO₂ thin films immersed in a 0.1 M LiClO₄ solution in CH₃CN. The absorption decrease in the 400-600 nm region reported primarily on the Ru^{II} oxidation while the growth in the 650-800 nm region reported primarily on the TPA⁰ oxidation.

Mesoporous, nanocrystalline TiO₂ thin films were dyed to comparable, saturation surface coverages with either **1x**, **1p**, **2x**, or **2p** from concentrated CH₃CN dyeing solutions. All four compounds displayed absorption bands between 400 and 600 nm that have been assigned to metal-to-ligand charge transfer bands associated with the Ru^{II} metal center, Figure 4.1.^{16,20,21} Chronoabsorptometry was used to measure the apparent diffusion coefficients, D , for electron transfer as was previously reported.^{2,10-15} Provided that the surface coverage exceeded the percolation threshold, all the redox centers in the thin film could be oxidized upon the application of a potential step suitable to oxidize both redox active groups, typically 300-500 mV past the most positive reduction potential, Scheme 4.2.^{10,19,22,23} Figure 4.1 shows that after such a potential step, a decrease of the visible absorption bands was observed, indicative of

oxidation of Ru^{II} to Ru^{III} , and a new absorption band appeared between 650 and 850 nm due to the oxidation of TPA^0 to TPA^+ . A brief examination of this data shows that the total experimental time, t_{exp} , necessary to completely oxidize the film was at least 2 times longer for **1x** over **1p** and 5 times longer for **2x** over **2p**. Hence, regardless of which redox center was oxidized first the *phenyl*-bridged compounds were oxidized more quickly than were the *xylyl*-bridged compounds. The precise time evolution of these spectral features provided quantitative information on the electron-transfer dynamics.

Scheme 4.2. An Idealized Representation of the Evolution of the Sensitized TiO_2 Films during a Chornoabsorptometry Experiment^a



^a(A) Before $t = 0$, all of the compounds on the surface are in the $\text{Ru}^{\text{II}}\text{-B-TPA}^0$ oxidation state. At $t = 0$, a potential is applied that is 500 mV past the most positive reduction potential of the two redox sites. Film oxidation is initiated at the FTO interface, and one (B) or two (C) “oxidation” fronts move away from the FTO substrate. (D) At times longer than t_{exp} , all of the molecules at the interface are completely oxidized.

The kinetic data were fit to the Anson equation, eq 4.3, where ΔA is the normalized absorbance change at time t , and d is the thickness of the TiO_2 film. It has been well-established that the oxidation is initiated at the transparent conductive oxide that supports the mesoporous thin film, and as time evolves, an “oxidation front” extends out through the film, Scheme 4.2B and 4.2C.^{10,11,19,23} As this front reaches the edges of the film, the available lateral electron-transfer pathways decrease, and the semi-infinite diffusion boundary conditions used to derive

eq 4.3 fail. Thus, only the first 60% of the total absorbance change was fit.¹⁰ The apparent diffusion coefficients of the individual redox sites were quantified by monitoring the absorption changes at 525 nm and 750 nm for the Ru^{III/II} and TPA^{0/+}, respectively. The data were also fit at wavelengths that correspond to isosbestic points that reported solely on Ru^{III/II} or TPA⁺⁰ oxidation and yielded, within error, the same apparent diffusion coefficients.¹⁸

$$\Delta A = \frac{2\sqrt{D}}{d\sqrt{\pi}} \sqrt{t} \quad (4.3)$$

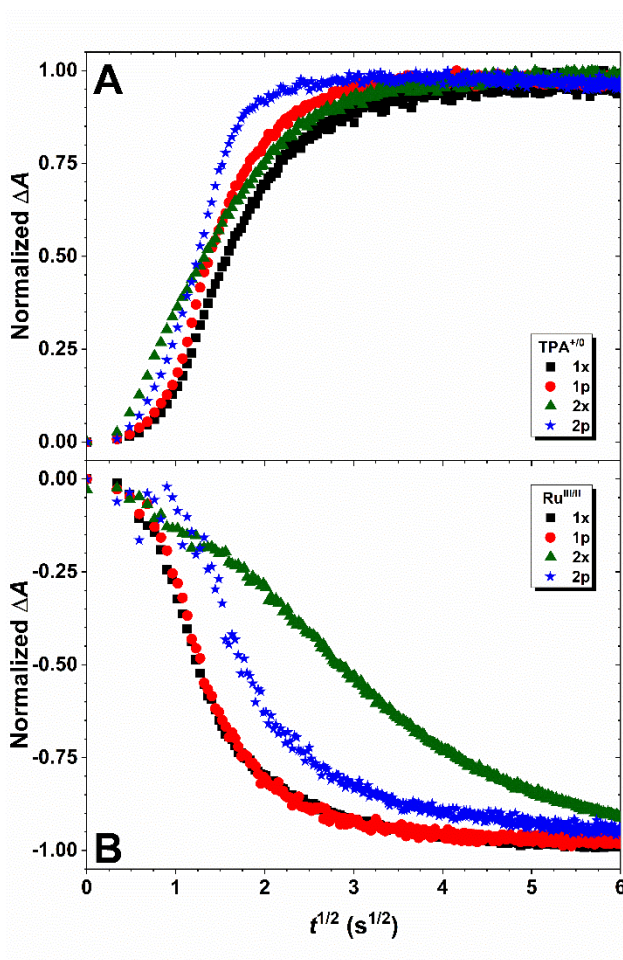


Figure 4.2. The normalized change in absorbance as a function of the square root of time measured after the application of a potential sufficient to oxidize both the TPA⁰ to TPA⁺ (A) and Ru^{II} to Ru^{III} (B).

Figure 4.2 shows the single-wavelength kinetic data. Plots of the individual kinetic data for each compound as well as the fits to the Anson equation are given in Figures 4.3 and 4.4 in

the 4.6 Additional Content section. The extracted D_{Ru} and D_{TPA} values are listed in Table 4.1. All of the measured D_{TPA} values fell between $3.1\text{--}4.6\times 10^{-8}$ cm²/s, about an order of magnitude smaller than what has been reported for self-exchange electron-transfer for surface-bound TPA films, $D_{\text{TPA}} = 10^{-7}$ cm²/s.¹⁰ Additionally, **1x**, **1p**, and **2p** possessed D_{Ru} values between $2.1\text{--}4.6\times 10^{-8}$ cm²/s. Previous reports of self-exchange electron transfer kinetics for Ru^{II} polypyridyl compounds anchored to metal oxides report $D_{\text{Ru}} = 10^{-9}$ cm²/s,^{12,13,24,25} which was comparable with the measured Ru^{III/II} apparent diffusion coefficient measured for **2x**. From these measured values, three interesting observations were readily apparent.

First, the measured D_{TPA} values were larger for the *phenyl*-bridged compounds relative to those with the *xylyl*-bridge. Previously published DFT calculations have shown that the *phenyl*-bridge facilitates delocalization of the TPA-centered orbitals across the thiophene bridge and the cyclometalating terpyridine moieties.^{16,17,20,21} Diffuse orbitals and favorable spatial arrangement of the frontier orbitals have been attributed to the rapid self-exchange rates observed with Ru(LL)(dcb)(NCS)₂ anchored to metal oxide surfaces, where dcb was a 2,2'-bipyridyl-4,4'-dicarboxylic acid and LL was either a second dcb (N3) or 4,4'-dimethyl-2,2'-bipyridine (dmb).¹⁴ In these compounds, the Ru-based $d\pi$ orbitals were significantly delocalized onto the NCS⁻ groups. Gratzel and coworkers found that lateral self-exchange electron transfer was dramatically faster for dmb, behavior that was attributed to more effective *intermolecular* coupling between the *cis*-Ru(NCS)₂ redox centers relative to N3. More diffuse orbitals plus rotational mobility about the *phenyl*-bridge for the compounds reported here should enhance orbital overlap between neighboring TPA groups resulting in larger diffusion coefficients relative to the *xylyl*-bridged compounds.

Second, the measured $\text{Ru}^{\text{III/II}}$ diffusion coefficients were *insensitive* to the identity of the bridge in **1x** and **1p** and proceeded with diffusion coefficients that were comparable to $\text{TPA}^{+/0}$. Based on the previously reported diffusion coefficients; however, one might anticipate that after the potential step the $\text{TPA}^{+/0}$ oxidation front would move more rapidly than would the $\text{Ru}^{\text{III/II}}$ front (Scheme 4.2C). Assuming the inherent diffusion coefficients are similar to those previously reported, $D_{\text{TPA}} > D_{\text{Ru}}$, the kinetic product for *intermolecular* electron transfer would be $\text{Ru}^{\text{II}}\text{-B-TPA}^+$ for **1x** and **1p**. However, as $\text{Ru}^{\text{III}}\text{-B-TPA}^0$ is thermodynamically favored ($E^\circ_{\text{TPA}} > E^\circ_{\text{Ru}}$), rapid *intramolecular* electron transfer from Ru^{II} to TPA^+ would provide an alternative, kinetically faster mechanism for Ru^{II} oxidation compared to lateral self-exchange alone. This would serve to enhance the $\text{Ru}^{\text{III/II}}$ diffusion coefficients measured in **1x** and **1p** compared to previous reports and likely explains why the $\text{TPA}^{+/0}$ and $\text{Ru}^{\text{III/II}}$ oxidation fronts move together (Scheme 4.2B). It is important to note that the comproportionation of neighboring $\text{Ru}^{\text{III}}\text{-B-TPA}^+$ and $\text{Ru}^{\text{II}}\text{-B-TPA}^0$, if formed, may also move electrons through the film, and would enhance the $\text{Ru}^{\text{III/II}}$ oxidation kinetics similarly.

Finally, in contrast to **1x** and **1p**, the $\text{Ru}^{\text{III/II}}$ diffusion coefficients abstracted for **2x** were a factor of 5 *smaller* than for **2p** and both were smaller than those for $\text{TPA}^{+/0}$. For these compounds, TPA^0 is thermodynamically oxidized first and the *intramolecular* equilibrium favors $\text{Ru}^{\text{II}}\text{-B-TPA}^+$ ($E^\circ_{\text{TPA}} < E^\circ_{\text{Ru}}$). Based on the previously reported diffusion coefficients for Ru or TPA only films, the expected differences in the diffusion coefficients should be readily observed as the two oxidation fronts would move separately through the film (Scheme 4.2C). This was clearly observed in the case of **2x**, Figure 4.1 and Figure 4.2 green triangles where the TPA^+ absorption growth saturates well before the Ru^{II} absorption loss.

A closer examination of the Ru^{III/II} oxidation for **2p** in Figure 4.2B provided an interesting insight. At early times, Ru^{III/II} oxidation for **2x** and **2p** proceeded at the same rate; however, once the TPA⁺⁰ oxidation neared completion ($t^{1/2} \approx 1.25 \text{ s}^{1/2}$), the Ru^{III/II} diffusion coefficient in **2p** increased significantly. Fits to the Anson equation after this initial “induction” period yielded a diffusion coefficient of $4.5 \times 10^{-8} \text{ cm}^2/\text{s}$ which was the same as those measured in **1p** and **1x** for Ru^{III/II} oxidation. This change in the measured diffusion coefficient could be attributed to a change in the electron-transfer mechanism in the molecule. Before the TPA⁺⁰ oxidation was complete, the Ru^{III/II} electron diffusion occurred predominantly through self-exchange electron transfer. As TPA⁰ oxidation neared completion, the *intramolecular* electron-transfer mechanism began to dominate and the TPA^{0/+} mediated Ru^{II} oxidation. In the absence of significant *intramolecular* electronic coupling (**2x**), the two redox sites were only oxidized by self-exchange electron transfer. The *intramolecular* mechanism is feasible in the case of **2p** as the H_{DA} is larger than in **2x**. In a separate report, Grätzel *et al.* utilized Ru(LL)(dcb)(NCS)₂, where LL was either 4,4-bis(tridecyl)-2,2'-bipyridine (N621) or 4,4'-bis[(*E*)-2-(4-diphenylamino)phenyl)ethenyl]-2,2'-bipyridine (HW456) to demonstrate that TPA moieties, when oxidized second in a coupled system, enhanced the measured diffusion coefficients of the Ru^{III/II} moiety, which supports the observations here.¹⁵ In their system, strong electronic coupling facilitated through a conjugated linker between Ru^{II} and TPA⁰ would be expected and therefore the more rapid Ru^{III/II} diffusion coefficients measured in HW456 compared to N621 fall in line with our observations here.

4.4 Conclusion

In conclusion, lateral *intermolecular* electron transfer at metal oxide interfaces was investigated with molecules that have two redox active groups linked together with a *xyx*-

bridge or a *phenyl*-bridge. The phenyl-bridged compounds promoted more rapid *intermolecular* electron transfer between the TPA moieties, behavior attributed to more diffuse frontier orbitals that enhance *intermolecular* electronic coupling. In addition, the rapid $\text{TPA}^{+/0}$ self-exchange previously reported in the literature was exploited to enhance $\text{Ru}^{\text{III/II}}$ oxidation kinetics under conditions where $\text{Ru}^{\text{II}}\text{-B-TPA}^+ \rightarrow \text{Ru}^{\text{III}}\text{-B-TPA}^0$ was thermodynamically favored (**1x** and **1p**) or in cases where the *intramolecular* electronic coupling was large (**1p** and **2p**). The use of molecules with multiple redox active groups has therefore provided new insights into lateral electron-transfer reactivity and provides a promising strategy to control electron transport across oxide surfaces for applications in solar energy conversion.

4.5 Acknowledgements

This research is supported by the National Science Foundation (NSF) under Award CHE-1465060. T.C.M. would like to acknowledge the NSF Graduate Research Fellowship for support (Grant No. DGE-1144081).

4.6 Additional Content

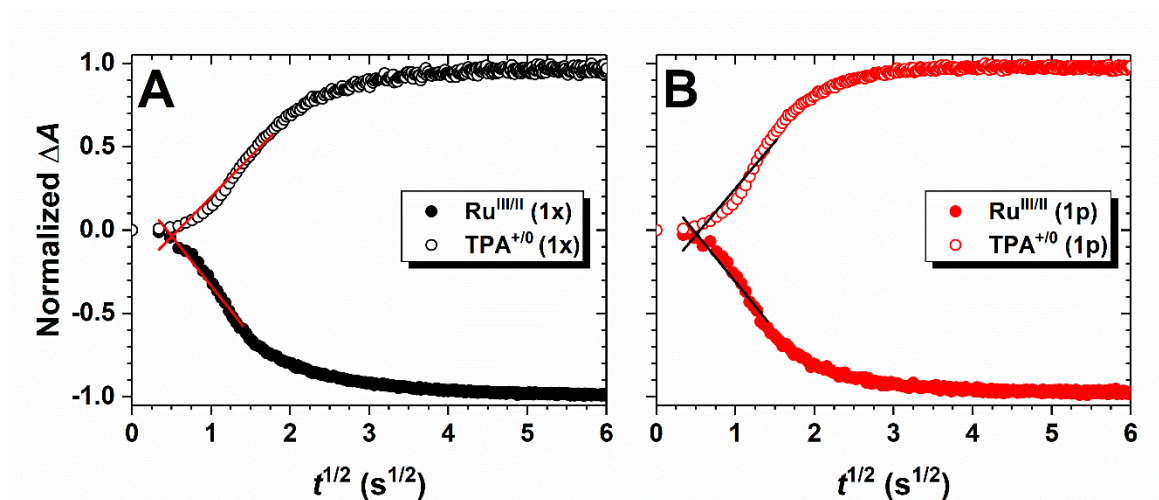


Figure 4.3. The normalized change in absorbance plotted against the square root of time for **1x** (A) and **1p** (B) monitored at 525 nm ($\text{Ru}^{\text{III/II}}$) and 750 nm ($\text{TPA}^{+/0}$). Overlaid are the lines of best fit to the Anson equation for each set of kinetic data through the initial 60% of the total change.

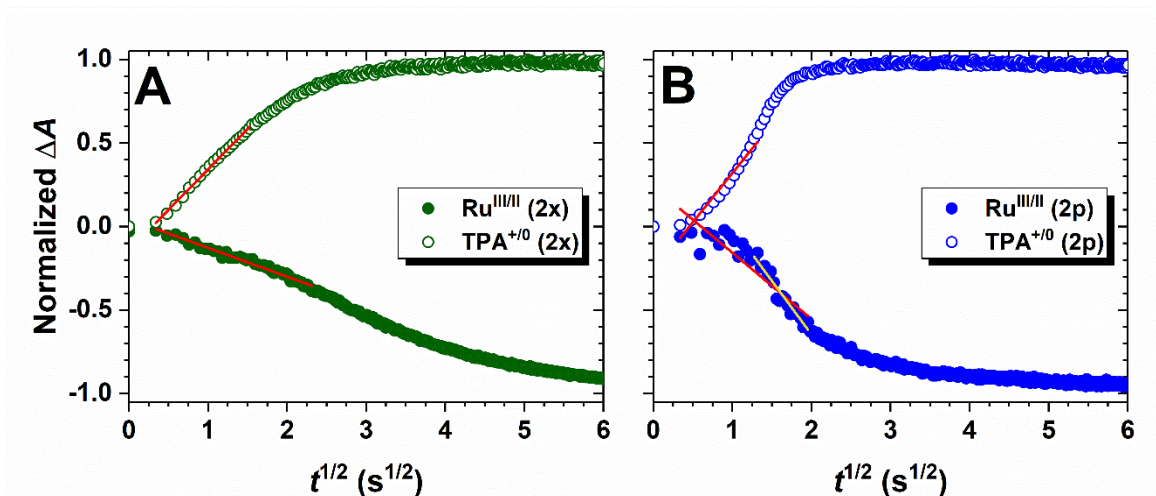


Figure 4.4. The normalized change in absorbance plotted against the square root of time for **2x** (A) and **2p** (B) monitored at 525 nm ($\text{Ru}^{\text{III/II}}$) and 750 nm ($\text{TPA}^{+/0}$). Overlaid are the lines of best fit to the Anson equation for each set of kinetic data through the initial 60% of the total change. For **2p**, the $\text{Ru}^{\text{III/II}}$ oxidation kinetics were also fit after the “induction” period ($t^{1/2} > 1.25 \text{ s}^{1/2}$) and is overlaid (gold line) on the data.

REFERENCES

- (1) Sampaio, R. N.; DiMarco, B. N.; Meyer, G. J. Activation Energies for Electron Transfer from TiO₂ to Oxidized Dyes: A Surface Coverage Dependence Correlated with Lateral Hole Hopping. *ACS Energy Lett.* **2017**, *2*, 2402-2407.
- (2) Sampaio, R. N.; Müller, A. V.; Polo, A. S.; Meyer, G. J. Correlation between Charge Recombination and Lateral Hole-Hopping Kinetics in a Series of *cis*-Ru(phen')(dcb)(NCS)₂ Dye-Sensitized Solar Cells. *ACS Appl. Mater. Interfaces* **2017**, *9*, 33446-33454.
- (3) Ashford, D. L.; Gish, M. K.; Vannucci, A. K.; Brennaman, M. K.; Templeton, J. L.; Papanikolas, J. M.; Meyer, T. J. Molecular Chromophore–Catalyst Assemblies for Solar Fuel Applications. *Chem. Rev.* **2015**, *115*, 13006-13049.
- (4) Brennan, B. J.; Durrell, A. C.; Koepf, M.; Crabtree, R. H.; Brudvig, G. W. Towards Multielectron Photocatalysis: A Porphyrin Array for Lateral Hole Transfer and Capture on a Metal Oxide Surface. *Phys. Chem. Chem. Phys.* **2015**, *17*, 12728-12734.
- (5) Moia, D.; Cappel, U. B.; Leijtens, T.; Li, X.; Telford, A. M.; Snaith, H. J.; O'Regan, B. C.; Nelson, J.; Barnes, P. R. F. The Role of Hole Transport between Dyes in Solid-State Dye-Sensitized Solar Cells. *J. Phys. Chem. C* **2015**, *119*, 18975-18985.
- (6) Moia, D.; Szumska, A.; Vaissier, V.; Planells, M.; Robertson, N.; O'Regan, B. C.; Nelson, J.; Barnes, P. R. F. Interdyer Hole Transport Accelerates Recombination in Dye Sensitized Mesoporous Films. *J. Am. Chem. Soc.* **2016**, *138*, 13197-13206.
- (7) Chen, H.-Y.; Ardo, S. Direct Observation of Sequential Oxidations of a Titania-Bound Molecular Proxy Catalyst Generated through Illumination of Molecular Sensitizers. *Nat. Chem.* **2017**, *10*, 17-23.
- (8) Brennan, B. J.; Regan, K. P.; Durrell, A. C.; Schmittenmaer, C. A.; Brudvig, G. W. Solvent Dependence of Lateral Charge Transfer in a Porphyrin Monolayer. *ACS Energy Lett.* **2017**, *2*, 168-173.
- (9) Moia, D.; Vaissier, V.; Lopez-Duarte, I.; Torres, T. S.; Nazeeruddin, M. K.; O'Regan, B. C.; Nelson, J.; Barnes, P. R. F. The Reorganization Energy of Intermolecular Hole Hopping between Dyes Anchored to Surfaces. *Chem. Sci.* **2014**, *5*, 281-290.
- (10) Bonhôte, P.; Gogniat, E.; Tingry, S.; Barbé, C.; Vlachopoulos, N.; Lenzmann, F.; Comte, P.; Grätzel, M. Efficient Lateral Electron Transport inside a Monolayer of Aromatic Amines Anchored on Nanocrystalline Metal Oxide Films. *J. Phys. Chem. B* **1998**, *102*, 1498-1507.
- (11) Trammell, S. A.; Meyer, T. J. Diffusional Mediation of Surface Electron Transfer on TiO₂. *J. Phys. Chem. B* **1999**, *103*, 104-107.

- (12) Hu, K.; Meyer, G. J. Lateral Intermolecular Self-Exchange Reactions for Hole and Energy Transport on Mesoporous Metal Oxide Thin Films. *Langmuir* **2015**, *31*, 11164-11178.
- (13) DiMarco, B. N.; Motley, T. C.; Balok, R. S.; Li, G.; Siegler, M. A.; O'Donnell, R. M.; Hu, K.; Meyer, G. J. A Distance Dependence to Lateral Self-Exchange across Nanocrystalline TiO₂. A Comparative Study of Three Homologous Ru^{III/II} Polypyridyl Compounds. *J. Phys. Chem. C* **2016**, *120*, 14226-14235.
- (14) Wang, Q.; Zakeeruddin, S. M.; Nazeeruddin, M. K.; Humphry-Baker, R.; Grätzel, M. Molecular Wiring of Nanocrystals: NCS-Enhanced Cross-Surface Charge Transfer in Self-Assembled Ru-Complex Monolayer on Mesoscopic Oxide Films. *J. Am. Chem. Soc.* **2006**, *128*, 4446-4452.
- (15) Li, X.; Nazeeruddin, M. K.; Thelakkat, M.; Barnes, P. R. F.; Vilar, R. N.; Durrant, J. R. Spectroelectrochemical Studies of Hole Percolation on Functionalised Nanocrystalline TiO₂ Films: A Comparison of Two Different Ruthenium Complexes. *Phys. Chem. Chem. Phys.* **2011**, *13*, 1575-1584.
- (16) Hu, K.; Robson, K. C.; Beauvilliers, E. E.; Schott, E.; Zarate, X.; Arratia-Perez, R.; Berlinguette, C. P.; Meyer, G. J. Intramolecular and Lateral Intermolecular Hole Transfer at the Sensitized TiO₂ Interface. *J. Am. Chem. Soc.* **2014**, *136*, 1034-1046.
- (17) Hu, K.; Blair, A. D.; Piechota, E. J.; Schauer, P. A.; Sampaio, R. N.; Parlane, F. G. L.; Meyer, G. J.; Berlinguette, C. P. Kinetic Pathway for Interfacial Electron Transfer from a Semiconductor to a Molecule. *Nat. Chem.* **2016**, *8*, 853-859.
- (18) Piechota, E. J.; Troian-Gautier, L.; Sampaio, R. N.; Brennaman, M. K.; Hu, K.; Berlinguette, C. P.; Meyer, G. J. Optical Intramolecular Electron Transfer in Opposite Directions through the Same Bridge That Follows Different Pathways. *J. Am. Chem. Soc.* **2018**, *140*, 7176-7186.
- (19) Heimer, T. A.; D'Arcangelis, S. T.; Farzad, F.; Stipkala, J. M.; Meyer, G. J. An Acetylacetonate-Based Semiconductor-Sensitizer Linkage. *Inorg. Chem.* **1996**, *35*, 5319-5324.
- (20) Robson, K. C. D.; Koivisto, B. D.; Yella, A.; Sporinova, B.; Nazeeruddin, M. K.; Baumgartner, T.; Grätzel, M.; Berlinguette, C. P. Design and Development of Functionalized Cyclometalated Ruthenium Chromophores for Light-Harvesting Applications. *Inorg. Chem.* **2011**, *50*, 5494-5508.
- (21) Robson, K. C. D.; Sporinova, B.; Koivisto, B. D.; Schott, E.; Brown, D. G.; Berlinguette, C. P. Systematic Modulation of a Bichromic Cyclometalated Ruthenium(II) Scaffold Bearing a Redox-Active Triphenylamine Constituent. *Inorg. Chem.* **2011**, *50*, 6019-6028.
- (22) Blauch, D. N.; Saveant, J. M. Dynamics of Electron Hopping in Assemblies of Redox Centers. Percolation and Diffusion. *J. Am. Chem. Soc.* **1992**, *114*, 3323-3332.

- (23) Blauch, D. N.; Saveant, J. M. Effects of Long-Range Electron Transfer on Charge Transport in Static Assemblies of Redox Centers. *J. Phys. Chem.* **1993**, *97*, 6444-6448.
- (24) Hanson, K.; Brennaman, M. K.; Ito, A.; Luo, H.; Song, W.; Parker, K. A.; Ghosh, R.; Norris, M. R.; Glasson, C. R. K.; Concepcion, J. J.; Lopez, R.; Meyer, T. J. Structure–Property Relationships in Phosphonate-Derivatized, Ru(II) Polypyridyl Dyes on Metal Oxide Surfaces in an Aqueous Environment. *J. Phys. Chem. C* **2012**, *116*, 14837-14847.
- (25) Swierk, J. R.; McCool, N. S.; Saunders, T. P.; Barber, G. D.; Mallouk, T. E. Effects of Electron Trapping and Protonation on the Efficiency of Water-Splitting Dye-Sensitized Solar Cells. *J. Am. Chem. Soc.* **2014**, *136*, 10974-10982.

CHAPTER 5: Thermal Bimolecular Electron Transfer in the Marcus Inverted Region: Exploiting Nonadiabatic Electron Transfer⁴

5.1 Introduction

That electron transfer rate constants should decrease as the reaction exergonicity increases was one of the most intriguing predictions of Marcus theory.¹⁻⁵ It was nearly 30 years from Marcus's prediction until electron transfer kinetics in the Marcus-inverted region were demonstrated. Using organic electron donors and acceptors tethered by a steroid spacer, Closs and Miller unambiguously demonstrated electron transfer kinetics that possessed a decreasing rate constant with increasing reaction driving force thereby avoiding diffusion-limited kinetics typically observed in bimolecular electron transfer reactions.^{6,7} Since this observation in the 1980s, Marcus-inverted behavior has been well-established for donors and acceptors that are covalently-linked, frozen in a medium, or electrostatically pre-associated.^{2,3,6-13} However, only a few studies have shown inverted behavior for thermal, bimolecular electron transfer in fluid solution.^{8,9,11,12} In this work, evidence for bimolecular, Marcus-inverted electron transfer is presented for reactions between Ru³⁺ and Co²⁺ polypyridyl compounds in fluid acetonitrile solutions.

⁴This chapter contains results that are a part of ongoing research. Presented are the results and preliminary interpretation of the data obtained. This work was completed in collaboration with Eric J. Piechota, Rachel Bangle, and Ludovic Troian-Gautier.

The nonadiabatic Marcus equation, eq 5.1, has been used to successfully describe many electron transfer reactions.^{1,2,5,14} Here, k_{et} is the electron transfer rate constant, λ is the total reorganization energy consisting of both outer-sphere and inner-sphere contributions, k_B is the Boltzmann constant, T is the absolute temperature, H_{DA} is the electronic coupling matrix element between electron donor and electron acceptor, ΔG° is the Gibbs free energy associated with the electron transfer, and \hbar is the reduced Planck constant.^{1,3,5,15} From this equation, it is clear that weakly-coupled (small H_{DA}) electron donors and electron acceptors will undergo slow electron transfer reactions. These reactions are said to be in the nonadiabatic regime, where, in theory, inverted-electron transfer behavior may be observed.^{1,3,5,15}

$$k_{et} = \left(\frac{2\pi}{\hbar}\right) \left(\frac{|H_{DA}|^2}{\sqrt{4\pi\lambda k_B T}}\right) e^{\left(\frac{-(\Delta G^\circ + \lambda)^2}{4\lambda k_B T}\right)} \quad (5.1)$$

Electron transfer reactions which involve $\text{Co}^{\text{III/II}}$ polypyridyl compounds are noted for their unusually slow electron transfer rates.¹⁶⁻²⁵ Co^{3+} polypyridyl compounds are d^6 , low-spin transition metal compounds with an electronic configuration of (t_{2g}^6) assuming pseudo-octahedral geometry.^{20,23} However, Co^{2+} polypyridyl compounds are predominantly high-spin d^7 compounds at room temperature with an electronic configuration of $(t_{2g}^5)(e_g^{*2})$.^{20,23} Population of the antibonding e_g^* orbitals leads to significant structural distortion of these molecules which raise the inner-sphere reorganization energies. Indeed, when comparing $[\text{Ru}(\text{bpy})_3]^{3+/2+}$ and $[\text{Co}(\text{bpy})_3]^{3+/2+}$ self-exchange reactions in aqueous conditions, $[\text{Ru}(\text{bpy})_3]^{3+/2+}$ rate constants are on the order of $10^8 \text{ M}^{-1}\text{s}^{-1}$ with reorganization energies of 0.7 to 1 eV, while $[\text{Co}(\text{bpy})_3]^{3+/2+}$ rate constants are on the order of $10 \text{ M}^{-1}\text{s}^{-1}$ with reorganization energies of 2 to 2.5 eV.¹⁸ This has caused some to implicate the nuclear factors as the cause for slow electron transfer rates.^{18,26}

Here, flash photolysis of Ru^{2+} polypyridyl compounds in the presence of Co^{3+} polypyridyl compounds was used to generate Ru^{3+} and Co^{2+} compounds, and the back-electron transfer rate constants were quantified. Analysis of the reaction rate constants with the driving force revealed electron transfer that exhibited Marcus-inverted behavior. Due to the highly nonadiabatic system, reaction rates were limited by the probability of electron transfer and not by diffusional encounters. This allowed for Marcus-inverted behavior to be observed.

5.2 Experimental Methods

5.2.1 Materials

The following solvents and reagents were obtained from the indicated commercial supplier and used without further purification: methanol (MeOH, Fisher, certified ACS), hexafluorophosphoric acid (HPF_6 , Aldrich, 55 wt% in H_2O), acetonitrile (CH_3CN , Burdick and Jackson, spectrophotometric grade), ethanol (EtOH, Decon Laboratories, Inc., anhydrous 200 Proof), dichloromethane (Fisher, certified ACS), ammonium hexafluorophosphate (NH_4PF_6 , Aldrich, $\geq 95\%$), sulfuric acid (H_2SO_4 , Fisher, Certified ACS Plus), diethyl ether (Fisher, certified ACS), 4,4'-dimethoxy-2,2'-bipyridine (MeObpy, Sigma-Aldrich, 97%), 4,4'-di-*tert*-butyl-4,4'-bipyridine (dtb, Sigma-Aldrich, 98%), 4,4'-dimethyl-2,2'-bipyridine (dmb, Combi-Blocks), 1,2-dichlorobenzene (Sigma-Aldrich, ReagentPlus®, 99%), neutral alumina (Sigma-Aldrich, activated Brockmann 1), lithium perchlorate (LiClO_4 , Sigma-Aldrich, 99.99% trace metal basis), ferrocene (Aldrich, 98%). 4-amino-2,2'-bipyridine (mab), 4,4'-diamino-2,2'-bipyridine (dab), 4,4'-difluoro-2,2'-bipyridine (Fbpy), 4,4'-dibromo-2,2'-bipyridine (Brbpy), 2,2'-bipyridyl-4,4'-dicarboxylic acid (dcb), 4,4'-dimethylester-2,2'-bipyridine (dmeb), 4,4'-bis(trifluoromethyl)-2,2'-bipyridine (btfmb), $\text{Ru}(1,4\text{-cyclooctadiene})_2\text{Cl}_2$ polymer (Poly-Ru), $[\text{Ru}(\text{dtb})_2\text{Cl}_2]$, $[\text{Ru}(\text{btfmb})_2\text{Cl}_2]$, $[\text{Ru}(\text{dtb})_2(\text{dmeb})](\text{PF}_6)_2$, $[\text{Ru}(\text{bpy})_3](\text{PF}_6)_2$,

[Ru(bpy)₂(dmeb)](PF₆)₂, [Ru(dmeb)₃](PF₆)₂, [Ru(deeb)₃](PF₆)₂, [Ru(btmb)₃](PF₆)₂, [Ru(deeb)(bpz)₂](PF₆)₂, and [Ru(bpz)₃](PF₆)₂ were available from previous studies or were made as previously reported.^{21,27-39} An Anton-Paar Microwave Synthesis Reactor Monowave 300 was used to carry out reactions in sealed microwave reaction vials for the specified reactions below.

5.2.2 General Procedure for the Synthesis of [Ru(R₂bpy)₂Cl₂]

The synthesis of the [Ru(R₂bpy)₂Cl₂], where R₂bpy is 4,4'-substituted-2,2'-bipyridine, was carried out by a previously published method and is briefly described here.³⁰ Into a reaction flask, Poly-Ru (1 eq.) and R₂bpy (2.1 eq.) were combined with 50 mL of 1,2-dichlorobenzene and heated to 180 °C for 2 h under an inert atmosphere. Once cooled, the reaction mixture was added to 250 mL of diethyl ether to precipitate the product which was collected via filtration. The dark purple-to-black solids were washed with excess diethyl ether and dried under vacuum. Typical yields were greater than 50%. The compounds were used as isolated without further purification.

5.2.3 General Procedure for the Synthesis of the Cobalt Compounds

[Co(bpy)₃](PF₆)₂, [Co(bpy)₃](PF₆)₃, [Co(dmb)₃](PF₆)₂, and [Co(dmb)₃](PF₆)₃ were made following previously reported methods.²¹ To briefly summarize, CoCl₂·6H₂O (1 eq.) and R₂bpy (3.1 eq.) were combined in a reaction flask with 75 mL of MeOH. The reaction was heated to reflux for 2 h. Once cooled, an excess of NH₄PF₆ was added to the reaction mixture to precipitate a pale-yellow solid which was collected via filtration and washed with a small amount of MeOH. The compound was dried under vacuum and used without further purification.

To obtain the Co^{3+} polypyridyl compounds, a chemical oxidation was achieved by adding an excess of NOBF_4 to an CH_3CN solution containing the $[\text{Co}(\text{R}_2\text{bpy})_3](\text{PF}_6)_2$. The reaction mixture was allowed to stir for 1 h at room temperature after which the solvent was removed by evaporation. The crude Co^{3+} polypyridyl compound was dissolved in the minimal amount of CH_3CN to which a large excess of NH_4PF_6 was added. This solution was added to diethyl ether to precipitate the desired product. The yellow solid was collected by filtration and was washed with MeOH to remove any remaining NH_4PF_6 salt. The compound was dried in a vacuum and used without further purification.

5.2.4 Synthesis of $[\text{Ru}(\text{dtb})_2(\text{dab})](\text{PF}_6)_2$

$[\text{Ru}(\text{dtb})_2\text{Cl}_2]$ (400 mg, 0.56 mmol) and 4,4'-(NH_2)₂-2,2'-bipyridine (115 mg, 0.62 mmol) were placed in a round bottom flask in the presence of 20 mL of a 1:1 (v/v) $\text{H}_2\text{O}/\text{EtOH}$ mixture. The mixture was heated at reflux for 6 hours. After reaction, the mixture was concentrated to approximately 10 mL under reduced pressure and a saturated NH_4PF_6 aqueous solution was added. The formed precipitate was filtered, washed with water, a minimum amount of ice-cold ethanol and diethyl ether. The product was obtained as an orange powder (540 mg, 87% yield). ^1H NMR (500 MHz, CD_3CN) δ 8.43 (d, J = 9.1 Hz, 4H), 7.77 (d, J = 6.0 Hz, 2H), 7.54 (d, J = 5.9 Hz, 2H), 7.41 (dd, J = 15.5, 4.0 Hz, 4H), 7.32 (d, J = 6.0 Hz, 2H), 6.95 (d, J = 6.4 Hz, 2H), 6.52 (d, J = 5.0 Hz, 2H), 5.53 (s, 4H), 1.42 (s, 18H), 1.39 (s, 18H). ESI-MS. Found (calcd) for $\text{C}_{46}\text{H}_{58}\text{N}_8\text{Ru}^{2+}$: m/z 412.19060 (412.19139).

5.2.5 Synthesis of $[\text{Ru}(\text{dtb})_2(\text{mab})](\text{PF}_6)_2$

$[\text{Ru}(\text{dtb})_2\text{Cl}_2]$ (300 mg, 0.42 mmol) and 4- NH_2 -2,2'-bipyridine (80 mg, 0.47 mmol) were placed in a round bottom flask in the presence of 20 mL of a 1:1 (v/v) $\text{H}_2\text{O}/\text{EtOH}$ mixture. The mixture was heated at reflux overnight. After reaction, the mixture was evaporated under

reduced pressure and the residue was dissolved in 5 mL of water. A saturated NH_4PF_6 aqueous solution was then added to induce precipitation of the complex. The formed precipitate was filtered, washed with water, a minimum amount of ice-cold ethanol and diethyl ether. The product was finally purified by flash chromatography on Al_2O_3 using $\text{DCM}/\text{CH}_3\text{CN}$ 9:1 \rightarrow 7:3 (v/v) as the eluent. The product was obtained as an orange powder (370 mg, 80% yield). ^1H NMR (500 MHz, CD_3CN) δ 8.48 (dt, $J = 4.9, 2.3$ Hz, 4H), 8.27 (d, $J = 8.2$ Hz, 1H), 8.00 (td, $J = 7.9, 1.5$ Hz, 1H), 7.76 (d, $J = 6.0$ Hz, 1H), 7.68 – 7.62 (m, 3H), 7.58 (dd, $J = 17.0, 6.0$ Hz, 2H), 7.44 (dd, $J = 6.1, 2.0$ Hz, 1H), 7.42 – 7.33 (m, 4H), 7.01 (d, $J = 6.4$ Hz, 1H), 6.60 (dd, $J = 6.4, 2.5$ Hz, 1H), 5.60 (d, $J = 6.1$ Hz, 2H), 1.47 – 1.39 (m, 36H). ESI-MS. Found (calcd) for $\text{C}_{46}\text{H}_{57}\text{N}_7\text{Ru}^{2+}$: m/z 404.68539 (404.68594).

5.2.6 Synthesis of $[\text{Ru}(\text{MeObpy})_2(\text{dmeb})](\text{PF}_6)_2$

Into a reaction flask, $[\text{Ru}(\text{MeObpy})_2\text{Cl}_2]$ (72.5 mg, 0.120 mmol) was combined with dmeb (33.3 mg, 0.122 mmol) and 35 mL of 1:1 (v/v) $\text{MeOH}/\text{H}_2\text{O}$. The reaction mixture was heated to reflux for overnight. Once cooled, the crude reaction mixture was evaporated to dryness and dissolved in the minimum amount of 1:1 (v/v) $\text{MeOH}/\text{H}_2\text{O}$. The compound was purified using size exclusion chromatography (Sephadex LH-20) with a 1:1 (v/v) $\text{MeOH}/\text{H}_2\text{O}$. Small fractions were collected and the purity of each were assessed by UV-visible spectroscopy. Similar fractions were combined and evaporated to dryness. A red solid was collected. Anion metathesis was performed by dissolving the product into the minimum amount of H_2O and precipitating with HPF_6 . The red solid was collected by filtration and washed with H_2O . (101.1 mg, 79% yield) ^1H NMR (600 MHz, CD_3CN) δ 9.00 (d, $J = 1.2$ Hz, 2H), 8.04 – 8.01 (m, 4H), 8.00 (d, $J = 2.6$ Hz, 2H), 7.80 (dd, $J = 5.8, 1.5$ Hz, 2H), 7.50 (d, $J = 6.5$ Hz, 2H), 7.36 (d, $J = 6.5$ Hz, 2H), 6.99 (dd, $J = 6.5, 2.6$ Hz, 2H), 6.88 (dd, $J = 6.5, 2.6$ Hz,

2H), 4.01 (s, 6H), 3.99 (s, 6H), 3.97 (s, 6H). ESI-MS. Found (calcd) for $C_{38}H_{36}N_6O_8Ru^{2+}$: m/z 403.0808 (403.0819).

5.2.7 Synthesis of $[Ru(dmb)_2(dmeb)](PF_6)_2$

Into a microwave reaction vial, $[Ru(dmb)_2Cl_2]$ (102.5 mg, 0.190 mmol) was combined with dmeb (51.8 mg, 0.190 mmol) and 6 mL of 1:1 (v/v) MeOH/H₂O. The reaction mixture was heated in a microwave reactor for 1 h at 100 °C. Once cooled, the reaction mixture was evaporated to dryness, and then dissolved in CH₃CN. The crude product was purified using column chromatography (neutral alumina). A gradient elution was used starting with neat CH₃CN to elute the starting materials. The concentration of H₂O was slowly increased and several orange bands were collected which was attributed to partially hydrolyzed product as has been previously observed.³⁹ The fractions were combined, dried under vacuum, and dissolved in ~25 mL of MeOH, and the solution was acidified by the addition of 1 mL of concentrated H₂SO₄. The reaction mixture was heated to reflux overnight. Once cooled, the reaction mixture was added to ~200 mL of H₂O. Anion metathesis was performed through the addition of several mL of a saturated NH₄PF₆ solution which precipitated an orange product. The orange product was collected by filtration, washed with a small amount of H₂O, and collected. (60.0 mg, 30.7% yield)

5.2.8 Synthesis of $[Ru(Fbpy)_2(dcb)](PF_6)_2$

Into a microwave reaction vial, $[Ru(Fbpy)_2Cl_2]$ (64.6 mg, 0.116 mmol) was combined with dcb (28.2 mg, 0.115 mmol) and 20 mL of 1:1 (v/v) MeOH/H₂O. The reaction mixture was heated in a microwave reactor for 20 min at 160 °C. Once cooled, the crude orange solution was evaporated to dryness, and then dissolved in the minimum amount of a 1:1 (v/v) MeOH/H₂O. The compound was purified using size exclusion chromatography (Sephadex LH-

20) with a 1:1 (v/v) MeOH/H₂O. Small fractions were collected and the purity of each were assessed by UV-visible spectroscopy. Similar fractions were combined and the solution was evaporated to dryness. Anion metathesis was performed by dissolving the product in the minimum amount of H₂O followed by the addition of 1 mL of HPF₆ to precipitate an orange/red product. The final product was collected by filtration, washed with a small amount of H₂O and diethyl ether, and collected. (68.4 mg, 58.1% yield) ESI-MS. Found (calcd) for C₃₂H₂₀F₄N₆O₄Ru²⁺: *m/z* 365.0254 (365.0263).

5.2.9 Synthesis of [Ru(Fbpy)₂(dmeb)](PF₆)₂

Into the reaction flask, [Ru(Fbpy)₂(dcb)](PF₆)₂ (25.8 mg, 0.025 mmol) was dissolved into 30 mL of MeOH. The solution was acidified with 1 mL of concentrated H₂SO₄. The reaction mixture was heated to reflux overnight. Once cooled, the reaction mixture was added to ~200 mL of H₂O. An orange product was precipitated out of solution upon the addition of several mL of a saturated solution of aqueous NH₄PF₆. The orange product was collected by filtration, washed with a small amount of H₂O, and collected. (21.0 mg, 79.2% yield) ¹H NMR (500 MHz, CD₃CN) δ 9.04 (d, *J* = 1.2 Hz, 2H), 8.32 (ddd, *J* = 11.4, 9.0, 2.7 Hz, 4H), 7.95 (d, *J* = 5.7 Hz, 2H), 7.82 (dd, *J* = 5.8, 1.7 Hz, 2H), 7.75 (t, *J* = 6.5 Hz, 2H), 7.63 (t, *J* = 6.5 Hz, 2H), 7.34 (td, *J* = 6.8, 2.7 Hz, 2H), 7.25 (td, *J* = 7.1, 2.8 Hz, 2H), 4.00 (s, 6H).

5.2.10 Synthesis of [Ru(Brbpy)₂(dmeb)](PF₆)₂

Into a microwave reaction vial, [Ru(Brbpy)₂Cl₂] (104.0 mg, 0.130 mmol) was combined with dmeb (37.2 mg, 0.137 mmol) and 6 mL of 1:1 (v/v) MeOH/H₂O. The reaction mixture was heated in a microwave reactor for 1 h at 100 °C. Once cooled, the reaction mixture was evaporated to dryness, and then dissolved in CH₃CN. The crude product was purified using column chromatography (neutral alumina). A gradient elution was used starting with neat

CH₃CN to elute the starting materials. The concentration of H₂O was slowly increased and an orange band was collected. The red-orange product was dissolved in ~25 mL of MeOH, and the solution was acidified by the addition of 1 mL of concentrated H₂SO₄. The reaction mixture was heated to reflux overnight. Once cooled, the reaction mixture was added to ~250 mL of H₂O. Anion metathesis was performed through the addition of several mL of a saturated NH₄PF₆ solution which precipitated an orange product. The red-orange product was collected by filtration, washed with a small amount of H₂O, and collected. (25.3 mg, 15.1% yield) ¹H NMR (500 MHz, CD₃CN) δ 9.03 (d, *J* = 1.2 Hz, 2H), 8.75 (d, *J* = 1.9 Hz, 2H), 8.73 (d, *J* = 1.9 Hz, 2H), 7.92 (d, *J* = 5.8 Hz, 2H), 7.82 (dd, *J* = 5.8, 1.7 Hz, 2H), 7.65 (dd, *J* = 6.1, 2.0 Hz, 2H), 7.59 – 7.54 (m, 4H), 7.44 (d, *J* = 6.1 Hz, 2H), 3.99 (s, 6H).

5.2.11 Synthesis of [Ru(btmb)₂(dmb)](PF₆)₂

Into a microwave reaction vial, [Ru(btmb)₂Cl₂] (111.3 mg, 0.147 mmol) was combined with dmb (40.7 mg, 0.150 mmol) and 6 mL of 1:1 (v/v) MeOH/H₂O. The reaction mixture was heated in a microwave reactor for 3.5 h at 100 °C. Once cooled, the reaction mixture was evaporated to dryness, and then dissolved in CH₃CN. The crude product was purified using column chromatography (neutral alumina). A gradient elution was used starting with neat CH₃CN to elute the starting materials. The concentration of H₂O was slowly increased and an orange band was collected. The bright orange product was dissolved in ~25 mL of MeOH, and the solution was acidified by the addition of 1 mL of concentrated H₂SO₄. The reaction mixture was heated to reflux overnight. Once cooled, the reaction mixture was added to ~250 mL of H₂O. Anion metathesis was performed through the addition of several mL of a saturated NH₄PF₆ solution which precipitated an orange product. The orange product was collected by filtration, washed with a small amount of H₂O, and collected. (88.7 mg, 98.3%

yield) ^1H NMR (500 MHz, CD_3CN) δ 9.08 (s, 2H), 8.95 (s, 4H), 7.98 (d, $J = 3.7$ Hz, 2H), 7.92 (d, $J = 3.7$ Hz, 2H), 7.89 (d, $J = 3.7$ Hz, 2H), 7.85 (s, 2H), 7.72 (d, $J = 4.2$ Hz, 2H), 7.69 (d, $J = 3.8$ Hz, 2H), 4.00 (s, 6H).

5.2.12 Nuclear Magnetic Resonance Spectroscopy (NMR)

^1H NMR spectra were obtained on the Bruker Avance III spectrometer operating at 500 or 600 MHz spectrometer at room temperature, and the peaks referenced to the solvent peaks.⁴⁰ Data was processed using MestReNova 11.0.

5.2.13 Electrospray Ionization Mass Spectrometry (ESI-MS)

Samples were analyzed with a hybrid LTQ FT (ICR 7T) (ThermoFisher, Bremen, Germany) mass spectrometer. Samples were introduced via a micro-electrospray source at a flow rate of 3 $\mu\text{L}/\text{min}$. Over 200 time domain transients were averaged in the mass spectrum. ESI source conditions were set as: sheath gas (nitrogen) 3 arb, auxiliary gas (nitrogen) 0 arb, sweep gas (nitrogen) 0 arb, capillary temperature 275 $^\circ\text{C}$, capillary voltage 35 V and tube lens voltage 110 V. The mass range was set to 150-1000 m/z . All measurements were recorded at a resolution setting of 100,000. Solutions were analyzed at 0.1 mg/mL or less based on responsiveness to the ESI mechanism. Xcalibur (ThermoFisher, Bremen, Germany) was used to analyze the data. Molecular formula assignments were determined with Molecular Formula Calculator (v 1.2.3). Low-resolution mass spectrometry (linear ion trap) provided independent verification of molecular weight distributions. All observed species were singly charged, as verified by unit m/z separation between mass spectral peaks corresponding to the ^{12}C and $^{13}\text{C}^{12}\text{C}_{n-1}$ isotope for each elemental composition.

5.2.14 Spectroscopy

All steady-state UV-visible spectra were recorded on either a Varian Cary 50 or Varian Cary 60 spectrophotometer at room temperature in a quartz cuvette with a 1.0 cm pathlength. The molar absorption coefficients were determined through the serial dilution of a stock solution.

Nanosecond transient absorption spectra were acquired on an apparatus similar to one previously reported.⁴¹ To briefly summarize, samples were excited by a Q-switched, pulsed Nd:YAG laser (Quantel U.S.A. (Big Sky) Brilliant B: 5-6 ns full width at half-maximum, 1 Hz, ~10 mm diameter spot size) doubled to 532 nm. The laser pulse was passed through an OPO and tuned to 488 nm with 3-5 mJ/pulse irradiance. The probe beam was a 150 W Xe arc lamp which was aligned perpendicular to the excitation laser pulse. For measurements below 100 μ s, the probe lamp was pulsed to decrease the signal to noise ratio. The probe beam was detected using a monochromator (SPEC 1702/04) optically coupled to an R928 photomultiplier tube (Hamamatsu). Data acquisition was achieved using a digital oscilloscope (LeCroy 9450, Dual 330 MHz) coupled to a computer. The overall instrument response time was 10 ns. Each set of transient data consisted of an average of 150 laser pulses for each sample.

Acetonitrile solutions used during the nanosecond transient absorption experiments contained a Ru²⁺ polypyridyl compound ($\sim 2.5 \times 10^{-5}$ M) as the chromophore and a Co³⁺ polypyridyl compound (2.5×10^{-3}) as the quencher. To ensure pseudo-first order kinetics, Co²⁺ polypyridyl compound (10^{-4} M) was added. Solutions were sparged with Ar for at least 30 min prior to measurements.

5.2.15 Spectroelectrochemistry

Spectroelectrochemical measurements were used to quantify the formal reduction potential of each compound in CH₃CN solutions containing 0.1 M LiClO₄. The absorbance changes in solution were monitored as increasingly more positive potentials were applied to the solution. Each potential was held until the absorbance became invariant with time. Measurements were performed using a WaveNow potentiostat (Pine Research Instrumentation, Inc.) coupled to an AvaSpec UL2048 UV-Visible spectrometer and an AvaLight Deuterium/Halogen light source (Avantes) all controlled by the AfterMath software (Pine Research Instrumentation, Inc.). A three-electrode arrangement was used with a Pt honeycomb microelectrode (Pine Research Instrumentation, Inc.), a Pt counter electrode (Pine Research Instrumentation, Inc.), and a nonaqueous Ag/AgCl pseudoreference electrode (Pine Research Instrumentation, Inc.) filled with a CH₃CN solution containing 0.1 M LiClO₄. The pseudoreference was calibrated against the ferrocenium/ferrocene redox couple which is 0.310 V vs the standard calomel electrode (SCE) in 0.2 M LiClO₄/CH₃CN, and SCE is 0.241 V vs the normal hydrogen electrode (NHE).⁴² All values herein are reported vs NHE.

5.2.16 Electrochemistry

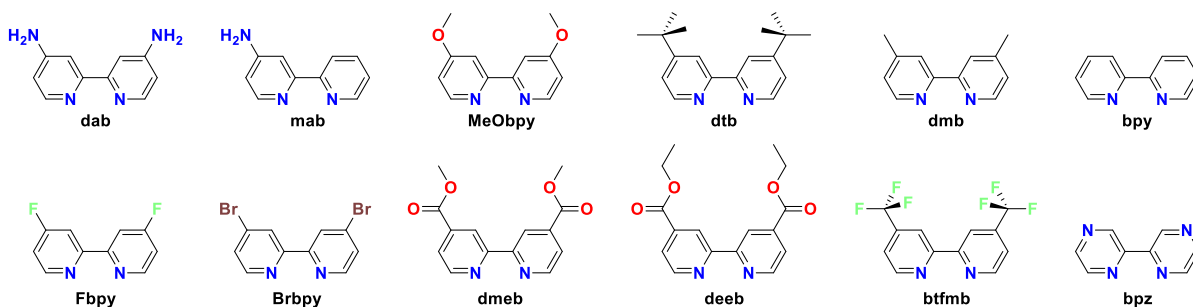
Cyclic voltammetry was used to measure the formal reduction potentials of [Co(bpy)₃](PF₆)₂ and [Co(bpy)₃](PF₆)₂ using a WaveNow potentiostat (Pine Research Instrumentation, Inc.). A three-electrode arrangement was used with Pt discs as the working and counter electrodes and a nonaqueous Ag/AgCl pseudoreference electrode (Pine Research Instrumentation, Inc.) filled with a CH₃CN solution containing 0.1 M LiClO₄ calibrated to Fc^{+/0} redox couple. The scan rate was 0.1 V/s.

5.2.17 Data Analysis

Data analysis was performed in OriginPro 2017 with least-squares error minimization achieved using the Levenberg-Marquardt method. The reported error for the fitting parameters are the standard errors from the fitting process. Spectroelectrochemical data were analyzed in Wolfram Mathematica 10.4, and least-squares error minimization was achieved using the Levenberg-Marquardt method.

5.3 Results and Discussion

Scheme 5.1. Polypyridyl Ligands Utilized in this Study



A series of 14 Ru^{2+} polypyridyl compounds were synthesized using the ligands depicted in Scheme 5.1, with $[\text{Ru}(\text{dtb})_2(\text{dab})](\text{PF}_6)_2$, $[\text{Ru}(\text{dtb})_2(\text{mab})](\text{PF}_6)_2$, $[\text{Ru}(\text{MeObpy})_2(\text{dmeb})](\text{PF}_6)_2$, $[\text{Ru}(\text{dmb})_2(\text{dmeb})](\text{PF}_6)_2$, $[\text{Ru}(\text{Fbpy})_2(\text{dmeb})](\text{PF}_6)_2$, $[\text{Ru}(\text{Brbpy})_2(\text{dmeb})](\text{PF}_6)_2$, and $[\text{Ru}(\text{btmb})_2(\text{dmeb})](\text{PF}_6)_2$ being reported for the first time. A typical synthetic procedure required two steps: (1) preparation of the $[\text{Ru}(\text{R}_2\text{bpy})_2\text{Cl}_2]$ precursor, where R_2bpy is a 4,4'-substituted-2,2'-bipyridine, followed by (2) coordination of the final polypyridyl ligand. All $[\text{Ru}(\text{R}_2\text{bpy})_2\text{Cl}_2]$ precursors were made according to literature procedures with high yields.³⁰ Coordination of the final polypyridyl ligand was accomplished using either traditional reflux or microwave conditions. When either dmeb or deeb was used in the reaction, both sets of conditions sometimes resulted in the partial hydrolysis of the ester groups to carboxylic acids. The desired ester form was easily reacquired by heating the

hydrolyzed compound in neat alcohol acidified by ~1 mL of concentrated H₂SO₄. The structural identity of the 7 new compounds were confirmed by ¹H NMR and high-resolution mass spectroscopy. The Co²⁺ and Co³⁺ polypyridyl compounds were made according to the standard literature methods.²¹

The UV-visible spectra for all 14 Ru²⁺ polypyridyl compounds were measured in neat CH₃CN. Each compound displayed a broad absorbance feature between 400 and 525 nm with molar absorption coefficients, ϵ , between 10900 and 21700 M⁻¹cm⁻¹. These features were consistent with the metal-to-ligand charge transfer (MLCT) bands typical for Ru²⁺ polypyridyl compounds.⁴³⁻⁴⁶ Additional higher energy transitions were observed at wavelengths lower than 375 nm. These features were assigned to intraligand π -to- π^* transitions as has been reported previously.^{43,45} The wavelength of the maximum MLCT absorbance, λ_{MLCT} , and the ϵ values for each compound are tabulated in Table 5.1. Co²⁺ and Co³⁺ polypyridyl compounds only weakly absorbed in the visible region with ϵ values of 100 M⁻¹cm⁻¹ or less.^{21,24}

Spectroelectrochemistry was used to quantify the formal reduction potential, $E^\circ(\text{Ru}^{3+/2+})$, for each compound in CH₃CN solutions containing 0.1 M LiClO₄. The absorbance was monitored as increasingly more positive potentials were applied, Figure 5.1. After each potential step, the absorbance was allowed to reach a constant value before further increasing the applied potential. A given compound was said to be completely oxidized to the Ru³⁺ oxidation state when further potential increases yielded no additional changes in the UV-visible spectrum. For the Ru²⁺ polypyridyl compounds, oxidation resulted in the loss of the MLCT transition as well as a growth of a broad, weak feature centered near 700 nm which have been attributed to ligand-to-metal charge transfer (LMCT) transitions.⁴⁷

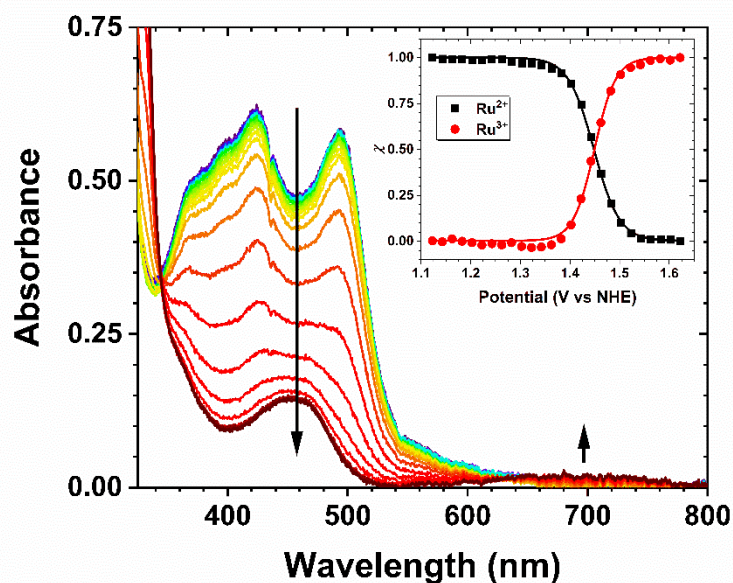


Figure 5.1. Spectroelectrochemical oxidation of $[\text{Ru}(\text{dtb})_2(\text{dmeb})](\text{PF}_6)_2$ in a CH_3CN solution containing 0.1 M LiClO_4 . The inset shows the mole fraction of the Ru^{2+} and Ru^{3+} compounds as a function of the applied potential. Overlaid is a fit to the modified Nernst equation, eq 5.2.

Standard addition of the Ru^{2+} and Ru^{3+} spectra was used to determine the mole fraction, χ , of the both species, inset Figure 5.1.⁴⁸ The $E^\circ(\text{Ru}^{3+/2+})$ were determined using a modified-Nernst equation, eq 5.2, where E_{app} is the applied potential and α is an ideality factor used to describe deviations from the expected 59 mV/decade change in the ratio the Ru^{2+} and Ru^{3+} concentrations.⁴⁹ All of the measured α were within error 1, and the electrochemistry followed Nernstian behavior. The measured $E^\circ(\text{Ru}^{3+/2+})$ are tabulated in Table 5.1 and ranged from 1.13 to 2.22 V vs NHE in agreement with previously published values for similar Ru polypyridyl compounds.^{30,50}

$$\chi = \left(1 + 10^{\left(\frac{E_{\text{app}} - E^\circ}{0.059\alpha} \right)} \right)^{-1} \quad (5.2)$$

Concentrated solutions, 2.5×10^{-3} M, of $[\text{Co}(\text{bpy})_3]^{2+}$ and $[\text{Co}(\text{dmb})_3]^{2+}$ were also analyzed by spectroelectrochemistry. Figure 5.2 shows the spectra measured as a function of applied potential for $[\text{Co}(\text{bpy})_3]^{2+}$ and is representative of both Co compounds. Both

compounds displayed only minor spectral changes at wavelengths greater than 400 nm. This is in agreement with reported spectral changes for $[\text{Co}(\text{bpy})_3]^{3+/2+}$ in aqueous conditions.⁵¹ Due to weak absorbance features in the visible region, cyclic voltammetry was used to measure the $E^\circ(\text{Co}^{3+/2+})$. The inset of Figure 5.2 shows a cyclic voltammogram obtained for $[\text{Co}(\text{bpy})_3]^{2+}$ in 0.1 M $\text{LiClO}_4/\text{CH}_3\text{CN}$ solutions. Both $[\text{Co}(\text{bpy})_3]^{2+}$ and $[\text{Co}(\text{dmb})_3]^{2+}$ displayed a reversible oxidation wave at 0.56 V and 0.43 V vs NHE, respectively, that was consistent with previously reported values.^{21,24}

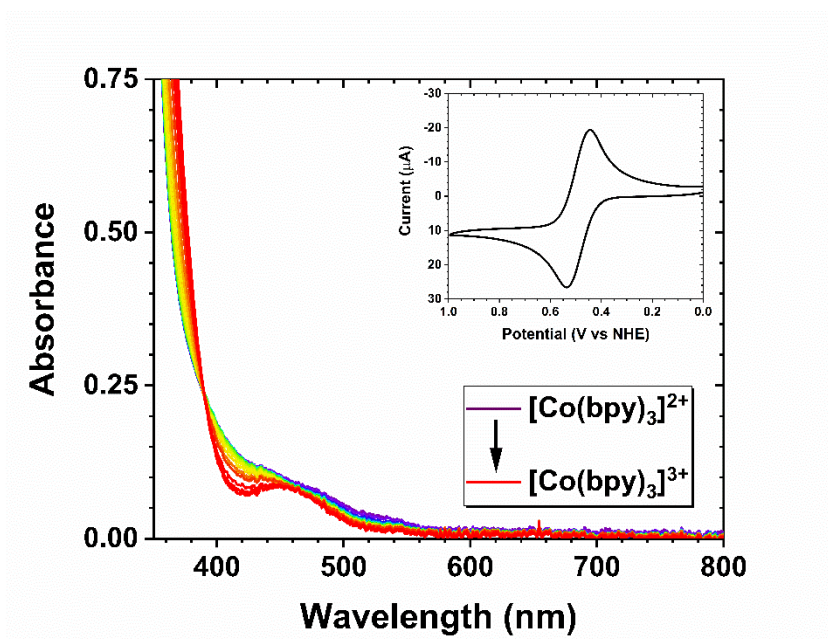


Figure 5.2. Spectroelectrochemical oxidation of $[\text{Co}(\text{bpy})_3](\text{PF}_6)_2$ in a CH_3CN solution containing 0.1 M LiClO_4 . The inset is a cyclic voltammogram obtained for $[\text{Co}(\text{bpy})_3](\text{PF}_6)_2$ in 0.1 M $\text{LiClO}_4/\text{CH}_3\text{CN}$ solutions at a scan rate of 0.1 V/s.

Table 5.1. Spectroscopic, Thermodynamic, and Kinetic Data for the Ru^{II} and Co^{II} Polypyridyl Compounds

					[Co(bpy) ₃] ^{3+/2+}		[Co(dmb) ₃] ^{3+/2+}	
	Compound	$\lambda_{\text{MLCT}}^{a,b}$ (nm)	$E^\circ(\text{M}^{3+/2+})^c$ (V vs NHE)	τ (ns)	$-\Delta G^\circ$ (eV)	k_{et} (10 ⁶ M ⁻¹ s ⁻¹)	$-\Delta G^\circ$ (eV)	k_{et} (10 ⁶ M ⁻¹ s ⁻¹)
	[Co(dmb) ₃] ²⁺	-	0.43	-	-	-	-	-
	[Co(bpy) ₃] ²⁺	-	0.56	-	-	-	-	-
1	[Ru(dtb) ₂ (dab)] ²⁺	474 (11300)	1.13	360	0.57	0.07	0.70	0.44
2	[Ru(dtb) ₂ (mab)] ²⁺	465 (14500)	1.23	670	0.67	0.18	0.80	0.95
3	[Ru(MeObpy) ₂ (dmeb)] ²⁺	504 (10900)	1.32	220	0.76	2.09	0.89	1.91
4	[Ru(dtb) ₂ (dmeb)] ²⁺	493 (11500)	1.44	540	0.88	1.88	1.01	1.44
5	[Ru(dmb) ₂ (dmeb)] ²⁺	489 (13100)	1.47	660	0.91	5.72	1.04	2.18
6	[Ru(bpy) ₃] ²⁺	451 (14000) ^d	1.48	890	0.92	3.24	1.05	3.48
7	[Ru(bpy) ₂ (dmeb)] ²⁺	478 (13900)	1.56	890	1	5.10	1.13	3.64
8	[Ru(F ₂ bpy) ₂ (dmeb)] ²⁺	474 (12900)	1.61	1170	1.05	5.92	1.18	4.31
9	[Ru(Br ₂ bpy) ₂ (dmeb)] ²⁺	470 (17800)	1.66	1530	1.10	10.11	1.23	7.06
10	[Ru(deeb) ₃] ²⁺	466 (21700) ^e	1.80 ^g	2100 ^g	1.24	1.01	1.37	<i>j</i>
11	[Ru(CF ₃ bpy) ₂ (dmeb)] ²⁺	458 (17700)	1.82	1320	1.26	6.92	1.39	<i>j</i>
12	[Ru(CF ₃ bpy) ₃] ²⁺	460 (20100)	1.99 ^h	1280	1.43	2.85	1.56	<i>j</i>
13	[Ru(bpz) ₂ (deeb)] ²⁺	450 (17000) ^f	2.03 ^g	1750 ^g	1.47	2.00	1.60	<i>j</i>
14	[Ru(bpz) ₃] ²⁺	440 (13000) ^d	2.22 ⁱ	800 ⁱ	1.66	5.70	1.79	<i>j</i>

^aThe value in parentheses is the molar absorption coefficient in units of M⁻¹cm⁻¹. ^bError is ± 2 nm. ^cError is ± 0.01 V. ^dTaken from Ref 52. ^eTaken from Ref 53. ^fTaken from Ref 54. ^gTaken from Ref 55. ^hTaken from Ref 37. ⁱTaken from Ref 56. ^jNo measurable quenching detected.

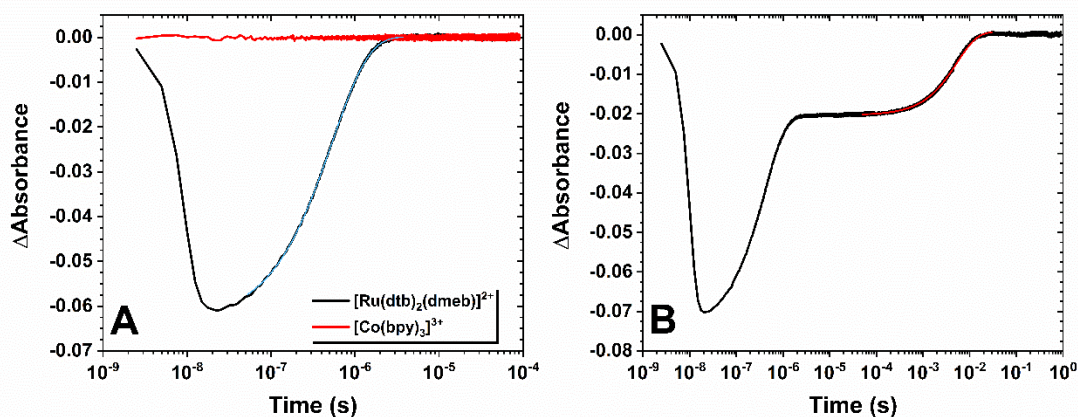
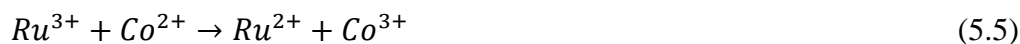


Figure 5.3. (A) Nanosecond transient kinetic data acquired for a CH₃CN solution containing only [Ru(dtb)₂(dmeb)](PF₆)₂ (black, λ_{exc} , 488 nm; probe, 520 nm) or only [Co(bpy)₃](PF₆)₂ (red, λ_{exc} , 488 nm; probe, 470 nm). Overlaid in blue is a single-exponential fit for the excited-state decay of [Ru(dtb)₂(dmeb)](PF₆)₂. (B) Nanosecond transient kinetic data acquired for an acetonitrile solution containing 2.5×10^{-5} , 1×10^{-4} , and 2.5×10^{-3} M of [Ru(dtb)₂(dmeb)](PF₆)₂, [Co(bpy)₃](PF₆)₂, and [Co(bpy)₃](PF₆)₃, respectively (λ_{exc} , 488 nm; probe, 495 nm; laser fluence, 4.8 mJ/pulse). Overlaid in red is a fit to pseudo-first order kinetics.

Nanosecond transient absorption (TA) spectroscopy was used to carry out the flash photolysis experiments. Figure 5.3A shows representative kinetic data obtained from CH₃CN solutions containing only [Ru(dtb)₂(dmeb)]²⁺ or only [Co(bpy)₃]³⁺ after excitation with a 488 nm laser pulse. For solutions containing only Ru²⁺, excitation resulted in the formation of the Ru²⁺ excited state, Ru^{2+*}, which appeared as a bleach of the MLCT in the transient data. These data were fit to a single-exponential, and the excited-state lifetimes, τ , are tabulated in Table 5.1. Note that the τ for [Ru(dtb)₂(dab)](PF₆)₂ and [Ru(dtb)₂(mab)](PF₆)₂ were obtained from photoluminescence decay kinetics. Excited-state decay for all Ru²⁺ compounds were complete by 10 μ s. Excitation of solutions containing only Co³⁺ displayed no transient signal.

Representative kinetic data acquired from the flash photolysis experiment is given in Figure 5.3B for a solution containing 2.5×10^{-5} M [Ru(dtb)₂(dmeb)](PF₆)₂, 1×10^{-4} M [Co(bpy)₃](PF₆)₃, and 2.5×10^{-3} M [Co(bpy)₃](PF₆)₂ monitored at 495 nm. A 488 nm laser pulse

was used to excite the Ru^{2+} chromophore ($\sim 2.5 \times 10^{-5}$ M) resulting in the formation of the Ru^{2+*} , eq 5.3, as observed for the Ru^{2+} -only samples. During the first μs of the experiment, both excited-state decay and diffusional quenching by Co^{3+} (2.5×10^{-3} M), eq 5.4, were occurring concomitantly.⁵¹ After 5 μs , these reactions were complete, and the remaining bleach was attributed to the Ru^{3+} generated by the quenching reaction.^{16,51} The back-electron transfer reaction was monitored between the resulting Co^{2+} and the Ru^{3+} at times greater than 5 μs , eq 5.5.



Excess Co^{2+} (10^{-4} M) was added to the solution to ensure pseudo-first order kinetics. The data acquired at the λ_{MLCT} were fit to a single-exponential to obtain a first-order rate constant for the back-electron transfer reaction, k_{obs} . With knowledge of the Co^{2+} concentration, the second-order back-electron transfer rate constant, k_{et} , was calculated from the k_{obs} . The transient data acquired at the MLCT maximum almost exclusively reported on the Ru kinetics. The contribution from $Co^{3+/2+}$ redox chemistry were assumed to be negligible as the change in ϵ values associated with $Co^{3+/2+}$ was $\leq 10^2 \text{ M}^{-1}\text{cm}^{-1}$ as opposed to $\geq 10^4 \text{ M}^{-1}\text{cm}^{-1}$ for the $Ru^{3+/2+}$ as determined by spectroelectrochemical measurements.⁵¹

It is important to note that Co^{2+} has been shown to quench Ru^{2+*} through primarily an oxidative pathway in aqueous conditions, eq 5.6, resulted in the formation of Co^+ in solution.¹⁶ It was expected that some quenching by Co^{2+} may occur in CH_3CN . Therefore, the large excess Co^{3+} in solution served two purposes. First, the large concentration was used to maximize the diffusional encounters between Ru^{2+*} and Co^{3+} to ensure that eq 5.4 was the dominant

quenching pathway and to maximize the concentration of Ru^{3+} generated. Second, the large excess of Co^{3+} in solution would favor comproportionation chemistry between any Co^+ generated and Co^{3+} by eq 5.6 resulting in the formation of two equivalents of Co^{2+} , eq 5.7, a process with 1.28 V of driving force.¹⁶ Thus, confidence was high that the back-electron transfer reaction monitored at the longer time scales was reporting on the desired Ru^{3+} and Co^{2+} electron transfer.



In the most exergonic back-electron transfer reactions between Ru^{3+} and $[\text{Co}(\text{dmb})_3]^{2+}$, no oxidative quenching was observed. This may be due to a decrease in the driving force for quenching by electron transfer. As the $E^\circ(\text{Ru}^{3+/2+})$ for the became more positive, it would be expected that the excited-state reduction potential, $E^\circ(\text{Ru}^{3+/2+*})$, would also become lower in energy.^{30,57} If $E^\circ(\text{Ru}^{3+/2+*})$ became to positive, it would no longer be a potent enough photoreductant to reduce the Co^{3+} , and thus, no long-lived bleach would be observed. Experiments are underway to test this hypothesis.

The measured k_{et} values for the back-electron transfer reaction spanned two orders of magnitude from 10^5 to $10^7 \text{ M}^{-1}\text{s}^{-1}$. The reaction rate for the back-electron transfer between $[\text{Ru}(\text{bpy})_3]^{3+}$ and $[\text{Co}(\text{bpy})_3]^{2+}$ has been reported in aqueous conditions to be $2 \times 10^8 \text{ M}^{-1}\text{s}^{-1}$.^{18,51,58} This differ from the value of $3.24 \times 10^6 \text{ M}^{-1}\text{s}^{-1}$ measured here and it is not clear why. Based on the Marcus two-sphere continuum model, switching to solvents with a smaller dielectric constant (i.e. from H_2O to CH_3CN) should increase the rate of electron transfer.^{1,3,15,59} However, comparable rates of electron transfer have been reported for the

reaction of $\text{Co}^{3+/2+}$ compounds and a large number of transition metal and organic molecules in CH_3CN .^{17,19}

The diffusion coefficient for other Ru^{2+} polypyridyl compounds has been shown to be $9.2 \times 10^{-10} \text{ cm}^2 \text{ s}^{-1}$.^{54,55} The diffusion coefficients for $[\text{Co}(\text{bpy})_3]^{2+}$ and $[\text{Co}(\text{dmb})_3]^{2+}$ measured by cyclic voltammetry in CH_3CN solutions have been reported to be $9.1 \times 10^{-10} \text{ cm}^2 \text{ s}^{-1}$ and $7.7 \times 10^{-10} \text{ cm}^2 \text{ s}^{-1}$.²¹ Using equation 5.8 the diffusion-limited reaction rate constant, k_d , was calculated for the back-electron transfer reaction where N_A is Avogadro's number, and D_{Ru} and D_{Co} are the apparent diffusion coefficients for Ru^{3+} and Co^{2+} , respectively.⁵⁴ β and R_C are given by equations 5.9 and 5.10, where R is the sum of the ionic radii of Ru^{3+} and Co^{2+} , z_{Co} and z_{Ru} are the charges of the compounds, e is the elementary charge, ϵ_R is the relative permittivity of the solvent, and ϵ_0 is the vacuum permittivity. Assuming that the ionic radii for Ru^{3+} and Co^{2+} is 6.5 \AA , the diffusion-limited rate constants for the back-electron transfer reactions of Ru^{3+} with $[\text{Co}(\text{bpy})_3]^{2+}$ and $[\text{Co}(\text{dmb})_3]^{2+}$ are $1.25 \times 10^8 \text{ M}^{-1} \text{ s}^{-1}$ and $1.15 \times 10^8 \text{ M}^{-1} \text{ s}^{-1}$, respectively.^{54,60} Thus, the slow reaction rates observed for the back-electron transfer reaction were not diffusion limited.

$$k_d = 4\pi N_A (D_{\text{Ru}} + D_{\text{Co}}) \beta \quad (5.8)$$

$$\beta = \frac{R_C}{e \frac{R}{R_C} - 1} \quad (5.9)$$

$$R_C = \frac{z_{\text{Co}} z_{\text{Ru}} e^2}{4\pi \epsilon_R \epsilon_0 k_B T} \quad (5.10)$$

Figure 5.4 shows the back-electron transfer rate constants for each Ru^{3+} compound with either $[\text{Co}(\text{bpy})_3]^{2+}$ or $[\text{Co}(\text{dmb})_3]^{2+}$ versus the driving force for the back-electron transfer reaction. The driving force was determined from the formal reduction potentials measured by spectroelectrochemistry. Overlaid are fits to the Marcus equation. A global fit procedure was

used to fit the data where H_{DA} was shared between the two data. From the fitting analysis, the H_{DA} that fit both data sets was 0.02 ± 0.001 meV with reorganization energies of 1.1 ± 0.1 eV and 1.4 ± 0.1 eV for the reactions with $[\text{Co}(\text{bpy})_3]^{2+}$ and $[\text{Co}(\text{dmb})_3]^{2+}$, respectively.

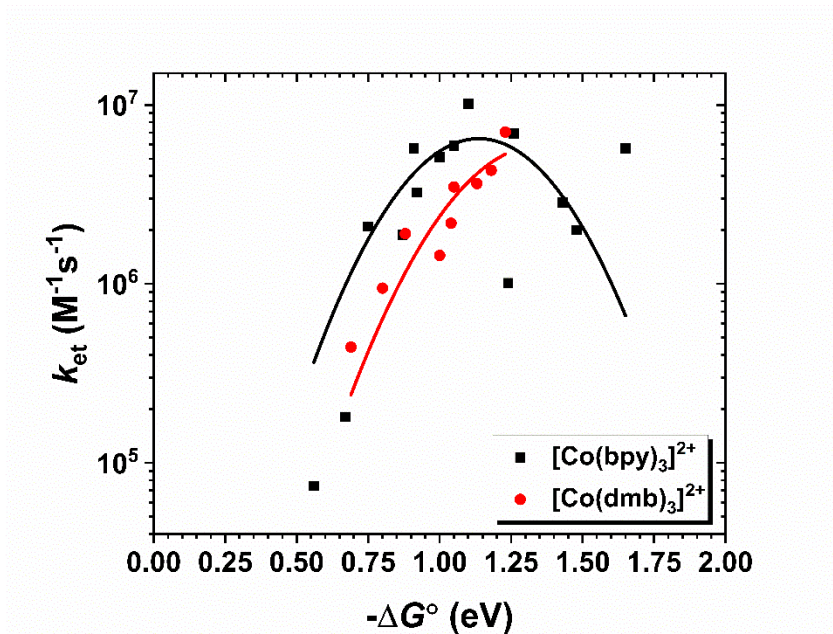


Figure 5.4. The dependence of the back-electron transfer rate constant, k_{et} , on the driving force, ΔG° . Overlaid are the fits to the nonadiabatic Marcus equation, eq 5.1. The electronic coupling matrix element, H_{DA} , was a shared parameter during the fitting process and was found to be 0.02 ± 0.001 meV. The reorganization energies, λ , were found to be 1.1 ± 0.1 eV and 1.4 ± 0.1 eV for the back-electron transfer reactions with $[\text{Co}(\text{bpy})_3]^{2+}$ and $[\text{Co}(\text{dmb})_3]^{2+}$, respectively.

In the case of the back-electron transfer between $[\text{Co}(\text{bpy})_3]^{2+}$ and Ru^{3+} , Marcus-inverted behavior was observed. This was somewhat unexpected. The Marcus-inverted region has historically been absent for bimolecular electron transfer due to diffusion-limited electron transfer kinetics, and reports of inverted behavior relied on electron donors or acceptors that were covalently-linked, dispersed in frozen media, or pre-associated through electrostatic interactions.^{2,3,6-13} Only a few examples of thermal, bimolecular electron transfer in the Marcus-inverted region exist.^{8,9,11,12} In these reports, the authors used electron donors and acceptors that were significantly different in size to raise the diffusion-limited rate constant in

accordance with the Einstein-Smoluchowski relation.^{9,12} Therefore, electron transfer was not diffusion limited, and rapid electron transfer rates were measured.

Here, the small H_{DA} obtained for these reactions indicated that these reactions were nonadiabatic. Therefore, the probability of crossing the potential energy surfaces during electron transfer became rate limiting rather than diffusion. This allowed for the observation of Marcus-inverted behavior. The large inner-sphere reorganization energies and spin restrictions of $\text{Co}^{3+/2+}$ have been implicated as the dominant factor in the sluggish rates.²³ The large structural differences between the high-spin and low-spin states of Co should lead to a larger λ and a larger barrier to the electron transfer reaction. In agreement with this, the λ values reported here (1.1 and 1.4 eV) were larger than what is typically reported for electron transfer reactions between Ru polypyridyl compounds, 0.7 to 1.0 eV.^{1,60}

Marcus-inverted behavior has been reported in the regeneration reaction between oxidized chromophores on the surface of metal oxides and Co^{2+} polypyridyl redox mediators in the solution in dye-sensitized solar cells.^{22,61} In these reactions, the measured λ were found to be between 0.59 and 0.70 eV which were smaller than expected for the corresponding reactions in fluid solution. However, this solar cell data have been called in to question due to the unusually small diffusion rate constants of Co polypyridyl compounds within the mesoporous network of the metal oxide films.^{62,63} Reorganization energies have been measured for electron transfer between covalently-linked Co^{2+} and Ru^{3+} compounds has been shown to be ~ 1.3 eV.^{18,26} The reorganization energy for bimolecular electron transfer between Co^{2+} and Ru^{3+} in aqueous conditions have also been reported to be ~ 1.3 eV.²⁶ These reports are consistent with the values reported here.

5.4 Conclusions

Flash photolysis of Ru^{2+} polypyridyl compounds in the presence of Co^{3+} polypyridyl compounds was used to generate Ru^{3+} and Co^{2+} compounds in solution. The back-electron transfer rate constants were quantified using transient absorption spectroscopy and the measured second-order rate constants were found to be between 10^5 and $10^7 \text{ M}^{-1}\text{s}^{-1}$. These reaction rates were below the diffusion-limited rate constants predicted by the Stokes-Einstein relation of $10^8 \text{ M}^{-1}\text{s}^{-1}$. A plot of the reaction rate constants against the driving force for back-electron transfer revealed electron transfer that exhibited Marcus-inverted behavior. Fits to the nonadiabatic Marcus equation yielded an H_{DA} that was $0.02 \pm 0.001 \text{ meV}$ which indicated electron transfer was nonadiabatic. The reorganization energies obtained from the fits were $1.1 \pm 0.1 \text{ eV}$ and $1.4 \pm 0.1 \text{ eV}$ for the reactions with $[\text{Co}(\text{bpy})_3]^{2+}$ and $[\text{Co}(\text{dmb})_3]^{2+}$, respectively, consistent with previous explanations for the unusually slow $\text{Co}^{3+/2+}$ electron transfer self-exchange rates. This study represents a rare example of Marcus-inverted behavior for a bimolecular electron transfer reaction that is preceded by diffusional encounters.

REFERENCES

- (1) Sutin, N. Theory of Electron Transfer Reactions: Insights and Hindsights. In *Prog. Inorg. Chem.*; John Wiley & Sons, Inc.: 1983; pp 441-498.
- (2) A., M. R. Electron Transfer Reactions in Chemistry: Theory and Experiment (Nobel Lecture). *Angew. Chem. Int. Ed.* **1993**, *32*, 1111-1121.
- (3) Turro, N. J.; Ramamurthy, V.; Scaiano, J. C. *Principles of Molecular Spectroscopy*. University Science Books: Sausalito, California, United States, 2009; p 1-495.
- (4) Marcus, R. A. On the Theory of Oxidation-Reduction Reactions Involving Electron Transfer. I. *J. Chem. Phys.* **1956**, *24*, 966-978.
- (5) Marcus, R. A.; Sutin, N. Electron transfers in chemistry and biology. *Biochim. Biophys. Acta, Bioenerg.* **1985**, *811*, 265-322.
- (6) Miller, J. R.; Calcaterra, L. T.; Closs, G. L. Intramolecular long-distance electron transfer in radical anions. The effects of free energy and solvent on the reaction rates. *J. Am. Chem. Soc.* **1984**, *106*, 3047-3049.
- (7) Closs, G. L.; Miller, J. R. Intramolecular Long-Distance Electron Transfer in Organic Molecules. *Science* **1988**, *240*, 440-447.
- (8) Fox, L. S.; Kozik, M.; Winkler, J. R.; Gray, H. B. Gaussian Free-Energy Dependence of Electron-Transfer Rates in Iridium Complexes. *Science* **1990**, *247*, 1069-1071.
- (9) Guldi, D. M.; Asmus, K.-D. Electron Transfer from C₇₆ (C_{2v}') and C₇₈ (D₂) to Radical Cations of Various Arenes: Evidence for the Marcus Inverted Region. *J. Am. Chem. Soc.* **1997**, *119*, 5744-5745.
- (10) Kumbhakar, M.; Manna, A.; Sayed, M.; Kumar, A.; Pal, H. Observation of the Marcus Inverted Region for Bimolecular Photoinduced Electron-Transfer Reactions in Viscous Media. *J. Phys. Chem. B* **2014**, *118*, 10704-10715.
- (11) Gould, I. R.; Ege, D.; Moser, J. E.; Farid, S. Efficiencies of photoinduced electron-transfer reactions: role of the Marcus inverted region in return electron transfer within geminate radical-ion pairs. *J. Am. Chem. Soc.* **1990**, *112*, 4290-4301.
- (12) Turró, C.; Zaleski, J. M.; Karabatsos, Y. M.; Nocera, D. G. Bimolecular Electron Transfer in the Marcus Inverted Region. *J. Am. Chem. Soc.* **1996**, *118*, 6060-6067.
- (13) Venkatesh, Y.; Munisamy, V.; Ramakrishna, B.; Kumar, P. H.; Mandal, H.; Bangal, P. R. Photoinduced bimolecular electron transfer from aromatic amines to pentafluorophenyl porphyrin combined with ultrafast charge recombination persistence with Marcus inverted region. *Phys. Chem. Chem. Phys.* **2017**, *19*, 5658-5673.

- (14) Hu, K.; Meyer, G. J. Lateral Intermolecular Self-Exchange Reactions for Hole and Energy Transport on Mesoporous Metal Oxide Thin Films. *Langmuir* **2015**, *31*, 11164-11178.
- (15) Sutin, N. Nuclear, electronic, and frequency factors in electron transfer reactions. *Acc. Chem. Res.* **1982**, *15*, 275-282.
- (16) Krishnan, C. V.; Brunschwig, B. S.; Creutz, C.; Sutin, N. Homogeneous catalysis of the photoreduction of water. 6. Mediation by polypyridine complexes of ruthenium(II) and cobalt(II) in alkaline media. *J. Am. Chem. Soc.* **1985**, *107*, 2005-2015.
- (17) Macartney, D. H.; Mak, S. Kinetics of electron-transfer reactions of the Co(bpyO₂)^{32+/3+} couple in acetonitrile. *Can. J. Chem.* **1992**, *70*, 39-45.
- (18) Song, X.; Lei, Y.; Van Wallendael, S.; Perkovic, M. W.; Jackman, D. C.; Endicott, J. F.; Rillema, D. P. Photoinduced electron-transfer processes involving covalently linked ruthenium and cobalt polypyridyl complexes: comparison of electronic coupling in bridged and nonbridged ruthenium and cobalt complexes. *J. Phys. Chem.* **1993**, *97*, 3225-3236.
- (19) Keeney, L.; Hynes, M. J. Electron transfer reactions of tris(polypyridine)cobalt(III) complexes, [Co(N-N)₃]³⁺, with verdazyl radicals in acetonitrile solution. *Dalton Trans.* **2005**, 133-138.
- (20) Krivokapic, I.; Zerara, M.; Daku, M. L.; Vargas, A.; Enachescu, C.; Ambrus, C.; Tregenna-Piggott, P.; Amstutz, N.; Krausz, E.; Hauser, A. Spin-crossover in cobalt(II) imine complexes. *Coord. Chem. Rev.* **2007**, *251*, 364-378.
- (21) Feldt, S. M.; Gibson, E. A.; Gabrielsson, E.; Sun, L.; Boschloo, G.; Hagfeldt, A. Design of Organic Dyes and Cobalt Polypyridine Redox Mediators for High-Efficiency Dye-Sensitized Solar Cells. *J. Am. Chem. Soc.* **2010**, *132*, 16714-16724.
- (22) Feldt, S. M.; Wang, G.; Boschloo, G.; Hagfeldt, A. Effects of Driving Forces for Recombination and Regeneration on the Photovoltaic Performance of Dye-Sensitized Solar Cells using Cobalt Polypyridine Redox Couples. *J. Phys. Chem. C* **2011**, *115*, 21500-21507.
- (23) Mosconi, E.; Yum, J.-H.; Kessler, F.; Gómez García, C. J.; Zuccaccia, C.; Cinti, A.; Nazeeruddin, M. K.; Grätzel, M.; De Angelis, F. Cobalt Electrolyte/Dye Interactions in Dye-Sensitized Solar Cells: A Combined Computational and Experimental Study. *J. Am. Chem. Soc.* **2012**, *134*, 19438-19453.
- (24) Chen, K. Y.; Du, C.; Patrick, B. O.; Berlinguette, C. P. High-Voltage Dye-Sensitized Solar Cells Mediated by [Co(2,2'-bipyrimidine)₃]²⁺. *Inorg. Chem.* **2017**, *56*, 2383-2386.
- (25) Weaver, M. J.; Yee, E. L. Activation parameters for homogeneous outer-sphere electron-transfer reactions. Comparisons between self-exchange and cross reactions using Marcus' theory. *Inorg. Chem.* **1980**, *19*, 1936-1945.

- (26) Yoshimura, A.; Nozaki, K.; Ikeda, N.; Ohno, T. Photoinduced electron transfer and back electron transfer within binuclear complexes of ruthenium(II) and cobalt(III). *J. Am. Chem. Soc.* **1993**, *115*, 7521-7522.
- (27) Maerker, G.; Case, F. H. The Synthesis of Some 4,4'-Disubstituted 2,2'-Bipyridines. *J. Am. Chem. Soc.* **1958**, *80*, 2745-2748.
- (28) Doi, T.; Nagamiya, H.; Kokubo, M.; Hirabayashi, K.; Takahashi, T. Synthesis of a tetrabenzyl-substituted 10-membered cyclic diamide. *Tetrahedron* **2002**, *58*, 2957-2963.
- (29) Staats, H.; Eggers, F.; Haß, O.; Fahrenkrug, F.; Matthey, J.; Lüning, U.; Lützen, A. Towards Allosteric Receptors – Synthesis of Resorcinarene-Functionalized 2,2'-Bipyridines and Their Metal Complexes. *Eur. J. Org. Chem.* **2009**, *2009*, 4777-4792.
- (30) Ashford, D. L.; Brennaman, M. K.; Brown, R. J.; Keinan, S.; Concepcion, J. J.; Papanikolas, J. M.; Templeton, J. L.; Meyer, T. J. Varying the Electronic Structure of Surface-Bound Ruthenium(II) Polypyridyl Complexes. *Inorg. Chem.* **2015**, *54*, 460-469.
- (31) O'Donnell, R. M.; Sampaio, R. N.; Li, G.; Johansson, P. G.; Ward, C. L.; Meyer, G. J. Photoacidic and Photobasic Behavior of Transition Metal Compounds with Carboxylic Acid Group(s). *J. Am. Chem. Soc.* **2016**, *138*, 3891-3903.
- (32) Lies, S. D.; Lin, S.; Yoon, T. P. Visible Light Photocatalysis of Radical Cation Diels-Alder Cycloadditions: Preparation of Tris(2,2'-bipyrazyl) Ruthenium(II) Bis(tetrakis(3,5-bis(trifluoromethyl)phenyl)borate). *Organic Syntheses* **2016**, *93*, 178-199.
- (33) Chadwick, N.; Kumar, D. K.; Ivaturi, A.; Grew, B. A.; Upadhyaya, H. M.; Yellowlees, L. J.; Robertson, N. Isomer Dependence of Efficiency and Charge Recombination in Dye-Sensitized Solar Cells Using Ru Complex Dyes Bearing Halogen Substituents. *Eur. J. Inorg. Chem.* **2015**, *2015*, 4878-4884.
- (34) Troian-Gautier, L.; Beauvilliers, E. E.; Swords, W. B.; Meyer, G. J. Redox Active Ion-Paired Excited States Undergo Dynamic Electron Transfer. *J. Am. Chem. Soc.* **2016**, *138*, 16815-16826.
- (35) Schwalbe, M.; Schäfer, B.; Görls, H.; Rau, S.; Tschierlei, S.; Schmitt, M.; Popp, J.; Vaughan, G.; Henry, W.; Vos, J. G. Synthesis and Characterisation of Poly(bipyridine)ruthenium Complexes as Building Blocks for Heterosupramolecular Arrays. *Eur. J. Inorg. Chem.* **2008**, *2008*, 3310-3319.
- (36) Xia, H.; Zhu, Y.; Lu, D.; Li, M.; Zhang, C.; Yang, B.; Ma, Y. Ruthenium(II) Complexes with the Mixed Ligands 2,2'-Bipyridine and 4,4'-Dialkyl Ester-2,2'-bipyridine as Pure Red Dopants for a Single-Layer Electrophosphorescent Device. *J. Phys. Chem. B* **2006**, *110*, 18718-18723.

- (37) Furue, M.; Maruyama, K.; Oguni, T.; Naiki, M.; Kamachi, M. Trifluoromethyl-substituted 2,2'-bipyridine ligands. Synthetic control of excited-state properties of ruthenium(II) tris-chelate complexes. *Inorg. Chem.* **1992**, *31*, 3792-3795.
- (38) Bergeron, B. V.; Meyer, G. J. Reductive Electron Transfer Quenching of MLCT Excited States Bound To Nanostructured Metal Oxide Thin Films. *J. Phys. Chem. B* **2003**, *107*, 245-254.
- (39) Brady, M. D.; Sampaio, R. N.; Wang, D.; Meyer, T. J.; Meyer, G. J. Dye-Sensitized Hydrobromic Acid Splitting for Hydrogen Solar Fuel Production. *J. Am. Chem. Soc.* **2017**, *139*, 15612-15615.
- (40) Fulmer, G. R.; Miller, A. J. M.; Sherden, N. H.; Gottlieb, H. E.; Nudelman, A.; Stoltz, B. M.; Bercaw, J. E.; Goldberg, K. I. NMR Chemical Shifts of Trace Impurities: Common Laboratory Solvents, Organics, and Gases in Deuterated Solvents Relevant to the Organometallic Chemist. *Organometallics* **2010**, *29*, 2176-2179.
- (41) Argazzi, R.; Bignozzi, C. A.; Heimer, T. A.; Castellano, F. N.; Meyer, G. J. Enhanced Spectral Sensitivity from Ruthenium(II) Polypyridyl Based Photovoltaic Devices. *Inorg. Chem.* **1994**, *33*, 5741-5749.
- (42) Bard, A. J.; Faulkner, L. R. *Electrochemical Methods : Fundamentals and Applications*. 2nd Edition ed.; Wiley: New York, 2001.
- (43) Arias-Rotondo, D. M.; McCusker, J. K. The photophysics of photoredox catalysis: a roadmap for catalyst design. *Chem. Soc. Rev.* **2016**, *45*, 5803-5820.
- (44) Durham, B.; Caspar, J. V.; Nagle, J. K.; Meyer, T. J. Photochemistry of $\text{Ru}(\text{bpy})_3^{*2+}$. *J. Am. Chem. Soc.* **1982**, *104*, 4803-4810.
- (45) Meyer, T. J. Photochemistry of metal coordination complexes: metal to ligand charge transfer excited states. *Pure Appl. Chem.* **1986**, *58*, 1193-1206.
- (46) Thompson, D. W.; Ito, A.; Meyer, T. J., $[\text{Ru}(\text{bpy})_3]^{2+*}$ and other remarkable metal-to-ligand charge transfer (MLCT) excited states. *Pure Appl. Chem.* **2013**, *85*, 1257.
- (47) Kalyanasundaram, K.; Zakeeruddin, S. M.; Nazeeruddin, M. K. Ligand to metal charge transfer transitions in Ru(III) and Os(III) complexes of substituted 2,2'-bipyridines. *Coord. Chem. Rev.* **1994**, *132*, 259-264.
- (48) Brigham, E. C.; Meyer, G. J. Ostwald Isolation to Determine the Reaction Order for $\text{TiO}_2(\text{e}^-)\text{S}^+ \rightarrow \text{TiO}_2\text{S}$ Charge Recombination at Sensitized TiO_2 Interfaces. *J. Phys. Chem. C* **2014**, *118*, 7886-7893.
- (49) Ardo, S.; Achey, D.; Morris, A. J.; Abrahamsson, M.; Meyer, G. J. Non-Nernstian Two-Electron Transfer Photocatalysis at Metalloporphyrin- TiO_2 Interfaces. *J. Am. Chem. Soc.* **2011**, *133*, 16572-16580.

- (50) Al-Rawashdeh, N. A. F.; Chatterjee, S.; Krause, J. A.; Connick, W. B. Ruthenium Bis-diimine Complexes with a Chelating Thioether Ligand: Delineating 1,10-Phenanthrolyl and 2,2'-Bipyridyl Ligand Substituent Effects. *Inorg. Chem.* **2014**, *53*, 294-307.
- (51) Berkoff, R.; Krist, K.; Gafney, H. D. Measurement of the rates of the electron-transfer reactions between $\text{Ru}(\text{bpy})_3^{3+}$ and $\text{Co}(\text{phen})_3^{2+}$ or $\text{Co}(\text{phen})_3^{2+}$ by flash photolysis techniques. *Inorg. Chem.* **1980**, *19*, 1-7.
- (52) Rillema, D. P.; Allen, G.; Meyer, T. J.; Conrad, D. Redox Properties of Ruthenium(II) Tris Chelate Complexes Containing the Ligands 2,2'-Bipyrazine, 2,2'-Bipyridine, and 2,2'-Bipyrimidine. *Inorg. Chem.* **1983**, *22*, 1617-1622.
- (53) Farnum, B. H.; Gardner, J. M.; Marton, A.; Narducci-Sarjeant, A. A.; Meyer, G. J. Influence of ion pairing on the oxidation of iodide by MLCT excited states. *Dalton Trans.* **2011**, *40*, 3830-3838.
- (54) Gardner, J. M.; Abrahamsson, M.; Farnum, B. H.; Meyer, G. J. Visible Light Generation of Iodine Atoms and I-I Bonds: Sensitized I- Oxidation and I_3^- Photodissociation. *J. Am. Chem. Soc.* **2009**, *131*, 16206-16214.
- (55) Farnum, B. H.; Jou, J. J.; Meyer, G. J. Visible light generation of I-I bonds by Ru-tris(diimine) excited states. *Proc. Natl. Acad. Sci. U.S.A.* **2012**, *109*, 15628-15633.
- (56) Ross, H. B.; Boldaji, M.; Rillema, D. P.; Blanton, C. B.; White, R. P. Photosubstitution in tris chelate complexes of ruthenium(II) containing the ligands 2,2'-bipyrazine, 2,2'-bipyrimidine, 2,2'-bipyridine, and 4,4'-dimethyl-2,2'-bipyridine: energy gap control. *Inorg. Chem.* **1989**, *28*, 1013-1021.
- (57) Ardo, S.; Meyer, G. J. Photodriven heterogeneous charge transfer with transition-metal compounds anchored to TiO_2 semiconductor surfaces. *Chem. Soc. Rev.* **2009**, *38*, 115-164.
- (58) Sandrini, D.; Gandolfi, M. T.; Maestri, M.; Bolletta, F.; Balzani, V. Electron-transfer quenching of the luminescence of ruthenium and osmium polypyridine complexes by cobalt(III) complexes. *Inorg. Chem.* **1984**, *23*, 3017-3023.
- (59) Barbara, P. F.; Meyer, T. J.; Ratner, M. A. Contemporary Issues in Electron Transfer Research. *J. Phys. Chem.* **1996**, *100*, 13148-13168.
- (60) DiMarco, B. N.; Motley, T. C.; Balok, R. S.; Li, G.; Siegler, M. A.; O'Donnell, R. M.; Hu, K.; Meyer, G. J. A Distance Dependence to Lateral Self-Exchange across Nanocrystalline TiO_2 . A Comparative Study of Three Homologous $\text{Ru}^{\text{III/II}}$ Polypyridyl Compounds. *J. Phys. Chem. C* **2016**, *120*, 14226-14235.
- (61) Feldt, S. M.; Lohse, P. W.; Kessler, F.; Nazeeruddin, M. K.; Gratzel, M.; Boschloo, G.; Hagfeldt, A. Regeneration and recombination kinetics in cobalt polypyridine based

- dye-sensitized solar cells, explained using Marcus theory. *Phys. Chem. Chem. Phys.* **2013**, *15*, 7087-97.
- (62) Xie, Y.; Baillargeon, J.; Hamann, T. W. Kinetics of Regeneration and Recombination Reactions in Dye-Sensitized Solar Cells Employing Cobalt Redox Shuttles. *J. Phys. Chem. C* **2015**, *119*, 28155-28166.
- (63) Nelson, J. J.; Amick, T. J.; Elliott, C. M. Mass Transport of Polypyridyl Cobalt Complexes in Dye-Sensitized Solar Cells with Mesoporous TiO₂ Photoanodes. *J. Phys. Chem. C* **2008**, *112*, 18255-18263.

CHAPTER 6: Excited-State Decay Pathways of Tris(bidentate) Cyclometalated Ruthenium(II) Compounds⁵

6.1 Introduction

Ru(II) polypyridyl compounds have been utilized in many applications spanning solar energy harvesting,^{1,2} photocatalysis,^{3,4} chemical sensing,⁵ and photodynamic therapy^{6,7} to name a few. This class of compounds is marked by their long (μs) excited-state lifetimes, photochemical and electrochemical stability, and tunability of their electronic structure through ligand modification. Tailoring of these properties through design choices is made possible by the well-established, detailed understanding of the photophysics and photochemistry of Ru(II) polypyridyl compounds developed over the past sixty years.⁸⁻¹⁵ In the past decade, tris(bidentate) cyclometalated Ru(II) compounds, $[\text{Ru}(\text{N}^{\wedge}\text{N})_2(\text{C}^{\wedge}\text{N})]^+$, where $\text{N}^{\wedge}\text{N}$ is a 2,2'-bipyridine (bpy) or substituted-bpy ligand and $\text{C}^{\wedge}\text{N}$ is the cyclometalating ligand 2-phenylpyridine (ppy) or its derivatives, have received increasingly more attention due to the discovery of more mild synthetic procedures and overall solar conversion efficiencies of over 10% in dye-sensitized solar cells.¹⁶⁻¹⁹ However, few detailed studies exist which characterize the excited-state photophysics of these compounds.^{20,21} Here, a systematic, electrochemical and spectroscopic study of a series of $[\text{Ru}(\text{N}^{\wedge}\text{N})_2(\text{C}^{\wedge}\text{N})]^+$ compounds is reported.

⁵This chapter was previously published in the *Inorganic Chemistry*. Reprinted with permission from Motley, T. C.; Troian-Gautier, L.; Brennaman, M. K.; Meyer, G. J. Excited-State Decay Pathways of Tris(bidentate) Cyclometalated Ruthenium(II) Compounds. *Inorg. Chem.* **2017**, 56, 13579-13592. Copyright 2017 American Chemical Society.

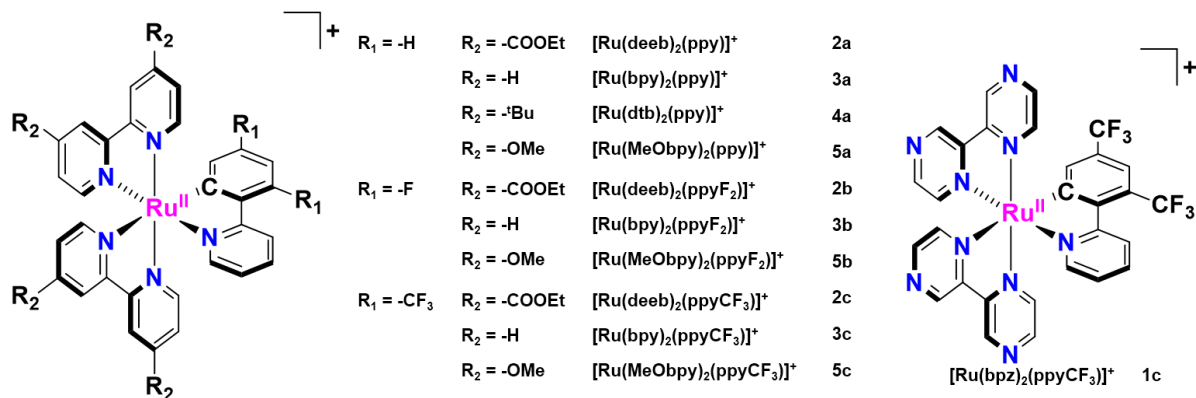
The dominant visible absorption feature of $[\text{Ru}(\text{bpy})_3]^{2+}$, the prototypical Ru(II) polypyridyl compound, is a metal-to-ligand charge transfer (MLCT) band.^{9,22-25} Higher-energy transitions below 350 nm are ligand-centered π to π^* transitions.⁹ Upon photoexcitation into the MLCT band, an electron is excited from a metal-centered t_{2g} orbital to one of the π^* orbitals on one of the bpy ligands. This transition from the highest-occupied molecular orbital (HOMO) to the lowest-unoccupied molecular orbital (LUMO) forms a $^1\text{MLCT}$ state which quickly undergoes intersystem crossing (<300 fs) and vibrational relaxation (ps) to form a $^3\text{MLCT}$ state.^{13,26} Note that due to the large spin-orbit coupling imparted by having a heavy atom such as Ru, the spin quantum number is a poor descriptor; however, the formalism is well established in the field and will be used here.^{27,28}

Photoluminescence from the $^3\text{MLCT}$ state occurs on the μs timescale with quantum yields of a few percent at room temperature.^{29,30} Through careful temperature-dependent spectroscopic studies, this $^3\text{MLCT}$ state has been shown to consist of at least three closely-spaced $^3\text{MLCT}$ states with varying degrees of singlet character that are at thermal equilibrium above 120 K.^{22,23,28,31,32} The excited-state lifetime for $[\text{Ru}(\text{bpy})_3]^{2+}$ exhibits a significant temperature-dependence above 120 K due to activated crossing from the $^3\text{MLCT}$ to ligand-field (LF), e_g^* orbitals which leads to ligand-loss photochemistry.^{7,24,33} For many Ru(II) polypyridyl compounds, the thermally-equilibrated $^3\text{MLCT}$ and LF states are not sufficient as a framework to model the weak temperature-dependence of excited-state relaxation near room temperature. An additional non-emissive state, often called the fourth $^3\text{MLCT}$, was postulated with an energy barrier for activated crossing between 600 and 1000 cm^{-1} .^{9,29,34-37} These observations have been successfully extended to Os(II) polypyridyl compounds.³⁶

Relative to its Ru(II) polypyridyl congener, $[\text{Ru}(\text{N}^{\wedge}\text{N})_2(\text{C}^{\wedge}\text{N})]^+$ has one nitrogen atom

replaced with an isoelectronic carbanion which forms a cyclometalating C-Ru bond. For these cyclometalated compounds, this one change has a profound effect, especially on electronic structure and excited-state lifetime. The decreased symmetry (C_1) of these molecules probably underlies their broad MLCT transitions between 350 and 650 nm.^{17,18,38-40} While the LUMO is still localized on a single N[^]N ligand as for $[\text{Ru}(\text{bpy})_3]^{2+}$, the HOMO is an orbital delocalized across the metal center and the phenyl ring of C[^]N as has been shown through numerous DFT studies.^{17,18,38-40} This has led some to assign these transitions as mixed-metal/ligand-to-ligand charge transfer. It has also been asserted that strong σ -donation from the carbanion leads to the significant destabilization of the LF state making it inaccessible upon photoexcitation at room temperature resulting in enhanced photostability.^{17,18,20,38-42} Furthermore, cyclometalation clearly changes the photophysics of the molecule as evidenced by the previous reports of a short (ns) excited-state lifetime and miniscule quantum yield (<0.5%) for photoluminescence.^{18,21,38-40} Considering the reduced energy gap between the ground and excited states of these cyclometalated compounds, the energy gap law has been suggested to explain the accelerated excited-state relaxation, yet this has not been experimentally evaluated.^{18,21,38-40}

Scheme 6.1. Tris(bidentate) Cyclometalated Ru(II) Compounds Used in this Study



To our knowledge, no comprehensive study of the electrochemical and photophysical properties of $[\text{Ru}(\text{N}^{\wedge}\text{N})_2(\text{C}^{\wedge}\text{N})]^+$ compounds has been conducted despite their emerging importance. For this reason, a series of cyclometalated chromophores was synthesized, Scheme 6.1, and their ground- and excited-state properties were investigated through spectroscopic and electrochemical means. Photoluminescence spectra at 77 K in frozen glasses and at room temperature were obtained for these compounds. The origin of the short, excited-state lifetimes is reported in the context of the energy gap law and Franck-Condon lineshape analyses. Furthermore, the temperature dependence of the excited states between 273 and 343 K is reported. The conceptual framework that has been rigorously developed for describing Ru(II) and Os(II) polypyridyl excited-states has been extended to a series of $[\text{Ru}(\text{N}^{\wedge}\text{N})_2(\text{C}^{\wedge}\text{N})]^+$ compounds to uncover new photophysical insights for these cyclometalated compounds.

6.2 Experimental Methods

6.2.1 Materials

The following solvents and reagents were obtained from the indicated commercial supplier and used without further purification: acetonitrile (CH_3CN , Burdick and Jackson, spectrophotometric grade), dichloromethane (Fisher, certified ACS), ethanol (EtOH, Decon Laboratories, Inc., anhydrous 200 Proof), methanol (MeOH, Fisher, certified ACS), diethyl ether (Fisher, certified ACS), hexanes (Fisher, certified ACS), chloroform (Fisher, certified ACS), acetone (Fisher, certified ACS), basic alumina (Sigma-Aldrich, activated Brockmann 1), neutral alumina (Sigma-Aldrich, activated Brockmann 1), silica-gel (Silicycle, Siliaflash[®] P60), 2,2'-bipyridine (bpy, Aldrich, 99+%), 4,4'-di-*tert*-butyl-2,2'-bipyridine (dtb, Sigma-Aldrich, 98%), 4,4'-dimethoxy-2,2'-bipyridine (MeObpy, Sigma-Aldrich, 97%), argon gas (Airgas, 99.999%), lithium perchlorate (LiClO_4 , Sigma-Aldrich, 99.99% trace metal basis),

ferrocene (Aldrich, 98%), benzeruthenium(II) chloride dimer (Sigma-Aldrich, 97%), 2-phenylpyridine (ppy, Sigma-Aldrich, 98%), 2-(2,4-difluorophenyl)pyridine (ppyF₂, Sigma-Aldrich, 97%), potassium carbonate (K₂CO₃, Em Science, anhydrous), and potassium hexafluorophosphate (KPF₆, Aldrich, 98%). 4,4'-bis(ethoxycarbonyl)-2,2'-bipyridine (deeb),^{43,44} 2-(2,4-bis-(trifluoromethylphenyl)pyridine (ppyCF₃),⁴⁵ 2,2'-bipyrazine (bpz),⁴⁶ [Os(bpy)₃](PF₆)₂,²⁵ [Ru(bpy)₃](PF₆)₂,³⁷ [Ru(bpz)₃](PF₆)₂,⁴⁷ [Ru(deeb)₃](PF₆)₂,⁴⁸ and [Ru(dtb)₃](PF₆)₂ were synthesized as previously reported. An Anton-Paar Microwave Synthesis Reactor Monowave 300 was used to carry out reactions in sealed microwave reaction vials for the specified reactions below.

6.2.2 General Procedure for the Synthesis of [Ru(C^N)(CH₃CN)₄](PF₆)

Benzeneruthenium(II) chloride dimer (0.2 mmol), C^N (0.4 mmol), K₂CO₃ (0.8 mmol), and KPF₆ (0.8 mmol) were added to 6 mL of CH₃CN. The reaction mixture was heated at 100 °C in a sealed, microwave reaction vial for 1 h. The crude product was purified by column chromatography (basic alumina, 3% dichloromethane in CH₃CN), and the first colored band was collected. The pure product was dried under vacuum. All characterization data matched previously reported results.^{19,49,50}

6.2.3 Synthesis of [Ru(ppy)(CH₃CN)₄](PF₆)

Isolated as a yellow solid (183.9 mg, 82% yield). ¹H NMR: (400 MHz, CD₃CN) δ 8.92 (ddd, *J* = 5.6, 1.6, 0.8 Hz, 1H), 7.97 (dd, *J* = 7.4, 1.2 Hz, 1H), 7.86 (dt, *J* = 8.1, 1.1 Hz, 1H), 7.77 – 7.68 (m, 2H), 7.16 (ddd, *J* = 7.2, 5.7, 1.5 Hz, 1H), 7.09 (td, *J* = 7.3, 1.4 Hz, 1H), 6.94 (td, *J* = 7.4, 1.3 Hz, 1H), 2.51 (s, 3H), 2.00 (s, 6H), 1.96 (s, 3H).

6.2.4 Synthesis of [Ru(ppyF₂)(CH₃CN)₄](PF₆)

Isolated as a yellow-green solid (230.7 mg, 94% yield). ¹H NMR: (400 MHz, CD₃CN)

δ 8.97 (ddd, $J = 5.7, 1.7, 0.8$ Hz, 1H), 8.18 – 8.11 (m, 1H), 7.78 (dddd, $J = 8.2, 7.3, 1.7, 0.9$ Hz, 1H), 7.51 (dd, $J = 8.7, 2.4$ Hz, 1H), 7.20 (ddd, $J = 7.3, 5.7, 1.4$ Hz, 1H), 6.48 (ddd, $J = 13.0, 9.5, 2.4$ Hz, 1H), 2.52 (s, 3H), 2.02 (s, 6H), 1.96 (s, 3H).

6.2.5 Synthesis of $[Ru(ppyCF_3)(CH_3CN)_4](PF_6)$

Isolated as an orange solid (250.4 mg, 88% yield). 1H NMR: (400 MHz, CD_3CN) δ 9.15 (ddd, $J = 5.7, 1.8, 0.8$ Hz, 1H), 8.56 – 8.51 (m, 1H), 8.25 – 8.20 (m, 1H), 7.86 (ddd, $J = 8.5, 7.5, 1.7$ Hz, 1H), 7.58 (d, $J = 1.9$ Hz, 1H), 7.33 (ddd, $J = 7.3, 5.6, 1.2$ Hz, 1H), 2.52 (s, 3H), 2.01 (s, 6H), 1.96 (s, 3H).

6.2.6 Synthesis of $[Ru(deeb)_2(ppy)](PF_6)$

Into a reaction flask, $[Ru(ppy)(CH_3CN)_4](PF_6)$ (71.8 mg, 0.13 mmol) and deeb (141 mg, 0.47 mmol) were added to 30 mL of EtOH. The suspension was heated to reflux for 15 h. The black product was purified by column chromatography (basic alumina, 3:1 chloroform: CH_3CN), and the first dark green band to elute was collected and taken to dryness to yield a black solid. The product was further purified by recrystallization through the slow vapor diffusion of diethyl ether into CH_3CN to afford black crystals (46.1 mg, 36% yield). All characterization data matched previously reported results.⁴⁹ 1H NMR: (400 MHz, $DMSO-d_6$) δ 9.19 (d, $J = 0.9$ Hz, 1H), 9.11 (d, $J = 1.8$ Hz, 1H), 9.07 (t, $J = 2.4$ Hz, 2H), 8.23 (d, $J = 8.2$ Hz, 1H), 8.16 (d, $J = 6.0$ Hz, 1H), 8.02 (d, $J = 5.6$ Hz, 1H), 7.99 – 7.93 (m, 3H), 7.92 (dd, $J = 5.6, 1.6$ Hz, 1H), 7.88 (dd, $J = 6.0, 1.8$ Hz, 1H), 7.86 – 7.80 (m, 2H), 7.71 (dd, $J = 6.0, 1.9$ Hz, 1H), 7.44 (dd, $J = 6.1, 1.4$ Hz, 1H), 7.07 (ddd, $J = 7.2, 5.7, 1.4$ Hz, 1H), 6.92 (td, $J = 7.4, 1.3$ Hz, 1H), 6.83 (td, $J = 7.3, 1.3$ Hz, 1H), 6.18 (dd, $J = 7.4, 1.3$ Hz, 1H), 4.47 – 4.35 (m, 8H), 1.39 – 1.31 (m, 12H).

6.2.7 Synthesis of $[Ru(bpy)_2(ppy)](PF_6)$

Into a reaction flask, $[Ru(ppy)(CH_3CN)_4](PF_6)$ (120.0 mg, 0.21 mmol) and bpy (71.1 mg, 0.46 mmol) were combined with 10 mL of EtOH and heated to reflux for 17 h. The crude product was purified by column chromatography (basic alumina, CH_3CN), and the first violet fraction to elute was collected and evaporated to dryness yielding the violet product (108.4 mg, 72% yield). All characterization data matched previously reported results.⁵¹ 1H NMR: (400 MHz, CD_3CN) δ 8.45 (d, J = 8.2 Hz, 1H), 8.38 (d, J = 8.0 Hz, 1H), 8.32 (d, J = 7.0 Hz, 1H), 8.30 (d, J = 7.0 Hz, 1H), 8.05 (ddd, J = 5.6, 1.5, 0.7 Hz, 1H), 8.01 (d, J = 8.1 Hz, 1H), 7.97 (ddd, J = 8.2, 7.6, 1.6 Hz, 1H), 7.86 – 7.75 (m, 6H), 7.72 (ddd, J = 5.8, 1.2, 0.7 Hz, 1H), 7.68 (ddd, J = 8.2, 7.5, 1.6 Hz, 1H), 7.56 (ddd, J = 5.8, 1.4, 0.7 Hz, 1H), 7.40 (ddd, J = 7.6, 5.4, 1.2 Hz, 1H), 7.23 – 7.17 (m, 3H), 6.95 – 6.86 (m, 2H), 6.82 (td, J = 7.2, 1.4 Hz, 1H), 6.41 (dd, J = 7.4, 1.4 Hz, 1H).

6.2.8 Synthesis of $[Ru(dtb)_2(ppy)](PF_6)$

Into a reaction flask, $[Ru(ppy)(CH_3CN)_4](PF_6)$ (161.2 mg, 0.29 mmol) and dtb (161.8 mg, 0.60 mmol) were combined with 25 mL of MeOH. The reaction mixture was heated to reflux for 15 h. The crude reaction mixture was evaporated to dryness. The dark purple solid was purified by column chromatography (neutral alumina, 1.5% MeOH in dichloromethane), and the first colored fraction was collected and evaporated to dryness. The product was further purified by recrystallization through the diffusion of hexanes into dichloromethane. The resulting violet crystals were collected (90.6 mg, 34 % yield). All characterization data matched previously reported results.⁵² 1H NMR: (400 MHz, CD_3CN) δ 8.47 (d, J = 1.9 Hz, 1H), 8.39 (d, J = 2.1 Hz, 1H), 8.34 (dd, J = 7.3, 2.1 Hz, 2H), 7.99 (d, J = 8.5 Hz, 1H), 7.90 (d, J = 6.0 Hz, 1H), 7.84 – 7.80 (m, 1H), 7.72 (d, J = 5.8 Hz, 1H), 7.68 – 7.62 (m, 2H), 7.60 – 7.53

(m, 2H), 7.43 (dd, $J = 5.9, 1.9$ Hz, 1H), 7.21 (ddd, $J = 9.1, 6.1, 2.1$ Hz, 2H), 7.15 (dd, $J = 6.1, 2.1$ Hz, 1H), 6.91 (ddd, $J = 7.2, 5.7, 1.3$ Hz, 1H), 6.85 (td, $J = 7.4, 1.3$ Hz, 1H), 6.77 (td, $J = 7.3, 1.3$ Hz, 1H), 6.44 (dd, $J = 7.4, 1.3$ Hz, 1H), 1.41 (s, 9H), 1.39 – 1.34 (m, 27H).

6.2.9 Synthesis of $[Ru(MeObpy)_2(ppy)](PF_6)$

Into a reaction flask, $[Ru(ppy)(CH_3CN)_4](PF_6)$ (136.0 mg, 0.24 mmol) and MeObpy (100.0 mg, 0.46 mmol) were combined with 10 mL of CH_3CN . The reaction mixture was heated at 160 °C for 1 h using a microwave reactor. The reaction mixture was evaporated to dryness. The crude product was purified using column chromatography (neutral alumina, 3:1 chloroform: CH_3CN), and the first dark-brown band to elute was collected and dried. The product was dissolved in the minimum amount of acetone and crashed out with hexanes. The dark-purple to brown solid was collected via filtration (81.2 mg, 42% yield). 1H NMR: (400 MHz, $DMSO-d_6$) δ 8.36 (d, $J = 2.6$ Hz, 1H), 8.30 (d, $J = 2.7$ Hz, 1H), 8.24 (dd, $J = 4.5, 2.8$ Hz, 2H), 8.06 (d, $J = 7.9$ Hz, 1H), 7.93 (br s, 1H), 7.72 – 7.66 (m, 1H), 7.63 (d, $J = 6.4$ Hz, 2H), 7.57 (d, $J = 5.7$ Hz, 1H), 7.36 (br s, 1H), 7.28 (br s, 1H), 7.21 (dd, $J = 6.3, 2.5$ Hz, 1H), 7.07 – 6.92 (m, 4H), 6.83 (br s, 1H), 6.64 (br s, 1H), 6.31 (br s, 1H), 3.99 (s, 3H), 3.95 (s, 3H), 3.93 (s, 3H), 3.91 (s, 3H). ESI-MS: Found (calcd.) for $C_{35}H_{32}N_5O_4Ru$ m/z^+ 688.1489 (688.1498). EA: Found (calcd.) for $C_{35}H_{32}F_6N_5O_4PRu$: C 51.10 (50.48), H 4.13 (3.87), N 8.57 (8.41).

6.2.10 Synthesis of $[Ru(deeb)_2(ppyF_2)](PF_6)$

Into a reaction flask, $[Ru(ppyF_2)(CH_3CN)_4](PF_6)$ (114.9 mg, 0.19 mmol) and deeb (122.8 mg, 0.41 mmol) were combined with 30 mL of EtOH. The suspension was heated to reflux for 24 h. The crude reaction mixture was evaporated to dryness. The dark-purple solid was purified by column chromatography (neutral alumina, 3:1 chloroform: CH_3CN), and the first purple band to elute was collected and evaporated to dryness. The compound was

recrystallized by the slow vapor diffusion of diethyl ether into CH₃CN to afford dark violet crystals (57.5 mg, 29% yield). All characterization data matched previously reported results.⁴⁹

¹H NMR: (400 MHz, DMSO-*d*₆) δ 9.20 (d, *J* = 1.8 Hz, 1H), 9.13 (d, *J* = 1.8 Hz, 1H), 9.12 – 9.08 (m, 2H), 8.26 (d, *J* = 8.5 Hz, 1H), 8.15 (d, *J* = 5.9 Hz, 1H), 7.97 (d, *J* = 5.7 Hz, 1H), 7.94 – 7.86 (m, 6H), 7.73 (dd, *J* = 5.9, 1.8 Hz, 1H), 7.55 (dd, *J* = 5.8, 1.6 Hz, 1H), 7.12 (ddd, *J* = 7.3, 5.6, 1.3 Hz, 1H), 6.69 (ddd, *J* = 12.9, 9.4, 2.4 Hz, 1H), 5.75 (dd, *J* = 7.9, 2.4 Hz, 1H), 4.47 – 4.35 (m, 8H), 1.39 – 1.31 (m, 12H).

6.2.11 Synthesis of [Ru(*bpy*)₂(*ppyF*₂)](PF₆)

Into a reaction flask, [Ru(*ppyF*₂)(CH₃CN)₄](PF₆) (186.9 mg, 0.31 mmol) and *bpy* (99.5 mg, 0.64 mmol) were added to 20 mL of CH₃CN. The reaction mixture was heated at 160 °C for 20 min in a microwave reactor. The reaction mixture was evaporated to dryness. The crude product was purified using column chromatography (neutral alumina, 3:1 chloroform:CH₃CN), and the reddish-purple fraction was collected and evaporated to dryness. The product was dissolved in the minimum amount of CH₃CN and recrystallized by the slow vapor diffusion of diethyl ether into CH₃CN affording red-violet crystals (29.3 mg, 13% yield). All characterization data matched previously reported results.²¹ ¹H NMR: (400 MHz, DMSO-*d*₆) δ 8.78 (d, *J* = 8.2 Hz, 1H), 8.71 (d, *J* = 8.1 Hz, 1H), 8.67 (d, *J* = 4.5 Hz, 1H), 8.65 (d, *J* = 4.5 Hz, 1H), 8.22 (d, *J* = 8.4 Hz, 1H), 8.11 (td, *J* = 7.9, 1.5 Hz, 1H), 8.00 – 7.93 (m, 3H), 7.92 (dd, *J* = 5.7, 1.4 Hz, 1H), 7.84 – 7.78 (m, 1H), 7.75 (dd, *J* = 5.5, 1.4 Hz, 1H), 7.66 (dd, *J* = 5.9, 1.3 Hz, 1H), 7.64 (dd, *J* = 5.9, 1.2 Hz, 1H), 7.60 (dd, *J* = 5.7, 1.4 Hz, 1H), 7.56 (ddd, *J* = 7.2, 5.4, 1.1 Hz, 1H), 7.45 – 7.37 (m, 3H), 7.10 (ddd, *J* = 7.2, 5.7, 1.3 Hz, 1H), 6.59 (ddd, *J* = 12.3, 9.4, 2.4 Hz, 1H), 5.82 (dd, *J* = 8.2, 2.3 Hz, 1H).

6.2.12 Synthesis of $[Ru(MeObpy)_2(ppyF_2)](PF_6)$

Into a reaction flask, $[Ru(ppyF_2)(CH_3CN)_4](PF_6)$ (115.9 mg, 0.19 mmol) and MeObpy (88.5 mg, 0.41 mmol) were combined with 15 mL of CH_3CN . The reaction mixture was heated at 160 °C for 1 h in a microwave reactor. The crude maroon reaction mixture was taken to dryness. The solid was purified by column chromatography on neutral alumina. A gradient elution was used starting with 19:1 chloroform: CH_3CN to first elute excess MeObpy followed by 3:1 chloroform: CH_3CN . The first violet fraction to elute was collected and taken to dryness. The compound was further purified by dissolving it in the minimal amount of acetone and precipitating it from solution with hexanes. The violet powder was collected via filtration (34.9 mg, 21% yield). 1H NMR: (400 MHz, $DMSO-d_6$) δ 8.36 (d, J = 2.6 Hz, 1H), 8.31 (d, J = 2.6 Hz, 1H), 8.28 (dd, J = 6.4, 2.8 Hz, 2H), 8.18 (d, J = 8.5 Hz, 1H), 7.77 – 7.69 (m, 2H), 7.59 (dd, J = 12.8, 6.4 Hz, 2H), 7.41 (d, J = 6.5 Hz, 1H), 7.32 (d, J = 6.5 Hz, 1H), 7.18 (dd, J = 6.3, 2.6 Hz, 1H), 7.09 – 7.03 (m, 4H), 6.50 (ddd, J = 12.2, 9.4, 2.4 Hz, 1H), 5.99 (dd, J = 8.3, 2.4 Hz, 1H), 3.98 (s, 3H), 3.96 (s, 3H), 3.93 (s, 3H), 3.92 (s, 3H). ESI-MS: Found (calcd.) for $C_{35}H_{30}F_2N_5O_4Ru$ m/z^+ 724.1296 (724.1309). EA: Found (calcd.) for $C_{35}H_{30}F_8N_5O_4PRu$: C 48.26 (48.39), H 3.73 (3.48), N 8.13 (8.06).

6.2.13 Synthesis of $[Ru(bpz)_2(ppyCF_3)](PF_6)$

Into a reaction flask, $[Ru(ppyCF_3)(CH_3CN)_4](PF_6)$ (222.1 mg, 0.32 mmol) and bpz (101.7 mg, 0.64 mmol) were combined in 25 mL of EtOH. The reaction mixture was heated to reflux for 7 days. The crude, dark-violet reaction mixture was evaporated to dryness. Column chromatography (basic alumina, CH_3CN) was used to purify the compound. Deionized water was slowly added to the eluent to speed up the elution of the product. Several colored impurities eluted first followed by a large maroon band which was collected and evaporated to

dryness. The crude maroon product was further purified by dissolving the compound in the minimum amount of CH₃CN and allowing for the slow vapor diffusion of diethyl ether to yield dark maroon crystals (63.8 mg, 24% yield). ¹H NMR: (400 MHz, CD₃CN) δ 9.77 (d, *J* = 1.4 Hz, 1H), 9.65 (d, *J* = 1.3 Hz, 1H), 9.60 (d, *J* = 1.3 Hz, 1H), 9.58 (d, *J* = 1.3 Hz, 1H), 8.64 (d, *J* = 3.1 Hz, 1H), 8.43 – 8.38 (m, 4H), 7.93 (ddd, *J* = 8.7, 7.5, 1.7 Hz, 1H), 7.88 (dd, *J* = 3.3, 1.3 Hz, 1H), 7.86 (dd, *J* = 3.0, 1.4 Hz, 1H), 7.78 (dd, *J* = 3.4, 1.3 Hz, 1H), 7.74 (ddd, *J* = 5.6, 1.7, 0.8 Hz, 1H), 7.66 (dd, *J* = 3.4, 1.2 Hz, 1H), 7.64 (d, *J* = 1.8 Hz, 1H), 7.18 (ddd, *J* = 7.2, 5.7, 1.3 Hz, 1H), 6.82 (s, 1H). ESI-MS: Found (calcd.) for C₂₉H₁₈F₆N₉Ru m/z⁺ 708.0619 (708.0633). EA: Found (calcd.) for C₂₉H₁₈F₁₂N₉PRu: C 40.60 (40.86), H 2.31 (2.13), N 14.55 (14.79).

6.2.14 Synthesis of [Ru(deeb)₂(ppyCF₃)](PF₆)

Into a reaction flask, [Ru(ppyCF₃)(CH₃CN)₄](PF₆) (250.4 mg, 0.36 mmol) and deeb (220.3 mg, 0.73 mmol) were combined in 25 mL of EtOH. The reaction mixture was heated to reflux for 38 h. The dark-violet reaction mixture was cooled and evaporated to dryness. The compound was dissolved in the minimum amount of 400:1 CH₃CN: sat. KPF₆(aq) and purified on a silica gel column. The amount of sat. KPF₆(aq) was carefully increased until a dark-purple band began to move on the column. This band was collected and taken to dryness. The band was dissolved in ~50 mL chloroform and was washed three times with deionized water to remove excess salt. The organic layer was evaporated to dryness. Further purification was achieved by dissolving the compound in the minimum amount of dichloromethane and precipitating it with hexanes to yield a purple solid which was collected by filtration (122.4 mg, 30% yield). ¹H NMR: (400 MHz, CD₃CN) δ 9.00 (s, 1H), 8.94 (d, *J* = 1.7 Hz, 1H), 8.90 (s, 2H), 8.38 (d, *J* = 9.2 Hz, 1H), 8.08 (d, *J* = 5.9 Hz, 1H), 7.89 – 7.82 (m, 5H), 7.70 (dtd, *J* =

12.0, 5.9, 1.7 Hz, 4H), 7.58 (s, 1H), 7.10 (t, $J = 6.4$ Hz, 1H), 6.87 (s, 1H), 4.48 – 4.39 (m, 8H), 1.43 – 1.37 (m, 12H). ESI-MS: Found (calcd.) for $C_{45}H_{38}F_6N_5O_8Ru$ m/z^+ 992.1674 (992.1668). EA: Found (calcd.) for $C_{45}H_{38}F_{12}N_5O_8PRu$: C 46.91 (47.45), H 3.52 (3.37), N 6.18 (6.16).

6.2.15 Synthesis of $[Ru(bpy)_2(ppyCF_3)](PF_6)$

Into a reaction flask, $[Ru(ppyCF_3)(CH_3CN)_4](PF_6)$ (221.7 mg, 0.32 mmol) and bpy (100.4 mg, 0.64 mmol) were added to 6 mL of CH_3CN . The reaction mixture was heated for 1 h at 100 °C in a microwave reactor. The deep-red reaction mixture was evaporated to dryness. The crude product was purified by column chromatography (silica gel, 400:1 CH_3CN : sat. $KPF_6(aq)$), and a maroon band was collected and taken to dryness. The crude product was then dissolved in ~50 mL of chloroform and washed three times with deionized water to remove excess salt. The organic fraction was evaporated to dryness. Further purification was achieved by dissolving the compound into the minimum amount of dichloromethane and precipitating the compound in hexanes. The maroon solid was collected via filtration (70.3 mg, 26% yield). 1H NMR: (400 MHz, CD_3CN) δ 8.47 (d, $J = 8.2$ Hz, 1H), 8.40 (d, $J = 8.0$ Hz, 1H), 8.34 (t, $J = 8.1$ Hz, 3H), 8.01 (td, $J = 7.9, 1.6$ Hz, 1H), 7.91 – 7.82 (m, 5H), 7.81 – 7.73 (m, 2H), 7.65 (dd, $J = 9.3, 5.7$ Hz, 2H), 7.50 (s, 1H), 7.41 (dd, $J = 7.5, 5.5$ Hz, 1H), 7.29 – 7.18 (m, 3H), 7.06 (t, $J = 6.6$ Hz, 1H), 6.98 (s, 1H). ESI-MS: Found (calcd.) for $C_{33}H_{22}F_6N_5Ru$ m/z^+ 704.0809 (704.0823). EA: Found (calcd.) for $C_{33}H_{22}F_{12}N_5PRu$: C 46.45 (46.71), H 2.83 (2.61), N 8.25 (8.24).

6.2.16 Synthesis of $[Ru(MeObpy)_2(ppyCF_3)](PF_6)$

Into a reaction flask, $[Ru(ppyCF_3)(CH_3CN)_4](PF_6)$ (52.6 mg, 0.075 mmol) and MeObpy (41.5 mg, 0.19 mmol) were combined in 4 mL of CH_3CN . The reaction mixture was heated at 100 °C for 1.5 h in a microwave reactor. The crude, violet reaction mixture was taken

to dryness. The solid was purified by column chromatography (neutral alumina). A gradient elution was used starting with 9:1 chloroform:CH₃CN to first elute excess MeObpy followed by 3:1 chloroform:CH₃CN. The first violet fraction to elute was collected and taken to dryness. The compound was further purified by dissolving it in the minimal amount of acetone and precipitating with hexanes. The violet solid was collected via filtration (12.3 mg, 17% yield). ¹H NMR: (400 MHz, CD₃CN) δ 8.34 (d, *J* = 8.4 Hz, 1H), 7.99 (d, *J* = 2.6 Hz, 1H), 7.96 (dd, *J* = 5.6, 0.9 Hz, 1H), 7.94 (d, *J* = 2.8 Hz, 1H), 7.92 (d, *J* = 2.8 Hz, 1H), 7.89 (d, *J* = 2.7 Hz, 1H), 7.74 (ddd, *J* = 8.7, 7.4, 1.7 Hz, 1H), 7.61 (d, *J* = 6.2 Hz, 1H), 7.56 (d, *J* = 6.5 Hz, 1H), 7.51 – 7.43 (m, 2H), 7.32 (d, *J* = 6.5 Hz, 1H), 7.17 (s, 1H), 7.06 (ddd, *J* = 7.1, 5.7, 1.3 Hz, 1H), 7.02 (dd, *J* = 6.3, 2.6 Hz, 1H), 6.90 (dd, *J* = 6.5, 2.8 Hz, 1H), 6.83 (dd, *J* = 6.5, 2.8 Hz, 1H), 6.79 (dd, *J* = 6.5, 2.8 Hz, 1H), 4.01 (s, 3H), 3.98 (s, 3H), 3.95 (s, 3H), 3.95 (s, 3H). ESI-MS: Found (calcd.) for C₃₇H₃₀F₆N₅O₄Ru m/z⁺ 824.1242 (824.1245) EA: Found (calcd.) for C₃₇H₃₀F₁₂N₅O₄PRu: C 45.23 (45.88), H 3.42 (3.12), N 7.22 (7.23).

6.2.17 Nuclear Magnetic Resonance Spectroscopy (NMR)

¹H NMR spectra were obtained on a Bruker Avance III 400 MHz spectrometer at room temperature with the observed signals referenced to the residual protio-solvent peaks.⁵³ ¹H NMR data was processed using MestReNova 11.0.

6.2.18 Electrospray Ionization-Mass Spectrometry (ESI-MS)

Samples were analyzed with a hybrid LTQ FT (ICR 7T) (ThermoFisher, Bremen, Germany) mass spectrometer. Samples were introduced via a micro-electrospray source at a flow rate of 3 μL/min. Over 200 time-domain transients were averaged in the mass spectrum. ESI source conditions were set as: sheath gas (nitrogen) 3 arb, auxiliary gas (nitrogen) 0 arb, sweep gas (nitrogen) 0 arb, capillary temperature 275 °C, capillary voltage 35 V and tube lens

voltage 110 V. The mass range was set to 150-1000 m/z . All measurements were recorded at a resolution setting of 100,000. Solutions were analyzed at 0.1 mg/mL or less based on responsiveness to the ESI mechanism. Xcalibur (ThermoFisher, Bremen, Germany) was used to analyze the data. Molecular formula assignments were determined with Molecular Formula Calculator (v 1.2.3). Low-resolution mass spectrometry (linear ion trap) provided independent verification of molecular weight distributions. All observed species were singly charged, as verified by unit m/z separation between mass spectral peaks corresponding to the ^{12}C and $^{13}\text{C}^{12}\text{C}_{c-1}$ isotope for each elemental composition.

6.2.19 Elemental Analysis (EA)

Elemental analysis for carbon, nitrogen, and hydrogen was performed by Atlantic Microlabs, LLC.

6.2.20 Square Wave Voltammetry

Square wave voltammetry was performed using an Epsilon electrochemical analyzer using a standard three-electrode arrangement. Glassy carbon disk electrodes were used as the working and counter electrodes. Potentials were measured against a nonaqueous silver wire pseudoreference electrode (Pine Research Instruments) filled with a CH_3CN solution containing 0.1 M LiClO_4 . The pseudoreference electrode was externally calibrated versus the ferrocenium/ferrocene ($\text{Fc}^{+/0}$) reduction potential in a CH_3CN solution containing 0.2 M LiClO_4 , which is 0.31 V vs the standard calomel electrode (SCE).⁵⁴ SCE is 0.241 V vs the normal hydrogen electrode (NHE).⁵⁴ All potentials reported are vs NHE unless otherwise stated.

6.2.21 UV-Visible Absorption

All steady-state UV-visible spectra were recorded on either a Varian Cary 50 or Varian

Cary 60 spectrophotometer at room temperature in a quartz cuvette with a 1.0 cm pathlength.

6.2.22 Steady-State Photoluminescence and Quantum Yield Determination

Room temperature photoluminescence (PL) spectra for $[\text{Ru}(\text{N}^{\wedge}\text{N})_2(\text{C}^{\wedge}\text{N})]^+$ and 77 K PL spectra for $[\text{Ru}(\text{N}^{\wedge}\text{N})_3]^{2+}$ and $[\text{Ru}(\text{N}^{\wedge}\text{N})_2(\text{C}^{\wedge}\text{N})]^+$ were recorded on an Edinburgh FLS920 Fluorescence Spectrophotometer using a 450 W Xenon arc lamp as the excitation source. PL was detected at a right angle to the excitation beam using a photomultiplier tube (Hamamatsu 2658P). Room temperature PL spectra for $[\text{Ru}(\text{N}^{\wedge}\text{N})_3]^{2+}$ were obtained on a Horiba Scientific FL-1000 Fluorolog using a 450 W Xenon arc lamp as the excitation source, and PL was detected at a right angle to the excitation beam using a photomultiplier tube (Hamamatsu R928P). Emission spectra were corrected for the instrument's spectral response. All room-temperature spectra were obtained from Ar-sparged samples in CH_3CN . The quantum yields of PL, Φ_{PL} , for the compounds were determined in CH_3CN at room temperature using comparative actinometry via the optically dilute method with either $[\text{Os}(\text{bpy})_3](\text{PF}_6)_2$ or $[\text{Ru}(\text{bpy})_3](\text{PF}_6)_2$ as the reference ($\Phi_{\text{PL}} = 0.005$ or $\Phi_{\text{PL}} = 0.095$).⁵⁵⁻⁵⁷ For 77 K measurements, the temperature was maintained using a Janis Dual Reservoir VPF System with 4-way fused quartz windows. All 77 K spectra were obtained from compounds in 4:1 EtOH:MeOH glasses.

6.2.23 Temperature-Dependent, Time-Resolved Photoluminescence

Time-resolved PL data were collected on the FLS920 by the time-correlated single photon counting technique (TCSPC). Excitation was achieved with a 444.2 nm diode laser (Edinburgh Instruments EPL-445, 73 ps full-width at half-maximum pulse width) operated at either 2, 5, 10, or 20 MHz (0.488, 0.195, 0.098, 0.049 ns/point, respectively). The spectral bandwidth of the emission monochromator was set to 20 nm. A 630 nm, long-pass filter was used after the sample to eliminate scatter and second-order grating effects. Temperature control

over the range of 273 to 343 K (± 0.2 K) was achieved by using a thermoelectrically cooled, 4-window cuvette holder (Quantum Northwest TLC 50 controlled by aTC 125).

6.2.24 Single-Mode, Franck-Condon Lineshape Analysis

A single-mode, Franck-Condon lineshape analysis was used to analyze the 77 K PL spectra to provide quantitative information about the vibrational modes and structural changes involved in ground and excited states. Fitting was performed in Wolfram Mathematica 10.4, and least-squares error minimization was achieved using the Levenberg-Marquardt method. Details of this process are given elsewhere and only briefly discussed here.^{30,55} The PL intensities originally obtained as a function of wavelength were converted to quanta per second and recast as a function of wavenumber as detailed by Parker and Rees.⁵⁸ Equation 6.1 shows the form of the function used to fit the spectra. In the equation, $I(\tilde{\nu})$ is the PL intensity as a function of wavenumber, E_0 is the energy of the transition between the lowest vibrational levels of the ground and excited states, $\hbar\omega_M$ is the weighted-average vibronic acceptor mode observed in the PL spectrum, $\Delta\nu_{1/2}$ is the full-width at half-maximum of the vibrational components in the spectra, and S_M is the Huang-Rhys factor and is a measure of the geometric distortion between the ground and excited states. The vibronic quantum number in the ground state acceptor mode is given by ν , and all spectra were fit using the summation of $\nu = 0$ to $\nu = 5$ vibrational levels in the ground state. Using $\hbar\omega_M$ and S_M obtained from the 77 K PL spectra, the room temperature spectra were fit.

$$I(\tilde{\nu}) = \sum_{\nu=0}^5 \left[\left(\frac{E_0 - \nu\hbar\omega_M}{E_0} \right)^3 \left(\frac{S_M}{\nu!} \right) e^{\left(-4 \ln(2) \left(\frac{\tilde{\nu} - E_0 + \nu\hbar\omega_M}{\Delta\nu_{1/2}} \right)^2 \right)} \right] \quad (6.1)$$

6.2.25 Time-Correlated Single Photon Counting

Emission lifetimes, τ_{obs} , were obtained by fitting the TCSPC data using the free

software, DecayFit.⁵⁹ The emission trace was fit using a reconvolution process with the instrument response function (IRF) measured using a scattering suspension at the excitation wavelength.

6.2.26 Arrhenius Analysis

Arrhenius data fitting was performed in OriginPro 2016 with least-squares error minimization achieved using the Levenberg-Marquardt method.

6.3 Results

Scheme 6.1 shows the chemical structures of the compounds used in this study, including six new compounds: $[\text{Ru}(\text{MeObpy})_2(\text{ppy})]^+$, $[\text{Ru}(\text{MeObpy})_2(\text{ppyF}_2)]^+$, $[\text{Ru}(\text{bpz})_2(\text{ppyCF}_3)]^+$, $[\text{Ru}(\text{deeb})_2(\text{ppyCF}_3)]^+$, $[\text{Ru}(\text{bpy})_2(\text{ppyCF}_3)]^+$, and $[\text{Ru}(\text{MeObpy})_2(\text{ppyCF}_3)]^+$. The synthesis of each $[\text{Ru}(\text{N}^{\wedge}\text{N})_2(\text{C}^{\wedge}\text{N})]^+$ compound was performed in two steps: 1) reaction of a ruthenium dimer under basic conditions to promote C-H bond activation of the substituted-2-phenylpyridine ($\text{C}^{\wedge}\text{N}$) yielding the cyclometalated, solvato-complex followed by 2) coordination of the substituted-bipyridine ($\text{N}^{\wedge}\text{N}$) ligands. In step 1, formation of the cyclometalated intermediate was achieved with high yields that were comparable to previously reported procedures.^{19,49,50} The use of a microwave reactor significantly reduced reaction times (down to 1 h) relative to traditional heating conditions. Microwave reaction conditions also drastically reduced reaction times for coordination of the $\text{N}^{\wedge}\text{N}$ ligands, step 2; however, significant ligand scrambling was observed in several cases. Decarboxylation was evident in the cases of $[\text{Ru}(\text{deeb})_2(\text{C}^{\wedge}\text{N})]^+$ as has been previously reported for carboxylate- and ester-substituted bipyridines.⁶⁰ Therefore, traditional heating and microwave reaction conditions were attempted in all cases with the highest-yielding synthetic method for each reported in the Experimental Section.

Square wave voltammetry was performed for each compound in CH₃CN solutions containing 0.1 M LiClO₄ at room temperature with the measured redox potentials (E°) reported in Table 6.1. The square wave voltammogram for each cyclometalated compound exhibits four peaks as exemplified in the representative voltammogram for **[Ru(bpy)₂(ppy)]⁺**, Figure 6.1. In all cases, a reversible oxidation of the Ru metal center was observed, $E^\circ(\text{Ru}^{2+/+})$, Table 6.1. Two, reversible, ligand-based reductions were measured between -0.70 – -1.55 and -0.95 – -1.80 V vs NHE that were assigned to reductions of the two N^N ligands and are attributed as $E^\circ(\text{Ru}^{+/0})$ and $E^\circ(\text{Ru}^{0/-})$, respectively in Table 6.1.

At applied potentials more negative than -1.5 V, a third reduction, $E^\circ(\text{Ru}^{-/2-})$, was observed that resulted in the formation of a film on the glassy carbon electrode surface. Due to the broadness of this reduction peak in the square wave voltammogram as well as the film deposition, it was considered to be irreversible.^{61,62} Work by Thompson *et al.* on [Ir(ppy)₃] and [Ir(ppyF₂)₃] showed that the first ligand reduction for these compounds occurs near -1.8 and -2 V vs NHE, respectively.⁶³ By analogy, this reduction was ascribed to the C^N ligand, but this assignment is tentative. In the case of **[Ru(deeb)₂(C^N)]⁺** and **[Ru(bpz)₂(C^N)]⁺**, more than three reduction peaks were observed. It may be that the third reduction peak observed in these cases was a second reduction of a N^N ligand.

Table 6.1. Electrochemical Data for the Studied Compounds

N [^] N		Compound	<i>E</i> ^o (V vs NHE)					
			(Ru ^{2+/+})	(Ru ^{+/⁰})	(Ru ^{0/-1})	(Ru ^{-1/-2}) ^c	(Ru ^{2+/+*}) ^d	(Ru ^{+*/⁰}) ^e
bpz	1c	[Ru(bpz) ₂ (ppyCF ₃)] ⁺	1.31	-0.73	-0.97	-1.48	-0.43	1.01
	2a	[Ru(deeb) ₂ (ppy)] ⁺	0.87	-0.97	-1.23	-1.65	-0.91	0.81
	2b	[Ru(deeb) ₂ (ppyF ₂)] ⁺	1.00	-0.95	-1.18	-1.63	-0.68	0.73
	2c	[Ru(deeb) ₂ (ppyCF ₃)] ⁺	1.07	-0.90	-1.13	-1.44	-0.64	0.81
bpy	3a	[Ru(bpy) ₂ (ppy)] ⁺	0.69	-1.38	-1.69	-2.07	-1.04	0.35
	3b	[Ru(bpy) ₂ (ppyF ₂)] ⁺	0.77	-1.42	-1.70	-2.18	-1.03	0.38
	3c	[Ru(bpy) ₂ (ppyCF ₃)] ⁺	0.86	-1.34	-1.68	-2.03	-0.96	0.48
dtb	4a	[Ru(dtb) ₂ (ppy)] ⁺	0.56	-1.51	-1.80	-2.23	-1.21	0.26
MeObpy	5a	[Ru(MeObpy) ₂ (ppy)] ⁺	0.43	-1.54	-1.77	-2.16	-1.31	0.20
	5b	[Ru(MeObpy) ₂ (ppyF ₂)] ⁺	0.55	-1.53	-1.74	-2.11	-1.21	0.23
	5c	[Ru(MeObpy) ₂ (ppyCF ₃)] ⁺	0.61	-1.48	-1.69	-2.00	-1.26	0.39

^aAll data were obtained in CH₃CN solutions containing 0.1 M LiClO₄ using glassy carbon disk electrodes as the working and counter electrodes and a nonaqueous Ag/AgCl pseudoreference electrode externally calibrated to Fc^{+/⁰} in CH₃CN solutions containing 0.2 M LiClO₄ (0.31 V vs SCE). ^bError is ±0.01 V. ^cIrreversible reduction peak potential. ^dRu^{2+/+*} = Ru^{2+/+} - Δ*G*_{ES} where Δ*G*_{ES} is the energy stored in the excited state determined from the Franck-Condon analysis of the 293 K emission spectra determined by Δ*G*_{ES} = *E*₀ + (Δ*v*_{1/2})²/(16**k*_b**T**ln(2)).⁶⁴ ^eRu^{+*/⁰} = Ru^{+/⁰} + Δ*G*_{ES}.⁶⁵

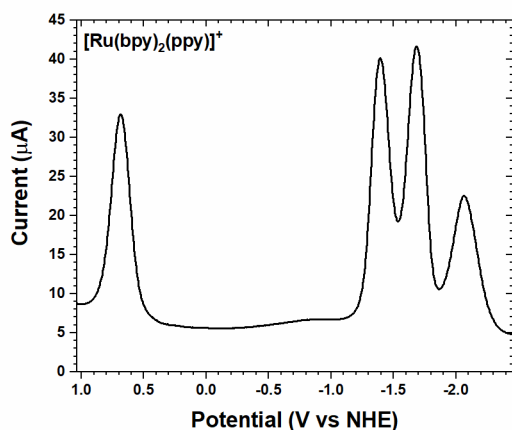


Figure 6.1. Square wave voltammogram for $[\text{Ru}(\text{bpy})_2(\text{ppy})]^+$ in an CH_3CN solution containing 0.1 M LiClO_4 at room temperature.

Figure 6.2 shows the UV-visible absorption and photoluminescence (PL) spectra for all compounds in CH_3CN . The spectra of $[\text{Ru}(\text{bpy})_2(\text{ppy})]^+$ and $[\text{Ru}(\text{bpy})_2(\text{ppyF}_2)]^+$ match previously reported spectra.^{21,38} For all $[\text{Ru}(\text{N}^{\wedge}\text{N})_2(\text{C}^{\wedge}\text{N})]^+$, two broad absorbance features were observed: one between 350–450 nm and a second between 500–600 nm with maximum molar absorption coefficients, ϵ , between 6,000 and 21,000 $\text{M}^{-1}\text{cm}^{-1}$. These bands have been assigned as metal-to-ligand charge transfer (MLCT) bands based on previously reported DFT calculations and ϵ assignments.^{17,18,38,39} In the case of $[\text{Ru}(\text{deeb})_2(\text{C}^{\wedge}\text{N})]^+$, an additional MLCT band appeared at around 500 nm. For all compounds, additional, higher-energy transitions with large ϵ values were observed at wavelengths lower than 350 nm consistent with intraligand $\pi \rightarrow \pi^*$ transitions.⁹ For each cyclometalated compound, the absorption maximum of the lowest-energy MLCT transition is tabulated in Table 6.2.

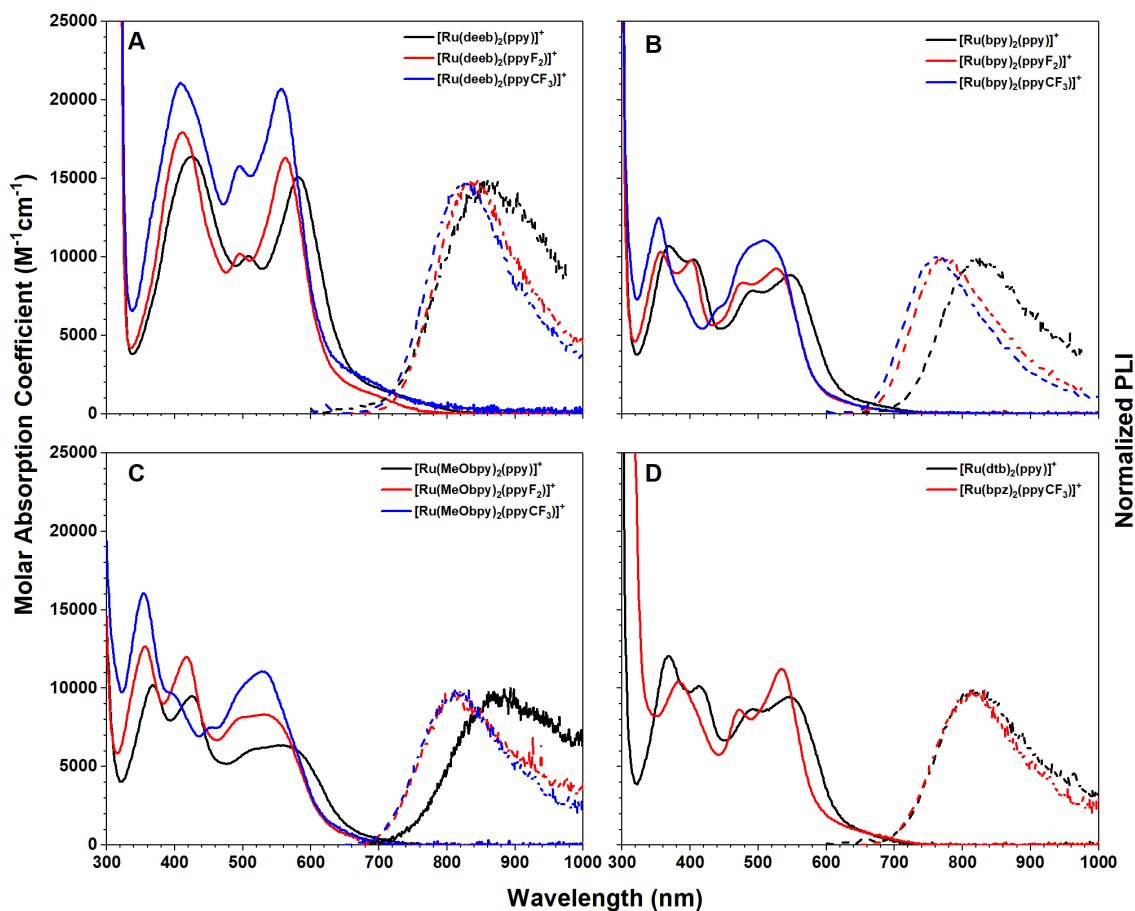


Figure 6.2. The UV-visible absorption (solid) and photoluminescence (dashed) spectra of (A) $[\text{Ru}(\text{deeb})_2(\text{C}^{\wedge}\text{N})]^+$, (B) $[\text{Ru}(\text{bpy})_2(\text{C}^{\wedge}\text{N})]^+$, (C) $[\text{Ru}(\text{MeObpy})_2(\text{C}^{\wedge}\text{N})]^+$, and (D) $[\text{Ru}(\text{N}^{\wedge}\text{N})_2(\text{C}^{\wedge}\text{N})]^+$ in Ar-sparged CH_3CN .

Visible-light excitation of $[\text{Ru}(\text{N}^{\wedge}\text{N})_2(\text{C}^{\wedge}\text{N})]^+$ at room temperature resulted in weak, broad, and featureless PL, exhibiting a substantial Stokes-like shift, Figure 6.2. For comparison, the PL of four tris(homoleptic) $\text{Ru}(\text{II})$ compounds, $[\text{Ru}(\text{N}^{\wedge}\text{N})_3]^{2+}$, were also acquired. For $[\text{Ru}(\text{N}^{\wedge}\text{N})_3]^{2+}$ and $[\text{Ru}(\text{N}^{\wedge}\text{N})_2(\text{C}^{\wedge}\text{N})]^+$, the PL maxima ranged from 600 to 650 nm and 760 to 880 nm, respectively, Table 6.2. Quantum yields for the PL, Φ_{PL} , were determined by comparative actinometry as described by Demas and Crosby using either $[\text{Ru}(\text{bpy})_3](\text{PF}_6)_2$ or $[\text{Os}(\text{bpy})_3](\text{PF}_6)_2$ ($\Phi_{\text{PL}} = 0.095$ or $\Phi_{\text{PL}} = 0.005$) as the actinometer for $[\text{Ru}(\text{N}^{\wedge}\text{N})_3]^{2+}$ or $[\text{Ru}(\text{N}^{\wedge}\text{N})_2(\text{C}^{\wedge}\text{N})]^+$,

Table 6.2. Summary of the Spectroscopic and Photophysical Data

	Compound	$\lambda_{\max}^{a,b,c}$ (nm)	E_{\max}^d (nm)	τ_{obs}^e (ns)	$\Phi_{\text{PL}}^{e,f}$	k_r^g (10^4 s^{-1})	k_{nr}^h (10^7 s^{-1})
1c	[Ru(bpz) ₂ (ppyCF ₃)] ⁺	535 (11200)	814	27.6 ± 1.2	0.0006	2	3.6
1d	[Ru(bpz) ₃] ²⁺	440 (13000) ⁱ	606	600 ⁱ	0.08	8	0.16
2a	[Ru(deeb) ₂ (ppy)] ⁺	582 (15100)	855	11.9 ± 0.4	0.0003	3	8.4
2b	[Ru(deeb) ₂ (ppyF ₂)] ⁺	563 (16300)	838	33.3 ± 0.8	0.0007	2	3.0
2c	[Ru(deeb) ₂ (ppyCF ₃)] ⁺	557 (20700)	824	34.8 ± 0.1	0.001	3	2.9
2d	[Ru(deeb) ₃] ²⁺	466 (21700) ^j	650	2100 ^j	0.20	6	0.041
3a	[Ru(bpy) ₂ (ppy)] ⁺	549 (8900)	825	12.5 ± 0.1	0.0004	3	8.0
3b	[Ru(bpy) ₂ (ppyF ₂)] ⁺	527 (9300)	775	32.3 ± 0.1	0.002	6	3.1
3c	[Ru(bpy) ₂ (ppyCF ₃)] ⁺	509 (11100)	761	40.1 ± 1.8	0.001	3	2.5
3d	[Ru(bpy) ₃] ²⁺	451 (14000) ⁱ	623	855 ⁱ	0.095 ^k	7	0.11
4a	[Ru(dtb) ₂ (ppy)] ⁺	546 (9500)	817	15.5 ± 0.1	0.0004	3	6.4
4d	[Ru(dtb) ₃] ²⁺	458 (13100) ^l	637	730 ^l	0.06	6	0.13
5a	[Ru(MeObpy) ₂ (ppy)] ⁺	554 (6400)	881	3.1 ± 0.1	0.0001	3	32
5b	[Ru(MeObpy) ₂ (ppyF ₂)] ⁺	533 (8300)	812	7.5 ± 0.2	0.0002	3	13
5c	[Ru(MeObpy) ₂ (ppyCF ₃)] ⁺	530 (11100)	800	9.6 ± 0.2	0.0004	4	10

^aValue reported for the lowest-energy, spin-allowed MLCT transition in CH₃CN at room temperature. ^bError is ±2 nm. ^cValue in parenthesis is the molar absorption coefficient (M⁻¹cm⁻¹) for that peak in acetonitrile. ^dError is ±5 nm. ^eLifetimes and quantum yields measured at 293 ± 2 K in Ar sparged acetonitrile. ^fError is ±20%. ^g $k_r = \Phi_{\text{PL}} \cdot \tau_{\text{obs}}^{-1}$. ^h $k_{\text{nr}} \approx \tau_{\text{obs}}^{-1}$. ⁱRef. 29. ^jRef. 41. ^kRef. 57. ^lRef. 52.

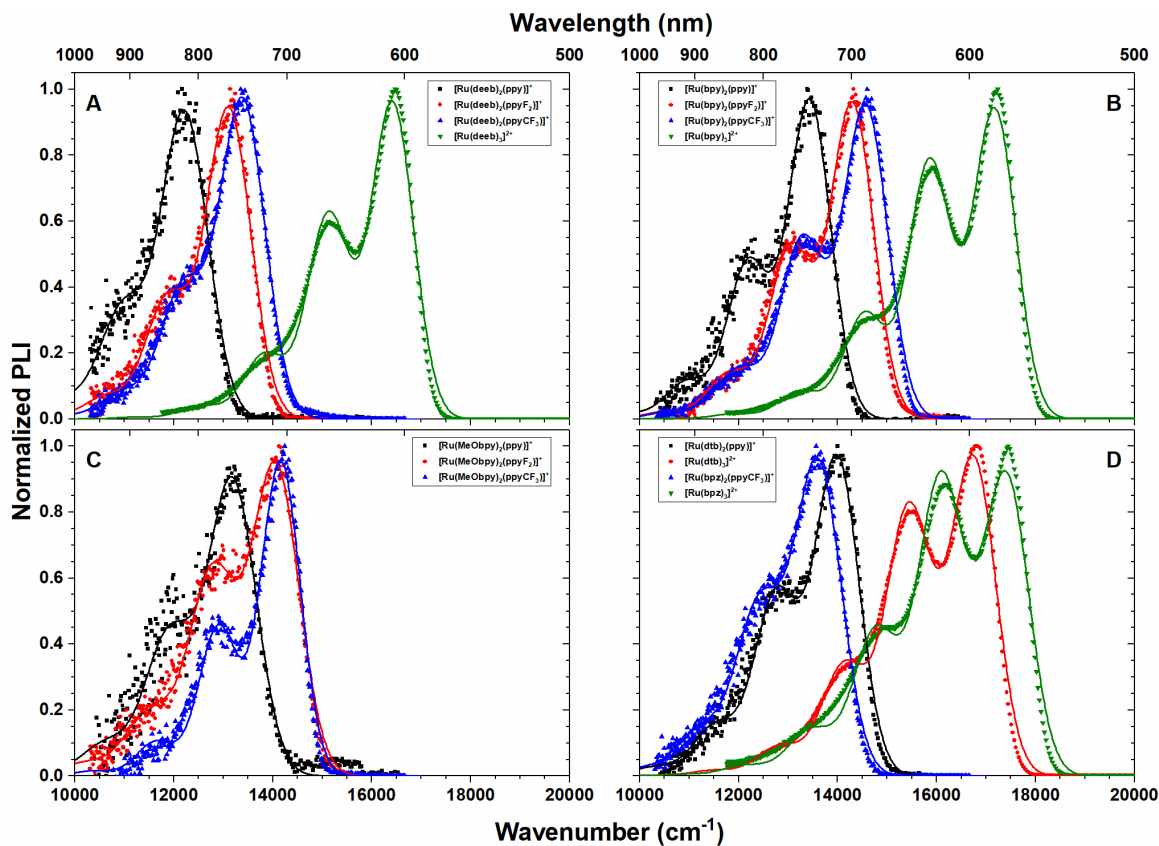


Figure 6.3. The steady-state photoluminescence spectra (dotted) and the fits (solid) obtained from the single-mode, Franck-Condon lineshape analysis of (A) $[\text{Ru}(\text{deeb})_2(\text{C}^\wedge\text{N})]^+$, (B) $[\text{Ru}(\text{bpy})_2(\text{C}^\wedge\text{N})]^+$, (C) $[\text{Ru}(\text{MeObpy})_2(\text{C}^\wedge\text{N})]^+$, and (D) $[\text{Ru}(\text{N}^\wedge\text{N})_2(\text{C}^\wedge\text{N})]^+$ in 4:1 EtOH:MeOH at 77 K

Table 6.3. Fitting Parameters Obtained from the Franck-Condon Lineshape Analysis^a

N [^] N		Compound	77 K				293 K ^b		
			E_0 (cm ⁻¹)	$\hbar\omega_m$ (cm ⁻¹)	S_m	$\Delta\nu_{1/2}$ (cm ⁻¹)	E_0 (cm ⁻¹)	$\Delta\nu_{1/2}$ (cm ⁻¹)	$\ln(F)$
bpz	1c	[Ru(bpz) ₂ (ppyCF ₃)] ⁺	13610	1190	0.71	1110	12400	1900	-17.9
	1d	[Ru(bpz) ₃] ²⁺	17400	1310	1.26	1090	17060	1440	-19.6
deeb	2a	[Ru(deeb) ₂ (ppy)] ⁺	12210	1240	0.49	1110	11550	2500	-16.7
	2b	[Ru(deeb) ₂ (ppyF ₂)] ⁺	13110	1230	0.52	1060	11920	1940	-18.5
	2c	[Ru(deeb) ₂ (ppyCF ₃)] ⁺	13390	1210	0.54	1070	12130	1920	-19.3
	2d	[Ru(deeb) ₃] ²⁺	16420	1290	0.83	1010	15780	1580	-22.1
bpy	3a	[Ru(bpy) ₂ (ppy)] ⁺	13430	1240	0.66	1010	12140	2040	-16.9
	3b	[Ru(bpy) ₂ (ppyF ₂)] ⁺	14300	1240	0.71	1020	12980	1870	-18.2
	3c	[Ru(bpy) ₂ (ppyCF ₃)] ⁺	14570	1280	0.75	1040	13240	1780	-17.7
	3d	[Ru(bpy) ₃] ²⁺	17170	1310	1.06	1010	16520	1520	-20.5
dtb	4a	[Ru(dtb) ₂ (ppy)] ⁺	13990	1230	0.75	1050	12270	2110	-16.2
	4d	[Ru(dtb) ₃] ²⁺	16750	1300	1.08	1070	16220	1530	-19.9
MeObpy	5a	[Ru(MeObpy) ₂ (ppy)] ⁺	13180	1270	0.65	1140	11270	2490	-13.9
	5b	[Ru(MeObpy) ₂ (ppyF ₂)] ⁺	14060	1270	0.87	1120	12340	2050	-14.5
	5c	[Ru(MeObpy) ₂ (ppyCF ₃)] ⁺	14160	1260	0.63	940	12490	2430	-17.0

^aError in $E_0 \pm 30$ cm⁻¹, $\hbar\omega_m \pm 10$ cm⁻¹, $S_m \pm 0.01$, $\Delta\nu_{1/2} \pm 20$ cm⁻¹. ^bFor these fits, $\hbar\omega_m$ and S_m were fixed to the 77 K values.

respectively.⁵⁵⁻⁵⁷ The $[\text{Ru}(\text{N}^{\wedge}\text{N})_3]^{2+}$ compounds displayed Φ_{PL} between 0.04 and 0.13 which agrees with previously published results.^{29,41,66} In the case of the cyclometalated compounds, $[\text{Ru}(\text{bpy})_2(\text{ppyF}_2)]^+$ was the brightest emitter with a Φ_{PL} of 0.002. All other compounds exhibited small Φ_{PL} between 0.001 and 0.0001.

Cooling the compounds to 77 K in 4:1 EtOH:MeOH glasses resulted in a hypsochromic shift in the PL spectra as well as the appearance of vibronic structure for all compounds, Figure 6.3. The PL maxima ranged from 575 to 610 nm for $[\text{Ru}(\text{N}^{\wedge}\text{N})_3]^{2+}$ and between 680 to 810 nm for $[\text{Ru}(\text{N}^{\wedge}\text{N})_2(\text{C}^{\wedge}\text{N})]^+$. A single-mode, Franck-Condon (FC) lineshape analysis for each of these PL spectra was performed, eq 6.1. In this analysis, four fitting parameters were used to describe the spectra: the energy of the transition between the lowest vibrational levels of the ground and excited states (E_0), the energy of the weighted-average, ground-state, acceptor vibrational mode ($\hbar\omega_{\text{M}}$), the Huang Rhys factor (S_{M}), and the spectral full-width at half-maximum ($\Delta\nu_{1/2}$). Table 6.3 displays the optimized parameters from the fits which are shown overlaid with the data in Figure 6.3. A unique fit was found in all cases through least-squares error minimization. With the constraint that the S_{M} and $\hbar\omega_{\text{M}}$ values acquired at 77 K were unchanged at 293 K, a unique solution to the FC lineshape analysis was found with the resulting E_0 and $\Delta\nu_{1/2}$ values tabulated in Table 6.3.

Time-correlated single photon counting (TCSPC) was used to record the time-resolved emission from photoexcited $[\text{Ru}(\text{N}^{\wedge}\text{N})_2(\text{C}^{\wedge}\text{N})]^+$ in Ar-sparged CH_3CN at room temperature. Figure 6.4A shows representative data obtained for $[\text{Ru}(\text{bpy})_2(\text{ppy})]^+*$. For each compound, excited-state relaxation followed first-order kinetics with the excited-state lifetime, τ_{obs} , obtained through the reconvolution of the instrument response function (IRF) and a simulated single exponential function to model the measured decay function, Figure 6.4A.⁵⁹

$[\text{Ru}(\text{bpy})_2(\text{ppyCF}_3)]^{+*}$ exhibited the longest lifetime of 40.1 ns with τ_{obs} for $[\text{Ru}(\text{bpz})(\text{ppyCF}_3)]^{+*}$, $[\text{Ru}(\text{deeb})(\text{ppyCF}_3)]^{+*}$, $[\text{Ru}(\text{deeb})(\text{ppyF}_2)]^{+*}$, and $[\text{Ru}(\text{bpy})(\text{ppyF}_2)]^{+*}$ ranging between 27.6 and 34.8 ns. All other compounds used in this study exhibited τ_{obs} values between 3.1 and 15.5 ns as shown in Table 6.2.

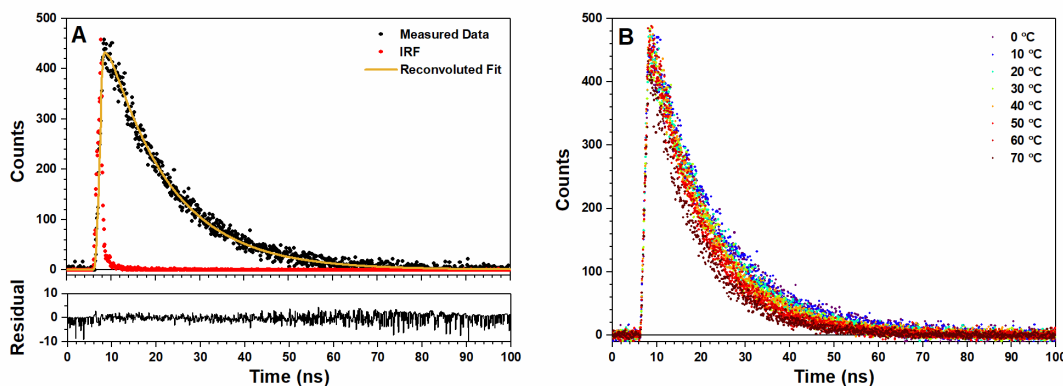


Figure 6.4. (A) Time-resolved PL data of $[\text{Ru}(\text{bpy})_2(\text{ppy})]^+$ following 444 nm pulsed diode laser excitation in neat CH_3CN at different temperatures. (B) An example of the reconvolution fitting used to fit the time-resolved PL data where the black is the measured PL data, red is the measured instrument response function (IRF) and the yellow trace is the reconvoluted fit provided by the DecayFit software. The bottom plot shows the residual of this fit.

Table 6.4. Parameters Obtained from the Arrhenius Analysis

N [^] N		Compound	k_0 (s ⁻¹)	A_1 (s ⁻¹)	A_1/k_0	E_a (cm ⁻¹)
bpz	1c	$[\text{Ru}(\text{bpz})_2(\text{ppyCF}_3)]^+$	2.5×10^7	1.1×10^9	44	950
deeb	2a	$[\text{Ru}(\text{deeb})_2(\text{ppy})]^+$	1.7×10^7	8.5×10^8	50	520
	2b	$[\text{Ru}(\text{deeb})_2(\text{ppyF}_2)]^+$	2.2×10^7	1.1×10^9	50	990
	2c	$[\text{Ru}(\text{deeb})_2(\text{ppyCF}_3)]^+$	2.1×10^7	7.9×10^8	37	940
	3a	$[\text{Ru}(\text{bpy})_2(\text{ppy})]^+$	3.8×10^7	6.4×10^8	30	560
bpy	3b	$[\text{Ru}(\text{bpy})_2(\text{ppyF}_2)]^+$	2.3×10^7	8.8×10^8	38	970
	3c	$[\text{Ru}(\text{bpy})_2(\text{ppyCF}_3)]^+$	1.7×10^7	2.8×10^8	17	720
dtb	4a	$[\text{Ru}(\text{dtb})_2(\text{ppy})]^+$	5.0×10^7	1.2×10^9	24	900
MeObpy	5a	$[\text{Ru}(\text{MeObpy})_2(\text{ppy})]^+$	8.2×10^7 ^a	1.3×10^9	16	340
	5b	$[\text{Ru}(\text{MeObpy})_2(\text{ppyF}_2)]^+$	1.0×10^8	1.6×10^9	15	800
	5c	$[\text{Ru}(\text{MeObpy})_2(\text{ppyCF}_3)]^+$	6.4×10^7	3.9×10^8	6	460

^aFixed during the fitting process. This value was determined by the average of k_0 from $[\text{Ru}(\text{MeObpy})_2(\text{ppyF}_2)]^+$ and $[\text{Ru}(\text{MeObpy})_2(\text{ppyCF}_3)]^+$.

Time-resolved emission for the cyclometalated compounds in Ar-sparged CH₃CN was obtained as a function of temperature between 273 and 343 K. A decrease in τ_{obs} was observed as the temperature increased, Figure 6.4B. The temperature-dependent, excited-state lifetime data were incorporated into an Arrhenius-style plot and were then modeled by the Arrhenius equation with an additional rate constant, k_0 , included for the temperature-independent component of excited-state decay, eq 6.2, where, A_1 is the pre-exponential factor, E_a is the activation energy for crossing into another excited state, k_B is the Boltzmann constant, and T is the temperature. Only one Arrhenius term was necessary to fit the data which was indicative of crossing into only one non-emissive excited-state. Parameters from the Arrhenius fit are tabulated in Table 6.4 and the fits are displayed in Figure 6.5. In all cases, the E_a was below 1000 cm⁻¹. Additionally, k_0 and A_1 were found to be on the order of 10⁷-10⁸ s⁻¹ and 10⁸-10⁹ s⁻¹, respectively.

$$\tau_{\text{obs}}^{-1} = k_0 + A_1 e^{\left(\frac{-E_a}{k_B T}\right)} \quad (6.2)$$

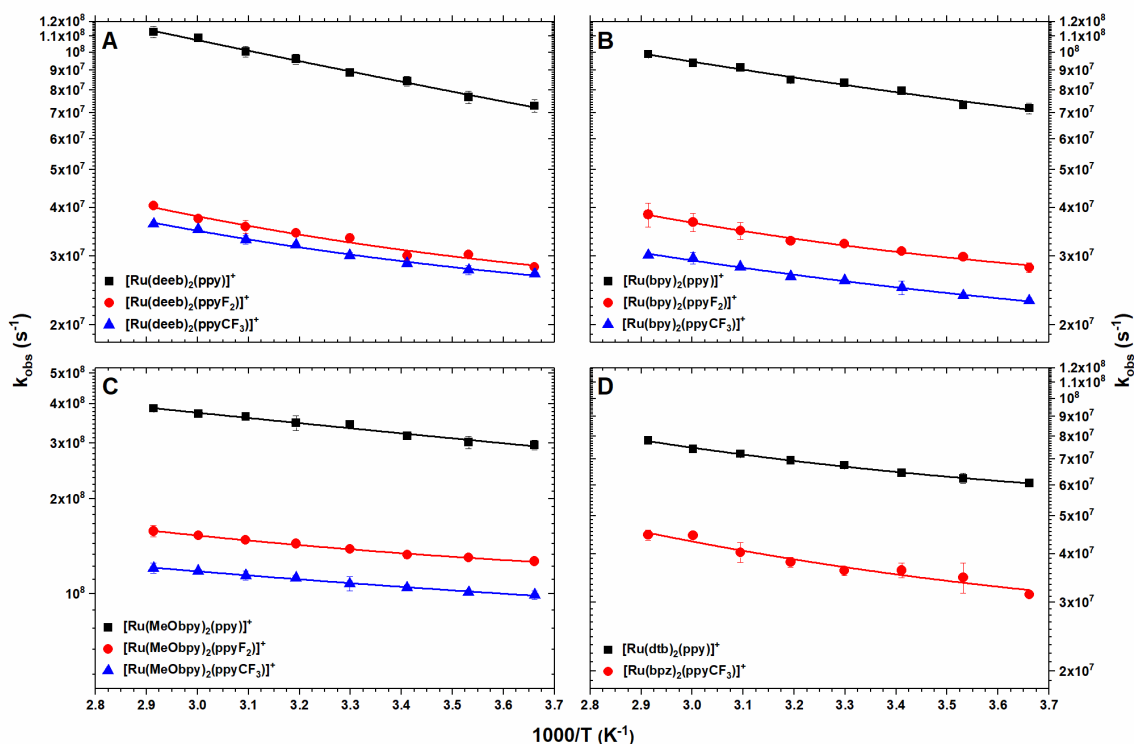


Figure 6.5. Photoluminescence lifetimes measured in CH_3CN plotted against the change in temperature in an Arrhenius plot for $[\text{Ru}(\text{deeb})_2(\text{C}^{\wedge}\text{N})]^+$ (A), $[\text{Ru}(\text{bpy})_2(\text{C}^{\wedge}\text{N})]^+$ (B), $[\text{Ru}(\text{MeObpy})_2(\text{C}^{\wedge}\text{N})]^+$ (C), and $[\text{Ru}(\text{N}^{\wedge}\text{N})_2(\text{C}^{\wedge}\text{N})]^+$ (D). Overlaid are the solid lines representing the best fits to the Arrhenius equation.

6.4 Discussion

With the emergence of tris(bidentate) cyclometalated Ru(II), $[\text{Ru}(\text{N}^{\wedge}\text{N})_2(\text{C}^{\wedge}\text{N})]^+$, as chromophores for solar energy applications, it is important to understand the photophysics and photochemistry of these compounds for future, tailored design. As highlighted in the introduction, two questions about these Ru(II) cyclometalated compounds were addressed through spectroscopic measurements. First, the applicability of the energy gap law to $[\text{Ru}(\text{N}^{\wedge}\text{N})_2(\text{C}^{\wedge}\text{N})]^+*$ excited-state decay was demonstrated through the modulation of the photophysical properties by ligand substitution confirming that the electronic origin of the rapid excited-state decay to be from a large vibronic overlap between the ground- and excited-

state wavefunctions. Second, the temperature-dependent emission lifetime data revealed that dissociative, ligand-field states for these cyclometalated compounds were not accessible at room temperature. Below, these conclusions are described first through the effects of ligand substitution on the electronic structure of these cyclometalated compounds followed by an examination of the excited-state properties in the context of the Franck-Condon parameters, the energy gap law, and the temperature-dependent excited-state lifetimes.

6.4.1 Effects of Ligand Substitution

One of the attractive features of Ru(II) polypyridyl compounds is the ability to tune their electrochemical and photophysical properties through the addition of substituents on the bpy backbone. This feature was exploited for the cyclometalated compounds used in this study. As the substituents in the 4 and 4' positions of the bpy become more electron-withdrawing, both the highest-occupied molecular orbital (HOMO) and the lowest-unoccupied molecular orbital (LUMO) are stabilized, as reflected in the formal reduction potentials, Table 6.1. As the electron-withdrawing ability decreases from MeObpy \rightarrow bpz, both the $E^\circ(\text{Ru}^{2+/+})$, HOMO, and the $E^\circ(\text{Ru}^{+/0})$, LUMO, shifted to more positive potentials by 0.7 and 0.75 V, respectively. These shifts arise from the increased stabilization of the π^* orbitals of the N^N ligand and the decreased Lewis basicity of the lone pair of electrons on N as the electron-donating ability of the substituent decreases. This results in more positive $E^\circ(\text{Ru}^{+/0})$ and $E^\circ(\text{Ru}^{2+/+})$, respectively.

For $[\text{Ru}(\text{N}^{\wedge}\text{N})_2(\text{C}^{\wedge}\text{N})]^+$, the tunability of the HOMO and LUMO is even more advantageous due to the ability to modulate the energy of the HOMO independently of the LUMO energy through substituents on C^N.^{18,21,38,39,42,49,50,67,68} Electron-withdrawing substituents on C^N increases the $E^\circ(\text{Ru}^{2+/+})$ by ~ 0.2 V moving from ppy \rightarrow ppyCF₃, and displays virtually no effect on the $E^\circ(\text{Ru}^{+/0})$ and $E^\circ(\text{Ru}^{0/-})$, as shown in Table 6.1. Strong

electron-withdrawing substituents reduces the Lewis basicity of the carbanion which moves the $E^\circ(\text{Ru}^{2+/+})$ to more positive potentials. This stabilization of the HOMO energy results in a hypsochromic shift of the MLCT transitions within each N[^]N series with ppyCF₃ possessing the highest-energy MLCT transitions, Figure 6.2.

6.4.2 Excited-State Characterization and the Energy Gap Law

All the cyclometalated compounds studied displayed weak photoluminescence (PL) at room temperature. The steady-state PL spectra displayed broad, featureless peaks that are typical of Ru(II) polypyridyl compounds.¹⁰ The quantum yields, Φ_{PL} , for $[\text{Ru}(\text{N}^{\wedge}\text{N})_2(\text{C}^{\wedge}\text{N})]^+$ were extremely small (≤ 0.002).

The excited-state relaxation of the Ru(II) cyclometalated compounds was well described by first-order decay kinetics. The excited-state lifetimes, τ_{obs} , for the compounds at 273 K are reported in Table 6.2. In all cases, τ_{obs} was between 3 and 40 ns, shorter than typically reported for many Ru(II) and Os(II) polypyridyl compounds (~ 100 ns to μs).^{10,29,36,41,55,69} From Φ_{PL} and τ_{obs}^{-1} , both the radiative, k_{r} , and non-radiative, k_{nr} , rate constants of excited-state decay were determined. In all cases, k_{r} was on the order of 10^4 s^{-1} which is comparable to the k_{r} determined for the $[\text{Ru}(\text{N}^{\wedge}\text{N})_3]^{2+*}$ analogues reported here and for previously reported Ru(II) and Os(II) compounds.^{55,69,70} The k_{nr} for all compounds was found to be on the order of 10^8 s^{-1} for $[\text{Ru}(\text{MeObpy})_2(\text{C}^{\wedge}\text{N})]^{+*}$, 10^7 s^{-1} for the remaining $[\text{Ru}(\text{N}^{\wedge}\text{N})_2(\text{C}^{\wedge}\text{N})]^{+*}$, and 10^5 to 10^6 s^{-1} for $[\text{Ru}(\text{N}^{\wedge}\text{N})_3]^{2+*}$. For these Ru(II) cyclometalated compounds, k_{nr} dominates the excited-state decay as evidenced by the small Φ_{PL} values.

Qualitatively, the 77 K PL spectra displayed vibronic structure that was modeled with single-mode, Franck-Condon (FC) lineshape analyses yielding the following parameters, tabulated in Table 6.3: the energy of the transition between the lowest vibrational levels of the

ground and excited states in cm^{-1} (E_0), the energy of the average acceptor vibrational mode in the ground state in cm^{-1} ($\hbar\omega_M$), the Huang-Rhys factor which is a measure of the geometric distortion between the ground and excited states (S_M), and the full-width at half-maximum of the Gaussian peaks in cm^{-1} ($\Delta\nu_{1/2}$).

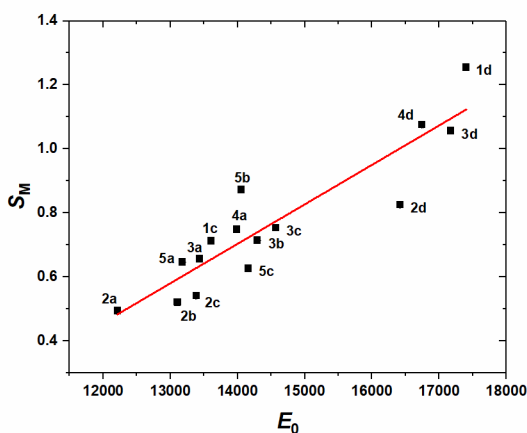


Figure 6.6. A comparison of the S_M vs E_0 for the indicated compounds, Table 6.3. The error in E_0 and S_M is ± 30 and ± 0.01 , respectively. Overlaid is the line of best fit with a slope of $1.23 \pm 0.15 \times 10^{-4} \text{ cm}$.

For the four $[\text{Ru}(\text{N}^{\wedge}\text{N})_3]^{2+}$ compounds analyzed here, the $\hbar\omega_M$ was found to be $1300 \pm 10 \text{ cm}^{-1}$, and these values were consistent with an average acceptor vibrational mode related to several C-C and C-N stretching modes in the bipyridine ligand as has been previously reported.^{71,72} Interestingly, the $\hbar\omega_M$ values for all Ru(II) cyclometalated compounds were smaller, between 1190 and 1280 cm^{-1} . This decrease was attributed to the enhanced π -backbonding from the electron-rich metal center to the π^* orbitals of the $\text{N}^{\wedge}\text{N}$ ligands. Furthermore, the S_M values for the cyclometalated compounds were smaller than for the polypyridyl compounds. The values reported for the cyclometalated compounds is consistent with previously reported FC fitting values reported for several $[\text{Ru}(\text{N}^{\wedge}\text{N})_2(\text{C}^{\wedge}\text{N})]^+$ compounds.²¹ The result indicates that cyclometalated compounds in the excited state are less

distorted from their ground state compared to the homoleptic polypyridyl compounds. This observation was not unexpected as it has been shown that S_M varies linearly with E_0 for similar compounds with excited states of the same electronic origin.⁷³ The rationale for this was as follows; as E_0 decreases, the extent to which the ground state and excited state mix should increase. With more mixing, the amount of charge transferred to the π^* orbitals of the N[^]N system in the excited state should decrease. Thus, the amount of distortion of the N[^]N ligand should decrease leading to smaller values of S_M . Figure 6.6 shows a plot of S_M as a function of E_0 , and a linear trend is observed.

Since non-radiative decay dominates the excited-state decay kinetics for all cyclometalated compounds studied, the energy gap law provides an excellent way to probe the factors governing non-radiative excited-state decay. This law proposed by Jortner *et al.* allows for the investigation of the dependence k_{nr} with E_0 .^{74,75} More specifically, it describes how the molecular vibrations within the compound influence k_{nr} . The energy gap law takes the form of eqs 6.3-6.5 as derived by Kober *et al.* and uses experimentally measurable parameters to relate E_0 and k_{nr} .⁵⁵ In these equations, β describes the vibronically induced electronic coupling between the ground and excited states, and F describes the vibronic wavefunction overlap between these states.

$$\ln(k_{nr}) = \ln(\beta) + \ln(F) \quad (6.3)$$

$$\ln(F) = \left(\frac{-1}{2}\right) \ln\left(\frac{\hbar\omega_M E_0}{(1000 \text{ cm}^{-1})^2}\right) - S_M - \frac{\gamma E_0}{\hbar\omega_M} + \frac{(\gamma+1)^2 \left(\frac{\Delta\nu_{1/2}}{\hbar\omega_M}\right)^2}{16\ln(2)} \quad (6.4)$$

$$\gamma = \ln\left(\frac{E_0}{S_M \hbar\omega_M}\right) - 1 \quad (6.5)$$

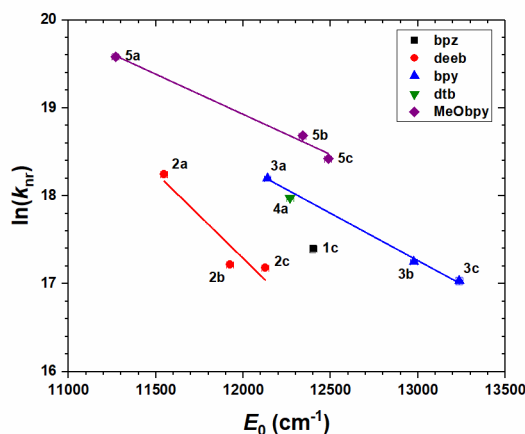


Figure 6.7. An energy gap law plot of $\ln(k_{nr})$ vs E_0 measured at 293 K in CH_3CN . The overlaid fits to eq 6.6 represent the line of best fit for the $[\text{Ru}(\text{deeb})_2(\text{C}^{\wedge}\text{N})]^+$, $[\text{Ru}(\text{bpy})_2(\text{C}^{\wedge}\text{N})]^+$, and $[\text{Ru}(\text{MeObpy})_2(\text{C}^{\wedge}\text{N})]^+$ with slopes of $(500 \text{ cm}^{-1})^{-1}$, $(900 \text{ cm}^{-1})^{-1}$, and $(1100 \text{ cm}^{-1})^{-1}$, respectively. Labels are given in Table 6.3.

Since the third term on the right-hand side of eq 6.4 is the dominant contributor to $\ln(F)$, eq 6.4 can be substituted into eq 6.3 and rewritten in the more commonly used form given by eq 6.6, where C is a constant which includes $\ln(\beta)$ and the minor contributors to $\ln(F)$.

$$\ln(k_{nr}) = C + \left(\frac{-\gamma}{\hbar\omega_M} \right) E_0 \quad (6.6)$$

Figure 6.7 shows the variation of the $\ln(k_{nr})$ with E_0 and the fits to eq 6.6. Since excited-state properties are largely influenced by the ligand where the excited state localizes, care must be taken when analyzing these data.^{55,65} For this reason, three series of compounds where the $\text{N}^{\wedge}\text{N}$ ligand remains the same were analyzed. Fits within the $[\text{Ru}(\text{deeb})_2(\text{C}^{\wedge}\text{N})]^+$, $[\text{Ru}(\text{bpy})_2(\text{C}^{\wedge}\text{N})]^+$, and $[\text{Ru}(\text{MeObpy})_2(\text{C}^{\wedge}\text{N})]^+$ series revealed that each $\text{N}^{\wedge}\text{N}$ series was described by a single line. Differences in the slopes of these fits may arise from variations in the vibrational wavefunction overlap, $\ln(F)$, the vibronically induced electronic coupling, $\ln(\beta)$, or both.

To investigate the origin of the rapid excited-state decay, $\ln(F)$ was computed from the FC parameters and plotted against $\ln(k_{nr})$ with fits overlaid to eq 6.3 and slopes fixed to unity,

Figure 6.8. Included in Figure 6.8 are data previously reported by others for $[\text{Ru}(\text{bpy})_2(\text{LL})]^{2+}$, $[\text{Os}(\text{bpy})_2(\text{LL})]^{2+}$, $[\text{Os}(\text{phen})_2(\text{LL})]^{2+}$, where LL is either one bidentate or two monodentate ancillary ligands.^{55,73} All of the Ru(II) cyclometalated compounds were reasonably well-described by a single line which indicated that $\ln(\beta)$ was essentially constant within the series of compounds. This demonstrates that the differences in the slopes for the $[\text{Ru}(\text{deeb})_2(\text{C}^{\wedge}\text{N})]^+$, $[\text{Ru}(\text{bpy})_2(\text{C}^{\wedge}\text{N})]^+$, and $[\text{Ru}(\text{MeObpy})_2(\text{C}^{\wedge}\text{N})]^+$ series observed in Figure 6.7 arise exclusively from the vibronic wavefunction overlap, $\ln(F)$.

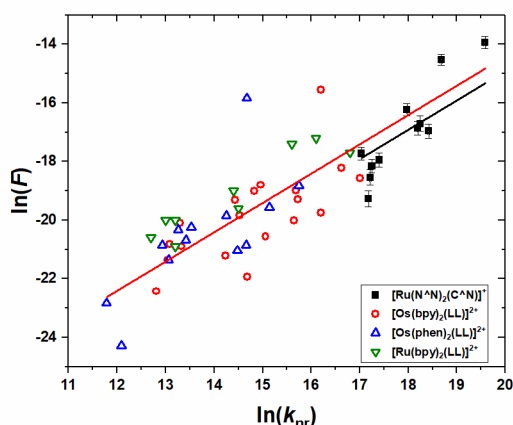


Figure 6.8. An energy gap law plot with the vibronic wavefunction overlap, $\ln(F)$, computed from the FC fitting parameters obtained at 293 K in CH_3CN for $[\text{Ru}(\text{N}^{\wedge}\text{N})_2(\text{C}^{\wedge}\text{N})]^+$ (black \blacksquare) with a fit (black line) to eq 6.3 with a fixed slope of unity which yielded an intercept of -34.9. Previously reported data for $[\text{Os}(\text{bpy})_2(\text{LL})]^{2+}$ (open red \bullet), $[\text{Os}(\text{phen})_2(\text{LL})]^{2+}$ (open blue \blacktriangle), and $[\text{Ru}(\text{bpy})_2(\text{LL})]^{2+}$ (open green \blacktriangledown) are also shown. The red line is a fit of eq 6.3 to all the data with the slope fixed to unity.

From Figure 6.8, it is also striking to note that the same fit reasonably described the Ru(II) cyclometalated compounds and the previously reported data for $[\text{Ru}(\text{bpy})_2(\text{LL})]^{2+}$, $[\text{Os}(\text{bpy})_2(\text{LL})]^{2+}$, and $[\text{Os}(\text{phen})_2(\text{LL})]^{2+}$.^{55,73} This indicates further that these transitions have similar electronic origin, i.e. same $\ln(\beta)$. The vibronically induced electronic coupling constant matrix element, V_K , was determined from the intercept of the fit in Figure 6.8 with eq 6.7. The magnitude of the intercept of the line that fits the Ru(II) cyclometalated compounds was 34.9

which corresponds to a V_K value of 1740 cm^{-1} . This value is slightly larger than those determined for the $[\text{Os}(\text{bpy})_2(\text{LL})]^{2+}$ and $[\text{Os}(\text{phen})_2(\text{LL})]^{2+}$ series (1300 cm^{-1}) and for the $[\text{Ru}(\text{bpy})_2(\text{LL})]^{2+}$ series (1120 cm^{-1}).^{55,73}

$$\beta = \left(\frac{\sqrt{2\pi} \cdot (1 \text{ s})}{\hbar \cdot (1000 \text{ cm}^{-1})} \right) V_K^2 \quad (6.7)$$

The FC fitting parameters and the subsequent analysis using the energy gap law coupled with comparisons to previously reported $\text{Ru}(\text{II})$ ⁷³ and $\text{Os}(\text{II})$ ⁵⁵ polypyridyl compounds demonstrate that these compounds follow the energy gap law and that the origin of the short excited-state lifetimes for the $\text{Ru}(\text{II})$ cyclometalated compounds is the increased vibronic overlap between the excited- and ground-state wavefunctions.

6.4.3 Arrhenius Analysis

To investigate the accessibility of other excited-state decay pathways available to $\text{Ru}(\text{II})$ cyclometalated compounds, the temperature dependence of τ_{obs}^{-1} was investigated, and the data fit to a modified Arrhenius equation. Of particular interest is the accessibility of the ligand-field (LF) states, which are dissociative in nature and lead to photochemical ligand-loss under prolonged illumination. It has previously been postulated that LF states are significantly destabilized due to the strong-field, C^N ligand and are inaccessible near room temperature.^{17,18,20,38,40,42,67} This postulate has made them an attractive molecule for solar energy harvesting in the past decade despite their short excited-state lifetimes.

The temperature dependence of the τ_{obs}^{-1} was measured between 273 and 343 K in fluid CH_3CN solutions, and these data were fit to a modified Arrhenius equation, Figure 6.5. The k_0 was allowed to float in all cases with the exception of $[\text{Ru}(\text{MeObpy})_2(\text{ppy})]^+$ where the fit would not converge when k_0 was allowed to float. Thus, only in this case was the k_0 value fixed to be the average of the k_0 found from the fits of $[\text{Ru}(\text{MeObpy})_2(\text{ppyF}_2)]^+$ and

[Ru(MeObpy)₂(ppyCF₃)]⁺. Results from the fitting process are listed in Table 6.4. Over the range of temperatures studied, a variation of 20-30% in τ_{obs} was observed. The A_1 and E_a values for the cyclometalated compounds were between 10^8 - 10^9 s⁻¹ and 300-1000 cm⁻¹, respectively. For Ru(II) polypyridyl compounds, E_a values below 1000 cm⁻¹ and A_1/k_0 below 100 are associated with activated crossing to a fourth ³MLCT state, while population of the LF states occurs with E_a values greater than 2000 cm⁻¹ and A_1/k_0 on the order of 10^7 to 10^9 .^{9,29,34-37} Thus, for these observations coupled with the small (<100) A_1/k_0 ratio is consistent with activated crossing to a fourth ³MLCT state,²⁹ and the dissociative LF states were not observed.

These results are consistent with previously published experimental and theoretical results. Rapid excited-state decay has been reported for [Ru(bpy)₂(NPP)]⁺, where NPP is 2-(3-nitrophenyl)pyridine, the only other reported **[Ru(N[^]N)₂(C[^]N)]⁺ with temperature-dependent, excited-state studies.²⁰ Within the temperature range from 120 to 140 K in 4:1 EtOH:MeOH, the authors measure E_a (960 cm⁻¹) which is consistent with the values reported here. DFT studies by Heinze and Kreitner for **[Ru(bpy)₂(ppy)]⁺** have predicted that the ligand-field state lies ~5500 cm⁻¹ above the ³MLCT and the barrier to populate this state is ~5800 cm⁻¹, which would require higher temperatures to access.⁴⁰**

Figure 6.9 shows a Jablonski-type diagram for Ru(II) cyclometalated compounds. These energy levels indicate that only one excited state is accessible within the temperature range studied, and the thermodynamic parameters indicate that this state is consistent with the population of a fourth ³MLCT. The strong-field nature of the C[^]N ligand destabilizes the LF states to a large extent such that these states are not significantly populated at temperatures below 343 K. These results predict an exceptional photostability of the cyclometalated compounds to prolonged illumination in solution.

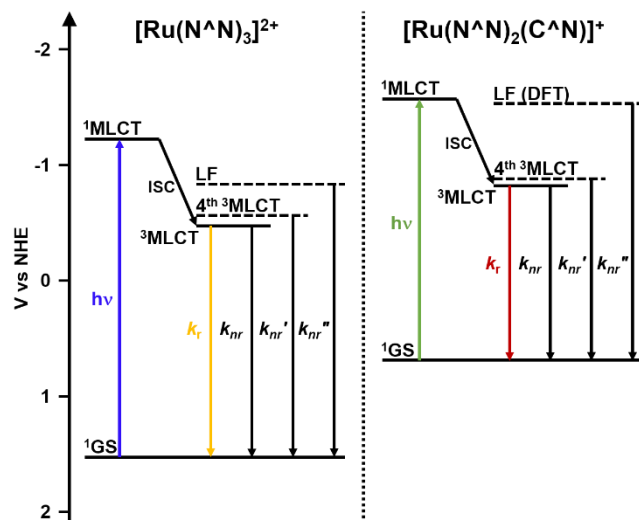


Figure 6.9. A Jablonski-type Diagram for $[\text{Ru}(\text{N}^{\wedge}\text{N})_3]^{2+}$ and $[\text{Ru}(\text{N}^{\wedge}\text{N})_2(\text{C}^{\wedge}\text{N})]^+$. The ^1GS is referenced to the $E^\circ(\text{Ru}^{2+/+})$. The dashed lines represent E_a from the $^3\text{MLCT}$ state. Note that ISC is short for intersystem crossing.

6.5 Conclusions

The photophysics and photochemistry of eleven tris(bidentate) cyclometalated Ru(II) compounds adhered to the energy gap law with rapid excited-state decay attributed to a large vibronic overlap between ground- and excited-state wavefunctions. Strikingly, the vibronically induced electronic coupling between the ground and excited states was found to be almost identical to that of Ru(II) and Os(II) polypyridyl compounds despite the profound differences in the HOMO between these two classes of compounds. Furthermore, there was no evidence for the population of dissociative ligand field states near room temperature. The temperature dependence of the excited states was consistent with the population of a non-emissive, fourth $^3\text{MLCT}$ state. This provides a basis for significantly enhanced photostability of this class of compounds and suggests that $[\text{Ru}(\text{N}^{\wedge}\text{N})_2(\text{C}^{\wedge}\text{N})]^+$ represents a more robust class of compounds for photochemical and photoelectrochemical applications.

6.6 Acknowledgements

This material is based upon work solely supported as part of the UNC EFRC: Center for Solar Fuels, an Energy Frontier Research Center funded by the U.S. Department of Energy, Office of Science, Office of Basic Energy Sciences under Award Number DE-SC0001011. T.C.M. acknowledges an individual NSF Graduate Research Fellowship for support (Grant No. DGE-1144081). The authors thank the University of North Carolina Department of Chemistry Mass Spectrometry Core Laboratory and Dr. B. Erhmann for assistance with mass spectrometry analysis.

6.7 Additional Content

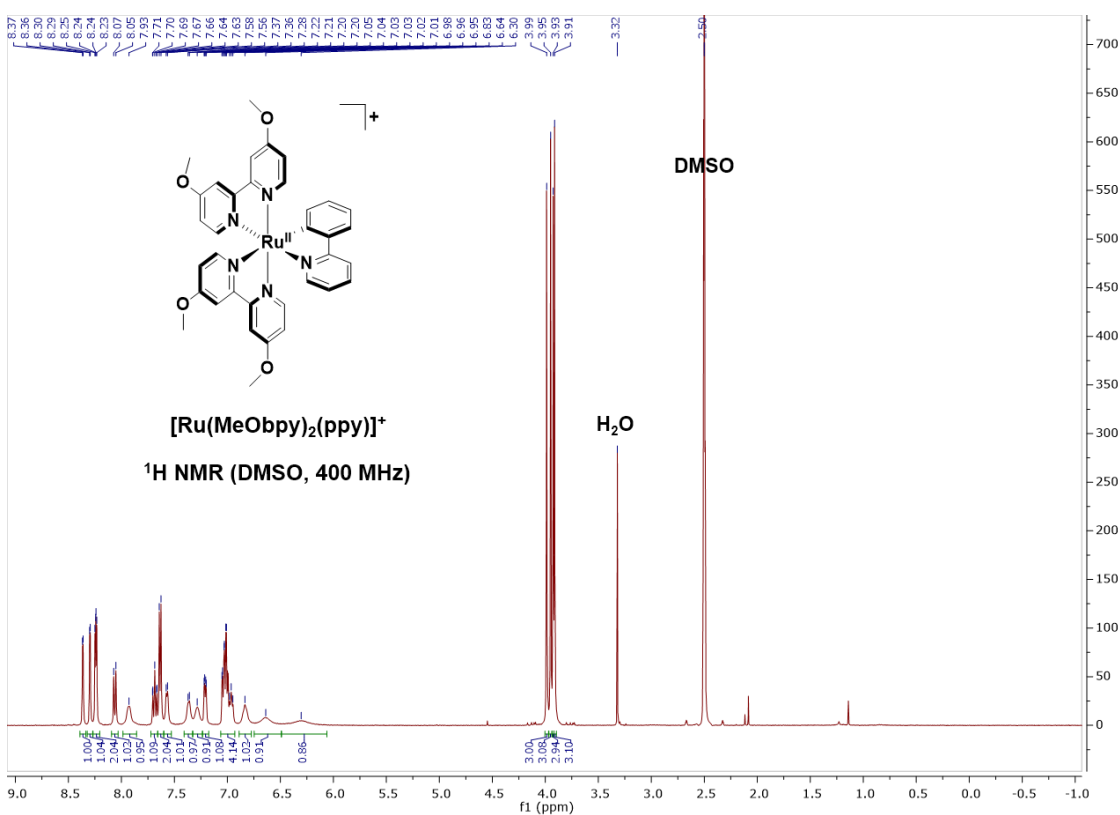


Figure 6.10. ^1H NMR spectrum of $[\text{Ru}(\text{MeObpy})_2(\text{ppy})]^+$ in d_6 -DMSO at 400 MHz and 298 K.

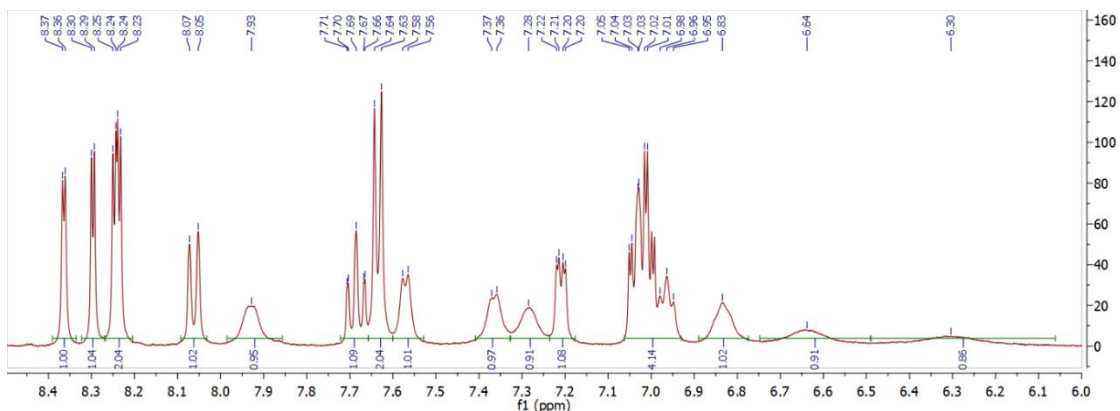


Figure 6.11. ^1H NMR spectrum of the aromatic region for $[\text{Ru}(\text{MeObpy})_2(\text{ppy})]^+$ in d_6 -DMSO at 400 MHz and 298 K.

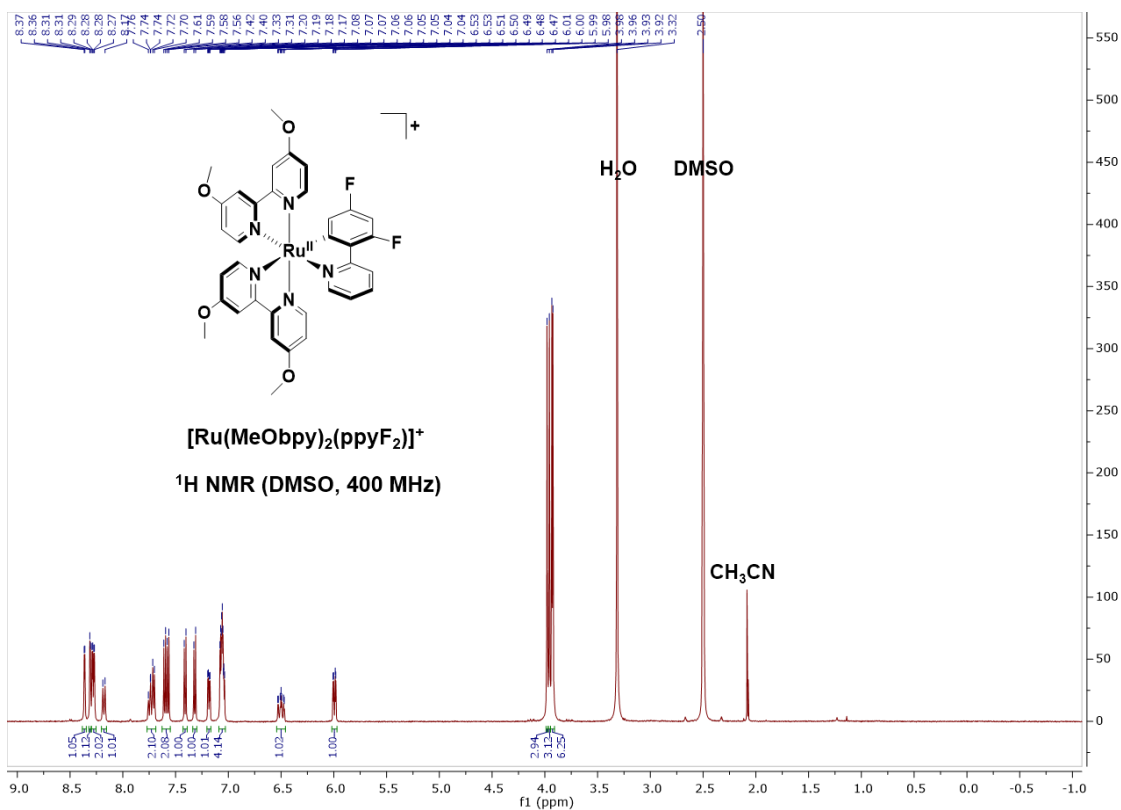


Figure 6.12. ^1H NMR spectrum of $[\text{Ru}(\text{MeObpy})_2(\text{ppyF}_2)]^+$ in d_6 -DMSO at 400 MHz and 298 K.

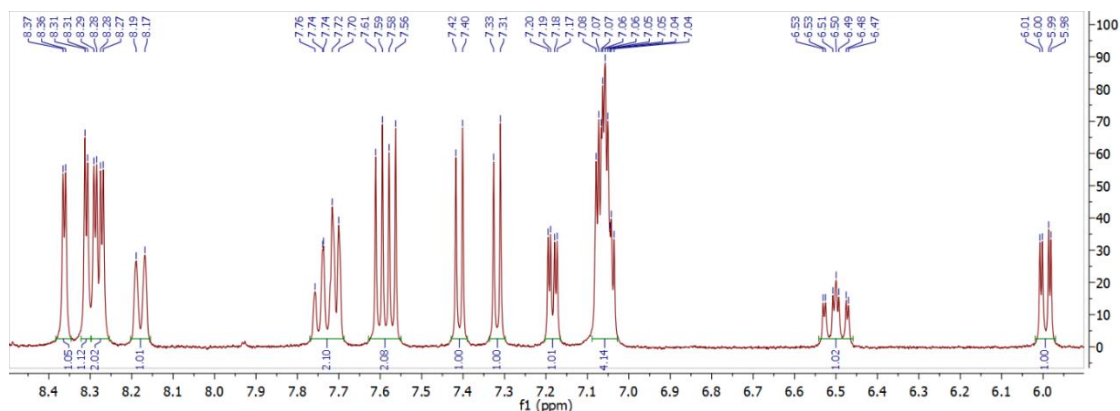


Figure 6.13. ^1H NMR spectrum of the aromatic region for $[\text{Ru}(\text{MeObpy})_2(\text{ppyF}_2)]^+$ in d_6 -DMSO at 400 MHz and 298 K.

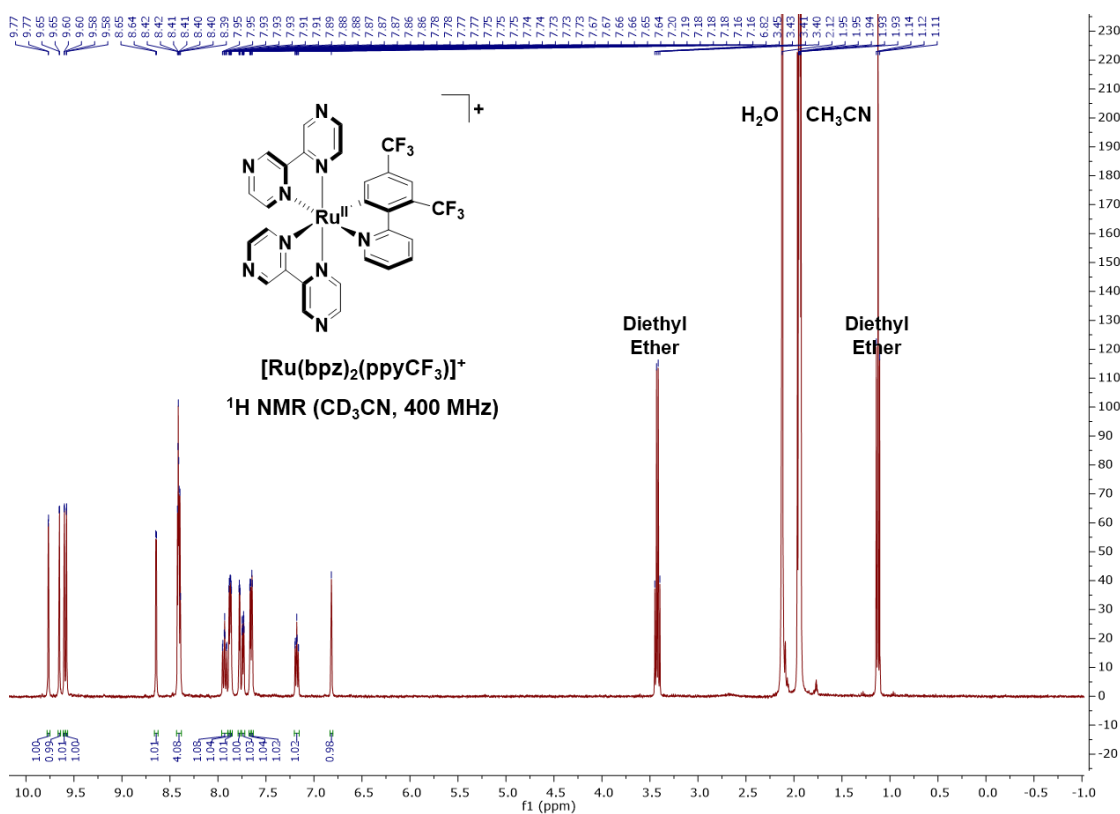
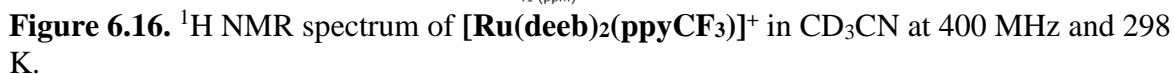
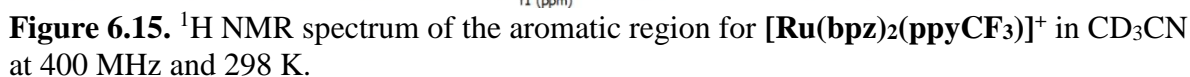


Figure 6.14. ^1H NMR spectrum of $[\text{Ru}(\text{bpz})_2(\text{ppyCF}_3)]^+$ in CD_3CN at 400 MHz and 298 K.



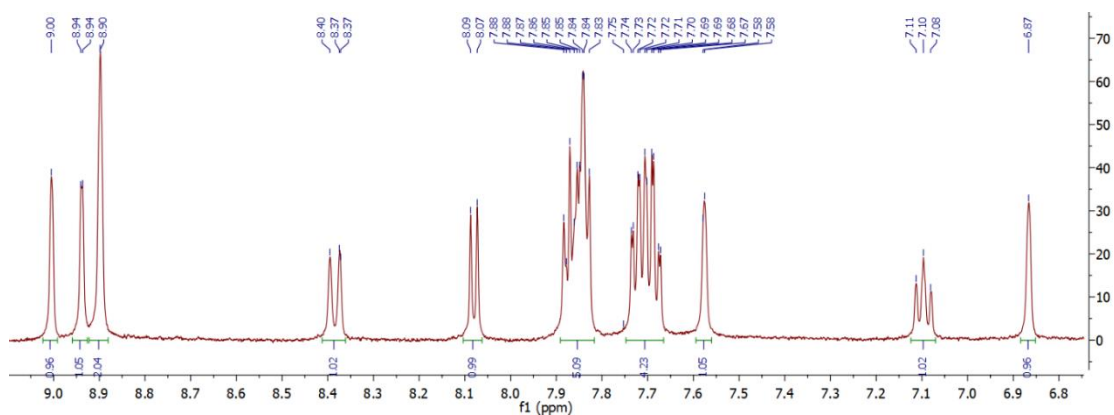


Figure 6.17. ^1H NMR spectrum of the aromatic region for $[\text{Ru}(\text{deeb})_2(\text{ppyCF}_3)]^+$ in CD_3CN at 400 MHz and 298 K.

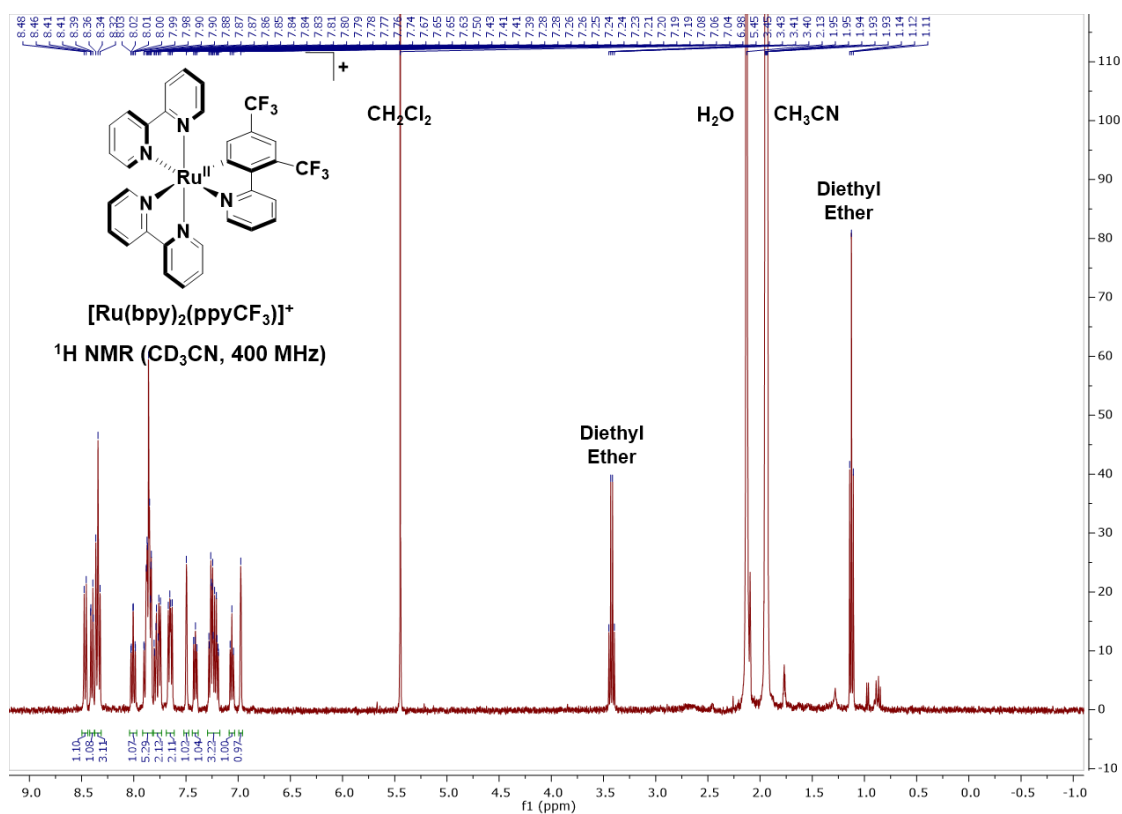


Figure 6.18. ^1H NMR spectrum of $[\text{Ru}(\text{bpy})_2(\text{ppyCF}_3)]^+$ in CD_3CN at 400 MHz and 298 K.

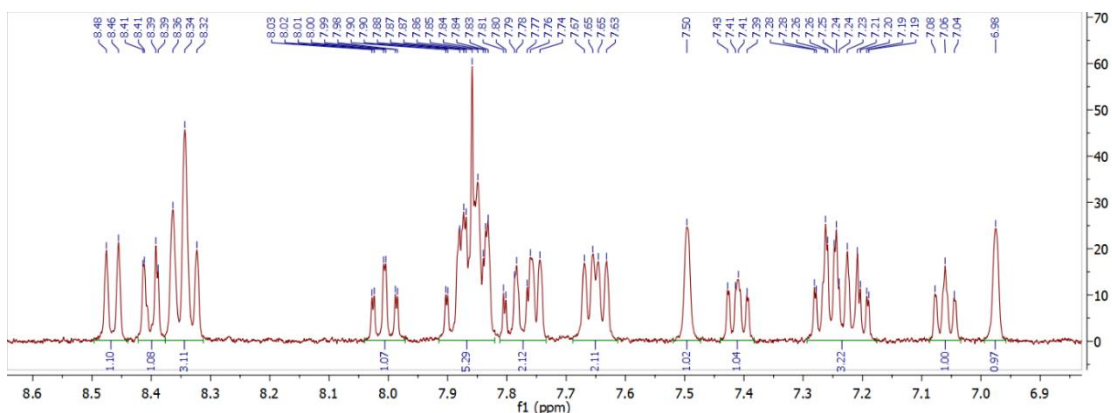


Figure 6.19. ^1H NMR spectrum of the aromatic region for $[\text{Ru}(\text{bpy})_2(\text{ppyCF}_3)]^+$ in CD_3CN at 400 MHz and 298 K.

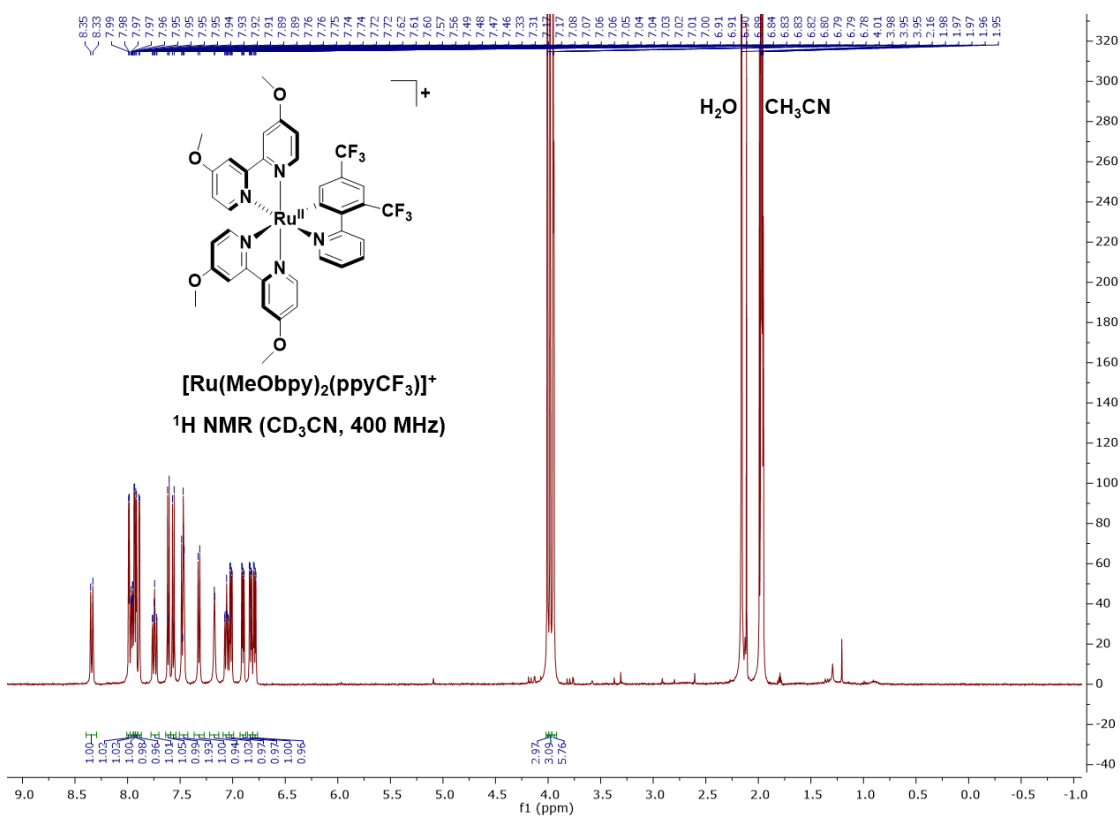


Figure 6.20. ^1H NMR spectrum of $[\text{Ru}(\text{MeObpy})_2(\text{ppyCF}_3)]^+$ in CD_3CN at 400 MHz and 298 K.

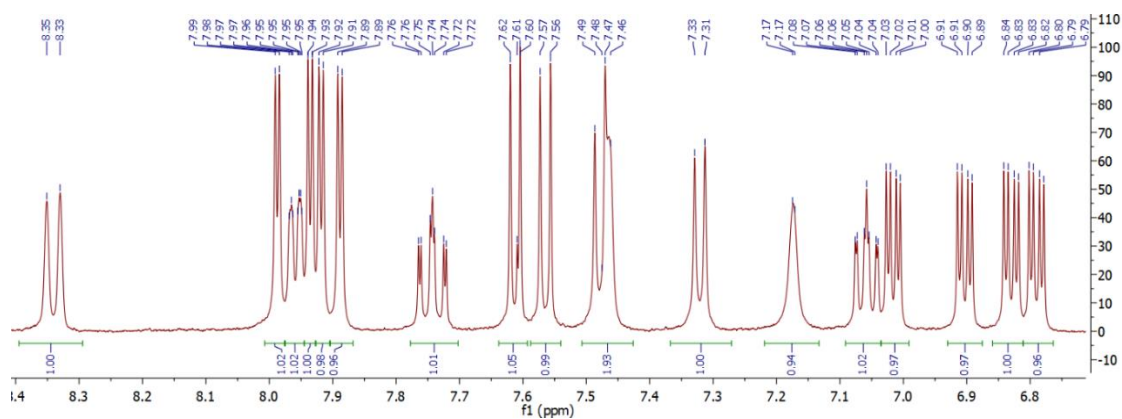


Figure 6.21. ^1H NMR spectrum of the aromatic region for $[\text{Ru}(\text{MeObpy})_2(\text{ppyCF}_3)]^+$ in CD_3CN at 400 MHz and 298 K.

REFERENCES

- (1) Ardo, S.; Meyer, G. J. Photodriven heterogeneous charge transfer with transition-metal compounds anchored to TiO₂ semiconductor surfaces. *Chem. Soc. Rev.* **2009**, 38, 115-164.
- (2) Meyer, T. J. Chemical Approaches to Artificial Photosynthesis. *Acc. Chem. Res.* **1989**, 22, 163-170.
- (3) Teegardin, K.; Day, J. I.; Chan, J.; Weaver, J. Advances in Photocatalysis: A Microreview of Visible Light Mediated Ruthenium and Iridium Catalyzed Organic Transformations. *Org. Process Res. Dev.* **2016**, 20, 1156-1163.
- (4) Ashford, D. L.; Gish, M. K.; Vannucci, A. K.; Brennaman, M. K.; Templeton, J. L.; Papanikolas, J. M.; Meyer, T. J. Molecular Chromophore–Catalyst Assemblies for Solar Fuel Applications. *Chem. Rev.* **2015**, 115, 13006-13049.
- (5) Beer, P. D.; Cadman, J. Electrochemical and optical sensing of anions by transition metal based receptors. *Coord. Chem. Rev.* **2000**, 205, 131-155.
- (6) Higgins, S. L. H.; Brewer, K. J. Designing Red-Light-Activated Multifunctional Agents for the Photodynamic Therapy. *Angew. Chem. Int. Ed.* **2012**, 51, 11420-11422.
- (7) White, J. K.; Schmehl, R. H.; Turro, C. An overview of photosubstitution reactions of Ru(II) imine complexes and their application in photobiology and photodynamic therapy. *Inorg. Chim. Acta* **2017**, 454, 7-20.
- (8) Paris, J. P.; Brandt, W. W. Charge Transfer Luminescence of a Ruthenium(II) Chelate. *J. Am. Chem. Soc.* **1959**, 81, 5001-5002.
- (9) Meyer, T. J. Photochemistry of metal coordination complexes: metal to ligand charge transfer excited states. *Pure Appl. Chem.* **1986**, 58, 1193-1206.
- (10) Forster, L. S. Thermal relaxation in excited electronic states of d³ and d⁶ metal complexes. *Coord. Chem. Rev.* **2002**, 227, 59-92.
- (11) Meyer, T. J. Excited-State Electron Transfer. In *Prog. Inorg. Chem.*; John Wiley & Sons, Inc.: 2007; pp 389-440.
- (12) Wagenknecht, P. S.; Ford, P. C. Metal centered ligand field excited states: Their roles in the design and performance of transition metal based photochemical molecular devices. *Coord. Chem. Rev.* **2011**, 255, 591-616.
- (13) Thompson, D. W.; Ito, A.; Meyer, T. J., [Ru(bpy)₃]^{2+*} and other remarkable metal-to-ligand charge transfer (MLCT) excited states. *Pure Appl. Chem.* **2013**, 85, 1257.
- (14) Sun, Q.; Mosquera-Vazquez, S.; Suffren, Y.; Hankache, J.; Amstutz, N.; Lawson Daku, L. M.; Vauthey, E.; Hauser, A. On the role of ligand-field states for the photophysical

- properties of ruthenium(II) polypyridyl complexes. *Coord. Chem. Rev.* **2015**, 282–283, 87-99.
- (15) Troian-Gautier, L.; Moucheron, C. Ruthenium^{II} Complexes bearing Fused Polycyclic Ligands: From Fundamental Aspects to Potential Applications. *Molecules* **2014**, *19*, 5028-5087.
- (16) Wadman, S. H.; Kroon, J. M.; Bakker, K.; Lutz, M.; Spek, A. L.; van Klink, G. P. M.; van Koten, G. Cyclometalated ruthenium complexes for sensitizing nanocrystalline TiO₂ solar cells. *Chem. Commun.* **2007**, 1907-1909.
- (17) Bessho, T.; Yoneda, E.; Yum, J.-H.; Guglielmi, M.; Tavernelli, I.; Imai, H.; Rothlisberger, U.; Nazeeruddin, M. K.; Grätzel, M. New Paradigm in Molecular Engineering of Sensitizers for Solar Cell Applications. *J. Am. Chem. Soc.* **2009**, *131*, 5930-5934.
- (18) Bomben, P. G.; Robson, K. C. D.; Koivisto, B. D.; Berlinguette, C. P. Cyclometalated ruthenium chromophores for the dye-sensitized solar cell. *Coord. Chem. Rev.* **2012**, *256*, 1438-1450.
- (19) Fernandez, S.; Pfeffer, M.; Ritleng, V.; Sirlin, C. An Effective Route to Cycloruthenated N-Ligands under Mild Conditions. *Organometallics* **1999**, *18*, 2390-2394.
- (20) Reveco, P.; Schmehl, R. H.; Cherry, W. R.; Fronczek, F. R.; Selbin, J. Cyclometalated Complexes of Ruthenium. 2. Spectral and Electrochemical Properties and X-ray Structure of Bis(2,2'-bipyridine)(4-nitro-2-(2-pyridyl)phenyl)ruthenium(II). *Inorg. Chem.* **1985**, *24*, 4078-4082.
- (21) Muro-Small, M. L.; Yarnell, J. E.; McCusker, C. E.; Castellano, F. N. Spectroscopy and Photophysics in Cyclometalated Ru^{II}-Bis(bipyridyl) Complexes. *Eur. J. Inorg. Chem.* **2012**, *2012*, 4004-4011.
- (22) Hager, G. D.; Crosby, G. A. Charge-Transfer Excited States of Ruthenium(II) Complexes. I. Quantum Yield and Decay Measurements. *J. Am. Chem. Soc.* **1975**, *97*, 7031-7037.
- (23) Hipps, K. W.; Crosby, G. A. Charge-Transfer Excited States of Ruthenium(II) Complexes. III. Electron-Ion Coupling Model for dπ* Configurations. *J. Am. Chem. Soc.* **1975**, *97*, 7042-7048.
- (24) Durham, B.; Caspar, J. V.; Nagle, J. K.; Meyer, T. J. Photochemistry of Ru(bpy)₃^{2+*}. *J. Am. Chem. Soc.* **1982**, *104*, 4803-4810.
- (25) Creutz, C.; Chou, M.; Netzel, T. L.; Okumura, M.; Sutin, N. Lifetimes, Spectra, and Quenching of the Excited States of Polypyridine Complexes of Iron(II), Ruthenium(II), and Osmium(II). *J. Am. Chem. Soc.* **1980**, *102*, 1309-1319.

- (26) Yeh, A. T.; Shank, C. V.; McCusker, J. K. Ultrafast Electron Localization Dynamics Following Photo-Induced Charge Transfer. *Science* **2000**, 289, 935-938.
- (27) Crosby, G. A.; Demas, J. N. Quantum Efficiencies on Transition Metal Complexes. II. Charge-Transfer Luminescence. *J. Am. Chem. Soc.* **1971**, 93, 2841-2847.
- (28) Harrigan, R. W.; Hager, G. D.; Crosby, G. A. Evidence for Multiple-State Emission from Ruthenium(II) Complexes. *Chem. Phys. Lett.* **1973**, 21, 487-490.
- (29) Rillema, D. P.; Allen, G.; Meyer, T. J.; Conrad, D. Redox Properties of Ruthenium(II) Tris Chelate Complexes Containing the Ligands 2,2'-Bipyrazine, 2,2'-Bipyridine, and 2,2'-Bipyrimidine. *Inorg. Chem.* **1983**, 22, 1617-1622.
- (30) Ito, A.; Meyer, T. J. The Golden Rule. Application for fun and profit in electron transfer, energy transfer, and excited-state decay. *Phys. Chem. Chem. Phys.* **2012**, 14, 13731-13745.
- (31) Hager, G. D.; Watts, R. J.; Crosby, G. A. Charge-Transfer Excited States of Ruthenium(II) Complexes. II. Relation of Level Parameters to Molecular Structure. *J. Am. Chem. Soc.* **1975**, 97, 7037-7042.
- (32) Kober, E. M.; Meyer, T. J. An electronic structural model for the emitting MLCT excited states of $\text{Ru}(\text{bpy})_3^{2+}$ and $\text{Os}(\text{bpy})_3^{2+}$. *Inorg. Chem.* **1984**, 23, 3877-3886.
- (33) Van Houten, J.; Watts, R. J. Photochemistry of Tris(2,2'-bipyridyl)ruthenium(II) in Aqueous Solutions. *Inorg. Chem.* **1978**, 17, 3381-3385.
- (34) Barigelletti, F.; Juris, A.; Balzani, V.; Belser, P.; Von Zelewsky, A. Excited-State Properties of Complexes of the $\text{Ru}(\text{diimine})_3^{2+}$ Family. *Inorg. Chem.* **1983**, 22, 3335-3339.
- (35) Wacholtz, W. F.; Auerbach, R. A.; Schmehl, R. H. Independent Control of Charge-Transfer and Metal-Centered Excited States in Mixed-Ligand Polypyridine Ruthenium(II) Complexes via Specific Ligand Design. *Inorg. Chem.* **1986**, 25, 227-234.
- (36) Lumpkin, R. S.; Kober, E. M.; Worl, L. A.; Murtaza, Z.; Meyer, T. J. Metal-to-Ligand Charge-Transfer (MLCT) Photochemistry: Experimental Evidence for the Participation of a Higher Lying MLCT State in Polypyridyl Complexes of Ruthenium(II) and Osmium(II). *J. Phys. Chem.* **1990**, 94, 239-243.
- (37) O'Donnell, R. M.; Johansson, P. G.; Abrahamsson, M.; Meyer, G. J. Excited-State Relaxation of Ruthenium Polypyridyl Compounds Relevant to Dye-Sensitized Solar Cells. *Inorg. Chem.* **2013**, 52, 6839-6848.
- (38) Bomben, P. G.; Robson, K. C. D.; Sedach, P. A.; Berlinguette, C. P. On the Viability of Cyclometalated Ru(II) Complexes for Light-Harvesting Applications. *Inorg. Chem.* **2009**, 48, 9631-9643.

- (39) Bomben, P. G.; Koivisto, B. D.; Berlinguette, C. P. Cyclometalated Ru Complexes of Type $[\text{Ru}^{\text{II}}(\text{N}^{\wedge}\text{N})_2(\text{C}^{\wedge}\text{N})]^z$: Physicochemical Response to Substituents Installed on the Anionic Ligand. *Inorg. Chem.* **2010**, *49*, 4960-4971.
- (40) Kreitner, C.; Heinze, K. Excited state decay of cyclometalated polypyridine ruthenium complexes: insight from theory and experiment. *Dalton Trans.* **2016**, *45*, 13631-13647.
- (41) Farnum, B. H.; Gardner, J. M.; Marton, A.; Narducci-Sarjeant, A. A.; Meyer, G. J. Influence of ion pairing on the oxidation of iodide by MLCT excited states. *Dalton Trans.* **2011**, *40*, 3830-3838.
- (42) Huang, J.-F.; Liu, J.-M.; Su, P.-Y.; Chen, Y.-F.; Shen, Y.; Xiao, L.-M.; Kuang, D.-B.; Su, C.-Y. Highly efficient and stable cyclometalated ruthenium(II) complexes as sensitizers for dye-sensitized solar cells. *Electrochim. Acta* **2015**, *174*, 494-501.
- (43) Ciana, L. D.; Dressick, W. J.; Von Zelewsky, A. Synthesis of 4,4'-Divinyl-2,2'-bipyridine. *J. Heterocycl. Chem.* **1990**, *27*, 163-165.
- (44) Oki, A. R.; Morgan, R. J. An Efficient Preparation of 4, 4'-Dicarboxy-2, 2'-Bipyridine. *Synth. Commun.* **1995**, *25*, 4093-4097.
- (45) Shavaleev, N. M.; Monti, F.; Scopelliti, R.; Armaroli, N.; Grätzel, M.; Nazeeruddin, M. K. Blue Phosphorescence of Trifluoromethyl- and Trifluoromethoxy-Substituted Cationic Iridium(III) Isocyanide Complexes. *Organometallics* **2012**, *31*, 6288-6296.
- (46) Bouilly, L.; Turck, A.; Plé, N.; Darabantu, M. Aryl-aryl bonds formation in pyridine and diazine series. Diazines part 41. *J. Heterocycl. Chem.* **2005**, *42*, 1423-1428.
- (47) Bergeron, B. V.; Meyer, G. J. Reductive Electron Transfer Quenching of MLCT Excited States Bound To Nanostructured Metal Oxide Thin Films. *J. Phys. Chem. B* **2003**, *107*, 245-254.
- (48) Kelly, C. A.; Farzad, F.; Thompson, D. W.; Meyer, G. J. Excited-State Deactivation of Ruthenium(II) Polypyridyl Chromophores Bound to Nanocrystalline TiO_2 Mesoporous Thin Films. *Langmuir* **1999**, *15*, 731-737.
- (49) Soman, S.; Xie, Y.; Hamann, T. W. Cyclometalated sensitizers for DSSCs employing cobalt redox shuttles. *Polyhedron* **2014**, *82*, 139-147.
- (50) Bomben, P. G.; Gordon, T. J.; Schott, E.; Berlinguette, C. P. A Trisheteroleptic Cyclometalated Ru^{II} Sensitizer that Enables High Power Output in a Dye-Sensitized Solar Cell. *Angew. Chem. Int. Ed.* **2011**, *50*, 10682-10685.
- (51) Ryabov, A. D.; Le Lagadec, R.; Estevez, H.; Toscano, R. A.; Hernandez, S.; Alexandrova, L.; Kurova, V. S.; Fischer, A.; Sirlin, C.; Pfeffer, M. Synthesis, Characterization, and Electrochemistry of Biorelevant Photosensitive Low-Potential Orthometalated Ruthenium Complexes. *Inorg. Chem.* **2005**, *44*, 1626-1634.

- (52) Aguilar-Lugo, C.; Le Lagadec, R.; Ryabov, A. D.; Valverde, G. C.; Morales, S. L.; Alexandrova, L. "Living" Radical Polymerization of Styrene Catalyzed by Cyclometalated Ruthenium(II) Complexes Bearing Nonlabile Ligands. *J. Polym. Sci., Part A: Polym. Chem.* **2009**, *47*, 3814-3828.
- (53) Fulmer, G. R.; Miller, A. J. M.; Sherden, N. H.; Gottlieb, H. E.; Nudelman, A.; Stoltz, B. M.; Bercaw, J. E.; Goldberg, K. I. NMR Chemical Shifts of Trace Impurities: Common Laboratory Solvents, Organics, and Gases in Deuterated Solvents Relevant to the Organometallic Chemist. *Organometallics* **2010**, *29*, 2176-2179.
- (54) Bard, A. J.; Faulkner, L. R. *Electrochemical Methods : Fundamentals and Applications*. 2nd Edition ed.; Wiley: New York, 2001.
- (55) Kober, E. M.; Caspar, J. V.; Lumpkin, R. S.; Meyer, T. J. Application of the Energy Gap Law to Excited-State Decay of Osmium(II)-Polypyridine Complexes: Calculation of Relative Nonradiative Decay Rates from Emission Spectral Profiles. *J. Phys. Chem.* **1986**, *90*, 3722-3734.
- (56) Crosby, G. A.; Demas, J. N. The Measurement of Photoluminescence Quantum Yields. A Review. *J. Phys. Chem.* **1971**, *75*, 991-1024.
- (57) Ishida, H.; Tobita, S.; Hasegawa, Y.; Katoh, R.; Nozaki, K. Recent advances in instrumentation for absolute emission quantum yield measurements. *Coord. Chem. Rev.* **2010**, *254*, 2449-2458.
- (58) Parker, C. A.; Rees, W. T. Correction of Fluorescence Spectra and Measurement of Fluorescence Quantum efficiency. *Analyst* **1960**, *85*, 587-600.
- (59) Preus, S. *DecayFit - Fluorescence Decay Analysis Software*, 1.4; FluorTools: www.fluortools.com.
- (60) Sun, Y.; Machala, M. L.; Castellano, F. N. Controlled microwave synthesis of Ru^{II} synthons and chromophores relevant to solar energy conversion. *Inorg. Chim. Acta* **2010**, *363*, 283-287.
- (61) O'Dea, J. J.; Osteryoung, J.; Osteryoung, R. A. Theory of Square Wave Voltammetry for Kinetic Systems. *Anal. Chem.* **1981**, *53*, 695-701.
- (62) Osteryoung, J. G.; Osteryoung, R. A. Square Wave Voltammetry. *Anal. Chem.* **1985**, *57*, 101-110.
- (63) Tamayo, A. B.; Alleyne, B. D.; Djurovich, P. I.; Lamansky, S.; Tsyba, I.; Ho, N. N.; Bau, R.; Thompson, M. E. Synthesis and Characterization of Facial and Meridional Tris-cyclometalated Iridium(III) Complexes. *J. Am. Chem. Soc.* **2003**, *125*, 7377-7387.
- (64) Farnum, B. H.; Jou, J. J.; Meyer, G. J. Visible light generation of I-I bonds by Ru-tris(diimine) excited states. *Proc. Natl. Acad. Sci. U.S.A.* **2012**, *109*, 15628-15633.

- (65) Ashford, D. L.; Glasson, C. R. K.; Norris, M. R.; Concepcion, J. J.; Keinan, S.; Brennaman, M. K.; Templeton, J. L.; Meyer, T. J. Controlling Ground and Excited State Properties through Ligand Changes in Ruthenium Polypyridyl Complexes. *Inorg. Chem.* **2014**, *53*, 5637-5646.
- (66) Staehle, R.; Reichardt, C.; Popp, J.; Sorsche, D.; Petermann, L.; Kastner, K.; Streb, C.; Dietzek, B.; Rau, S. Ruthenium Imidazophenanthroline Complexes with Prolonged Excited-State Lifetimes. *Eur. J. Inorg. Chem.* **2015**, *2015*, 3932-3939.
- (67) Robson, K. C. D.; Bomben, P. G.; Berlinguette, C. P. Cycloruthenated sensitizers: improving the dye-sensitized solar cell with classical inorganic chemistry principles. *Dalton Trans.* **2012**, *41*, 7814-7829.
- (68) Bomben, P. G.; Thériault, K. D.; Berlinguette, C. P. Strategies for Optimizing the Performance of Cyclometalated Ruthenium Sensitizers for Dye-Sensitized Solar Cells. *Eur. J. Inorg. Chem.* **2011**, *2011*, 1806-1814.
- (69) Caspar, J. V.; Meyer, T. J. Application of the Energy Gap Law to Nonradiative, Excited-State Decay. *J. Phys. Chem.* **1983**, *87*, 952-957.
- (70) Caspar, J. V.; Kober, E. M.; Sullivan, B. P.; Meyer, T. J. Application of the Energy Gap Law to the Decay of Charge-Transfer Excited States. *J. Am. Chem. Soc.* **1982**, *104*, 630-632.
- (71) Bradley, P. G.; Kress, N.; Hornberger, B. A.; Dallinger, R. F.; Woodruff, W. H. Vibrational Spectroscopy of the Electronically Excited State. 5. Time-Resolved Resonance Raman Study of Tris(bipyridine)ruthenium(II) and Related Complexes. Definitive Evidence for the "Localized" MLCT State. *J. Am. Chem. Soc.* **1981**, *103*, 7441-7446.
- (72) Danzer, G. D.; Kincaid, J. R. Resonance Raman Spectra of Homoleptic and Heteroleptic Complexes of Ruthenium(II) with Bipyridine and Bipyrazine in the Ground and ³MLCT Excited States. *J. Phys. Chem.* **1990**, *94*, 3976-3980.
- (73) Barqawi, K. R.; Murtaza, Z.; Meyer, T. J. Calculation of Relative Nonradiative Decay Rate Constants from Emission Spectral Profiles: Polypyridyl Complexes of Ruthenium(II). *J. Phys. Chem.* **1991**, *95*, 47-50.
- (74) Freed, K. F.; Jortner, J. Multiphonon Processes in the Nonradiative Decay of Large Molecules. *J. Chem. Phys.* **1970**, *52*, 6272-6291.
- (75) Englman, R.; Jortner, J. The energy gap law for radiationless transitions in large molecules. *Mol. Phys.* **1970**, *18*, 145-164.